

RECENT ADVANCES in ENERGY, ENVIRONMENT and MATERIALS

**Proceedings of the 2014 International Conference on Energy,
Environment and Material Science (EEMAS '14)**

**Saint Petersburg State Polytechnic University
Saint Petersburg, Russia
September 23-25, 2014**



RECENT ADVANCES in ENERGY, ENVIRONMENT and MATERIALS

**Proceedings of the 2014 International Conference on Energy,
Environment and Material Science (EEMAS '14)**

**Saint Petersburg State Polytechnic University
Saint Petersburg, Russia
September 23-25, 2014**

Copyright © 2014, by the editors

All the copyright of the present book belongs to the editors. All rights reserved. No part of this publication may be reproduced, stored in a retrieval system, or transmitted in any form or by any means, electronic, mechanical, photocopying, recording, or otherwise, without the prior written permission of the editors.

All papers of the present volume were peer reviewed by no less than two independent reviewers. Acceptance was granted when both reviewers' recommendations were positive.

Series: Energy, Environmental and Structural Engineering Series | 28

ISSN: 2227-4359

ISBN: 978-1-61804-250-7

RECENT ADVANCES in ENERGY, ENVIRONMENT and MATERIALS

**Proceedings of the 2014 International Conference on Energy,
Environment and Material Science (EEMAS '14)**

**Saint Petersburg State Polytechnic University
Saint Petersburg, Russia
September 23-25, 2014**

Organizing Committee

Editors:

Prof. Yuri B. Senichenkov, St. Petersburg State Politechnical University, Saint Petersburg, Russia

Prof. V. Korablev, St. Petersburg State Politechnical University, Saint Petersburg, Russia

Prof. Igor Chernorytski, St. Petersburg State Politechnical University, Saint Petersburg, Russia

Prof. N. Korovkin, St. Petersburg State Politechnical University, Saint Petersburg, Russia

Prof. S. Pozdnjkov, St. Petersburg State Politechnical University, Saint Petersburg, Russia

Prof. Klimis Ntalianis, Technological Educational Institute of Athens, Greece

Senior Program Chair

Prof. Ljubiša Kočinac, University of Nis,

Nis, Serbia

Program Chairs

Prof. Yuri B. Senichenkov,

St. Petersburg State Politechnical University,

Saint Petersburg, Russia

Prof. Constantin Udriste,

University Politehnica of Bucharest,

Bucharest

Romania

Prof. Marcia Cristina A. B. Federson,

Universidade de São Paulo,

São Paulo, Brazil

Tutorials Chair

Prof. Yury A. Rossikhin,

Voronezh State University of

Architecture and Civil Engineering,

Voronezh, Russia

Special Session Chair

Prof. Yuri B. Senichenkov,

St. Petersburg State Politechnical

University,

Saint Petersburg, Russia

Workshops Chair

Prof. Sehie Park,

The National Academy of Sciences,

Republic of Korea

Local Organizing Chair

Prof. Vadim Korablev,

St. Petersburg State Politechnical University,

Saint Petersburg, Russia

Publication Chair

Prof. Marina Shitikova,
Voronezh State University of Architecture and
Civil Engineering, Voronezh, Russia

Publicity Committee

Prof. Vjacheslav Yurko,
Saratov State University,
Astrakhanskaya, Russia
Prof. Myriam Lazard
Institut Supérieur d'Ingenierie de la Conception
Saint Die, France

International Liaisons

Professor Jinhu Lu, IEEE Fellow
Institute of Systems Science
Academy of Mathematics and Systems Science
Chinese Academy of Sciences
Beijing 100190, P. R. China
Prof. Olga Martin
Applied Sciences Faculty
Politehnica University of Bucharest
Romania
Prof. Vincenzo Niola
Departement of Mechanical Engineering for Energetics
University of Naples "Federico II"
Naples, Italy
Prof. Eduardo Mario Dias
Electrical Energy and Automation
Engineering Department
Escola Politecnica da Universidade de Sao Paulo
Brazil

Steering Committee

Prof. Dr. H. M. Srivastava, University of Victoria, Canada
Prof. Stefan Siegmund, Technische Universitaet Dresden, Germany
Prof. Natig M. Atakishiyev, National Autonomous University of Mexico, Mexico
Prof. Narcisa C. Apreutesei, Technical University of Iasi, Iasi, Romania
Prof. Imre Rudas, Obuda University, Budapest, Hungary

Program Committee

Prof. Germano Lambert-Torres, Itajuba, MG, Brazil
Prof. Jiri Klima, Technical faculty of CZU in Prague, Czech Republic
Prof. Goricanec Darko, University of Maribor, Maribor, Slovenia
Prof. Ze Santos, Rua A, 119. Conj. Jardim Costa do Sol, Brazil
Prof. Ehab Bayoumi, Chalmers University of Technology, Goteborg, Sweden
Prof. Luis Tavares Rua, Cmte Guyubricht, 119. Conj. Jardim Costa do Sol. Atalaia, Brazil

Prof. Igor Kuzle, Faculty of electrical engineering and computing, Zagreb, Croatia
Prof. Nikolay Djagarov, Technical University of Varna, Bulgaria
Prof. Darko Goricanec, University of Maribor, Maribor, Slovenia
Prof. Maria do Rosario Alves Calado, University of Beira Interior, Portugal
Prof. Gheorghe-Daniel Andreescu, "Politehnica" University of Timisoara, Romania
Prof. Patricia Jota, Av. Amazonas 7675, BH, MG, Brazil
Prof. Frangiskos V. Topalis, National Technical University of Athens, Greece
Prof. Bharat Doshi, John Hopkins University, Maryland, USA
Prof. Gang Yao, University of Illinois at Urbana - Champaign, USA
Prof. Lu Peng, Louisiana State University, Baton Rouge, LA, USA
Prof. Pavel Loskot, Swansea University, UK
Prof. N. Afgan, UNESCO Chair Holder, Instituto Superior Tecnico, Lisbon, Portugal
Prof. F. Akgun, Gebze Kocaeli, Turkey
Prof. Y. Baudoin, Royal Military Academy, Brussels, Belgium
Prof. M. Dasenakis, Dept. of Chemistry, University of Athens, Greece.
Prof. G. E. Froudakis, University of Crete, Herakleion, Greece
Prof. R.S.R. Gorla, Cleveland State University, Cleveland, Ohio, USA
Prof. M. Heiermann, Dr., Department of Technology Assessment and Substance Flow, Potsdam, Germany
Prof. C. Helmis, University of Athens, Athens, Greece
Prof. I. Kazachkov, National Technical University of Ukraine (NTUU KPI), Kyiv, Ukraine
Prof. A. M.A. Kazim, UAE University, United Arab Emirates
Prof. G. Kiriakidis, University of Crete, Herakleion, Greece
Prof. D. Kotzias, Institute for Health and Consumer Protection, European Commission-Joint Research Centre, Italy
Prof. A. Kurbatskiy, Novosibirsk State University, Department of Physics, Russia
Prof. S. Linderoth, Head of Research on Fuel Cells and Materials Chemistry at Riso National Laboratory. Denmark
Prof. P. Lunghi, Dipartimento di Ingegneria Industriale, Universita degli Studi di Perugia, Italy
Prof. C. Makris, A, Department of Computer Engineering and Informatics., University of Patras, Greece
Prof. J. Van Mierlo, Department of Electrotechnical Engineering and Energy Technology (ETEC) Vrije Universiteit Brussel, Belgium
Prof. S. Ozdogan, Marmara University, Goztepe Campus, Kuyubasi, Kadikoy, Istanbul, Turkey
Prof. P. Pardalos, Department of Industrial and Systems Engineering, University of Florida, USA
Prof. I. Poullos, Dept. of Chemistry, Aristotle University of Thessaloniki, Greece.
Prof. F. Rigas, School of Chemical Engineering, National Technical University of Athens, Greece.
Prof. S. Sohrab, Northwestern University, IL, USA
Prof. A. Stamou, National Technical University of Athens, Greece
Prof. A. I. Zouboulis, Dept. of Chemistry, Aristotle University of Thessaloniki, Greece.
Prof. Z. A. Vale, ISEP - Instituto Superior de Engenharia do Porto Rua António Bernardino de Almeida, Portugal
Prof. Zhibing Zhang, University of Birmingham, Birmingham, UK
Prof. Jean-Francois Gohy, Université catholique de Louvain, Belgium
Prof. Waler Caseri, ETH, Zurich, Switzerland
Prof. Jacques Desbrieres, Université De Pau Et Des Pays De L'Adour, France
Prof. Adrian Schumpe, Technical University of Braunschweig, Germany
Prof. Chris Bowen, University of Bath, Bath, UK
Prof. Jerzy Baldyga, Technical University of Warsaw, Poland
Prof. Alirio Rodrigues, University of Porto, Portugal
Prof. Mostafa Barigou, University of Birmingham, Birmingham, UK
Prof. Jaime Wisniak, Ben-Gurion University of the Negev, Beer-Sheva, Israel
Prof. Sohail Murad, University of Illinois at Chicago, USA
Prof. Konstantinos E. Kakosimos, Texas A&M University at Qatar, Doha, Qatar
Prof. Raghunath V. Chaudhari, University of Kansas, USA
Prof. Xijun Hu, The Hong Kong University of Science and Technology, Kowloon, Hong Kong

Prof. Deepak Kunzru, Indian Institute of Technology, Kanpur, India
Prof. Amit Bandyopadhyay, AAAS Fellow , ASM International Fellow , AIMBE Fellow and ACerS Fellow, Washington State University, Pullman, State of Washington, USA
Prof. Yong Ding, Georgia Institute of Technology, Atlanta, GA, USA
Prof. Yulin Deng, Georgia Institute of Technology, Atlanta, GA, USA
Prof. Paul H. Holloway, Distinguished Prof., University of Florida, Gainesville FL, USA
Prof. Saad Khan, North Carolina State University, Raleigh, North Carolina, USA
Prof. Manijeh Razeghi, Northwestern University, Evanston, IL, USA
Prof. Igor Sevostianov, New Mexico State University, Las Cruces, New Mexico, USA
Prof. Mohindar S. Seehra, West Virginia University, Morgantown, West Virginia, USA
Prof. Tao Liu, Florida State University, Tallahassee, Florida, USA
Prof. Daniel Guay, Institut National de la Recherche Scientifique (INRS), Universite du Quebec, Quebec, Canada
Prof. Tian Tang, University of Alberta, Edmonton, Alberta, Canada
Prof. Roland Frankenberger, University of Marburg, Marburg, Germany
Prof. Mohamedally Kurmoo, Universite de Strasbourg, Strasbourg, France
Prof. C. C. Sorrell, University of New South Wales, Sydney, NSW, Australia
Prof. Concepcion Lopez, Universitat de Barcelona, Barcelona, Spain
Prof. Alan Dalton, University of Surrey, Guildford, Surrey, UK
Prof. Kourosh Kalantar-Zadeh, RMIT University, Melbourne, Australia
Prof. Constantinos Tsitsilianis, University of Patras, Patras, Greece
Prof. Tetsu Yonezawa, Hokkaido University, Kita Ward, Sapporo, Hokkaido Prefecture, Japan
Prof. Daolun Chen, Ryerson University, Toronto, Ontario, Canada
Prof. Mohamed M. Chehimi, Universite Paris Diderot, Paris, France
Prof. Vincenzo Fiorentini, Universita degli studi di Cagliari, Cagliari, Italy
Prof. Tamas Ungar, Eotvos Lorand University (ELTE), Budapest, Hungary
Prof. Anthony W. Coleman, Universite Claude Bernard Lyon 1, Lyon, France
Prof. Albert Chin, IEEE Fellow, OSA Fellow, National Chiao Tung University, Hsinchu, Taiwan
Prof. Artur Cavaco-Paulo, Universidade do Minho, Braga, Portugal
Prof. Yoshihiro Tomita, Kobe University, Kobe, Japan
Prof. Jian Wang, Los Alamos National Laboratory, Los Alamos, NM, USA
Prof. Byung K. Kim, Pusan National University, Busan, South Korea
Prof. John T. Sheridan, University College Dublin, Belfield, Dublin, Ireland
Prof. Chi-Wai Chow, National Chiao Tung University, Hsinchu, Taiwan
Prof. Christian M. Julien, Universite Paris-6, Paris, France
Prof. Chun-Hway Hsueh, National Taiwan University, Taipei, Taiwan
Prof. Hyung-Ho Park, Yonsei University, Seodaemun-gu, Seoul, Korea
Prof. Victor M. Castano, Universidad Nacional Autonoma de Mexico, Mexioco City, Mexico
Prof. Peter Chang, University of Saskatchewan, Saskatoon, Saskatchewan, Canada
Prof. Dean-Mo Liu, National Chiao Tung University, HsinChu, Taiwan
Prof. Rui Vilar, Instituto Superior Tecnico, Lisboa, Portugal
Prof. Hugh J. Byrne, Dublin Institute of Technology, Dublin, Ireland
Prof. Won-Chun Oh, Hanseo University, Seosan-si, Chungcheongnam-do, South Korea
Prof. Yuanhua Lin, Tsinghua University, Haidian, Beijing, China
Prof. S.C. Tjong, City University of Hong Kong, Sham Shui Po District, New Kowloon, Hong Kong
Prof. Huan-Tsung Chang, National Taiwan University, Taipei City, Taiwan
Prof. Yoshitake Masuda, National Institute of Advanced Industrial Science and Technology (AIST), Tokyo, Japan
Prof. Jing Zhang, Donghua University, Shanghai, China
Prof. Veronica Cortes de Zea Bermudez, Universidade de Tras-os-Montes e Alto Douro, Vila Real, Portugal
Prof. Jun Zhang, Inner Mongolia University, Hohhot, Inner Mongolia, China
Prof. Israel Felner, Hebrew University of Jerusalem, Jerusalem, Israel
Prof. Sukhvinder Badwal, CSIRO Energy Technology, Australia
Prof. Te-Hua Fang, National Kaohsiung University of Applied Sciences (KUAS), Kaohsiung, Taiwan

Prof. Belkheir Hammouti, Mohammed Premier University, Oujda, Morocco
Prof. Mohd Sapuan Salit, Universiti Putra Malaysia, Selangor, Malaysia
Prof. Kwansoo Chung, Seoul National University, Seoul, South Korea
Prof. Zhongfang Chen, University of Puerto Rico, San Juan, Puerto Rico
Prof. Soon-Ku Hong, Chungnam National University, Daejeon, South Korea
Prof. Hannes Jonsson, University of Iceland, Reykjavik, Iceland
Prof. Culea Eugen, Technical University of Cluj-Napoca, Cluj-Napoca, Romania
Prof. Vesselin Dimitrov, University of Chemical Technology and Metallurgy, Sofia, Bulgaria
Prof. Shadpour Mallakpour, Isfahan University of Technology, Isfahan, Iran
Dr. Stergios Pispas, National Hellenic Research Foundation (NHRF), Athens, Greece
Dr. Anna Lukowiak, Polish Academy of Science, Wroclaw, Poland
Dr. Dimitris Tsiourvas, NCSR "Demokritos", IAMPPNM, Dept. of Physical Chemistry, 15310 Aghia Paraskevi, Attiki, Greece.

Additional Reviewers

Bazil Taha Ahmed	Universidad Autonoma de Madrid, Spain
M. Javed Khan	Tuskegee University, AL, USA
James Vance	The University of Virginia's College at Wise, VA, USA
Minhui Yan	Shanghai Maritime University, China
Angel F. Tenorio	Universidad Pablo de Olavide, Spain
Jose Flores	The University of South Dakota, SD, USA
Francesco Zirilli	Sapienza Universita di Roma, Italy
Kei Eguchi	Fukuoka Institute of Technology, Japan
Jon Burley	Michigan State University, MI, USA
Imre Rudas	Obuda University, Budapest, Hungary
Philippe Dondon	Institut polytechnique de Bordeaux, France
Zhong-Jie Han	Tianjin University, China
George Barreto	Pontificia Universidad Javeriana, Colombia
Frederic Kuznik	National Institute of Applied Sciences, Lyon, France
Stavros Ponis	National Technical University of Athens, Greece
Lesley Farmer	California State University Long Beach, CA, USA
Francesco Rotondo	Polytechnic of Bari University, Italy
Genqi Xu	Tianjin University, China
Manoj K. Jha	Morgan State University in Baltimore, USA
Hessam Ghasemnejad	Kingston University London, UK
Ole Christian Boe	Norwegian Military Academy, Norway
Deolinda Rasteiro	Coimbra Institute of Engineering, Portugal
Masaji Tanaka	Okayama University of Science, Japan
Takuya Yamano	Kanagawa University, Japan
Konstantin Volkov	Kingston University London, UK
José Carlos Metrôlho	Instituto Politecnico de Castelo Branco, Portugal
Moran Wang	Tsinghua University, China
Santoso Wibowo	CQ University, Australia
Yamagishi Hiromitsu	Ehime University, Japan
Kazuhiko Natori	Toho University, Japan
Abelha Antonio	Universidade do Minho, Portugal
Matthias Buyle	Artesis Hogeschool Antwerpen, Belgium
Tetsuya Yoshida	Hokkaido University, Japan
Miguel Carriegos	Universidad de Leon, Spain
Andrey Dmitriev	Russian Academy of Sciences, Russia
Dmitrijs Serdjuks	Riga Technical University, Latvia
Shinji Osada	Gifu University School of Medicine, Japan
Tetsuya Shimamura	Saitama University, Japan
Valeri Mladenov	Technical University of Sofia, Bulgaria
João Bastos	Instituto Superior de Engenharia do Porto, Portugal
Sorinel Oprisan	College of Charleston, CA, USA
Alejandro Fuentes-Penna	Universidad Autónoma del Estado de Hidalgo, Mexico
Xiang Bai	Huazhong University of Science and Technology, China
Eleazar Jimenez Serrano	Kyushu University, Japan

Table of Contents

Plenary Lecture 1: Stiff Models and Gradient Methods with the Exponential Relaxation <i>Igor G. Chernorutskiy</i>	13
Plenary Lecture 2: EMG-Analysis for Enhancing Efficiency and Performance of Electric Power Systems by Using Smart Grid Technology <i>Nikolay V. Korovkin</i>	14
Plenary Lecture 3: Modeling of Mechanism of State and Private Partnership Development of the Social Infrastructure in the Regions <i>Vladimir V. Gluhov</i>	15
Plenary Lecture 4: On Complete Monotonicity of Some Functions of the Mittag-Leffler Type in Non-Debye Relaxation Processes <i>Francesco Mainardi</i>	17
Plenary Lecture 5: From Physical to Mathematical Circuits: Theoretical and Practical Issues <i>Massimo Ceraolo</i>	18
Stand for Testing Asynchronous Machine with Wound Rotor <i>S. German-Galkin, V. Tomasov, A. Egorov</i>	21
Enhancement of Escalator Energy Performance with the Use of Double-Fed Engines <i>Korzinin N. M., Korovkin N. V., Silin N. V.</i>	26
Electromagnetic Forces and Field Distribution under Impulse Magnetic Field Impact on Solids of Revolution Made from Hard Ferromagnetic Materials <i>Egor A. Virva, Vasilij V. Titkov, Sergey I. Krivosheev, Yuri E. Adamyan</i>	32
Comparative Fuel Economy and Environmental Analysis of Conventional Hybrid and Plug-in Hybrid Vehicles <i>Morteza Montazeri-Gahjavarestani, Mehdi Mahmoodi-Kaleybar, Vahid Madanipour</i>	35
Different Approaches for Calculation of EMF Induced by the Currents of Overhead Line in the Shields of Buried Cables <i>Korovkin N. V., Minevich T. G.</i>	43
Improved Hydrolysis of Pretreated Lignocellulosic Biomass Using Mobile Enzyme Sequestration Platforms <i>Ruben Michael Ceballos, Ruben Michael Ceballos Jr., Asha Rani, Chelsea Teresa Morales, Natalia Alekseyevna Batchenkova</i>	47
Estimation of Induced EMF Value in Ground Wire During Ice-Melting Procedure <i>Nikolay Korovkin, Valeriy Goncharov, Nikolay Silin</i>	55

Influence of Process Parameters on the Microstructural and Mechanical Properties of Plasma Sprayed Nanostructured YSZ Coatings	58
<i>C. Lamuta, G. Di Girolamo, P. Caliandro, L. Pagnotta</i>	
Mathematical Model for Calculation of Power Consumption and Electromagnetic Noise of Resistance Welding Machines	66
<i>L. Sakhno, O. Sakhno, S. Dubitsky</i>	
Application of Multiobjective Optimization Methods for Power System State Control	70
<i>Nikolay V. Korovkin N., Mikhail V. Odintsov, Dmitry A. Akimov, Oleg V. Frolov</i>	
Parameters of the Polymerization Process of Error in Determining the Thermochemical Characteristics Insulation	74
<i>Yuliya V. Koroleva, Evgeniya V. Ivanova, Pavel A. Strizhak</i>	
Demand Response in Residential AC Load Using Rescheduling Strategy	77
<i>Monika Arora, Saurabh Chanana</i>	
Multiphysics Finite Element Analysis of Underground Power Cable Ampacity	84
<i>Simon Dubitsky, George Greshnyakov, Nikolay Korovkin</i>	
High Performance Concrete Using Blast Furnace Slag as Coarse Aggregate	90
<i>V. P. Singh</i>	
Capacitance and Impedance Methods of Electric Field Grading in Cable Joint and Termination	95
<i>George V. Greshnyakov, Simon D. Dubitskiy, Nikolay V. Korovkin</i>	
Redundant Generating Supply in Electric Power Systems	100
<i>Nikolay A. Belyaev, Nikolay V. Korovkin, Oleg V. Frolov, Vladimir S. Chudny</i>	
New Approach to the Power Network Protection Against Ultrawide Band Pulses	104
<i>Alexander T. Gazizov, Alexander M. Zabolotsky</i>	
Modeling of Grounding Systems of Power Lines under Pulse Influence	108
<i>Kirill I. Natreba, Nikolay V. Korovkin, Nikolay V. Silin</i>	
Authors Index	114

Plenary Lecture 1

Stiff Models and Gradient Methods with the Exponential Relaxation



Professor Igor G. Chernorutskiy

Saint Petersburg State Polytechnical University

Russia

E-mail: igcher@spbstu.ru

Abstract: 1. For a class of matrix gradient methods a new concept of the relaxation function is suggested. This concept allows to evaluate the effectiveness of each gradient optimization procedure, and to synthesize new methods for special classes of ill conditioned (stiff) non-convex optimization problems. According to the suggested formula , it is possible to build relevant search procedures for any given relaxation function.

2. The theorem about the relaxation conditions of each matrix gradient method is proven. Based on the concept of the relaxation functions it is given the geometric interpretation of relaxation properties of gradient methods. According to this interpretation it is possible to build a relaxation area, and to evaluate the speed of the objective function values decreasing.

3. The analysis of classical matrix gradient schemes such as simple gradient method, Newton's methods, Marquardt method is given. It is shown that the relaxation function and its geometric interpretation gives almost full information about the properties and capabilities of relevant gradient optimization methods.

4. A new class of matrix gradient methods with the exponential relaxation function (ERF) is suggested. It is shown that ERF-method summarizes the classical gradient methods including Newton methods, and Marquardt method. In contrast to these methods, ERF-methods have the relaxation functions, entirely located in the relaxation area, which significantly increases the computational efficiency of gradient methods.

5. The ERF-methods convergence for a wide class of non-convex objective functions is established.

Brief Biography of the Speaker: Dr. Chernorutskiy currently is a Professor of Saint-Petersburg State Polytechnical University (SPbSPU). Degrees (SPbSPU): Professor, 1990; Doctor of Technical Science, 1987; Associate Professor, 1982; Ph.D., 1978; M.S., 1970.

Professor Chernorutskiy is the Chair of Information & Control Systems Division of Computer Science and Engineering School (CSES).

Research Interests

Applied Software Engineering, Optimization Tools, Real - Time Systems Modeling and Simulation, Parameter Estimation, and Adaptive Optimization, Decision Support Systems, Artificial Intelligence and Expert Systems.

Plenary Lecture 2

Enhancing Efficiency and Performance of Electric Power Systems by Using Smart Grid Technology



Professor Nikolay V. Korovkin

Chef of Theoretical Electrical Engineering Department
Saint Petersburg State Polytechnical University
Russia

E-mail: nikolay.korovkin@gmail.com

Abstract: A new approach for optimization of power system states with Smart grid utilities will be proposed.

The development of electric power systems (EPS) goes to the construction of power plants, connection of new consumers to networks, introduction into service of new power transmission lines. The complication of electric power system structure and configuration results in reduction of their flexibility and has an adverse effect on the main indices of EPS performance: power distribution losses, power quality and power supply security. Actual conditions of operation and development of large EPS call for new control techniques to be introduced, that is why the elaboration of methods to control the power system operation and to optimize its states with respect to various criteria is now the trend of scientific researches of current concern.

Brief Biography of the Speaker: Education (degrees, dates, universities):

1978, Leningrad Polytechnic Institute, research engineer

1984, Leningrad State University, candidate of science (Phd)

1997, Saint Petersburg Polytechnic university, doctor of science

Career/Employment (employers, positions and dates):

1978, Leningrad State University, assistance professor

1984, Leningrad State University, docent

1997, Saint Petersburg Polytechnical university, professor

2010, Saint Petersburg Polytechnical university, head of Theoretical Electrical Engineering department

Plenary Lecture 3

Modeling of Mechanism of State and Private Partnership Development of the Social Infrastructure in the Regions



Professor, Doctor of Science, Vice Rector Vladimir V. Gluhov

Saint Petersburg State Polytechnical University
Polytechnicheskaja str., 29, 195251, St. Petersburg
Russia

E-mail: vicerector.me@spbstu.ru

Abstract: 1. There are identified and analyzed the problems of development of social infrastructure in the regions of Russia. It is developed the mechanism and proposed the forms of cooperation for their solution on the basis of private and state partnership.
2. It is developed institutional framework for interaction between city administrations and business communities, aimed at creating an environment for effective development of the social infrastructure in the regions.
3. It is developed the game theory approach for modeling the interaction of city administrations and businesses considering the possible development of the institutional environment.
4. It is described a class of cooperative games simulating the interaction of businesses and city administration.
5. It is proposed a mechanism for solving the problems of social infrastructure development based on the analysis of game interaction models of city administrations and businesses.

Brief Biography of the Speaker: Vice-Rector for administrative and economic activity of St. Petersburg State Polytechnic University, Professor of Russian-German Center of Management and Marketing “Progress”, laureate of state prize “President of Russian Federation Prize in Higher Education”, laureate of St. Petersburg governor prize for excellence in higher education, laureate of V.V. Novozhilov prize (the Russian Academy of Sciences).

Member of following Academies:

- International Academy of Technological Cybernetics
- International Academy of Informational Support
- Baltic Academy of Informational Support
- International Academy of Ecology and Security Sciences
- Academy of Humanities
- International Academy of Higher School Science
- Academy of Municipal Sciences

The scholarly works of Vladimir V. Gloukhov develop the “effective management” research area.

Vladimir V. Gloukhov developed the full system of optimization mathematical models for iron and steel enterprises, which found their places in engineering practice and were described in “Mathematical methods and models in manufacturing planning and management” scientific work. These models formed a basis of new school of thought and applied research area – optimization models of iron and steel production.

Vladimir V. Gloukhov has also developed some methods of economic analysis of newest technological processes (in the fields of powder metallurgy, laser processing, ferrous and non-ferrous industry), which have later been implemented in many production enterprises of Russia. The theory of economic analysis of newest technological processes allowed to form the “economics and management of innovation technologies” educational direction.

Plenary Lecture 4

On Complete Monotonicity of Some Functions of the Mittag-Leffler Type in Non-Debye Relaxation Processes



Professor Francesco Mainardi

Department of Physics, University of Bologna, and INFN
Via Irnerio 46, I-40126 Bologna, Italy
E-mail: francesco.mainardi@bo.infn.it.it

Abstract: In this talk we discuss some interesting examples of relaxation occurring in viscoelastic and dielectric materials, which are described by special completely monotone functions of the Mittag-Leffler type. This means that these response functions are represented by continuous distributions of elementary (i.e. exponential) relaxation processes via non-negative spectra of relaxation in frequency or time. In addition to the well known functions of Mittag-Leffler type in one and two parameters, we revisit two more general kinds of Mittag-Leffler functions in three parameters, that is the Prabhakar and the Kilbas-Saigo functions. For all these functions we prove the conditions on the parameters to ensure the complete monotonicity and compute the corresponding frequency spectra. For some study-cases we present numerical results with illustrative plots for the field variable and for the corresponding spectral distribution. We hope that our results can be adopted when the field variable is the response function associated with non-Debye relaxation processes found e.g. in dielectrics. In particular we have derived as noteworthy particular cases the classical models of non-Debye relaxation phenomena referred to as Cole-Cole, Davidson-Cole, Havriliak-Negami along with the so-called Kohlrausch-Williams-Watts (KWW) law based on the stretched exponential function.

Brief Biography of the Speaker: For a full biography, list of references on author's papers and books see:

Home Page: <http://www.fracalmo.org/mainardi/index.htm>

and <http://scholar.google.com/citations?user=UYxWyEEAAA&hl=en&oi=ao>

Plenary Lecture 5

From Physical to Mathematical Circuits: Theoretical and Practical Issues



Professor Massimo Ceraolo

University of Pisa

Italy

E-mail: massimo.ceraolo@unipi.it

Abstract: Electrical engineers typically talk about “circuits”, without first defining what a circuit really is. If we mean circuits to be sets of elements containing insulating and conducting material, as well as magnetic material, nearly everything is a circuit.

If, instead, we mean circuits as “sets of elements in which some wires that connect components to each other are clearly distinguishable”, they constitute a set (the set of all possible circuits) that is a bit more limited, and maybe clear enough.

When talking about circuits, typically electrical engineers think of this latter definition. In addition, they typically assume that Kirchhoff’s equations are valid for all circuits.

This creates theoretical and practical issues that are normally underestimated. In particular:

- Kirchhoff’s laws are not valid in general. In the speech examples of “circuits” (according to the above definition) for which they are not valid are reported;
- the very concept of “potential” of points of the circuits is vague if not totally wrong.

The speech will discuss this inconsistency thoroughly and proposes a solution to the issues the following approach:

- Systems in which electric and magnetic phenomena occur are simply called electromagnetic systems; for them Maxwell’s equations are valid, where Kirchhoff’s laws not only are not valid, but even loose meaning
- Systems in which electric magnetic phenomena occur and have a circuital shape, i.e. are composed by lumped components connected to each other by means of insulated wires, are called physical circuits. For them Maxwell’s equations are still valid; they are susceptible to be abstracted in such a way that, under given conditions, mathematical circuits can be inferred from them
- Mathematical circuits, or simply circuits, are abstracted structures, that constitute under given conditions, approximations of actual physical circuits, for which Kirchhoff’s equations are valid, or better, are postulated to be valid. As such, Kirchhoff’s equations are just the version of the continuity (charge conservation) equation and energy conservation for mathematical circuits. Instead of the Maxwell’s equations, for circuits Kirchhoff’s and constitutive equations are valid.

Once circuits (the short name of mathematical circuits) are defined, not all problems are solved.

In the speech, the author shows that to obtain circuits from physical circuits containing transmission lines, for which Kirchhoff's laws are valid, is not always possible; however, a special version of them, that will be called metacircuit, will be introduced.

Again, it will be discussed that in circuits with ideal transformers do not allow Kirchhoff's laws to be written in their more common form, and special treatment is needed.

Circuits are lumped component systems: i.e., systems composed by components that are connected to each other through interfaces. Therefore their behavior over time can be computer-simulated using object-oriented tools and languages. The final part of the speech will show that the modern simulation language Modelica has an approach that is one perfectly in line with the analysis of this speech, and even the graphical tricks used to evidence lumped components and connections are in total agreement with the Modelica approach.

This gives additional usefulness to the approach proposed in the speech, and in its companion paper.

Brief Biography of the Speaker: Born in 1960, he took his Ms Degree in Electrical Engineering from the University of Pisa, with honours, in 1985. For some years he has worked in an Italian private research centre. Since 1992 he has been working in Electric Power Systems first as a researcher, then as a professor.

He is full professor of Electric Power Systems since 2002, and teaches Electric and Hybrid Vehicles at the University of Pisa and on-board Electrical Systems at the Naval Academy of Livorno.

He is author or co-author of more than one hundred National and International scientific papers, mainly regarding power systems, electrochemical energy storage, and electric and hybrid vehicles.

He is the chairman of the School of Engineering of the University of Pisa, that coordinates teaching activities of around 250 researchers and professors.

He is the main author of the IEEE-Wiley book "Fundamentals of Electric Power Engineering – from Electromagnetics to Power Systems".

Stand for testing asynchronous machine with wound rotor

S. German-Galkin, V. Tomasov, A. Egorov

Abstract—This paper is about creating energy-saving test stands for asynchronous machine with a wound rotor. Proposed solutions allow to reduce by 5-10 time energy consumption of asynchronous machine during acceptance tests. The power from an external source of energy is spent only to compensate for losses and its consumption is minimal.

Keywords—Asynchronous machine with wound rotor, double-fed machine, energy consumption, energy efficiency, energy-saving test stands.

I. INTRODUCTION

A necessary step in the creation, operation and maintenance of electromechanical energy converters involves acceptance tests, confirming successful holding of the design performed, manufacture or repair and availability of the electric machine for use with specified technical parameters.

In recent years the requirements for energy efficiency of these tests have sharply increased, forcing the management of enterprises to think of new strategies in the field of energy resources consumption and to seek necessary engineering solutions to reduce them.

At present the engineering solutions to drastically reduce energy expenditure of machine-building enterprises, when conducting acceptance tests of electric machines, lie in the field of creating energy-saving test stands (ETS).

These stands are characterized by two fundamental features:

- 1) There is a closed energy loop consisting of two electric machines and making it possible to provide energy transmission between them, and in doing so one machine provides direct transmission of energy, and the second transmits energy in the opposite direction [4]. Thereby their mutual loading is achieved.
- 2) Owing to artificially implemented energy coupling between the two machines, the power from an external source of energy is spent only to compensate for losses and its consumption is minimal. Thus a considerable, 5-

This work is done with State financial backing of leading universities of the Russian Federation (grant 074-U01).

S. G. German-Galkin, professor of Maritime University Szczecin, Republic of Poland, professor of National Research University ITMO, Russian Federation (phone: 007-812-2338336; e-mail: ggsg@ya.ru).

V. S. Tomasov, Ph.D., National Research University ITMO, Russian Federation (phone: 007-812-2338336, e-mail: tomasov@ets.ifmo.ru).

A. V. Egorov, scientific associate, National Research University ITMO, Russian Federation (e-mail: alexeykey@rambler.ru).

10 times, energy saving is achieved that is especially important for high-power electric machines during long-time life tests [4].

II. FUNCTIONAL DIAGRAM OF THE STAND FOR TESTING ASYNCHRONOUS MACHINE WITH WOUND ROTOR

The asynchronous machine with a wound rotor (WR) may be connected in the scheme of double-fed machine (DFM). The functional diagram of DFM is shown in Figure 1.

Stator windings in DFM are connected directly to the power supply network ($U_1 = const$, $f_1 = const$), and the rotor windings are connected to a separate controlled power source (active semiconductor converter - ASC).

The active semiconductor converter consists of two semiconductor switches, combined by DC link with a capacitor filter.

The double-fed machine allows adjustment of an external and an internal flows of the active and reactive power at any speed of rotation of the rotor [1, 5, 7].

This DFM property allows to build energy-saving stands for testing the asynchronous machine with a wound rotor without using an additional electric machine.

III. MODES OF OPERATION, VECTOR AND ENERGY DIAGRAMS OF THE DOUBLE-FED MACHINE

Below all DFM modes of operation are considered in detail:

- 1) Motor and generator modes of operation at the speed below the synchronous;
- 2) Motor and generator modes of operation at the speed above the synchronous;

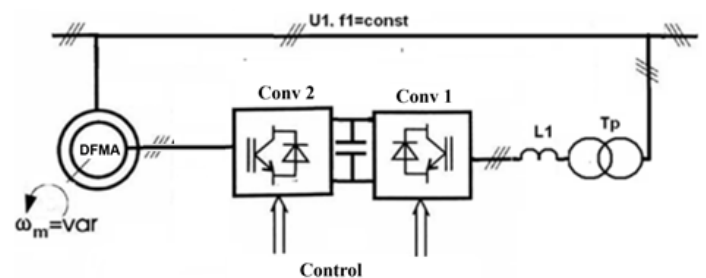


Fig. 1 the scheme of double-fed machine (DFM)

In all the listed modes, the set of equations defining electromagnetic processes of the machine in a steady state, using the method of resultant vector [1], [2], [5] is of the form:

$$\begin{aligned}\bar{U}_1 &= R_s \bar{I}_1 + jX_{ls} \bar{I}_1 + \bar{E}_1, \\ \frac{\bar{U}_2}{s} &= \frac{R_r}{s} \bar{I}_2 + jX_{lr} \bar{I}_2 + \bar{E}_2, \\ \bar{I}_m &= \bar{I}_1 + \bar{I}_2, \quad \bar{E}_1 = \bar{E}_2.\end{aligned}\quad (1)$$

Where \bar{U}_1 is a voltage in the network, $\bar{I}_1, \bar{E}_1 = j\omega_1 \bar{\Psi}_m = jX_m \bar{I}_m$ are a current and EMF in the stator winding, $\bar{U}_2, \bar{I}_2, \bar{E}_2 = j\omega_1 \bar{\Psi}_m = jX_m \bar{I}_m$ are reduced voltage current and EMF in the rotor winding, \bar{I}_m is a magnetizing current, $R_s, X_{ls} = \omega_1 L_{ls}$ are an active resistance and a leakage inductive reactance of the stator $R_r, X_{lr} = \omega_1 L_{lr}$ are reduced active resistance and leakage inductive reactance of the rotor, $X_m = \omega_1 L_m$ is an inductive reactance of magnetizing branch, s is a slip. An equivalent circuit of DFM, fitting (1), is listed in Fig. 2a.

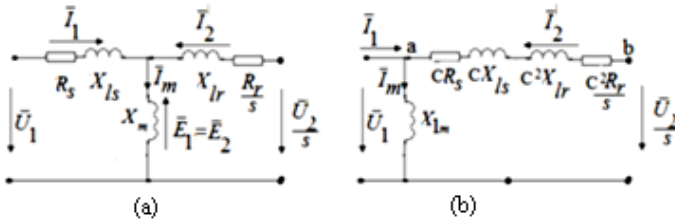


Fig. 2 The equivalent circuit of DFM

Voltage \bar{U}_2 is generated at the output of a semiconductor converter (*Conv 2* on Fig. 1). The first harmonic of the resulting voltage vector equals [6]:

$$\bar{U}_2 = \frac{m}{2} U_d \exp(j\delta) = \frac{m}{2} U_d (\cos \delta + j \sin \delta) \quad (2)$$

Where m is a modulation factor, δ is a modulation phase (phase of voltage \bar{U}_2 with respect to voltage \bar{U}_1 of the network).

For a qualitative assessment of DFM properties previously consider vector and energy diagrams. To this end transform a T-shaped equivalent circuit of DFM to a G-shaped equivalent circuit shown in Fig. 2b.

For the G-shaped equivalent circuit the value of C is determined from the equation $C = 1 + X_{ls}/X_m$ and for induction machines with capacity of 10 kW and above $C = 1$. A mathematical description of the G-shaped equivalent circuit can be written as:

$$\begin{aligned}\frac{\bar{U}_2}{s} &= \bar{U}_1 + R_2 \bar{I}_2 + jX_2 \bar{I}_2, \\ \bar{U}_1 &= jX_{1m} \bar{I}_m, \quad \bar{I}_m = \bar{I}_2 + \bar{I}_2.\end{aligned}\quad (3)$$

Where $R_2 = C \cdot R_s + C^2 R_r / s \approx R_s + R_r / s$, $X_2 = X_{ls} C + X_{lr} C^2 \approx X_{ls} + X_{lr}$, $X_{1m} = X_{ls} + X_m$ are active resistance and inductive reactances of the G-shaped equivalent circuit.

In assessing the energy properties of DFM, one should take into account that:

- 1) active power in the source is positive when the source gives up energy and negative when the source consumes energy;
- 2) reactive power in the source is positive (inductive) when its voltage leads the current and negative (capacitive), when its voltage lags behind the current;
- 3) mechanical shaft power is positive in the motor mode of DFM operation and negative - in the generator mode of DFM operation.

Fig. 3 shows the vector and energy diagrams of DFM operation in the motor modes with positive and negative slips, constructed according to (3).

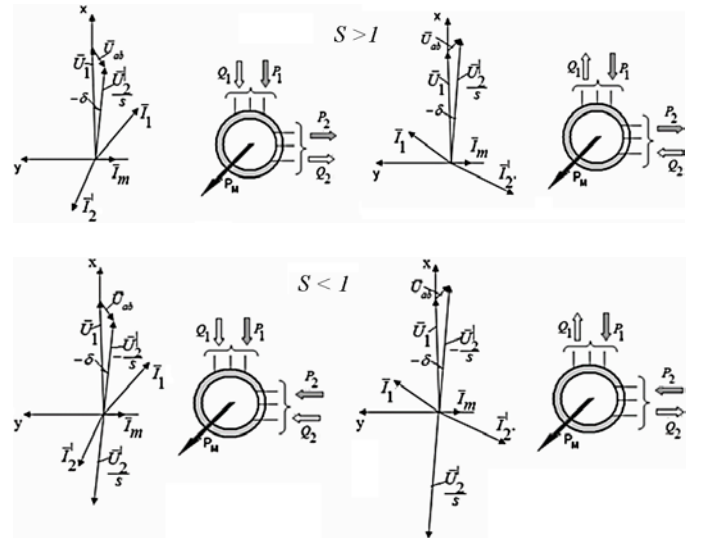


Fig. 3. DFM properties in independent frequency control of AP2 in the motor mode of operation

Fig. 4 shows the vector and energy diagrams of DFM operation in the generator mode with positive and negative slips, constructed according to (3).

The main properties of DFM obtained on the basis of qualitative analysis, are as follows:

- 1) direction of active power flows in the stator and rotor circuits testifies that when slips in DFM are positive, a closed energy loop is formed which is the bases for building an energy saving test stand;
- 2) motor mode of DFM occurs with negative δ , generator mode takes place with positive δ ;
- 3) the value of active power, transformed in the machine, is proportional to the value of δ ;
- 4) sign of reactive power in the stator circuit depends on the ratio of \bar{U}_1 and \bar{U}_2/s . When the value of voltage \bar{U}_1 exceeds the value of \bar{U}_2/s , the reactive power in the

stator circuit is positive (inductive). If value \bar{U}_2/s exceeds voltage \bar{U}_1 , the reactive power is negative in the stator circuit (capacitive), i.e. the machine is excited from the rotor side.

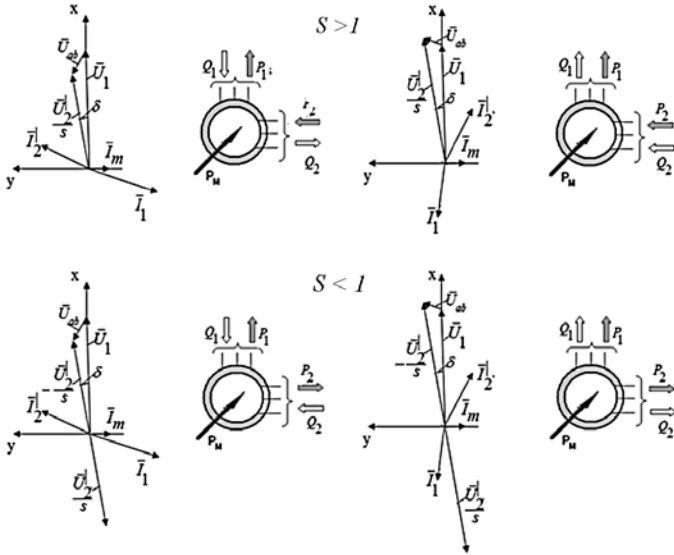


Fig. 4. DFM properties in independent frequency control of AP2 in the generator mode of operation

Thus, to determine electromagnetic, electromechanical and energy properties of the asynchronous machine with a wound rotor, it is necessary to connect the machine in DFM circuit and conduct a study of DFM at positive slips.

IV. INVESTIGATION CHARACTERISTICS OF THE DFM WITH POSITIVE SLIDES

The rotor winding of DFM is energized from the converter at the output of which the value of voltage, the phase of this voltage with respect to the mains voltage and frequency of the voltage $\omega_2 = \omega_1 - p\omega_m$ change.

The laws of rotor frequency control are similar to the laws of frequency control of the asynchronous machine by the stator circuit, i.e. it is required to maintain a certain relationship between ω_2 and U_2 . In what follows we consider DFM properties for the simplest law of frequency control.

$$\frac{U_2}{s} = \frac{\omega_1 U_2}{\omega_2} = U_{2m} = const \quad (4)$$

For quantitative estimation of DFM properties one should solve the set of equations (1), (2). This solution is carried out in a rotating coordinate system x (real axis), y (imaginary axis). In so doing voltage \bar{U}_1 coincides with the real axis x , and for the secondary voltage the ratio $U_{2m} = \omega_1 U_2 / \omega_2$ and δ phase are given.

The stator and rotor currents are determined by solving the equations:

$$\bar{I}_1 = \frac{\bar{U}_1 \left(\frac{R_r}{s} + jX_s \right) - j \frac{\bar{U}_2}{s} X_m}{(R_s + jX_s) \left(\frac{R_r}{s} + jX_s \right) - X_m^2} \quad (5)$$

$$\bar{I}_2 = \frac{\frac{\bar{U}_2}{s} (R_s + jX_s) - j \bar{U}_1 X_m}{(R_s + jX_s) \left(\frac{R_r}{s} + jX_s \right) - X_m^2} \quad (6)$$

An electromagnetic torque is determined from the equation [5], [8], [9]:

$$T_e = \frac{3}{2} p L_m \cdot (\bar{I}_2 \times \bar{I}_1) = \frac{3}{2} p L_m (I_{2x} I_{1y} - I_{2y} I_{1x}) \quad (7)$$

The energy properties of DFM are determined after calculating currents from (5), (6) in accordance with the listed below expressions:

$$\begin{aligned} P_1 &= 1.5 \cdot U_1 \cdot I_{1x}, \quad Q_1 = -1.5 \cdot U_1 \cdot I_{1y}, \\ Q_2 &= 1.5 \cdot (U_{2y} I_{2x} - U_{2x} I_{2y}), \\ P_m &= T_e \cdot \omega_m = T_e (1-s) \omega_1 / p, \\ P_2 &= 1.5 \cdot (U_{2x} I_{2x} + U_{2y} I_{2y}) - P_m \text{sign}(s). \end{aligned} \quad (8)$$

A further study was carried out for DFM in which the machine 215 HP (160kW), 400 V, 50 Hz, 1487 RPM has the following parameters: $R_s = 13,79 \cdot 10^{-3}$ Ohm, $L_{ls} = 0.152 \cdot 10^{-3}$ H, $R_r = 7.728 \cdot 10^{-3}$ Ohm, $L_{lr} = 0.152 \cdot 10^{-3}$ H, $L_m = 7.69 \cdot 10^{-3}$ H.

All variables of DFM are calculated and constructed using relative (dimensionless) values (pu-per units), which are determined in dividing the calculated variables by basic values. For the machine with the above parameters, the basic values of the variables are calculated from formulas and are equal to: $P_b = 160$ kVA, $U_b = 400$ V, $Z_b = U_b^2 / P_b = 1.0$ Ohm, $I_b = U_b / (\sqrt{3} Z_b) = 231.2$ A, $\omega_b = 2\pi f_n = 314$ Hz, $T_b = \sqrt{3} p U_n I_b / \omega_b = 1019$ Nm.

The results of DFM study in frequency control from the rotor side are shown in Fig. 5.

Fig. 5 a, b shows dependences of the active power in the network, the stator and rotor circuits, electromagnetic torque and power at the machine shaft upon a slip in the motor and generator modes of DFM operation when the slip changes in the range from 0 to 1.

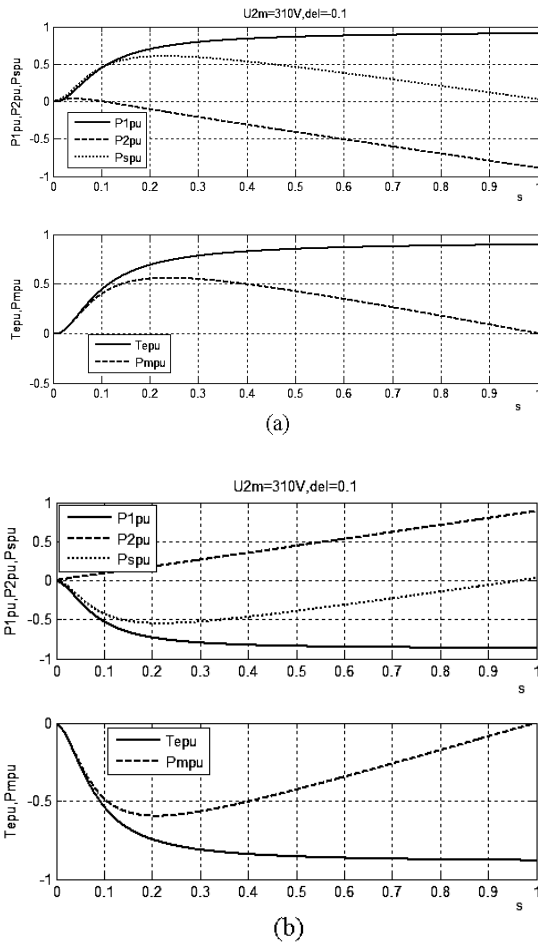


Fig. 5. DFM characteristics in independent frequency control in the motor (a) and generator (b) modes of operation

The quantitative estimation of DFM properties permits the following conclusions to be made:

- 1) energy savings in the stand for WR testing is achieved with considerable slips, in this case the most efficient mode is the mode of short circuit ($s = 1.0$);
- 2) with considerable slips DFM is a source of torque;
- 3) electric power consumed by DFM from the network in the motor mode is determined by difference in the stator and rotor powers;
- 4) similarly the mechanical power, consumed by DFM from the shaft, is also determined by difference in the stator and rotor power.

Therefore, an electromagnetic power, circulating in DFM, can be tens of times greater than the power of an external source (electrical or mechanical).

The adjusting properties of DFM are demonstrated in Fig. 6.

These characteristics are obtained by solving (1), (2). They were calculated at a constant slip of $s = 1.0$. The power consumed by DFM from external sources at $s = 1.0$ in the motor ($\delta < 0$) and generator ($\delta > 0$) modes, is expended only to compensate for losses in the machine.

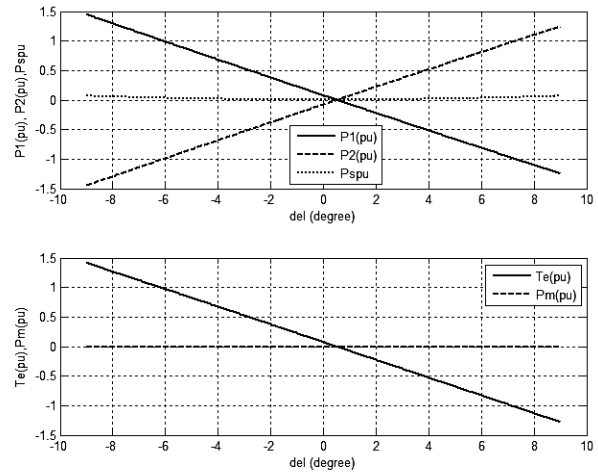


Fig.6. Adjusting properties of DFM at $s = 1.0$

V. SIMULATION RESULTS

The simulation results of a simulation model of DFM in the package *Simulink* are presented in Fig.7 for a positive slip. The oscillograms of voltages and currents in the stator and rotor circuits were taken in transient conditions. The change from the motor mode of operation to the generator one was carried out by an abrupt angle change from $\delta -0.05$ radian to $+0.05$ radian at the time of $t = 0.3$ s.

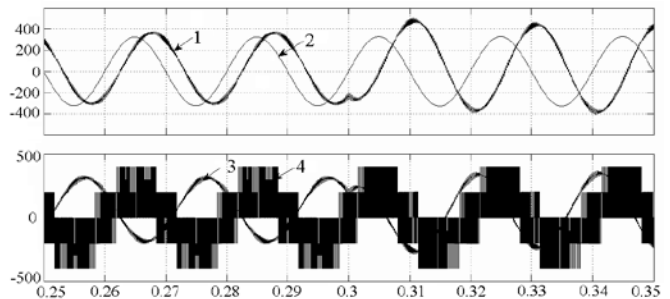


Fig.7. Results of DFM model simulation at $s = 1.0$. Where 1 - I_1 , 2 - U_1 , 3 - I_2 , 4 - U_2 .

The simulation results show that in transient conditions there are not current (power) overloads both in the stator and the rotor circuits, the time of transient process approximately amounts to one and half cycle of the network frequency.

VI. CONCLUSION

In the test stands where the main requirement is energy efficiency, one can use some simple algorithms for double-fed machine control. The variation range of DFM slips should be chosen depending upon the purpose of system application.

For the test stands it is more energy efficient to design DFM in the range of positive slips.

REFERENCES

- [1] Botvinnik M, Shakaryan Y. "A managed machine of alternating current," Nauka, Moscow, 1969.
- [2] Bulgakov A. "The new theory of control rectifiers," Nauka, Moscow, 1970.
- [3] German-Galkin S. "Investigation of electromagnetic energy and properties of double-power machines," Vestnik UrGUPS, #3, 2012.
- [4] Zherve G. K. "Promyshlennye ispytaniya elektricheskikh mashin," Energoizdat, Leningrad, 1984.
- [5] Onishchenko G. B., Lokteva. I.L. "Asinkhronnye ventil'nye kaskady i dvigateli dvojnogo pitaniya," Energiya, Moscow, 1979.
- [6] Rozanov Y. K. "Silovaya elektronika," Izdatel'skii dom MEI, Moscow, 2007.
- [7] Khvatov S. V., Titov V.G., Poskobko A.A. "Asinkhronno-ventil'nye nagruzhayushchie ustroystva," Energoizdat, Moscow, 1986.
- [8] Bogalecka E., "Zagadnienia sterowania maszyną dwustronnie zasilaną pracującą jako prądnica w systemie elektroenergetycznym," Prace Naukowe Wyższej Szkoły Morskiej w Gdyni, Gdynia, 1997.
- [9] Kaźmierkowski M.P, Tunia H. "Automatic Control of Converter-Fed Drives," ELSEVIER, Amsterdam-London-New York-Tokyo, 1994.

Enhancement of escalator energy performance with the use of double-fed engines

Korzinin N.M.^{1,2}, Korovkin N.V.², Silin N.V.³

¹Project department of the metro building company in St. Petersburg

²St.-Petersburg State Polytechnic University

³Far Eastern Federal University, FEFU Vladivostok, Russia

Abstract. The problem of enhancement of escalator engine energy efficiency has been studied in the paper, experimental and design values of escalator engine currents and powers have been shown as well as the results of simulation giving the opportunity to use double-fed engines so as to improve the energy performance of escalator engines.

Keywords - wound-rotor induction motor, double-fed engine, escalator, frequency converter.

I. INTRODUCTION

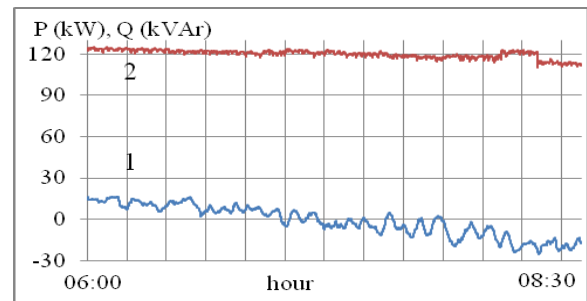
In 5 subway lines of 113,6 km total length there are 67 stations and 255 escalators. At deep stations escalators LT-2 with asynchronous wound-rotor induction motors AKE of 180 or 200 kW capacity are usually used. The present paper studies energy characteristics of escalator drives and modern approaches for their improvement as far as it concerns AKE 180 kW engines.

As a rule, there are 3 or 4 escalators installed at a station, their operation mode – ascending and descending motion - is established by operational staff according to passenger traffic flow and in this context the load of escalators during different day hours is also different. It is important that the peak load makes about 40-45 per cent of engine power rating that results from measurements of active and reactive powers at one of subway stations (Fig. 1,a and b). Active power reduction on Fig. 1b means that the escalator No. 2 is ascending while unloading the escalator No. 1.

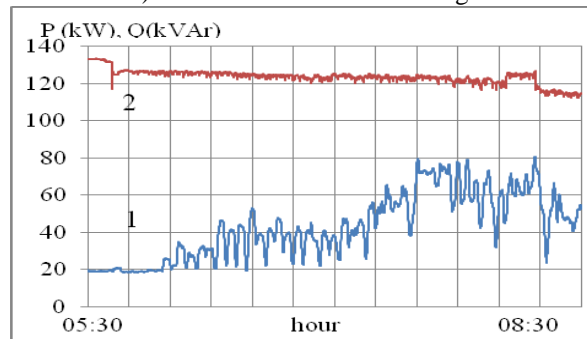
Power supply of escalators is to be performed according to the first or second reliability category [3]. A simplified diagram of escalator power supply is shown on Fig. 2.

II. PROBLEM FORMULATION

The problem of escalator energy performance is crucial. The main mean to do it is to use capacitor devices with controlled (YKP58-0,4-150-25-Y) or fixed (KC1-0,38-18) capacitance.



a) Escalator no. 1 is descending



b) Escalator no. 3 is ascending .

Fig. 1 Results of active (1) and reactive (2) power measurements.

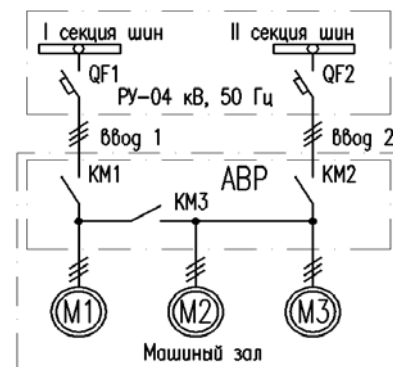


Fig. 2. Simplified circuit diagram of escalators. ABP – automatic transfer switch; KM1-3 – power contacts; M1, M2, M3 – wound-rotor induction motors.

In Table 1 are shown the values of active, reactive and lost powers in cable line and supply transformer at step-down substation [1]:

$$\Delta P = \frac{P^2 + Q^2}{U^2} r, \quad (1)$$

where: $U = 380$ V; P , Q - active and reactive powers; ΔP - lost power; $r = 0.024$ - cable line and transformer resistance.

If we take into consideration that the typical operation time of subway stations makes 18 hours per day and $\Delta P = 2.5$ kW and reactive power compensation is ensured by two capacitor devices KC1-0,38-18 per one input, annual electric power losses will constitute about 16 MW*h per escalator. These losses will make ~ 7 MW*h if the reactive power compensation is total. It should be noted that the losses will increase if two or more escalators are operating from one input.

Table 1

Type of operation	P, kW	Q, kVAr	ΔP , kW
At compensation by two capacitor devices KC1-0,38-18 (upon start-up project)			
Off-load operation	20	72	0.93
Operation at 60% load (up)	125	86	3.8
At reactive power fed by network equal approximately to zero			
Off-load operation	20	0	0.06
Operation at 60% load (up)	125	0	2.6

It was proposed to use for total reactive power compensation automatic devices YKR58-0,4-150-25-Y operating in automatic mode. However, on duty contacts burning has been detected in power circuits (Fig. 3), they have been shut down up to ascertain causes.



Fig 3. Burned power contacts

III PROBLEM SOLUTION

1. Description of proposed device.

We would suggest to use as an alternative capacitor device a wound-rotor induction motor by way of double-fed engine. When ac machine is operating in steady state mode MMF vectors of stator and rotor rotate in a synchronous way. As the resultant MMF vector of stator windings rotates with angular

speed $\omega_{0\dot{Y}\dot{E}} = 2\pi f_1$ and that one of rotor with ω speed, MMF vector of rotor windings must rotate in relation to rotor at a speed which is proportional to motor's sliding motion s so as to synchronise them:

$$\omega_s = \omega_{0\dot{Y}\dot{E}} - p_{II}\omega = s\omega_{0\dot{Y}\dot{E}} \quad (2)$$

If the engine speed is below synchronous one, the MMF vector rotates sideways the rotor spinning and if it is above the synchronous speed it rotates right-about. To make rotate the MMF vector about the rotor the current in windings must have the slip frequency f_2 to be determined from expression [2]:

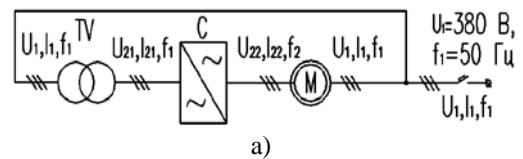
$$s\omega_{0\dot{Y}\dot{E}} = 2\pi f_2, \quad f_2 = f_1 s \quad (3)$$

Let us consider two operation modes of double-fed engine: synchronous and asynchronous. In sync operation the slip frequency is given irrespective of angular speed. In this case specific frequency f_2 and, according to (2), specific speed ω not depending on a load correspond to each value of control signal. By changing the frequency f_2 one may control this speed. In sync operation the double-fed engine operates as synchronous machine. The speed may be controlled in this operation mode [2]. Further researches will show to what extent such a capability may be required. Here we shall show only design values of escalator stairs motion speed under various operating conditions at rated value of 0.75 m/s [4]:

- in off-load operation – 0.7994 m/s;
- under design conditions – 0.7822 m/s;
- in operation at 60% load – 0.7895 m/s;
- in regenerative braking operation at 60% load – 0.8081 m/s.

In asynchronous operation of double-fed engine the frequency of power source connected to secondary windings due to inner control loop is kept equal to slip frequency $f_1 s$, in this case only the amplitude and voltage phase of the source are to be controlled [2].

The proposed device contains a transformer TV and a frequency converter C (Fig. 4a).



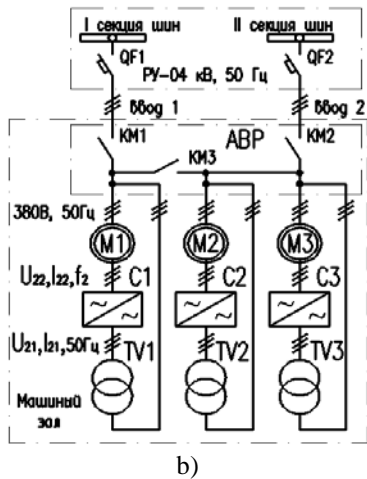


Fig.4. Simplified diagram of proposed device (a) and potential diagram of device connection to escalator engines (b).

2. Rotor voltage under conditions of reactive power compensation

Let us specify the rotor voltage phase from the condition of constant moment:

$$\delta = \arctg\left(-\frac{r'_2}{s\sigma x'_2}\right), \quad (4)$$

where $r'_2 = 0.0131$; $x'_2 = 1.3$ – active resistance and inductance of rotor phase reduced to stator, $\sigma = 0.1$ – leakage factor.

Then we shall establish the value of reactive current component of the stator $i_{1\beta}$ and determine the respective value of rotor current:

$$i_{2\beta} = -\frac{U_{ph}}{k_1 x_1} - \frac{i_{1\beta}}{k_1}, \quad (5)$$

where $U_{ph} = 220$ V – phase voltage; $x_1 = 1.34$ Ohm – inductance of stator phase; $k_1 = 0.934$ – nondimensional coefficient; Module of rotor voltage:

$$U_{22} = sk_1 U_{ph} \left(1 - \frac{i_{2\beta}(r_2'^2 + s^2 \sigma^2 x_2'^2)}{U_{ph} s^2 \sigma x_2' k_1}\right) \times \left(\cos \delta - \frac{r_2' \sin \delta}{s \sigma x_2'}\right)^{-1} \quad (6)$$

Let the escalator No. 1 operate under conditions of proper reactive power compensation and compensation of reactive power of escalators No. 2 and No. 3. They operate under conditions of variable speed control and from one input at 60% load (Fig. 4b). Table 2 shows the results of calculations of stator and rotor currents of engines M1, M2, M3 under conditions and operating modes specified above.

Table 2

Stator I_1 , rotor I_2 (A) currents and rotor voltage	Escalators		
	№1 up	№2 down	№3 down

(V).	$U_{22}=0$	$U_{22} \neq 0$		
Re(I_1)	189	186	-175	-175
Im(I_1)	-185	330	-188	-188
$ I_1 $	264	377	257	257
Re(I_2)	-160	-160	163	163
Im(I_2)	20	-437	21	21
$ I_2 $	162	465	164	164
Re(U_{22})	0	1,1	20	20
Im(U_{22})	0	-8.8	-2.5	-2.5
$ U_{22} $	0	8.84	20.2	20.2
	Re(I_{11})+ Re(I_{12})+ Re(I_{13})	Im(I_{11})+ Im(I_{12})+ Im(I_{13})	Re(I_{21})+ Re(I_{22})+ Re(I_{23})	Im(I_{21})+ Im(I_{22})+ Im(I_{23})
$U_{22}=0$	-161	-561		
$U_{22} \neq 0$ and transformer ratio 20	-152.7	-26.25	8.3	19.75

As we can see, in the absence of rotor voltage U_{22} 370 kVAr of reactive power are fed from network and 106 kW of active power is supplied to it.

At $U_{22} \neq 0$ the rotor reactive power is reduced up to 17 kVAr and an insignificant decrease of active power supply to the network occurs.

3. Simulation under rated conditions.

3.1. Design values of parameters of rotor model are the following: $Z_2 = 0.0191 + j0.0695$ – resistance, Ohm; $s\dot{E}_2 = -5.57\sqrt{2}e^{-109}$ – engine EMF, V; $f_2 = 1.055$ – frequency, Hz.

A specified rotor current value $\dot{I}_2 = 296\sqrt{2}e^{-163}$ ensuring the compensation of reactive power of one of engines under rated conditions and its graphical chart are given on (Fig. 5).

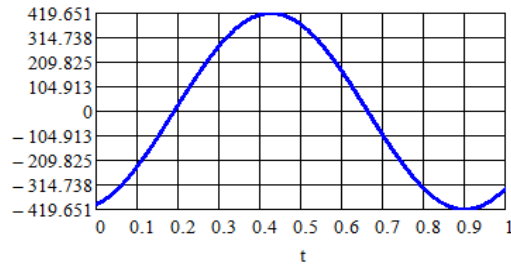


Fig.5. Specified rotor current.

3.2. Thyristor converter simulation

The issues related to the simulation of this type of diagrams and determination of their electromagnetic characteristics are considered in [5-11]. The voltage in transformer secondary winding is: $\dot{U}_{21} = 91\sqrt{2}$. Design values of a filter - $L = 0.001153$ H; $C = 3.16$ F;

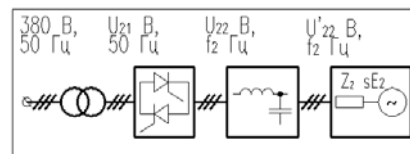
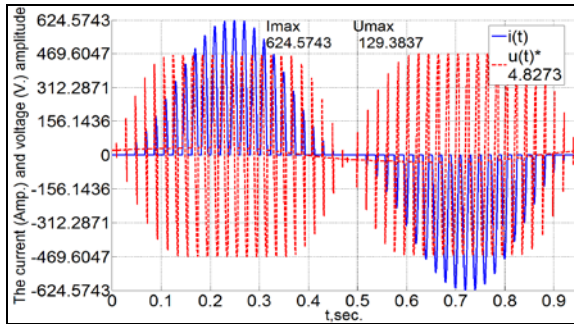
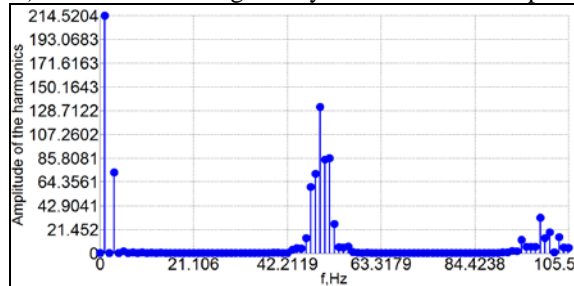


Fig. 6. Simplified diagram of thyristor converter

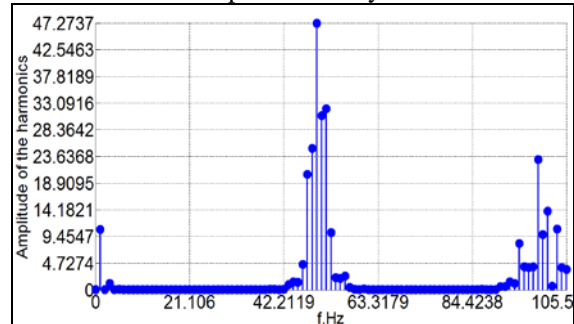
On Fig. 7 there are current and voltage charts (a, d, f) in power components of thyristor converter of phase L1 and their harmonic composition (b, c, e, j) within ranges shown on figures.



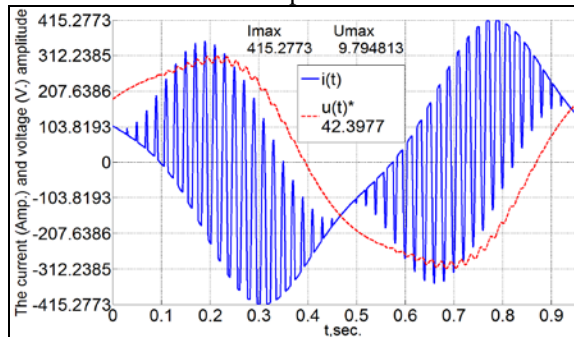
a) Current and voltage at thyristor converter output.



b) Current harmonic composition at thyristor converter output.



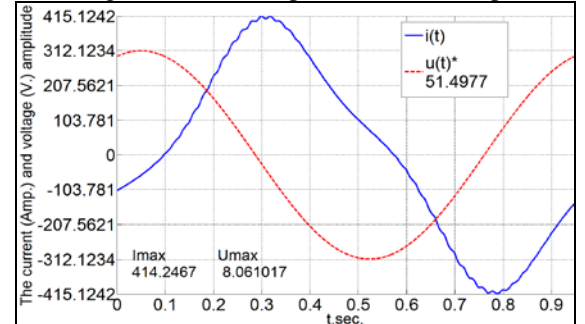
c) Voltage harmonic composition at thyristor converter output.



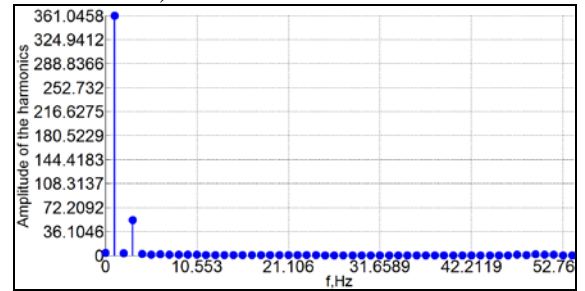
d) Current and voltage at filter capacitor.



e) Voltage harmonic composition at filter capacitor.



f) Rotor current and MMF.



j) Rotor current harmonic composition.

Fig. 7. Currents and voltages (a, d, f) of thyristor phase converter elements L1 and their harmonic composition (b, c, e, j).

As it is shown on Fig. 7, f the shape and the value of rotor current are close to target values (Fig. 5).

3.3. Simulation of frequency converter with independent voltage inverter (IVI) and pulse-width modulation (PWM) of 1 kHz frequency

The voltage of transformer secondary winding is: $\dot{U}_{21} = 4.6\sqrt{2}$. Design values of a filter are: $L = 0.0007598$ H; $C = 0.022$ F.

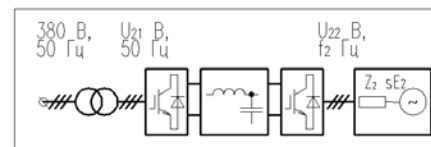


Fig. 8. Simplified diagram of frequency converter with IVI and PWM.

On Fig. 9 are shown current and voltage curves (a,d) in main power elements of phase frequency converter L1 and their harmonic composition (b, c, e, f) within ranges given on figures.

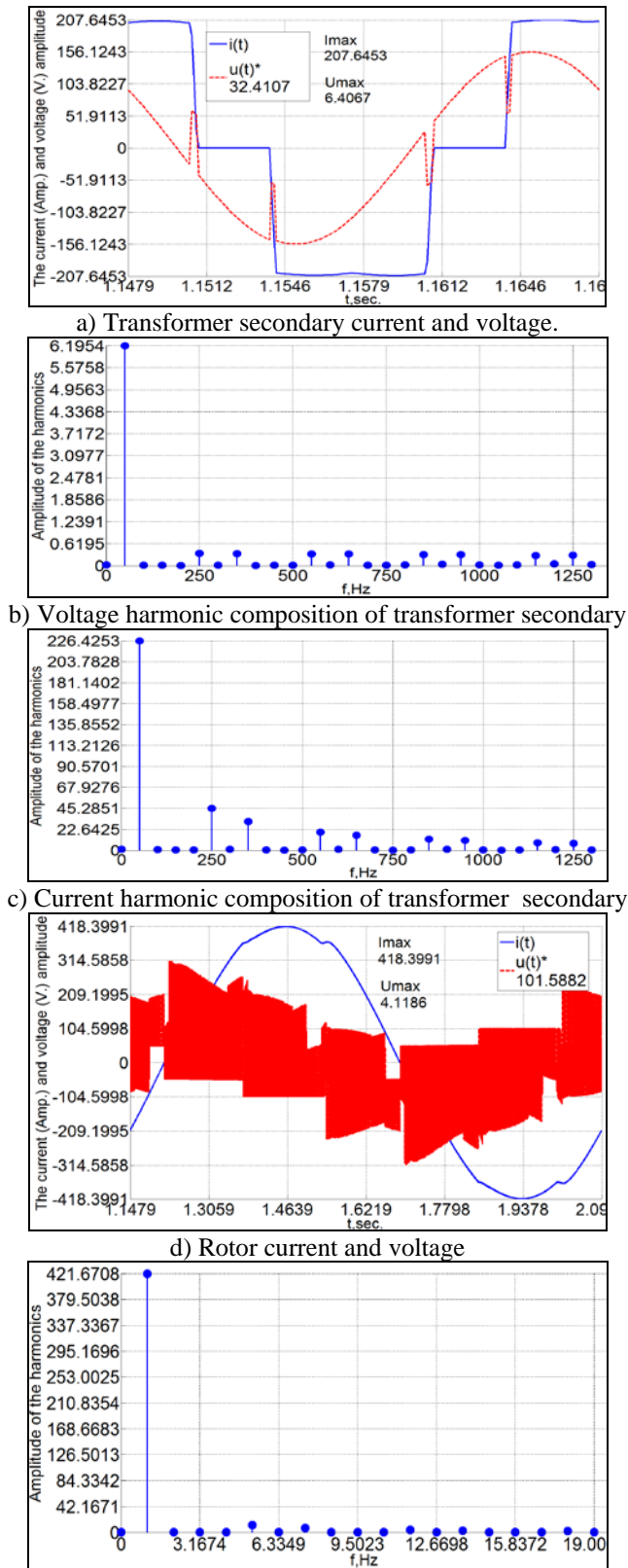


Fig. 9. Currents and voltages (a, d) of phase L1 frequency converter elements with IVI and PWM and their harmonic composition (b, c, e, f).

As it is shown on Fig. 9d, the shape and value of rotor current are close to target values (Fig. 5).

IV CONCLUSION

Performed calculations show that a proposed device allows to ensure a total compensation of reactive power and thus to halve electric power losses.

Major advantages of a proposed solution are as follows:

- device implementation on various component base;
- variable speed capability of escalator stairs;
- low power of transformer TV and converter C that results in a relatively low cost and small size;
- system implementation on mobile platform. In this case it is proposed to install the system as close as possible to escalator engine.
- enhancement of escalator operation reliability. On default, the device may be shut down without escalator stopping.

A specific diagram of a proposed device should be defined according to requirements as per rotor current control performance, cost, mass and dimensions parameters of component base.

REFERENCE:

- [1] Demirchyan K.S. Theoretical basis of electrical engineering [text] / K.S. Demirchyan, L.R. Neiman, N.V. Korovkin – M.: SPb.: v.1, v.2 Piter, 2004.
- [2] Onischenko G.B., Lokteva I.L. Asynchronous valve cascade converters and double-fed engines. – M.: Energia, 1979.-200 p.
- [3] SP-32-105-2004 (code of practice). Underground electric railways. Design and construction rules. Publishing house: Russian Academy of Public Administration, 2004.
- [4] Regulations on Installation and Safe Operation of escalators (PB 10-77-94). Approved by the Decree of Gosgortehnadzor of Russia dated 02.08.94 No.47.
- [5] Adalev, A.S., Korovkin, N.V., Hayakawa, M., Nitsch, J.B. Deembedding and unterminating microwave fixtures with the genetic algorithm (2006) IEEE

Transactions on Microwave Theory and Techniques, 54(7), art. no. 1650456, pp. 3131-3139.

- [6] Adalev, A.S., Korovkin, N.V., Hayakawa, M. Identification of electric circuits described by ill-conditioned mathematical models. (2006) IEEE Transactions on Circuits and Systems I: Regular Papers, 53 (1), pp. 78-91.
- [7] Kuchinsky, G., Kozhevnikov, M., Schilin, O., Vekhoreva, L., Korovkin, N., Selina, E., Potienko, A. Compact power high-voltage pulse capacitor for quasi-rectangular nanosecond impulses formation. (1999) Digest of Technical Papers-IEEE International Pulsed Power Conference, 2, pp. 1449-1452.
- [8] Adalev, A.S., Korovkin, N.V., Hayakawa, M. Using linear relations between experimental characteristics in stiff identification problems of linear circuit theory. (2008) IEEE Transactions on Circuits and Systems I: Regular Papers, 55 (5), pp. 1237-1247.
- [9] Korovkin, N.V., Balagula, Y.M., Adalev, A.S., Nitsch, J. A method of a disturbance source localization in a power system. (2005) 2005 IEEE Russia Power Tech, PowerTech, art. no. 4524765.
- [10] Adaleva, A.S., Hayakawa, M., Korovkin, N.V. Identification of electric circuits: Problems and methods of solution accuracy enhancement. (2005) Proceedings – IEEE International Symposium on Circuits and Systems, art. no. 1464754, pp. 980-983.
- [11] Korovkin, N.V., Berlin, E.M., Efimov, K.A. The operation modes of the controlled electric transmission with the link based on the multiphase thyrister switch phase converter (1991) Izvestiya Akademii Nauk Energetika, (1), pp. 28-37.

Nikolay V. Korovkin was born in Leningrad, Russia, on January 09, 1954. He received the M.S., Ph.D. and Doctor degrees in electrical engineering, all from St. Petersburg State Polytechnical University in 1977, 1984, and 1995 respectively. He worked as a Professor for the University of Electro-Communications (Tokyo, Japan), for the Swiss Federal Institute of Technology (EPFL) Switzerland, and for Otto-von-Guericke University (Magdeburg, Germany). His main scientific interests are EMC problems, stiff systems, impulse processes in linear and non-linear systems, "soft" methods of optimization. Now he is the head of the department of Theoretical Engineering in St. Petersburg State Polytechnical University. Prof. N. Korovkin is a Member of the Academy of Electrotechnical Science of the Russian Federation, (since 1996).

Nikolay Vitalevich Silin, Prof., Doctor of Engineering. He is working in the position of the Chairman of the Theoretical and General Electrical Engineering Department of the State Educational Institution of Higher Professional Education «Far Eastern National Technical University» of the Federal Agency for Education, 690900, city of Vladivostok.

Nikolay M. Korzinin was born in Rybinsk, Yaroslavl Region, Russia, on December 19, 1977. In 1993 he finished Professional Lyceum No. 32 in the town of Rybinsk with major electrical technician. In 2009 he graduated from «Saint Petersburg State University Electrotechnician University «LETI» named after V.I. Ulyanov (Lenin)», majoring in «Electric drive and automation of industrial-scale plant and technological complexes». Now he is working at the Project Department of the Metrobuilding Company in St. Petersburg in the position of the leading engineer of the Electrical Engineering Department. His main activity is project documentation development and automation of electrical engineering design. His main scientific interests are EMC problems, stiff systems, impulse processes in linear and non-linear systems, "soft" methods of optimization.

Electromagnetic forces and field distribution under impulse magnetic field impact on solids of revolution made from hard ferromagnetic materials

Egor A. Virva, Vasilii V. Titkov, Sergey I. Krivosheev, Yuri E. Adamyan

Abstract—The problem of description of impulse electromagnetic processes in a conductive medium with magnetic hysteresis is solved using Preisach model. Distribution of volume density of the magnetic force for cylindrical system with finite length inductor inside ferromagnetic pipes obtained. It is shown that finite residual force integral at the zero boundary field occurs at considering of hysteresis.

Keywords—magnetic permeability, Preisach model, ferromagnetic, volume force.

I. INTRODUCTION

THERE is a range of technologies related to the impact of impulse magnetic field on conductors. In particular, we can distinguish magnetic stamping [1, 2], excitation of vibrations in elastic bodies [3], generation of strong magnetic fields [4].

In these technologies, the most common form of the magnetic field impulse acting on the conductor is damped periodic function

$$H(t) = H_m \cdot \exp(-\Delta \cdot t) \cdot \sin(\omega \cdot t) \quad (1)$$

where H_m – magnitude of impulse, Δ - damping ratio, ω – periodic component frequency.

From it follows the formula that sign-alternating magnetic field is generated on the conductive material boundary which creates time-varying currents and forces, distributed in a certain way in the medium. For non-ferromagnetic conductor these modes are well studied in a number of papers [5-7]. However, in implementation of technologies mentioned

above, in particular, excitation of mechanical vibrations applied to ferromagnetic conductors (industrial steels) characterized by hysteresis, a number of issues remains poorly studied. Presence of spatially distributed residual magnetization resulting from the use of finite size inductors modifies conditions for repeated application of impulses. This may hinder reproduction of results in systems that require repeated exposure to impulse magnetic field. The analysis of literature [8] showed that there is a theoretical problem of describing the electromagnetic forces in conductive medium with hysteresis.

Note that all these features are particularly manifested when the peak values of magnetic flux density lay in the range near saturation point, which for steel is $B_s = 1-2$ T.

This paper is an attempt to find at least a partial solution to the mentioned problems of description of impulse electromagnetic processes in a conductive medium with magnetic hysteresis.

II. STATEMENT OF THE PROBLEM

Analysis of these processes applied to the magnetization of a pipe segment using a short inductor located inside it (Fig. 2) is carried out. For parameters of oscillatory impulse meeting the conditions of experiment (1) field equations with consideration of magnetic hysteresis can be conveniently written as:

$$\Delta \vec{A} + \text{rot} \vec{M} + \mu_0 \vec{J}_e = \sigma \mu_0 \frac{\partial \vec{A}}{\partial t}, \quad (2)$$

where \vec{A} – magnetic vector potential, \vec{M} – magnetization of medium, μ_0 – magnetic permeability of vacuum, \vec{J}_e – external current density vector, σ – electric conductivity coefficient.

To describe the phenomenon of hysteresis Preisach model is used [9] which, in spite of its relative complexity, is one of the closest to the physical nature of the phenomenon.

According to this model, the magnetization M of the material per volume unit of ferromagnetic is determined by a combination of magnetic moments of elementary domains,

This work is done by the authors on their own initiative.
The author Yu.E. Adamian is with Saint-Petersburg State Polytechnical University, Russia, yuriadamian@gmail.com
The author S.I. Krivosheev is with Saint-Petersburg State Polytechnical University, Russia, ksi.mgd@gmail.com
The author V.V. Titkov is with Saint-Petersburg State Polytechnical University, Russia, titkovprof@yandex.ru
The author E.A. Virva is with “D.V. Efremov Scientific Research Institute of Electrophysical Apparatus”. (NII EFA), Russia, evyrva@gmail.com

which may be in one of two states m1 and m2. Each domain jump-switches from state m1 to state m2 when the magnetic field strength reaches $H = a$. Backwards switch of a domain with decreasing field strength occurs at the point $H = b$. If we set a certain distribution function of switching fields for domain array $S(a, b)$, then total magnetization M can be calculated as the difference between integrals over the area in a plane coordinate system a, b - Preisach plane [10].

$$M = \int_{R^+} S(a, b) da db - \int_{R^-} S(a, b) da db. \quad (3)$$

Commonly used approximation for distribution function of magnetic moments switching fields in the Preisach model is a Gaussian function $S(a, b) = \exp\left(-\frac{a^2+b^2}{\Delta^2}\right)$. Preisach model provides a convenient continuous description of magnetization-demagnetization process under asymmetric curves of current alteration, describing any particular hysteresis loop.

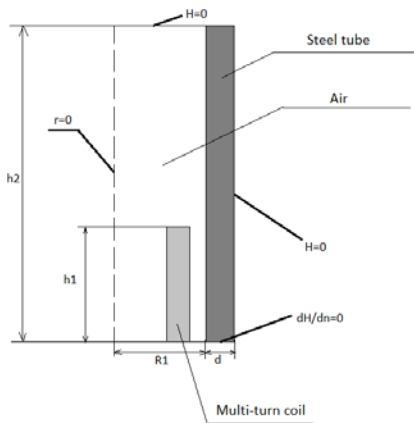


Figure 1. Pipe segment with a short inductor

According to the scheme shown magnetization in a certain state can be represented as a set of stages

$$M(t) = -E(a_0, b_0) + \sum_{k=1}^K [E(a_k, b_{k-1}) - E(a_k, b_k)],$$

where a_0, b_0 – correspond to initial point of magnetization curve, a_k, b_k - specify the sequence of increase and decrease of magnetic field respectively, $E(a, b)$ – Everett function, obtained by numerical integration of the Gaussian distribution of magnetic moments density in (3). Everett function is tabulated and used in numerical calculations using the interpolation procedure [11].

When performing numerical calculations, tabulation and interpolation of Everett function can be avoided by using its derivative

$$DE(a, b) = \frac{dE(a, b)}{da} = \exp\left(-\frac{a^2}{\Delta^2}\right) \int_b^a \exp\left(-\frac{y^2}{\Delta^2}\right) dy.$$

Then current value of magnetization can be obtained by using expressions and

$$M(a) = \begin{cases} M(b) + g \int_b^a DE(x, b) dx, & \frac{\partial a}{\partial t} \geq 0 \\ M(b) + g \int_b^a DE(x, b) dx, & \frac{\partial a}{\partial t} \leq 0 \end{cases} \quad (4)$$

where $a=H/H^*$. Coefficient $g=2$ with $b=0$ and $g=1$ for the rest of integration intervals.

Numerical algorithm used for solution of the equation (2) is a combination of finite element method in the conducting region (tube wall) and the boundary element method in the non-conducting (air) area. Comparison of calculation results for soft- and hard ferromagnetic conductor shows that presence of hysteresis effect alters the distribution of the magnetic field in the interior of the conductor.

Besides we can note the presence of residual magnetization with sources in ferromagnetic material, which is distributed in space by absolute value as well as by direction of the induction vector. When performing technological operations, an axial displacement of the inductor simultaneously with application of repeated impulses of the magnetic field can take place. Then the initial distribution of the field in the pipe wall for subsequent pulses will differ from the case of first pulse. In the middle part of the inductor noticeable radial field component may occur along with an axial field. This may affect the discussed below distribution of electromagnetic forces in the pipe wall.

In the general case of dependence $B = f(H)$ according to [12] the magnetic field strength tensor can be represented as:

$$T^{ij} = - \int_0^B H dB \delta_{ij} + H_i B_j \quad (5)$$

If the magnetic field induction B depends linearly on the strength H , then from (5) we can easily get the Maxwell strength tensor.

Let us use the well-known expression for the volume density of the force from the strength tensor:

$$f_i = \sum_{m=i,j,k} \frac{\partial T^{mi}}{\partial x_m} = - \frac{\partial}{\partial x_i} \int_0^B H dB + H_i \frac{\partial B_i}{\partial x_i} + B_i \frac{\partial H_i}{\partial x_i} + H_j \frac{\partial B_i}{\partial x_j} + B_i \frac{\partial H_j}{\partial x_j} + H_k \frac{\partial B_i}{\partial x_k} + B_i \frac{\partial H_k}{\partial x_k} + H_k \frac{\partial B_k}{\partial x_i} - H_k \frac{\partial B_k}{\partial x_i} + H_j \frac{\partial B_j}{\partial x_i} - H_j \frac{\partial B_j}{\partial x_i}$$

taking into consideration that

$$B_i \frac{\partial H_i}{\partial x_i} + B_i \frac{\partial H_j}{\partial x_j} + B_i \frac{\partial H_k}{\partial x_k} = (\vec{B} \cdot (\nabla \cdot \vec{H}))_i$$

$$H_k \frac{\partial B_i}{\partial x_k} - H_k \frac{\partial B_k}{\partial x_i} - H_j \frac{\partial B_j}{\partial x_i} + H_j \frac{\partial B_i}{\partial x_j} = (\text{rot} \vec{H} \times \vec{B})_i,$$

$$H_i \frac{\partial B_i}{\partial x_i} + H_j \frac{\partial B_j}{\partial x_i} + H_k \frac{\partial B_k}{\partial x_i} = ((\nabla \otimes \vec{B}) \cdot \vec{H})_i,$$

where \otimes - dyadic product, and $\nabla = \sum_{m=i,j,k} \vec{e}_m \frac{\partial}{\partial x_m}$.

After all transformations we get the following expression for volume density of the force:

$$\vec{f} = -\nabla \int_0^B H dB + (\nabla \otimes \vec{B}) \cdot \vec{H} + \vec{B} \cdot (\nabla \cdot \vec{H}) + \text{rot} \vec{B} \times \vec{H}$$

which represents in case of axial-cylindrical symmetry:

$$\left\{ \begin{aligned} f_r &= -\nabla_r \int_0^B H dB + B_r \frac{\partial H_r}{\partial r} + H_r \frac{\partial B_r}{\partial r} + \\ &\quad \frac{H_r B_r}{r} + B_r \frac{\partial H_z}{\partial z} + H_z \frac{\partial B_r}{\partial z} \\ f_z &= -\nabla_z \int_0^B H dB + H_r \frac{\partial B_z}{\partial r} + B_z \frac{\partial H_r}{\partial r} + \\ &\quad \frac{H_r B_z}{r} + H_z \frac{\partial B_z}{\partial z} + B_z \frac{\partial H_z}{\partial z} \end{aligned} \right. \quad (6)$$

III. CALCULATIONS RESULTS

Finally as results of calculation we obtained distribution of magnetic field in the ferromagnetic material and distribution of electromagnetic force with and without consideration of the hysteresis effect. Figure 2 shows the distribution of the magnetic field induction and Fig. 3 - electromagnetic force in the ferromagnetic material at axial coordinate $z = 0$ at the time of the inductor current zero ($t=T/2$).

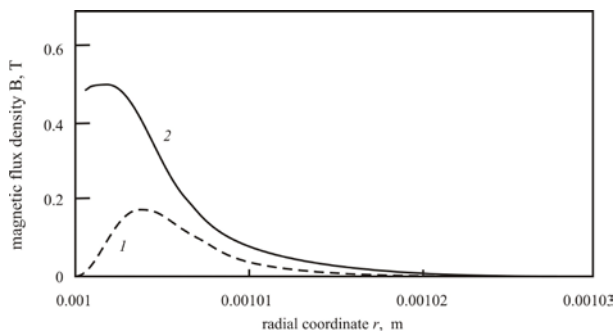


Figure 2. Radial distribution of magnetic field induction in the pipe material without (1) and with (2) consideration of hysteresis.

From these figures one can see presence of residual induction on the pipe wall due to the hysteresis properties of the material, as well as presence of the force density. In both cases force peaks are close to maxima of magnetic induction gradient. Substantial difference takes place in the magnetic force integral in radial direction. For anhysteretic material this integral is equal to zero at zero boundary field that

corresponds to widely used “magnetic pressure” concept. And considering hysteresis we see non-zero residual force integral at the same boundary condition.

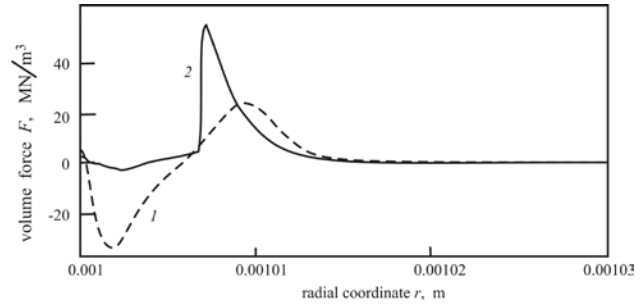


Figure 3. Volume force density radial distribution in the ferromagnetic material without (1) and with (2) consideration of hysteresis.

Developed model of magnetic field diffusion into conducting material with consideration of real magnetization curve distinguishes specific effects in forming of volumetric forces in the material. It is necessary to take into consideration the presences of these effects at determination of loading parameters of conductors in pulse magnetic deforming.

REFERENCES

- [1] N. Bessonov, S. Golovashchenko, “Numerical Simulation of Pulsed Electromagnetic Stamping Processes”, *1st International Conference on High Speed Forming*, 2004, pp. 83-92
- [2] R. Andersson, M. Syk, “Electromagnetic Pulse Forming of Carbon Steel Sheet Metal”, *3rd International Conference on High Speed Forming*, 2008, pp. 1-12
- [3] M. Hirao, H. Ogi, “EMATS for science and industry :noncontacting ultrasonic measurements”, Boston : Kluwer Academic Publishers, 2003, 369 p.
- [4] F. Herlach , N. Miura, “High Magnetic Fields Science and Technology”, World Scientific Pub Co Inc, 336 p
- [5] A. Podoltsev, A. Kucheryavaya, “Elements of theory and numeric calculations of electromagnetic processes in conducting mediums”, Kiev: Electrodynamics Inst., 1999, 362 p.
- [6] G. Schneerson, “Fields and transients in ultra-high current equipment”, Moscow: Energoatomizdat, 1992, 410 p.
- [7] G. Knopfel , “Ultra-high impulse magnetic fields”, Moscow: Mir, 1982.
- [8] R. Rosenzweig, “Ferrohydrodynamics”, Moscow: Mir, 1989.
- [9] Y. Adamyan, E. Virva, S. Krivosheev, V. Titkov, “Diffusion of impulse magnetic field and electromagnetic forces in ferromagnetic materials”, *Technical Physics Journal*, vol. 44, №4, 2013, pp. 1-7.
- [10] F. Preisach, *Zeitschrift fur physic*, vol. 94, 1935, p 277.
- [11] J. Perard, M. Poloujadoff , «Asynchronous Performance of Hysteresis motors under unbalanced conditions”, *Electrical machines and Electro Mechanics Quarterly*, vol. 1, No. 4, 1977, pp.377-389
- [12] M. Kuczman, “Dynamic Preisach hysteresis model”, *Journal of advanced research and physics*, vol. 1, №1, 2010.
- [13] L. Landau, E. Lifshitz, “Theoretical physics vol. 8: Electrodynamics of continuous mediums”, Moscow: Nauka, 1982.

Comparative fuel economy and environmental analysis of conventional hybrid and Plug-in hybrid vehicles

Morteza Montazeri-Gahjavarestani, Mehdi Mahmoodi-Kaleybar, Vahid Madanipour

Abstract— Hybrid vehicle is one of the main solutions to overcome emissions and energy consumption problems. In particular, battery, power-train system, energy management controller, vehicle performance attributes and driving habits greatly influence the relative value of HEVs. The aim of this study is to compare their effect on the energy consumption and emissions criteria of conventional hybrid vehicle and Plug-in hybrid vehicle those contain different control strategies. For this purpose, ADVISOR simulations have been conducted and the results for parallel configuration have been compared for various real world driving cycles. Then fuzzy rule-based controller system developed for energy management system, which has been optimized by genetic algorithm. The control strategy primarily targets the minimization of fuel consumption, while reducing emissions and meeting the power demand during real world driving cycles. Results specified optimal transmission and battery systems over a given cycle. Furthermore, simulation results indicate that plug-in hybrid vehicle with optimized control strategy in relative to conventional hybrid vehicles is more sufficient in fuel efficiency and emissions reduction. Finally, effects of initial SOC and hybridization factor are investigated on parallel hybrid vehicle performance to evaluate fuel consumption and emissions.

Keywords— Fuel consumption, Genetic fuzzy controller, Hybrid vehicle, Plug-in hybrid vehicle

I. INTRODUCTION

The reduction of transport-generated emissions and fuel consumption is currently a problem of global interest. When it comes to energy security and climate change concerns, cars and trucks are considered one of the principal problems. They consume relatively a big portion of the fuel in the world and emit a large amount of greenhouse gas. To overcome these problems, hybrid electric vehicles (HEVs) can be considered as alternative means of transportation. In comparison with conventional vehicles, fuel economy and emissions reduction have been improved in HEVs [1]-[3].

HEV technology is considered as a successful solution to address some energy efficiency and emissions concerns about

vehicles. So, it has been foreseen that by 2035 almost 80% of all vehicles introduced to the market should be hybrids, diesels, or turbocharged gasoline engines [4]-[6]. Plug-in hybrid vehicles (PHEVs) represent the direction of vehicle development due to excellent fuel economy, environmental advantages and all electric drive capability, which have more battery capacity, different control strategy and could be connected to the electrical grid to charge their batteries.

The main factors effects on hybrid vehicular emissions and fuel consumption are hybrid vehicle type, driving style, vehicle component configuration and traffic condition. In this paper effects of these factors are investigated. For this purpose, at the first step real driving cycle is developed for Tehran city, which called Teh-car driving cycle. Then fuel consumption and emissions for optimized component configuration (transmission and battery system) are compared with various driving cycle. Finally, in order to evaluate the effects of energy management system, PHEV which has different control strategy than conventional hybrid vehicles, is simulated in ADVISOR.

One of the most significant factors in the performance of HEV and PHEV are control strategies, which play an important role in improving energy management of HEVs. Different strategies are used in previous studies which mainly are classified into rule based and optimization approaches [7] and [8]. Also, combined strategies which take the advantages of both optimization and rule-based methods are proposed in [8]-[11]. Pérez and Pilotta [12], P'erez et al. [13] and Sciarretta et al. [14] used a discrete approach and a DP algorithm for designing higher-level control which called "supervisory control". They implemented an algorithm to find the split between the two sources using a priori knowledge of the driving cycle. Solutions are suboptimal because of the treatment of the constraint on the consumed energy from the ESS.

Previous studies [15]-[20], already indicated that fuzzy logic controller is very suitable for hybrid vehicle control. It is an appropriate method for realizing an optimal tradeoff between the efficiencies of all components of the HEV. Montazeri and et.al. [16] described the application of the genetic algorithm for the optimization of the control parameters in parallel hybrid electric vehicles. Energy management system (EMS) proposed based on an electric assist control strategy (EACS), the fitness function was defined so as to minimize the vehicle engine fuel consumption

M. Montazeri-Gahjavarestani, Systems simulation and control laboratory, School of Mechanical engineering, Iran university of science and technology, (phone: 77240540-; fax 77240488; e-mail: Montazeri@iust.ac.ir).

M. Mahmoodi-kalyebar Systems simulation and control laboratory, School of Mechanical engineering, Iran university of science and technology (e-mail: M_mahmoodi_k@iust.ac.ir).

V. Madanipour, Systems simulation and control laboratory, School of Mechanical engineering, Iran university of science and technology (e-mail: madanipor@gmail.com).

and emissions. The driving performance requirements were then considered as constraints. In [21], a fuzzy EMS based on driving cycle recognition was proposed to improve the fuel economy of PHEV. The EMS can recognize the driving cycle based on learning vector quantization (LVQ).

In [22], two separated controllers using fuzzy logic called Mode Decision and Parallel-driving EMS has been employed to fulfill switching between the series and the parallel modes as well as the instantaneous power distribution. By considering the effect of the driving cycle on the EMS, a fuzzy EMS based on driving cycle recognition has been proposed to improve the fuel economy of a parallel hybrid electric vehicle. The EMS was composed of driving cycle recognition and a fuzzy torque distribution controller, which optimized simultaneously by using particle swarm optimization [21].

Vehicle components configuration are another key point in the design and development of hybrid vehicles. The effects of hybrid vehicle component and their matching on performance and efficiency in fuel consumption and emissions reduction has been investigated in [23] and [24].

In this paper combined controller including fuzzy and genetic algorithm, which called GA-Fuzzy is used to enhance optimal control strategy in HEV and PHEV. Then the effects of various combinations of transmission and energy storage systems over various driving cycles on parallel hybrid vehicle performance are compared.

II. MODELLING

There are basically two different hybrid architectures: (i) The series hybrid, in which the engine, coupled with a generator, powers the generator that recharges the batteries and/or supplies electric energy to the electric motor. The motor, in turn, provides torque to the wheels. (ii) The parallel hybrid vehicle is propelled by either the engine or the electric motor or both. The electric motor works as a generator to recharge the batteries during regenerative braking or when the engine is producing more power than needed to propel the vehicle. A parallel style powertrain is used in this study for a PHEV and HEV. The internal combustion engine and the electric motor are combined together through a torque combination device. As show in figure 1, the operation modes of parallel hybrid vehicle includes: only electric, electric assists, battery charring and regenerative braking, which should be managed properly by optimal EMS.

A. Conventional HEV

In this paper effects of powertrain component includes transmission and energy storage systems, in parallel HEV configuration are investigated. The transmission and energy storage systems efficiency are directly related to the emissions and fuel economies of all HEVs. In order to model different configuration of HEVs, automatic/manual transmission systems combined with Lead-acid/Lithium-ion batteries. Gearbox specifications are presented in table 1.

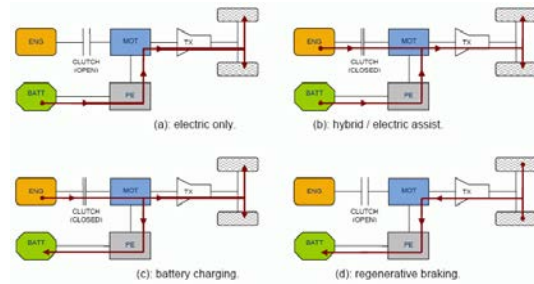


Fig. 1 operation modes of parallel configuration

Table 1. Manual transmission Gear Ratio and Corresponding Vehicle Speed

Gear number	Gear ratio	Vehicle speed (Km/h)
1	3.36	0-25
2	1.89	25-45
3	1.21	45-70
4	0.94	70-90
5	0.78	+90
Final drive	3.92	-

B. Plug-in HEV

PHEVs can be charged from external electric power sources [25]. Because of this significant advance in current hybrid vehicle technology, PHEVs use more electrical power over longer ranges, which is highly economical. Compared with conventional HEVs, PHEVs are equipped with a larger battery modules, which can power the vehicle by only using the stored energy charged from the power grid. Also, in comparison to electric vehicles (EV), they use two main source to propel the vehicle and has smaller energy storage systems. As shown in Fig. 2, PHEVs can be operated in tow main mode; charge depleting-charge sustaining (CD-CS) and blended modes.

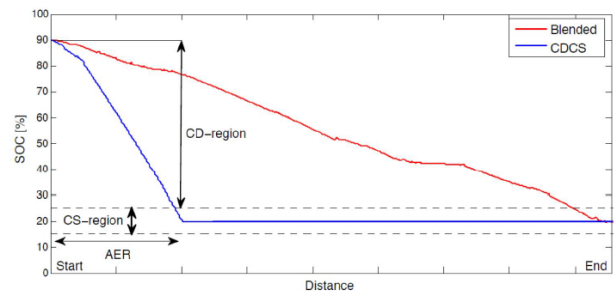


Fig. 2 SOC variation in different modes of PHEV

In the CD-CS mode, at the beginning of vehicle movement, only electric power from the battery is used (vehicle in all-electric mode) to achieve fuel efficiency, as long as the battery reaches its minimum threshold. Then, by the end of path, engine power is used to maintain the SOC level in minimum level. The Engine assists the motor only during peak power demand or high acceleration. The battery is depleted until it reaches a particular threshold. The battery is only charged in the event of regenerative braking. Unlike, in blended mode battery do not discharge quickly and at the end of the path before recharging, the SOC reaches the lowest level. In fact, the case of all-electric mode at the beginning of the path is removed, which ensures that the vehicle takes longer time to

reach charge sustaining operation. The prescribed limit for SOC in all modes is very sensitive and the control strategy sees to it that the state of charge of the battery does not fall below these limits. Due to this issue, it becomes more complicated to manage the energy distribution between the two drive trains for a PHEV. SAMAND PHEV parameters and component specifications are given in table 2.

Vehicle mass	1185
Rolling resistance	0.01
Aerodynamic coefficient	0.33
Frontal Area	2.2
Wheel Radius	0.33
Engine	National Engine 82 Kw
Electric motor	Siemens AC 75 kw
Lit-ion batteries	12 V-6Ah

III. DRIVING CYCLE DEVELOPMENT

A drive cycle is a speed-time sequence produced by different organizations for a certain type of vehicles in a particular environment to represent the real driving pattern to assess the performance of vehicles in various ways, as for example fuel consumption and polluting emissions.

As driving patterns vary for different zones, the available drive cycles obtained for certain countries and traffic conditions are not usually applicable for other areas. Therefore, many of researches has been performed on collecting traffic data to develop appropriate drive cycles for specified area and countries. In [26] various real driving cycles development procedure explained and their characteristics were compared. In this paper a real driving cycle based on the actual traffic condition in Tehran city is develop to conduct the actual measurements of exhaust emissions and fuel consumption of a test passenger vehicle. Then, characteristics of Teh-car cycle are compared with some of light vehicles cycles provided for other countries to investigate the difference between the various driving cycle and traffic conditions. Finally, this cycle has been utilized for modeling and simulation of PHEVs and HEVs.

A. Experimental data collection system

Data collection from the test road is the most important activity. Test road (e.g. city, highway, etc.) measured data are the inputs to the drive cycle preparation activity. The driving data includes date/time, number of satellites, longitude, latitude, speed and altitude of the vehicle during every second. In this paper, onboard electronic equipment was used and real world traffic data as shown in Figure 3 was collected, covering almost all the Tehran road network for a six month. For this purpose a vehicle fitted with a speed recorder, Global Positioning System (GPS), Advance Vehicle Location (AVL), accelerometer is driven over selected routes to collect data. The data are subsequently analyzed and characterized by the speed-acceleration relative frequency as well as by overall

parameters such as average speed and root mean square acceleration.



Fig. 3. Data collection routes of Tehran city

The AVL system, which is shown in Figure 4, operates on the basis of GPS which is a satellite-based navigation system. The X8 model AVL system has been used in this study. The data which is recorded every second includes some information such as date/time, number of the satellites, longitude, latitude, speed and altitude of the vehicle.

In order to analyze the driving data, a partitioning approach is proposed in this study based on definition of driving segments. A "driving segment" is defined as a part of vehicle's velocity profile in a period of time. Length of driving segments can be set to any desired value. Here regarding to the application of study in HEV control, length of segments is set to 10 second. Figure 5 depicts a sample of measured driving data containing four 1800 (s) driving segments and driving characteristics for developed Teh-car driving cycle. Also extreme segments were removed such as very high top speed segments. Only the vital segments were kept to be processed and finally give the resulting smooth Teh-car driving cycle.

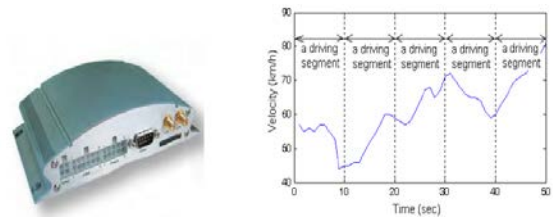


Fig. 4. X8 AVL system and velocity-time driving segmentation

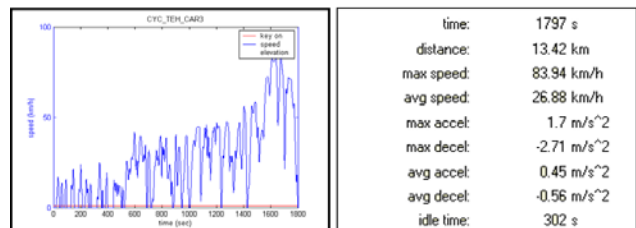


Fig. 5. Developed Teh-car driving cycle and its features

There are two major categories of driving cycles, legislative and non-legislative. According to legislative driving cycles, exhaust emissions specifications are imposed by governments for the car Emission Certification. Such cycles are the FTP-75 [26] used in the USA and the NEDC

used in Europe. Non-legislative cycles, such as the Hong Kong driving cycle [27], the Sydney driving cycle [28] and the presented Teh-car driving cycle [3], which are implicated for evaluation of fuel consumption and pollution for various area of traffic conditions.

Also, two categories of driving cycle's development can be found in the literature [29]. Synthesized or modal driving cycles are built by combining different phases of constant acceleration and speed, (like the NEDC and ECE). However in such driving cycles, the transition between the different phases is unrealistic. The other type is derived from actual driving data and is referred as "real world" cycle. Real world driving cycles are developed by recording speed-acceleration profiles while driving on the real world roadway network (often chasing a randomly selected vehicle). Such cycles are the FTP-75 in the US, and driving cycles for Hong Kong. Proposed Teh-car driving cycle is also one of the Real-World Driving cycles. These cycles are more dynamic, reflecting the more rapid acceleration and deceleration patterns experienced during on road conditions. This more dynamic driving in real world conditions results on higher emissions compared to those under the standard emissions (modal) test cycles. Three different urban drive cycles and their statistics, the US FTP and NEDC are illustrated in Figs 6-8 and table A1 respectively.

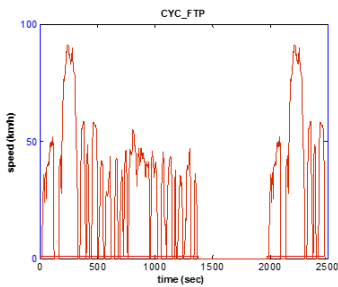


Fig.6 FTP driving cycle

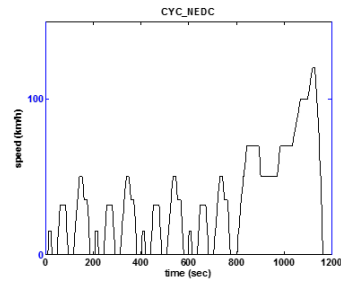


Fig.7 NEDC driving cycle

IV. CONTROL STRATEGY

The control strategies primarily target the minimization of fuel consumption, while meeting the power demand and also enhancing the drivability. The present work deals with the backward and forward modeling of a Power Split PHEV.

Control strategies play an important role in improving vehicle performance and managing energy usage for HEV and PHEV. There are two classes of control, i.e. rule-based (RB) control and optimization approaches control. In this paper fuzzy logic controller is developed for minimization of fuel consumption and emissions. The fuzzy torque distribution controller selects the corresponding membership functions and rules to control the hybrid system according to the identification results of the driving cycle recognition.

As shown in Fig.10, a fuzzy logic controller using the driver command, the state of charge of the energy storage, and the motor/generator speed, a set of rules have been developed, in a fuzzy controller, to effectively determine the split between the two power sources in various operation modes for HEV and PHEV with parallel configuration.

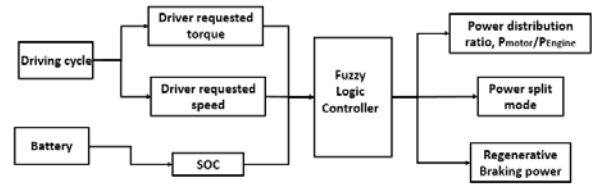


Fig.10. schematic of GA-Fuzzy lower level controller for HEV

Then, in order to optimize the fuzzy logic controller, genetic algorithm is utilized to tune fuzzy rules and parameters for both of the HEV and PHEV. The aim of the proposed FLC is to minimize fuel consumption and engine emissions simultaneously. This objective is the integral of fuel consumption and engine emissions over a driving cycle as follows:

$$J(x) = \frac{1}{w_1 + w_2 + w_3} \left(w_1 \int_0^{T_{DC}} \frac{FC}{FC} dt + w_2 \int_0^{T_{DC}} \frac{HC + NO_x}{HC + NO_x} dt + w_3 \int_0^{T_{DC}} \frac{CO}{CO} dt \right) \quad (1)$$

where w_1 , w_2 and w_3 are weighting factors which are representing the importance on fuel economy, total HC and NO_x emissions and CO emissions respectively. This is one large degree of freedom, since the weights must be selected based on the design objectives. For instance, when the main objective is the minimization of the vehicle fuel consumption, the weight of FC is set to 1 and the weights of emissions will be less than 1. (FC), ($HC + NO_x$ and CO) are the target values extracted from the SAE-J1711 [30] emissions and fuel consumption standards, defined for normalization of objective function. In this study, the weights are considered to be equal for all the variables including the fuel consumption and emissions. x is a vector containing all parameters used to define the membership function, and T_{DC} is duration of driving cycle. Membership functions with five variables for SOC variation are shown in Fig. 11.

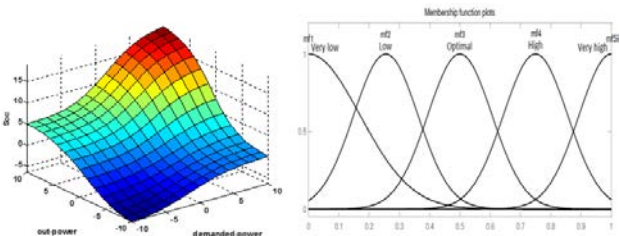


Fig.11. Membership function for SOC variation

In addition, the vehicle longitudinal dynamic requirements are defined as constraints. The following passenger vehicle constraints are used to ensure that the vehicle performance is not sacrificed during optimization [2]:

- Gradeability: 88.5 km/h at 6.5% grade for 20 min,
- Acceleration time: 0–97 km/h \leq 12 s, 64–97 km/h \leq 5.3 s, 0–137 km/h \leq 23.4 s,
- Maximum speed: \geq 137 km/hr,
- Maximum acceleration: \geq 0.5g's,
- Distance in 5s: \geq 42.7 m.

A combined backward-forward modeling hybrid vehicle model are utilized for implementation and simulation of the controller. Potential fuel economy improvement has been

shown by using fuzzy logic, relative to other controllers, which maximize only the efficiency of the engine.

V. RESULT

In this paper a new HEV and PHEV model called “Samand” are developed. In order to simulate in ADVISOR, 4 sequential Tehran driving cycles are selected. The whole distance of the cycle is 53689 meter which in PHEV mode at the end of the cycle, vehicle is connected to charger.

Parallel hybrid vehicle is modeled in ADVISOR software. Control strategy and component data are added by MATLAB/Simulink.

A. HEV Results

In the first step, to achieve optimal configuration for various driving cycles (FTP-NEDC-Teh-car), the effects of gearbox and battery on HEV’s fuel consumption and emissions are presented in tables 3 and 4 respectively.

Table 3. Fuel consumption and emissions rates for Manual and Automatic gearbox in various driving cycles

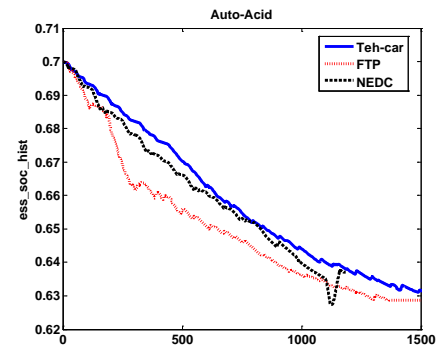
Driving cycle	Gearbox	FC	Nox	Co	HC
NEDC-2	Automatic	5.9	0.344	1.75	0.2
	Manual	6.7	0.360	2.13	0.29
FTP-3	Automatic	7	0.28	1.62	0.25
	Manual	6.1	0.26	1.27	0.28
Teh-car	Automatic	7.7	0.33	1.58	0.22
	Manual	6.6	0.32	1.38	0.17

Table 4. Fuel consumption and emissions rates for Lithium Ion and Lead-acid battery in various driving cycles

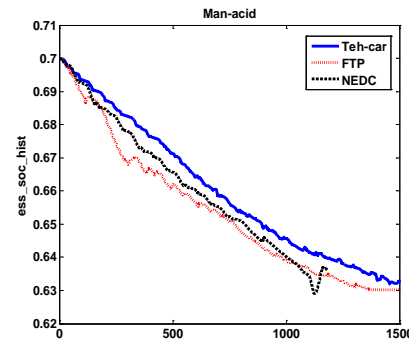
Driving cycle	Battery	FC	Nox	Co	HC
NEDC-2	Lit	5.9	0.34	1.75	0.20
	Pb	6.6	0.36	1.81	0.23
FTP-3	Lit	6.1	0.26	1.27	0.22
	Pb	6.3	0.26	1.30	0.28
Teh-car	Lit	6.6	0.32	1.38	0.17
	Pb	7.2	0.33	1.36	0.20

The results indicate that due to intensive change in real traffic driving cycles (FTP and Teh-car) Manual gearbox have improved the fuel economy and emissions. Whereas, in modal driving cycle (NEDC) automatic gearbox works more efficiently. Moreover, the results show that Teh-car driving cycle are more congested with intensive speed profile variation and stops. Also, as shown in table 4, lithium-ion batteries for all cycles reduce fuel consumption and emissions more than lead-acid batteries.

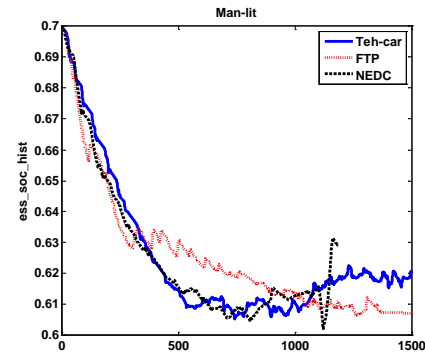
Also, the effects of different combination of transmission (automatic/manual) and battery (Lead acid/lithium-ion) on SOC for various cycles are illustrated in Figs. 12.



a) Automatic-Lead/acid configuration



b) Manual-Lead/acid configuration



c) Manual-lithium-ion configuration

Fig. 12. The effects of gearbox and battery on SOC variation in various driving cycles

B. Teh-car cycle results

In the next stage, the performance of HEV in various component combination in Teh-car cycle are evaluated. In order to investigate the gearbox and batteries effect on HEVS performance, the fuel convertor torque, loosed power in wheels and energy storage system efficiency are depicted in Figs. 13-14 respectively.

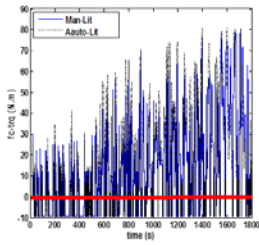


Fig. 13 effect of gearbox on output torque requested of the engine

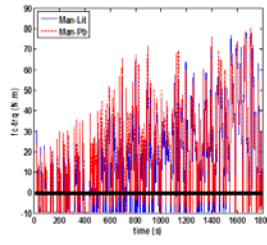


Fig. 14 effects of battery on output torque requested of the engine

Negative torques in Figs. 13 and 14 depicts regenerative torques which in manual gearbox and lithium-ion batteries are less than automatic and lead-acid ones respectively. Also, engine torques variation in automatic is more than manual which result in deviation of engine operation points from optimal zone. Furthermore, in order to analyze the energy storage system, for various configuration its efficiency is illustrated in Fig. 15. Results show that, lithium-ion batteries efficiency is much better than lead-acid one. Also, Comparison of automatic and manual gearboxes, which indicate that manual one in Teh-car improves the energy storage performance.

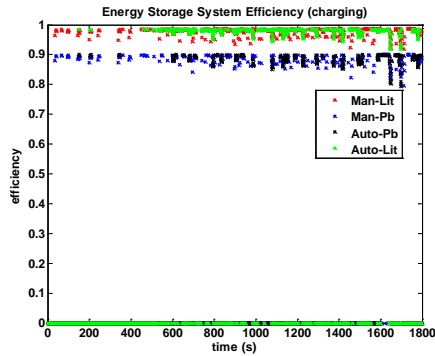


Fig. 15. Energy storage system efficiency in charging mode for various configuration

C. 4 sequential Teh-car cycle simulation

In this stage, in order to evaluate the control strategies performance in real world driving condition, computer simulations are carried out at four iteration of Teh-car cycle (Fig. 16). Also, gear shifting in 5 speed manual transmission during 4Teh-car cycle has been illustrated in Fig. 17.

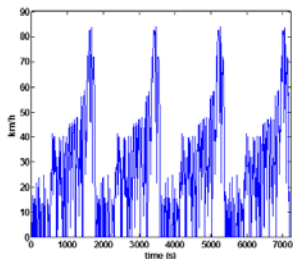


Fig. 16 4 iteration of Teh-car drive cycle

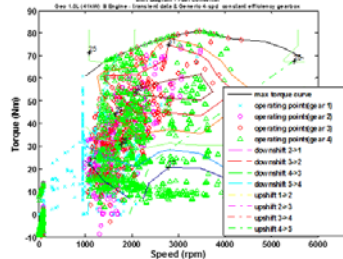


Fig. 17 gear shifting for optimal configuration of 4cycle Teh-car

D. Effects of initial SOC

Finally, simulation results for fuel consumption and emissions are compared to HEV according battery state of

charge. State of charge for HEV with 90%, 70% and 50% initial state of charging is considered. Simulation results include SOC variation, fuel consumption and emissions are compared for above mentioned conditions in figure 18, and table 5 respectively. The effects of SOC on HEV performance showed that, a higher initial values of SOC, leads to reduction of fuel consumption and emissions.

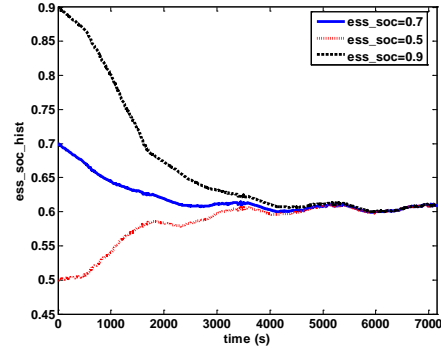


Fig. 18 effect of initial SOC

Table 5. Effects of initial SOC on HEV for 4 iteration of Teh-car driving cycle

Initial SOC	0.5	0.7	0.9
Distance (Km)	53.7	53.7	53.7
LpKm	9.1	7.6	6.6
Nox	0.221	0.179	0.161
Co	1.402	0.851	0.755
HC	0.241	0.167	0.138

E. PHEV simulation

Simulation results for fuel consumption and emissions are compared to PHEV and HEV according battery state of charge. At the first stage, state of charge for PHEV with 90% and 80% initial state of charging is considered. Then in the second stage simulation performed on HEV with the SOC of 20-90%. Simulation results include SOC variation, fuel consumption and emissions are compared for above mentioned conditions in figures 19, 20 and table 6 respectively.

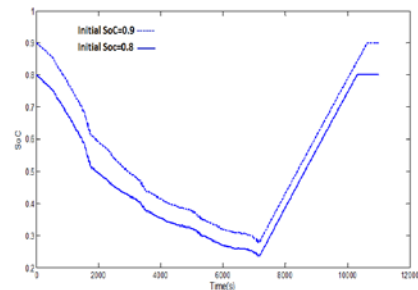


Fig. 19 PHEV Battery SOC variation in 4teh-car cycle

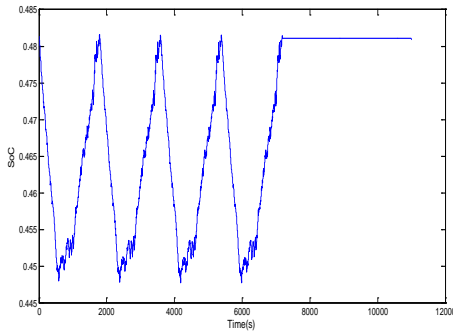


Fig. 20 HEV Battery SOC variation in 4teh-car cycle

Table 6. Simulation results and SOC effects

	FC	HC	NOx	Co	Equivalent electricity FC
PHEV, Initial SOC=90%	4.35	0.032	0.027	0.460	3.545 kWh \approx 0.68 Lit
PHEV, Initial SOC=80%	4.52	0.032	0.027	0.482	3.205 kWh \approx 0.617 Lit
HEV, SOC (20-90%)	6.21	0.031	0.018	0.945	-

This result indicated that the exhausted emissions and fuel consumption obtained of PHEV are less than HEVs. Also, the effects of SOC on PHEV performance showed that, a higher initial values of SOC , leads to reduction of fuel consumption and emissions.

Performance of internal combustion engine (ICE) and electrical motor (EM) of PHEV during driving cycle for both initial SOC conditions are illustrated in Figs. 21-24. The effects of the Initial SOC leveling of the battery are clearly evident in the figures. By the 90% initial SOC the operation points for both ICE and EM are close to the optimized situation and their dissipation are more less than 80% one, which as well as improves energy management efficiency, results in reduction of fuel consumption and exhaust emissions.

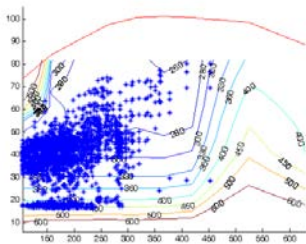


Fig. 21 Electrical motor performance (Initial SOC=90%)

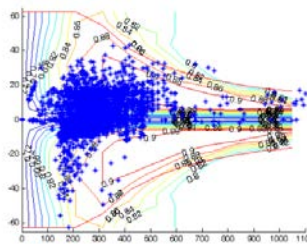


Fig. 22 ICE performance (Initial SOC=90%)

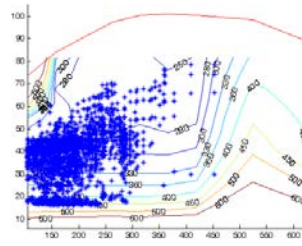


Fig. 23 Electrical motor performance (Initial SOC=80%)

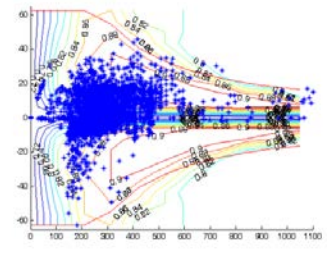


Fig. 24 ICE performance (Initial SOC=80%)

VI. CONCLUSION

Development of the particular city driving cycles allows obtaining much more accurate and relevant data on the car's fuel consumption and harmful exhaust emissions than the use of standard cycles elaborated for vehicles certification. This paper describes the development of Tehran passenger car drive cycle for simulation of PHEV to evaluate the fuel consumption and emissions. At the first stage experimental data acquisition of real traffic condition for Tehran city have been done to develop Teh-car driving cycle. At the second stage, Teh-car driving cycle are utilized for simulation of the HEV and PHEV to evaluate and compare the fuel consumption and emissions. Simulation results indicate better performance of PHEV in comparison to HEV one during Teh-car driving cycle. Finally, the effects of battery SOC investigated on PHEVs. A high initial SOC shifted operation point of ICE and EM to optimal condition which lead to reduce emissions and fuel consumption.

Development of the optimal configuration, energy management control strategy and powertrain component in various driving cycles in HEVs is resulted in reduction of fuel consumption and exhaust emissions with regard to its performance. Simulation results indicate better performance of manual transmission in comparison to automatic one during real world drive cycles. This paper utilizes the GA-Fuzzy controller strategy on parallel hybrid vehicle for both of the HEVs and PHEVs. Finally, initial SOC variation effects has been investigated on Fuel consumption and emissions for HEV and PHEV. PHEVs are even more suitable topologies than traditional HEVs for reducing fuel consumption and emissions. A PHEV can use the stored energy during the charge-depleting operation. This use of electrical energy can save considerable amount of fuel. PHEVs use lesser fuel than the conventional HEVs because of the fact that there is a provision for off-board charging of the vehicle. PHEVs enjoy the same benefits as conventional HEVs and also provide an opportunity for switching between fuel and electricity. The initial cost of the energy system are higher than the older cars. The balance between initial cost and running cost of the system must be established.

Table A1. Statistics of driving cycles

Driving cycle	Time (s)	Distance (Km)	Max. speed (Km/h)	Avg. speed (Km/h)	Max. accel. (m/s ²)	Max. decel. (m/s ²)	Avg. accel. (m/s ²)	Idle time (s)	No. stops
FTP	2477	17.17	91.25	25.82	1.48	-1.48	0.51	361	22
NEDC	1184	10.93	120	33.21	1.06	-1.39	0.54	298	13
Teh-car	1797	13.42	83.93	26.87	1.71	-2.71	0.45	302	20

References

- [1] Kutrašnik T., "Analytical framework for analyzing the energy conversion efficiency of different hybrid electric vehicle topologies", *Energy Conversion and Management*, vol. 50, 2009, pp., 1924–1938.
- [2] Montazeri-Gh, M., Poursamad, A., Ghalichi, B., "Application of genetic algorithm for optimization of control strategy in parallel hybrid electric vehicles", *Journal of the Franklin Institute*, vol. 343, pp. 420–435.
- [3] Montazeri-Gh, M., Naghizadeh, M., "Development of car drive cycle for simulation of emissions and fuel economy", 15th European Simulation Symposium Proceedings, Delft, Netherlands, October 2003.
- [4] Behnam Ganji, Abbas Z. Kouzani, and H.M. Trinh, "Drive Cycle Analysis of the Performance of Hybrid Electric Vehicles", Springer-Verlag Berlin Heidelberg, Part I, LNCS, 6328, 2010, pp. 434–444.
- [5] Liu, W., "Introduction to hybrid vehicle system modeling and control", John Wiley & Sons, Inc. ISBN 978-1-118-30840-0, 2013.
- [6] Neira, O.F.D., "Driving Cycle Properties and their Influence on Fuel Consumption and Emissions", Dissertation submitted to the Benjamin M. Statler College of Engineering and Mineral Resources West Virginia University, In partial fulfillment of the requirements for the degree of Doctor of Philosophy, In Mechanical Engineering, 2012.
- [7] Tie, S.F., Tan, C.H., "A Review of Energy Sources and Energy Management System in Electric Vehicles", *Renewable and Sustainable Energy Reviews*, Vol. 20, 2013, pp. 82–102.
- [8] Wirasingha, S.G., Emadi, A., "Classification and Review of Control Strategies for Plug-In Hybrid Electric Vehicles," *IEEE Transactions on Vehicular Technology*, Vol. 60, No. 1, 2011, pp. 111–122.
- [9] Montazeri, M., Poursamad, A. and Ghalichi, B., "Application of genetic algorithm for optimization of control strategy in parallel hybrid electric vehicles", *J. Franklin Institute*, vol. 343, 2006, pp. 420–435.
- [10] Chen, Z., Mi, C.C., Xiong, R., Xu, J., You, C., "Energy management of a power-split plug-in hybrid electric vehicle based on genetic algorithm and quadratic programming", *Journal of Power Sources*, Vol. 248, 2014, pp. 416–426.
- [11] Desai, C., "Design and Optimization of Hybrid Electric Vehicle Drivetrain And Control Strategy Parameters Using Evolutionary Algorithms", A Thesis in The Department of Electrical and Computer Engineering Presented in Partial Fulfillment of the Requirements for the Degree of Master of Applied Science (Electrical Engineering and Computer Science) at Concordia University Montréal, Québec, Canada, 2010.
- [12] Pérez, L. V., Pilotta, E. A., "Optimal power split in a hybrid electric vehicle using direct transcription of an optimal control problem", *Mathematics and Computers in Simulation*, Vol. 79, Issue 6, 2009, pp. 1959–1970.
- [13] Pérez, L. V., Bossio, G. R., Moitre, D., Garc'ia, G. O., "Optimization of power management in an hybrid electric vehicle using dynamic programming",
- [14] Sciarretta, A., Back, M., Guzzella, L., "Optimal control of parallel hybrid electric vehicles", *IEEE Trans. Control Syst. Technol.* Vol. 12, 2004.
- [15] Jalil, N., Kheir, N., and Salman, M., "Fuzzy Logic Control for Parallel Hybrid Vehicles", *IEEE Transactions on Vehicular Technology*, vol. 10, No. 3, 2002, pp. 460–468.
- [16] Montazeri-Gh, M., Poursamad, A., "Application of genetic algorithm for simultaneous optimization of HEV component sizing and control strategy", *Int. J. Alternative Propulsion*, Vol. 1, No. 1, 2006, pp. 63–78.
- [17] Li, S.G., Sharkh, S.M., Walsh, F.C., Zhang, C.N., "Energy and Battery Management of a Plug-In Series Hybrid Electric Vehicle Using Fuzzy Logic", *Veh. Technol., IEEE Trans.*, Vol. 60, Issue 8, 2011, pp. 3571–3585.
- [18] Kono, H., "Fuzzy control for hybrid electric vehicles," Master's thesis, Department of Electrical Engineering, The Ohio State University, 1998.
- [19] Martínez, J.S., Mulot, J., Harel, F., Hissel, D., Péra, M.C., John, R.I., Amiet, M., "Experimental validation of a type-2 fuzzy logic controller for energy management in hybrid electrical vehicles", *Engineering Applications of Artificial Intelligence*, Vol. 26, Issue 7, 2013, pp. 1772–1779.
- [20] Martínez, J.S., John, R.I., Hissel, D., Péra, M.C., "A survey-based type-2 fuzzy logic system for energy management in hybrid electrical vehicles", *Information Sciences*, Vol. 190, 2012, pp. 192–207.
- [21] Wu, J., Zhang, C. H., Cui, N.X., "Fuzzy Energy Management Strategy For A Hybrid Electric Vehicle Based On Driving Cycle Recognition", *International Journal of Automotive Technology*, Vol. 13, No. 7, 2012, pp. 1159–1167.
- [22] Liang, J., Zhang, J., Zhang, X., Yuan, S., Yin, C., "Energy management strategy for a parallel hybrid electric vehicle equipped with a battery/ultra-capacitor hybrid energy storage system", *Journal of Zhejiang University-SCIENCE A (Applied Physics & Engineering)*, Vol. 14(8), 2013, pp. 535–553.
- [23] Same, A., Stipe, A., Grossman, D., Park, J.W., "A study on optimization of hybrid drive train using Advanced Vehicle Simulator (ADVISOR)", *Journal of Power Sources*, vol. 195, 2010, pp. 6954–6963.
- [24] Pennestrì, E., Mariti, L., Valentini, P.P., Mucino, V.H., "Efficiency evaluation of gearboxes for parallel hybrid vehicles: Theory and applications", *Mechanism and Machine Theory*, Vol. 49, 2012, pp. 157–176.
- [25] He, Y., Chowdhury, M., Pisu, P., Ma, Y., "An energy optimization strategy for power-split drivetrain plug-in hybrid electric vehicles", *Transportation Research Part C: Emerging Technologies* Vol. 22, 2012, pp. 29–41.
- [26] Barlow, T. J., Latham, S., McCrae, I. S. and Boulter, P. G., "A reference book of driving cycles for use in the measurement of road vehicle emissions", Department of transport, Cleaner Fuels & Vehicles, 2009.
- [27] [21] Hung, W.T., Tong, H.Y., Lee, C.P., "Development of a Practical Driving Cycle Construction Methodology: A Case Study in Hong Kong", *Transportation Research, Part D: Transport & Environment*, Vol. 12, 2007, pp. 115–28.
- [28] Kent, H., Allen, G.H., and Rule, G., "A driving cycle for Sydney", *Journal of Transportation Research*, vol. 12, 1978, pp. 147–152.
- [29] Amirjamshidi, G., Roorda, M.J., "Development of Simulated Driving Cycles: Case study of the Toronto Waterfront Area", Annual meeting of Transportation Research part B, 2013.
- [30] Society of Automotive Engineers Surface Vehicle Recommended Practice: "SAE J1711 – Recommended Practice for Measuring Fuel Economy of Hybrid-Electric Vehicles", SAE Publication, Issued March 1999.

Different approaches for calculation of EMF induced by the currents of overhead line in the shields of buried cables

Korovkin N.V., Minevich T.G.

St. Petersburg State Polytechnic University, Russia

Abstract—Two approaches have been formulated to calculate EMF induced in the shield of buried cable. Integral or differential presentation of electrical and magnetic quantities is possible to be used in calculations of electromagnetic field parameters. The scope of application of each approach has been analyzed.

Keywords— electromagnetic field equations, magnetic flux, EMF, buried cable, high-voltage line.

I. INTRODUCTION

The problems of electromagnetic compatibility are to be resolved at designing and operating high-voltage and power-generating equipment. The increase of electronic devices, hardware and feeding cables density makes the assessment of electromagnetic interaction effects more and more essential. The components of power systems affect the environment that may result in information channel degradation, in digital device errors up to their physical damage and even to their burning. That is why the assessment of electromagnetic interaction effects is a topical problem nowadays, this problem is studied in multiple papers [1]-[3].

The present paper considers the comparison of two approaches of solution of the problem of EMF induction in buried cable by the currents of high-voltage line. For our purpose they may be called “integral” and “differential” approaches because the laws of electromagnetic field are supposed to be used in integral or differential forms.

To teach the subjects dealing with calculations of electromagnetic phenomena in power facilities and electrical devices means to know the laws of electromagnetic fields in integral form at the beginning of learning process. This will facilitate the comprehension by students of a complex-plane mechanism of electromagnetic field analysis. Besides that electric and magnetic phenomena will be studied singly in the context of “integral” approach. Such an approach will maintain a continuous complication of the material and will explain the conditions of prior manifestation of electric or magnetic phenomena. For example, in terms of electrical field these are spatial zones surrounding fixed electrified bodies, while for magnetic field there will be zones surrounding fixed permanent magnets.

For example, when considering magnetic phenomena it will be important to understand a fundamental and simultaneous availability of electrical phenomena and vice versa. In case of process analysis within the system of electrified fixed bodies the charges make a set of charges of elementary charged particles and each particle is surrounded by electromagnetic field. In this regard a total magnetic field is already small at tight spacing of electrified bodies.

When solving specific tasks from the point of view of only one part of electromagnetic field students and afterwards engineers and scientific workers do not cognize electric and magnetic fields as a unified electromagnetic field and perceive phenomena taking place in electrical devices as somewhat lopsided: either electric or magnetic.

II. PROBLEM FORMULATION

In discussing the relationships between electrical and magnetic phenomena experimental data and Maxwell's laws are usually cited which in their turn represent the compilation of experimental data. That is why the relationship of electrical and magnetic fields may be shown only in the form of known theoretical correlations. The most frequently occurring example of electrical and magnetic relationships is the law of electromagnetic induction, for example, EMF induction on the portion of cable being in the vicinity of another cable. Let the cables 1 and 2 be parallel one another and to earth (Fig. 1).

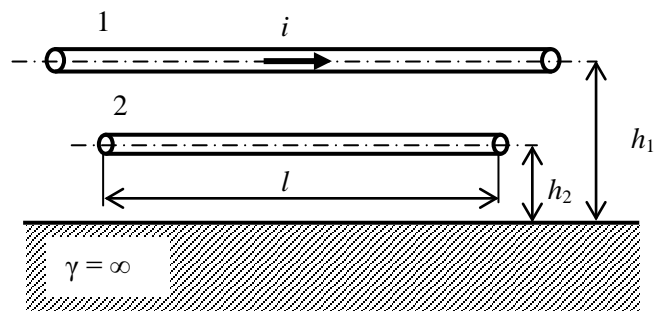


Fig. 1. Geometrical pattern of an original problem with non-uniform conductance of calculation zone and ideally conducting earth

The suspension height of first wire is h_1 , of second wire - h_2 . When specifying EMF created by current i in wire 2 of l length one should use the method of electrical images. In such a case the original problem (Fig. 1) may have the form of the problem shown on Fig. 2. Here a conducting medium is replaced by wire 1 image with charge sign changing (current reversal).

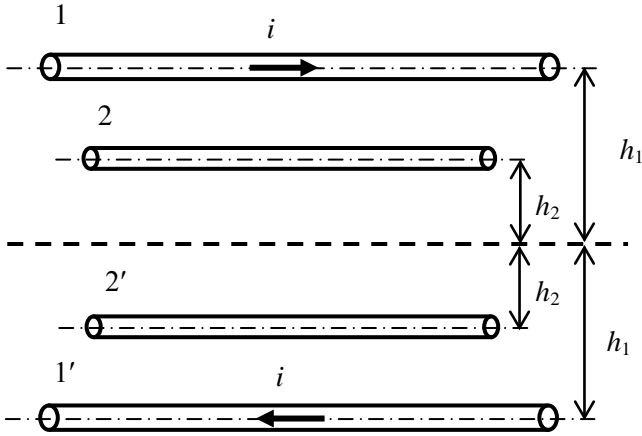


Fig. 2. Geometrical pattern of the problem with uniform conductance of calculation zone

A traditional approach for solving this type of problem is to define a magnetic strength created in some spatial zone limited by L contour. It means that the problem is considered as a “magnetic” one. Electric field characteristics are not taken into account in this case. Given the wire current, one may specify the magnetic field density or strength not in the point of wire 2 but in any point in space. Further on one may determine an integral quantity - flux through the surface limited by a chosen integration contour [5], [6].

In this case a rectangular contour L of l length and $2h_2$ width may be considered as contour L (Fig. 3).

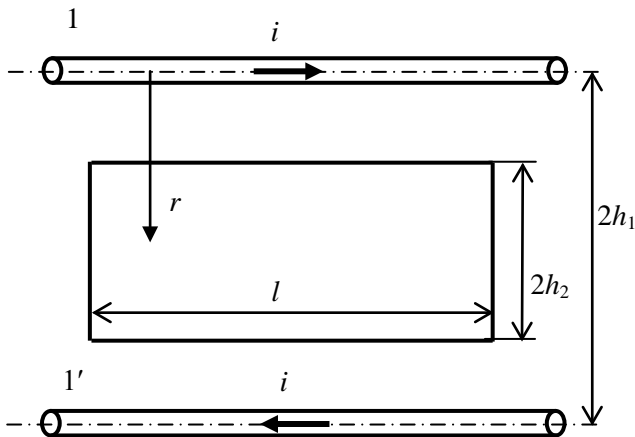


Fig. 3. Geometrical pattern of the problem with uniform conductance of calculation zone and chosen integration contour

Then, the magnetic strength created at a distance r from wire 1 will have two components [4]:

$$B_1 = \frac{\mu_0 i}{2\pi r} \text{ and } B_{1'} = \frac{\mu_0 i}{2\pi(2h_1 - r)},$$

while the magnetic strength Φ through L contour will be equal to

$$\Phi = \frac{\mu_0 i}{2\pi} l \int_{h_1-h_2}^{h_1+h_2} \left(\frac{1}{r} + \frac{1}{2h_1 - r} \right) dr = \frac{\mu_0 i}{\pi} l \ln \frac{h_1 + h_2}{h_1 - h_2}.$$

Now using the Faraday's law of electromagnetic induction we shall have:

$$e = -\frac{d\Phi}{dt} = -\frac{\mu_0}{\pi} l \ln \frac{h_1 + h_2}{h_1 - h_2} \frac{di}{dt}.$$

Or, taking into account that the current changes according to sinusoidal law with specific frequency ω , and passing into a complex domain we shall receive EMF induced in L contour:

$$\dot{E} = -j\omega\dot{\Phi} = -j\omega \frac{\mu_0 \dot{i}}{\pi} l \ln \frac{h_1 + h_2}{h_1 - h_2}. \quad (1)$$

To specify EMF induced on a portion of wire 2 of l length it is accepted to divide an obtained result in half, while accounting for the fact that the integration contour contains two parallel portions as long as l .

An approach described above may be extended on the calculation of EMF induced by the currents of overhead line (the height of overhead wire suspension being h_1) in the shield of cable buried at h_2 depth (Fig. 4). In this case the earth conductivity γ may be considered as a final quantity. Let us note the depth of electromagnetic field penetration in earth layer as h_0 , then we may define it following $h_0 = (2/\omega\mu\gamma)^{0.5}$.

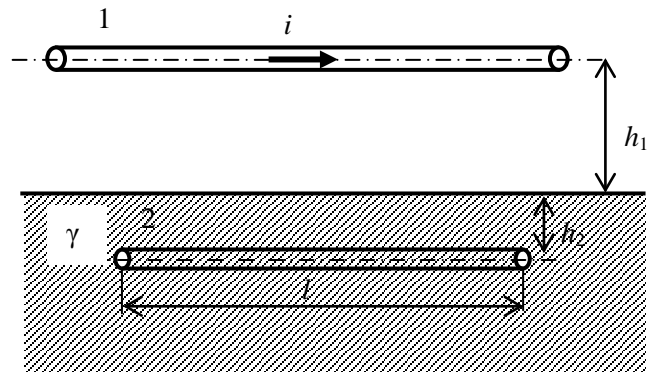


Fig. 4. Geometrical pattern of the problem with non-uniform conductance of calculation zone and non-ideally conducting earth

We may obtain a calculation zone shown on Fig. 5 by using the method of electrical images. Considering the designations given on Fig. 5 EMF induced in the shield of buried cable may be specified by using (1):

$$\dot{E} = -j\omega\dot{\Phi} = -j\omega\frac{\mu_0\dot{I}}{\pi}l\ln\frac{a+b}{a-b}.$$

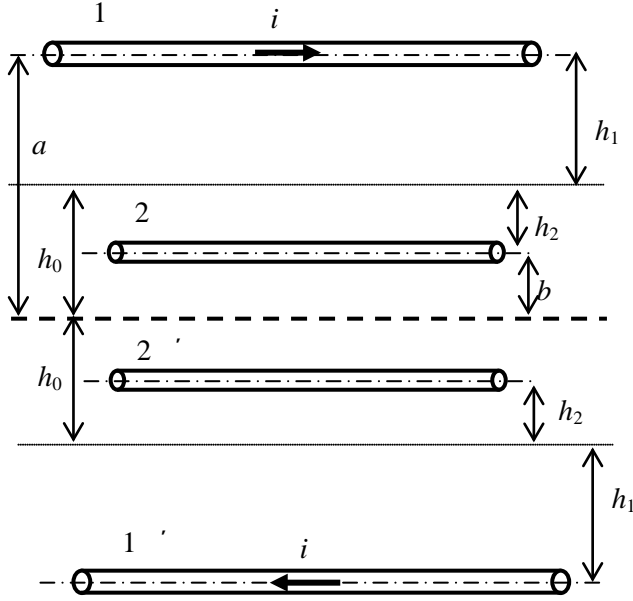


Fig. 5. Geometrical pattern of the problem with uniform conductance of calculation zone (non-ideally conducting earth is taken into consideration).

In calculations presented above the flux is a fundamental quantity. In this case the order of EMF calculation contains the following stages: one may specify by a given current value magnetic field vectors (magnetic density or strength), then he defines a flux (or flux linkage) through the surface limited by a certain contour and then EMF induced in this contour. A given consequence of electrical quantity determination through magnetic quantities is conditioned by historical development of electric engineering [4]. An empirical Faraday's law of electromagnetic induction allows to consider EMF as the rate of flux change. Such an approach is justified and is worth to be considered only if a real or imaginary contour of apparent shape is available

III. PROBLEM SOLUTION

Issues occurring with application of such an approach are manifested when it is required to define the influence of a wire with current on another wire, i.e. to specify the value of EMF induced in a wire not closed on a given section. Such issues occur when analyzing the processes taking place in power transmission lines. This may occur, for example, in assessing the effect of one three-phase wire on others. The situation becomes more complicated when a wire transposition is applied. Then the choice of contour

configuration limiting the surface through which the flux is to be determined, is controversial and an approach using Maxwell equations in differential and not integral (through magnetic flux) form seems to be optimal.

Now let us consider the problem solution (Fig. 4) by using the law of electromagnetic induction in differential formulation:

$$\text{rot } \mathbf{E} = -\frac{\partial \mathbf{B}}{\partial t}. \quad (2)$$

In cylindrical coordinate system when the direction of axis x is chosen as the current direction, there shall be only one vector component of electric field strength [4], [7] and equation (2) may be simplified as follows:

$$\begin{aligned} \text{rot } \dot{\mathbf{E}} &= \left(\frac{1}{r} \frac{\partial \dot{E}_x}{\partial \varphi} - \frac{\partial \dot{E}_\varphi}{\partial x} \right) e_r + \left(\frac{\partial \dot{E}_r}{\partial x} - \frac{\partial \dot{E}_x}{\partial r} \right) e_\varphi + \\ &+ \left(\frac{1}{r} \frac{\partial (r \dot{E}_\varphi)}{\partial r} - \frac{1}{r} \frac{\partial \dot{E}_r}{\partial \varphi} \right) e_x = \text{rot}_\varphi \dot{E}_x = -\frac{d\dot{E}_x}{dr} = -j\omega \dot{B}_\varphi. \end{aligned}$$

An angular component of magnetic induction vector may be defined as it was done in previous approach:

$$\dot{B}_\varphi = \frac{j\omega\mu_0\dot{I}}{2\pi} \left(\frac{1}{r} + \frac{1}{2a-r} \right).$$

To specify EMF induced in any point of cable shield one must solve a differential equation:

$$\frac{d\dot{E}_x}{dr} = \frac{j\omega\mu_0\dot{I}}{2\pi} \left(\frac{1}{r} + \frac{1}{2a-r} \right).$$

Given that the electric field strength on image plane is zero: $\dot{E}_x|_{r=a-b} = 0$. Then

$$\begin{aligned} \int_0^{\dot{E}_x} d\dot{E}_x &= \frac{j\omega\mu_0\dot{I}}{2\pi} \int_a^{a-b} \left(\frac{1}{r} + \frac{1}{2a-r} \right) dr, \\ \dot{E}_x &= \frac{j\omega\mu_0\dot{I}}{2\pi} \left[\ln \frac{a-b}{a} - \ln \frac{a+b}{a} \right] = \\ &= -\frac{j\omega\mu_0\dot{I}}{2\pi} \ln \frac{a+b}{a-b}. \end{aligned} \quad (3)$$

Knowing the value of electric field strength (3) it shall be easy to define the value of EMF induced on any cable portion [8]. For a portion whose length is l , an induced EMF is equal to

$$\dot{E} = \dot{E}_x l = -\frac{j\omega\mu_0\dot{I}}{2\pi} l \ln \frac{a+b}{a-b},$$

which coincides with already obtained result.

Two approaches of problem solution pertaining to the calculation of EMF induced in the shield of buried cable have been shown. In the first “integral” approach it is required to choose an integration contour. The shape of this contour is only evident when the both objects (wire with currents and that one where EMF is induced) are placed in parallel each another in the same plane. Once the total value of EMF is specified for a chosen (often imaginary) contour, it should be required to perform additional calculations to define EMF on a given section. The second approach does not require choosing of integration contour and allows obtaining EMF values directly upon values of electrical field strength on an arbitrary portion of cable. When using the second approach, one must find the solution of differential equation.

IV. CONCLUSION

The shown solutions of set problems are not the only result of the work presented by authors. The problems considered in this paper are rather simple; their solution is not difficult to obtain through application of both approaches. The authors suppose that the significance of this paper is not purely applicable for production needs but methodological one and they hope that the approaches of solving the problems of electrical engineering and electric power industry may help the researchers to form a correct comprehension of electromagnetic field properties.

REFERENCES

- [1] Adalev, A.S., Korovkin, N.V., Hayakawa, M., Nitsch, J.B. Deembedding and unterminating microwave fixtures with the genetic algorithm (2006) IEEE Transactions on Microwave Theory and Techniques, 54(7), art. no. 1650456, pp. 3131-3139.
- [2] Adalev, A.S., Korovkin, N.V., Hayakawa, M. Identification of electric circuits described by ill-conditioned mathematical models. (2006) IEEE Transactions on Circuits and Systems I: Regular Papers, 53 (1), pp. 78-91.
- [3] Kuchinsky, G., Kozhevnikov, M., Schilin, O., Vekhoreva, L., Korovkin, N., Selina, E., Potienko, A. Compact power high-voltage pulse capacitor for quasi-rectangular nanosecond impulses formation. (1999) Digest of Technical Papers-IEEE International Pulsed Power Conference, 2, pp. 1449-1452.
- [4] Demirchyan K.S. Theoretical principles of electrical engineering [text]/ K.S.Demirchyan, L.R.Neyman, N.V.Korovkin – M. – SPb.: v.1, v.2 Piter, 2004.
- [5] Adalev, A.S., Korovkin, N.V., Hayakawa, M. Using linear relations between experimental characteristics in stiff identification problems of linear circuit theory. (2008) IEEE Transactions on Circuits and Systems I: Regular Papers, 55 (5), pp. 1237-1247.
- [6] Korovkin, N.V., Berlin, E.M., Efimov, K.A. The operation modes of the controlled electric transmission with the link based on the multiphase thyrstiers switch phase convertor (1991) Izvestiya Akademii Nauk Energetika, (1), pp. 28-37.
- [7] Adaleva, A.S., Hayakawa, M., Korovkin, N.V. Identification of electric circuits: Problems and methods of solution accuracy enhancement. (2005) Proceedings – IEEE International Symposium on Circuits and Systems, art. no. 1464754, pp. 980-983.
- [8] Korovkin, N.V., Balagula, Y.M., Adalev, A.S., Nitsch, J. A method of a disturbance source localization in a power system. (2005) 2005 IEEE Russia Power Tech, PowerTech, art. no. 4524765.

Tatyana G. Minevich was born in Leningrad, Russia, on April 25, 1971. She has graduated the Saint-Petersburg Polytechnic University specializing in “Electrophysics and high-voltage engineering” in 1994. Candidate of Science {Engineering}, discipline 05.09.05 “Theoretical basis of electrical engineering” 2002, Saint-Petersburg Polytechnic University, Saint-Petersburg, Russia. She has been entitled as an associated professor in 2007.

Associated professor of SPbPU chair “Theoretical basis of electrical engineering”, Saint-Petersburg, Russia. Her scientific concerns cover calculations of the processes in linear and non-linear circuits of arbitrary structure, electrical network synthesis, problems pertaining to electromagnetic compatibility.

Nikolay V. Korovkin was born in Leningrad, Russia, on January 09, 1954. He received the M.S., Ph.D. and Doctor degrees in electrical engineering, all from St. Petersburg State Polytechnical University in 1977, 1984, and 1995 respectively. He worked as a Professor for the University of Electro-Communications (Tokyo, Japan), for the Swiss Federal Institute of Technology (EPFL) Switzerland, and for Otto-von-Guericke University (Magdeburg, Germany). His main scientific interests are EMC problems, stiff systems, impulse processes in linear and non-linear systems, “soft” methods of optimization. Now he is the head of the department of Theoretical Engineering in St. Petersburg State Polytechnical University. Prof. N. Korovkin is a Member of the Academy of Electrotechnical Science of the Russian Federation, (since 1996).

Improved Hydrolysis of Pretreated Lignocellulosic Biomass using Mobile Enzyme Sequestration Platforms

Ruben Michael Ceballos*, Ruben Michael Ceballos Jr., Asha Rani, Chelsea Teresa Morales, and Natalia Alekseyevna Batchenkova

Abstract—On a large commercial scale, cellulosic ethanol, a “second-generation” biofuel, has yet to become cost competitive with fossil fuel-based liquid fuel products (e.g., gasoline). In an effort to lower the per-gallon production cost of bioethanol, two stages within the production process have been the subject of intense investigation: pretreatment; and, enzymatic hydrolysis. In general, the development of advanced pretreatments is aimed at disrupting interactions between cellulose, hemicellulose, and lignin as well as enhancing the exposure of the cellulose network to sugar reducing (e.g., hydrolytic) enzymes. The identification of novel enzymes, the engineering of enzymes, and the use of platforms that enhance enzymatic efficiency comprise a second area of research focus. In this study, we present data showing that the use of a NASA-developed mobile enzyme sequestration platform (mESP) is effective in enhancing sugar reduction efficiency on acid- and alkaline- pretreated cellulosic feedstock. Further advancement of this technology could contribute to the development of a cost-competitive cellulosic ethanol product.

Keywords—bioethanol, cellulosic ethanol, enzyme platforms, lignocellulose degradation

I. INTRODUCTION

THE production of ethanol as a supplemental transportation fuel, and a partial substitute for gasoline, is ongoing. Feedstocks such as corn and sugarcane are the basis for more than 90% of the world’s current fuel ethanol supply [1], [2]. The use of *first-generation* feedstocks, which provide sucrose and starch, has been the subject of much debate since the production of ethanol from these sources can impact food supplies, in what is called the *food-versus-fuel* dilemma [3].

This work was supported in part by the U.S. National Science Foundation under grant #0803199 (PI-Ceballos) and grant #0929484 (PI-Ceballos). Support was also provided by the Environmental Microbiology and Biochemistry Research Station (EMBRs, LLC).

R.M.C. currently serve as the chief scientific officer of EMBRS, LLC (Bemidji, MN) and an Assistant Professor of Biology in the Division of Science and Mathematics at the University of Minnesota (Morris, MN). *Corresponding author (RMC) contact: email - embrs.ruben@gmail.com; phone - (406) 249-1248.

R.M.C., Jr., C.T.M., and N.A.B. served as undergraduate research assistants. R.M.C., Jr. is a biochemistry major at the University of Alabama (Birmingham, AL). C.T.M. is currently a graduate student in pharmaceutical sciences at the University of Montana (Missoula, MT). N.A.B. is a biochemistry major at the University of Minnesota (Morris, MN).

A.R. served as a post-doctoral scholar and is currently at the University of Illinois at Chicago (Chicago, IL)

An alternative to corn, sugarcane, and other first-generation feedstocks are *second-generation* feedstocks, which include forms of lignocellulosic biomass such as corn stover, bagasse, crop straws, perennial energy crops (i.e., grasses), woody energy crops (e.g., cottonwoods, poplar, bamboo), and forestry waste. Second-generation lignocellulosic biomass is arguably the most promising type of feedstock for bioethanol production due to its global abundance and availability. However, the conversion of lignocellulosic secondary substrates (i.e., cellulose and hemicellulose) to primary sugar substrates (e.g., glucose) for fermentation processes is challenging from an economic standpoint. Although multiple technologies exist for reducing complex carbohydrates, such as cellulose, to simple fermentable sugars, such as glucose, the costs associated with these conversion processes have limited wide-scale commercial production of cellulosic ethanol.

Two steps within the ethanol production process that have been studied in an attempt to reduce the per-gallon production cost of bioethanol are the feedstock pretreatment step and the enzyme-mediated sugar reduction step. Recent reviews [4], [5] and research articles [6]-[10] have been published on the latest advancements in pretreatment technology. In general, pretreatment technology is aimed at: partially dissolving the lignocellulosic matrix; disrupting cellulose, hemicellulose, and lignin interactions; and, exposing the cellulose structure for subsequent to enzymatic hydrolysis using sugar reducing enzymes (e.g., cellulases), which can degrade complex large carbohydrates to simpler fermentable sugars (e.g., glucose).

The enzymatic step within the bioethanol production process has also been a research focus. Four approaches have been undertaken to improve sugar reduction efficiency. First, discovery of novel cellulases and other lignocellulose degrading enzymes through bioprospecting has led to the identification of enzymes [11] that function more efficiently under conditions that are used in most bioethanol production processes (e.g., elevated temperatures and in acidic solutions). Second, researchers have attempted to alter the reaction conditions and employ enzyme “cocktails” to optimize enzymatic activity [12], [13], [14] while maximizing flow-through rates and end-product yields. Third, scientists have genetically altered or otherwise designed cellulose deconstruction enzymes that have high catalytic efficiency [15], [16], [17] under production conditions.

All of these approaches have met with some success; however, the level of enhancement has not led to significant reduction in production costs such that cellulosic ethanol is competitive with either first-generation ethanol or fossil-based liquid fuels. Although many of these enzyme technologies are viable from a technical perspective, the cost of producing such enzymes and the enzyme loads required for commercial scale production are economically prohibitive.

A fourth approach to enhance sugar reduction is to bolster enzymatic hydrolysis via the use of platforms [18], [19], [20]. Enzyme platform approaches stem from understanding the manner in which natural systems function. Specifically, cellulose degrading microorganisms, such as bacteria and fungi, employ expansive protein “scaffolds” to degrade cellulosic biomass. These large protein complexes are referred to as *cellulosomes* [21] and some researchers have attempted to mimic the natural cellulosome either wholly or in part to enhance sugar reduction efficiency in industrial processes. (Some research focused on enhancing hydrolysis using living microbes that express cellulosomes has also been conducted with limited success [22] - a fifth approach). These artificial cellulosomes have evolved into protein platforms that only vaguely resemble natural cellulosomes. Although, the same enzymes that are found in natural cellulosomes are often used in engineered enzyme platforms [19], as designer enzymes become more prevalent these artificial constructs less and less resemble natural cellulosome systems.

Indeed, platform technology can have several forms. Immobilized platforms bind lignocellulose deconstruction enzymes to columns or other surfaces that allow slurry to pass through or over an enzyme array [23], [18], [24]. Hydrolysis takes place as the, often pretreated biomass moves along the array and bound enzymes interact with substrate. This approach has been met with limited success [25], [26]. Although enzyme loading is more closely controlled using immobilized platforms, thereby reducing the loss of expensive enzymes to waste, accessibility – specifically, the ability of enzyme to thoroughly penetrate the biomass – is limited. This requires enhanced mixing strategies and slow perfusion rates.

More recently, the development of mobile platforms has emerged as a potential solution [19], [20]. One of the more promising constructs, a prototype called a “rosetzyme”, was developed in 2007-2009 as a mobile platform that could bind sugar reducing enzymes and still move through slurry as a large protein complex. At the core of the platform is an altered double-nonameric ring (18-mer) heat shock protein complex derived from a hyperthermophilic archaeon of the genus *Sulfolobus* (see Figs. 1-3). The subunits of the complex were modified to bind cellulosome enzymes of the cellulose-degrading bacteria *Clostridium thermocellum*. This mobile enzyme sequestration platform (mESP) was tested on an over-the-counter cellulose product – Avicel® [19]; however, it was never tested on actual pretreated feedstock.

After the project had been terminated at NASA, our lab reconstituted the system and tested it on actual feedstock. In this study, we demonstrated enhanced sugar reduction efficiency on pretreated substrate using this mESP technology.

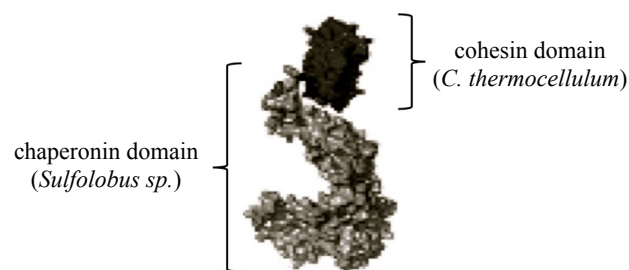


Figure 1 – Pymol model of HSP-coh fusion protein. Circular permutant of a group II chaperonin “heat-shock” protein (grey) from the archaeon *Sulfolobus* sp. (lab strain) linked to the cohesin (Type 1) protein (black) from the bacterium *Clostridium thermocellum*. (Image adopted and modified from [19] with permission)

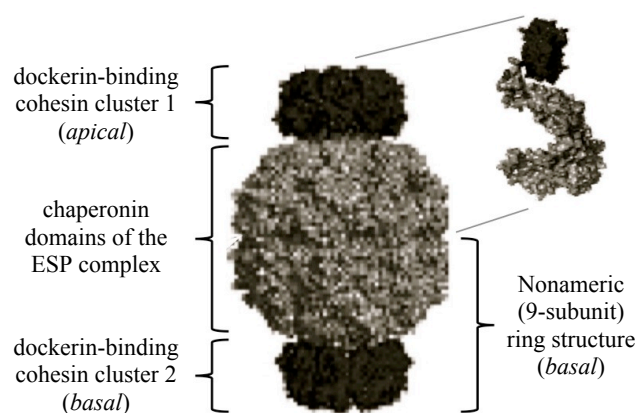


Figure 2 -Pymol model of ESP complex. Nine HSP-coh subunits comprise each of two ring structures that constitute the 18-mer ESP. Cohesin (type 1) domains from each subunit cluster at apical and basal extremities and are capable of binding enzymes equipped with a dockerin (type 1) domain. This model illustrates the “uncharged” (no bound enzymes) configuration. (Image adopted and modified from [19] with permission).

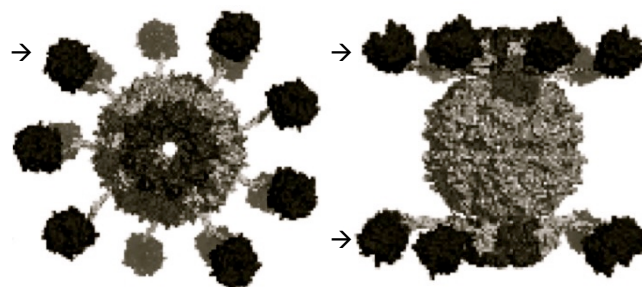


Figure 3 -Pymol model of enzyme-charged ESP complex. Top view (left) of an ESP complex with dockerin-containing enzymes bound. Side view (right) of an ESP complex showing enzyme binding (arrows) at apical and basal cohesin clusters. (Image adopted and modified from [19] with permission).

II. METHODS AND MATERIALS

A. mESP construction

As detailed in [19], a fusion protein was constructed using recombinant DNA methods. This fusion protein, HSP β -coh (Fig. 1) is composed of a circular permutant of HSP β [27], an archaeon (*Sulfolobus sp.*) heat-shock protein, and the cohesin module of CipA from the bacterium *Clostridium thermocellum* (residues 179-325; NCBI Q06851). This fusion construct contains a nine (9) amino acid linker (i.e., GGSGGSGGS) between the HSP β and cohesin domains. The DNA encoding the HSP β -coh fusion construct was inserted into a pET19b expression vector (Novagen). For storage the plasmid was transformed into DH5 α cells (Invitrogen). For overexpression of the fusion protein, the pET19b-HSP β -coh plasmid was transformed into another line of bacteria (*E. coli*) – namely, BL21 CodonPlus (DE3) RIL cells (Stratagene).

In the same manner, PCR-amplified genes for several cellulases (and other lignocellulose deconstruction enzymes) expressed by *C. thermocellum* (ATCC27405DTM) were stored and expressed as described in [19] and [27].

B. Protein Purification and Gel Electrophoresis

Overexpressed proteins including the HSP β -coh fusion protein and *C. thermocellum* enzymes were purified using a Fast Perfusion Liquid Chromatography (FPLC) system (Pharmacia/GE Amersham). A Superdex 200 size exclusion column and a Mono Q ion exchange column (GE Healthcare) were used to purify desired proteins from lysate. SDS-PAGE and western blot analysis were performed in initial rounds of expression to confirm the purity of protein suspensions and validate molecular weight.

C. mESP complex formation

To induce complex formation of 18 HSP-coh fusion proteins to form an 18-mer double ring enzyme sequestration platform (ESP), mixtures of the fusion proteins at 2 mg/ml were incubated with 1mM ATP and 50mM Mg²⁺ at 4°C for 8-12 hr. [Note that this approach was slightly modified from Mitsuzawa et al. (2009), in which 25mM Mg²⁺ was used]. Complex formation was confirmed using electron microscopy.

D. Transmission Electron Microscopy

Approximately 5 μ L of protein suspension was spotted onto a formvar-coated copper grid and incubated for 10 min in a humidity chamber. The grid was rinsed with distilled water and negatively stained with 2% (w/v) uranyl acetate for 2 min. The stain was wicked off and the sample was air-dried. Grids were imaged in a Hitachi H-7100 TEM at 75 kV. Images were captured at 60,000–150,000 \times magnification.

E. mESP charging (with enzymes)

To charge the ESP with cellulose-degrading enzymes, 7.72 μ M ESP complexes were incubated at room temperature for 15 min. with 6.86 μ M enzyme or enzyme cocktail in the presence of 0.7mM ATP, 17.4mM MgCl₂, and 5mM CaCl₂ in 22.2 μ l of a 50 mM Tris-maleate buffer (pH 6.0).

F. Pretreatment of lignocellulosic feedstock

Field-dried residues were obtained from local farms (Corvallis, OR). Feedstock was milled in a Wiley Mill (Model No. 4, Thomas Scientific, Swedesboro, NJ) equipped with a 2mm round-hole sieve. Ground feedstock was pretreated with dilute acid (1% w/w H₂SO₄) or, alternatively, dilute alkaline solution (1% w/w NaOH) at 10% solid loading at 180°C for 15 min. All pretreatments were performed in stainless steel tube reactors (316 stainless steel alloy; 19 mm diameter and 305 mm length with capped with Swagelok compression ferrule fittings). The rapid heating of the reactors to the desired temperature was achieved by immersing the reactors in a preheated sand bath (model SBL-2D, 4000 W, Techne Inc., Burlington, NJ) at 270°C and transferring the tubes to a preheated convection oven to maintain the temperature for the desired residence time. After the reaction time of 15 min, the reactors were immersed in ice-cold water to quench the reactions and bring the reactors to ambient temperature. Heating and cooling times for the reactors were less than four minutes.

G. Sugar Reduction Assays

Enzyme activity (specifically, sugar reduction efficiency) was measured by incubating 0.15% pretreated feedstock with 1.94 μ l of charged ESP suspension at 65°C for 16h in a 50 μ l reaction containing: 20mM Tris-maleate (pH 6.0), 1mM ATP, 25mM MgCl₂, and, 1mM CaCl₂ – followed by a colorimetric assay to assess sugar reduction efficiency. The colorimetric assay [28] compared hydrolytic efficiency between ESP-bound sugar-reducing enzymes versus the same enzymes free in solution (with no ESPs present). After the reaction, samples were centrifuged at 3000 RPM for 10 min. to remove residual particles of the pretreated biomass and diluted 10-fold in sterile DI water. Afterwards, 30 μ l of the dilute sample was mixed with 30 μ l of a 50mM Na₂CO₃/10mM KCl solution and 30 μ l of a 1.5mM K₃Fe(CN)₆ solution. This 90 μ l mixture was heated for 15 min at 99°C and then transferred to a well in a 96-well plate (or a 0.5ml microcentrifuge tube) containing 150 μ l of a 0.15% NH₄Fe(SO₄)₂·12 H₂O and 0.1% SDS/0.05N H₂SO₄. After incubation at room temperature for 15 min. OD_{690nm} readings were taken using a SpectraMAX M2e (Molecular Devices) automated plate reader (or a Nanodrop spectrophotometer). Both acid-pretreated (H₂SO₄) and alkaline-pretreated (NaOH) lignocellulose feedstock were tested in this manner under both ESP-bound enzyme and free enzyme in solution conditions.

III. RESULTS

HSP β -coh fusion proteins and enzymes were expressed using a bacterial (*E. coli*) overexpression system. Lysate was purified using FPLC and protein purity and molecular weight verification was confirmed by SDS-PAGE (*data not shown*).

Transmission electron microscopy (TEM) reveals HSP-coh fusion protein complexes (Figure 1). HSP-coh fusion proteins serve as subunits in the formation of a nonameric double-ring (18-mer) ESP complex resembling the size and configuration of natural group II chaperonin heat-shock protein complexes characteristic of *Sulfolobus* [29], [30].

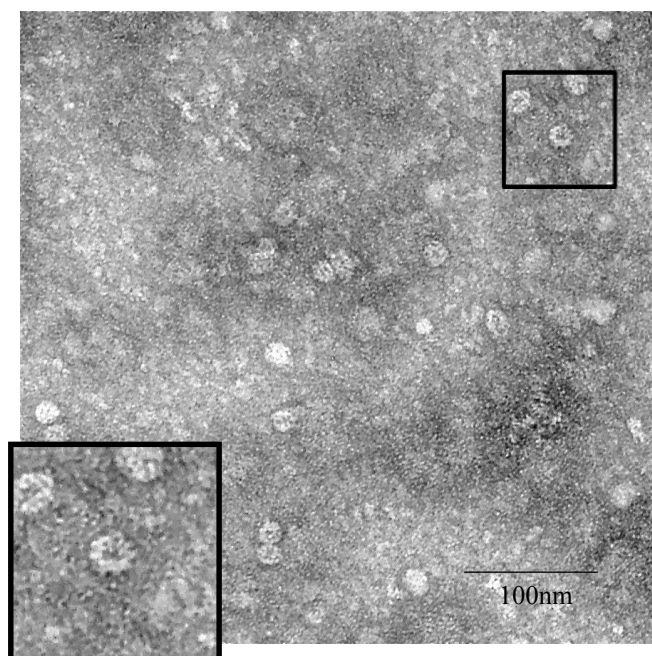


Figure 4 - Transmission electron micrograph of ESP complex. HSP-coh fusion proteins form functional double nonameric ring ESP complexes of approximately 18-22 nm in diameter. Inset shows ring structure with HSP-coh subunits visible.

Using software embedded in the electron microscope system, ESP diameter (18-22nm), when viewing perpendicular to the central pore, is consistent with reports on natural group II chaperonin complexes (also known as thermosomes) [29], [30].

Upon charging these ESPs with lignocellulose degradation enzymes, electron micrographs of the fusion protein complexes become amorphous globular structures under TEM (*data not shown*) due to the attachment of multiple enzymes to a single ESP via cohesin-dockerin interactions (*see* Figure 3).

Using a colorimetric assay [28] to measure the magnitude of hydrolysis during the treatment period, sugar reduction efficiency was assessed for different individual enzymes and for multi-enzyme complements. Two conditions were tested. Enzyme-only treatments consisted of enzymes free in solution without any ESP present. ESP-bound enzyme treatments were also tested on each substrate to determine if the use of ESPs enhanced sugar reduction efficiency.

Enzyme-only systems exhibited similar patterns of sugar reduction activity on both acid-pretreated corn stover (Fig. 5a) and acid-pretreated wheat straw (Fig. 5b). Specifically, the use of xylanase (X), an enzyme that preferentially breaks down hemicellulose [31], showed the greatest hydrolytic activity while CelR, a major processive endoglucanase of the *C. thermocellum* cellulosome [32], showed the least efficiency in reducing acid-treated substrate. Stover and wheat straw hydrolytic efficiency for single enzyme-only systems follows a $R < \beta < S < X$ trend.

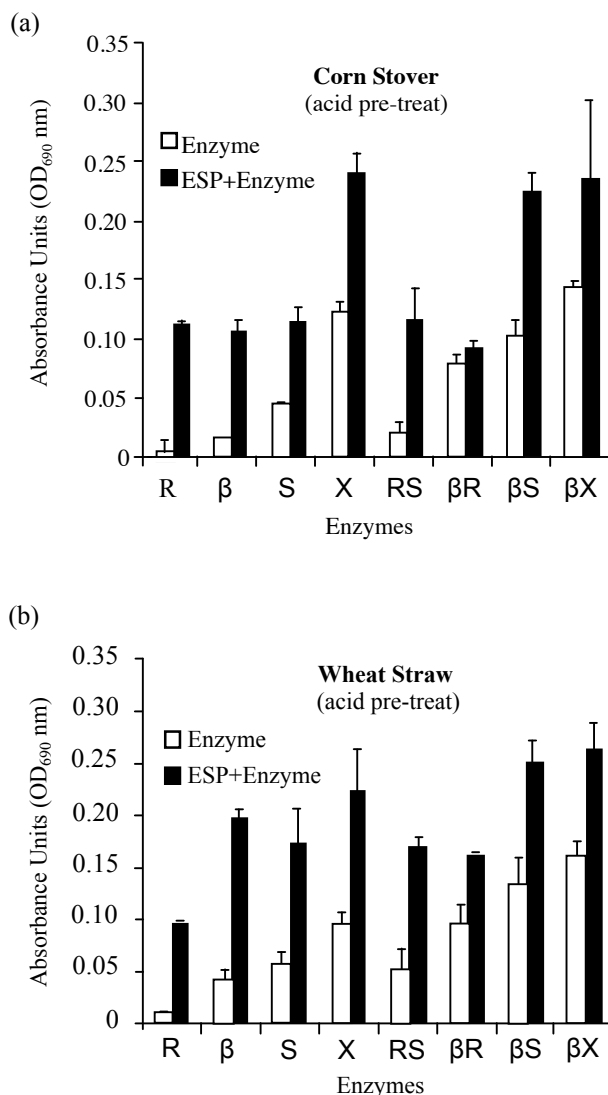


Figure 5 – Sugar reduction on acid-pretreated feedstock. Sulfuric acid (H_2SO_4) pretreated corn stover (*panel A*) and wheat straw (*panel B*) were subject to hydrolysis using enzymes bound to ESPs (black bars) versus free enzymes in solution without ESPs (white bars). *C. thermocellum* enzymes: R – CelR, β – β-glucosidase; S – Cel S, X – xylanase.

With one enzyme type bound to ESP, hydrolytic efficiency significantly increased over the free enzyme-only condition. However, on acid-pretreated corn stover, there was no significant difference between the ESP-bound advantage between ESP-R, ESP-β, and ESP-S constructs. However, the ESP-X system did exhibit a marked increase in sugar reduction efficiency over the other single enzyme charged ESPs for acid-pretreated stover. For single enzyme ESP-bound trials on acid pretreated stover a $R \approx \beta \approx S < X$ pattern of hydrolytic efficiency emerged. For all one enzyme bound cases, at least a two-fold increase in hydrolytic efficiency on acid-pretreated feedstock was observed.

For two-enzyme systems, hydrolytic efficiency on both acid-pretreated corn stover and acid-pretreated wheat straw exhibited a similar trend for free enzyme-only conditions: $RS < \beta R < \beta S < \beta X$ – even though a statistically significant difference did not emerge between βR vs. βS and βS vs. βX on acid-pretreated wheat straw.

When bound in pairs to ESPs, all two-enzyme complements tested (except for βR on stover) exhibited a significant enhancement of hydrolytic efficiency over the free-enzyme conditions. Although there was no significant difference between ESP-bound advantage using ESP- βS and ESP- βX , each these doubly-bound complements exhibited significantly higher hydrolytic efficiency than the ESP- RS and ESP- βR bound advantage. (Note that there was also no significant difference in ESP-bound advantage between the ESP- RS and ESP- βR constructs). For both acid-pretreated corn stover and acid-pretreated wheat straw, the ESP-bound hydrolytic advantage showed a $RS \approx \beta R \ll \beta S \approx \beta X$ pattern.

As observed in the single-enzyme ESP constructs, several of the two-enzyme ESPs showed about a two-fold increase in sugar reduction efficiency over the free-enzyme cocktail condition. These include: ESP- RS (both stover and straw); and, ESP- βS (stover). In general, these data show that the use of ESP systems on acid-pretreated corn stover and wheat straw result in a significant enhancement of hydrolytic and thus sugar reduction potential.

On alkaline-pretreated substrate, only one single-enzyme system was tested (Fig. 6). β -glucosidase (β) [33], a cellobiose hydrolase, exhibited only modest levels of sugar reduction activity. With β bound to platform, the ESP- β construct showed no appreciable difference in hydrolytic capacity over the free enzyme condition. Similar results were observed in the R-only, S-only, and X-only cases (*data not shown*). However, a few of the enzyme mixes did exhibit significant increases in sugar reduction efficiency on base-pretreated substrates. Furthermore, ESP-bound enzyme complements (e.g., RS and βX) showed significant enhancement in reduction capacity over the free enzyme in solution condition. The alkaline-pretreated substrate trials were limited since focus was on acid-pretreatment (*see Discussion*). It is notable that, in some cases, the magnitudes of ESP advantage in the alkaline-pretreatment trials in some cases were comparable to the acid-pretreatment trials.

Specifically, when β -glucosidase and xylanase are bound to ESP, hydrolytic efficiency over free enzyme in solution ranges from about a 1.4-fold to 1.7-fold increase with lower values observed in the alkaline-pretreatment case (Fig. 6). More variability was observed with the CelR and CelS complement bound to ESP. In alkaline pretreatment trials using ESP- RS , a 2.2-fold and 2.7-fold advantage was observed on wheat straw and corn stover, respectively. However, on acid-pretreated substrates, 3.4-fold and 6-fold ESP advantages were observed for wheat straw and corn stover, respectively (Fig. 5).

Overall, these data show that use of ESPs on feedstock that is alkaline-pretreated can also confer hydrolytic advantage over a free enzyme cocktail.

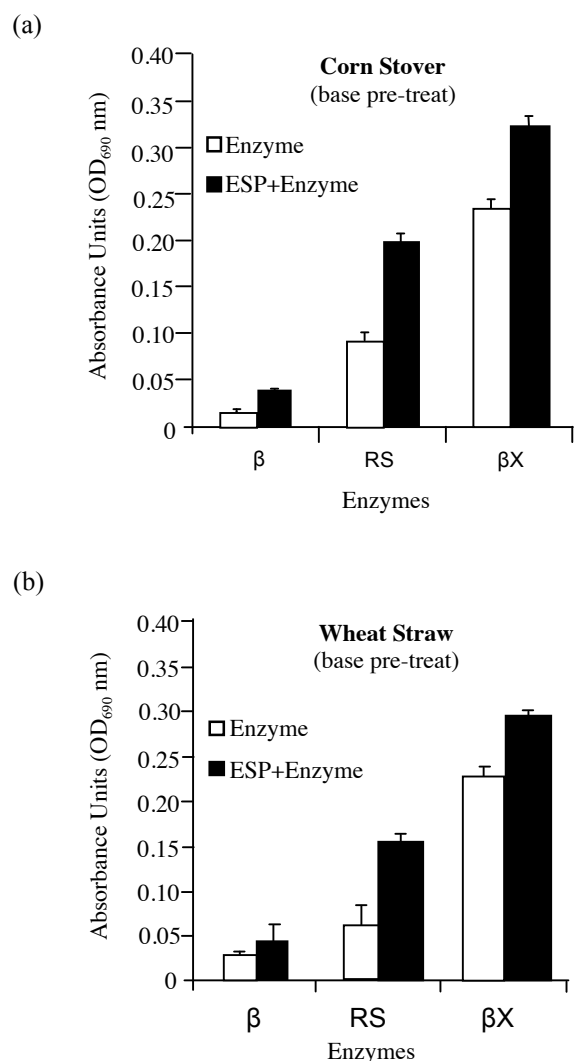


Figure 6 – Sugar reduction on alkaline-pretreated feedstock. Sodium hydroxide (NaOH) pretreated corn stover (*panel A*) and wheat straw (*panel B*) were subject to hydrolysis using enzymes bound to ESPs (black bars) versus free enzymes in solution without ESPs (white bars). *C. thermocellum* enzymes: R – CelR, β – β -glucosidase; S – Cel S, X – xylanase.

IV. DISCUSSION

Feedstock pretreatments typically consist of acid washes or alkaline washes that are designed to initiate deconstruction of lignocellulosic feedstock by inducing swelling in the matrix and interfering with cellulose, hemicellulose, and lignin interactions. After pretreatment, cellulose and hemicellulose are more exposed and susceptible to enzymatic action. Enzyme-mediated deconstruction of the matrix and hydrolysis of complex carbohydrates (e.g., cellulose) yielding simple fermentable sugars (e.g., glucose) in a highly efficient manner can be complicated. The nature of the lignocellulosic material (i.e., the percent composition of cellulose, hemicellulose, lignin, and other components) affects the efficiency of enzymatic action.

Specific sets of multi-enzyme “cocktails” applied simultaneously or sequentially will have different levels of sugar reduction efficiency on different substrates under different pretreatment conditions. In many processes, pretreatments can leave feedstock slurries with pH and temperature conditions that diminish enzymatic efficiency.

One approach to optimizing enzymatic efficiency is to discover unique enzymes that function under harsh conditions (e.g., low pH, high temperature). An alternative approach is to employ some type of protein scaffold to stabilize enzymes under such adverse conditions. If such platforms are not immobilized, then access to substrate and perfusion through the slurry is not a limiting factor. Here we employed a mobile enzyme sequestration platform (ESP) derived from a hyperthermoacidophilic archaeal heat-shock protein complex. The natural complex, a chaperonin complex, functions to protect proteins within the archaeal cell under conditions of stress (e.g., fluctuations in temperature and pH). Using the ESP, a genetically altered version of this complex, to which cellulases and other lignocellulolytic enzymes can bind, it was hypothesized that enzymatic efficiency could be enhanced on acid-pretreated feedstocks.

To test this hypothesis, acid-pretreated corn stover and wheat straw were subjected to enzymatic action under two conditions. The first condition consisted of having the enzymes free in solution with no ESP utilization. The second condition consisted of using the same enzyme or enzyme complement bound to the ESP.

Electron microscopy demonstrated that HSP-coh fusion proteins form double nonameric ring structures similar to the natural chaperonin complexes from archaea observed *in vitro* [29], [30]. Genetic modification and the resulting two-domain ESP subunit do not inhibit complex formation and apical and basal ends of the complex have exposed cohesin-binding sites. These cohesin binding sites are capable of interacting with any enzyme that contains a *C. thermocellum* dockerin (type I) domain. By charging the ESP with one type or multiple types of enzymes, it was demonstrated that enzymatic efficiency on acid-pretreated corn stover and wheat straw is significantly enhanced. With enzymes selected in this study, an approximate two-fold or greater increase in sugar reduction efficiency was common (with the exception of β R on stover).

Although our hypothesis was initially focused on feedstock that was acid-pretreated due to the fact that the chaperonin proteins from which these constructs were derived are found in hyperthermoacidophilic archaea, we also tested for enhancement of enzymatic efficiency on alkaline-pretreated feedstock, again in a free-enzyme versus ESP-bound enzyme case comparison.

On both acid-pretreated and alkaline-pretreated substrate, xylanase was notably effective at breaking down substrate in single-enzyme treatments. This is likely due to its ability to breakdown xylan, a main constituent of hemicellulose, into xylose, thereby disrupting hemicellulose cross-linking with key matrix components such as lignin [34]-[37]. Charged to the ESP, the efficacy of xylanase enzymatic action increased as much as two-fold on both acid-pretreated stover and straw.

CelR and β -glucosidase exhibited modest hydrolytic efficiency when used alone and free in solution. However, when bound to ESP, a 4- to 6-fold increase in sugar reduction capacity was commonly observed with ESP-R and ESP- β . However, when used in concert as an enzyme complement attached to ESP, ESP- β R on acid-pretreated corn stover showed no significant enhancement and a significant, but modest enhancement on acid-pretreated wheat straw. Furthermore, the overall level of hydrolytic efficiency was lower than ESP-R and ESP- β single-enzyme cases. Thus, no positive synergistic effect was observed. Instead, a “synergistic disadvantage” is apparent and likely due to the distinct modes of action between CelR and β -glucosidase. Whereas, CelR is an endoglucanase that targets internal bonds within the cellulose structure [32], β -glucosidase is an exoglucanase – specifically, a type 2 cellobiose hydrolase, that acts at the terminal non-reducing ends of cellulose to release β -D-glucose [38], [39]. Thus, the two enzymes bound simultaneously to platform may be acting competitively to access internal versus terminal binding sites on cellulose molecules. Also, both CelR and β -glucosidase are processive enzymes, thus a *binding-and-ratcheting* strategy along the molecule can inhibit the other enzyme from effectively hydrolyzing cellulose at the preferred binding site.

Interestingly, the ESP-bound CelR/CelS complement showed a marked (greater than 2-fold) increase in efficiency over the RS enzyme cocktail in both the acid-pretreated and base-pretreated cases on both feedstock types. Since both CelR and CelS are endoglucanases, the ESP-RS construct may allow these two enzymes to act synergistically in attaching to and hydrolyzing cellulose at internal binding sites.

However, the suggestion that charging an ESP with both an endoglucanase and an exoglucanase causes inhibition of one (or the other) enzyme does not necessarily hold. ESP- β S exhibited a significant enhancement in hydrolytic activity over the β S cocktail. A potential explanation for the difference in ESP- β R versus ESP- β S efficacy may reside in the fact that CelR is noted to be more processive than CelS. The ability for CelS to bind, catalyze, and release more readily than CelR may allow for some synergy in the ESP- β S case.

V. CONCLUSIONS

Although the nature of synergistic effects using different enzyme complements bound to ESPs need to be elucidated, it is clear from the data presented here that the use of ESPs can significantly enhance hydrolytic efficiency on acid-pretreated (and alkaline-pretreated) feedstock. It is important to note that the use of multiple ESPs, with only one enzyme type charged to each platform remains to be tested. In the present study, ESPs were charged with multiple enzymes (e.g., ESP-RS). Efficiency may be further enhanced by charging only one enzyme class (e.g., endoglucanases), or only one enzyme type (e.g., β), to individual ESPs. Enzyme-charged *platform cocktails* (e.g., ESP-R plus ESP-S) may prove to be more efficient than free enzyme cocktails or ESPs charged with multiple enzymes.

Furthermore, optimization of sugar reduction efficiency may require enzymes complements for customized for specific pretreated feedstock types. It is also possible that a combination of ESP-bound and free enzymes may provide the most efficient solution to maximizing hydrolytic efficiency. In conclusion, the use of thermo-tolerant and acid-tolerant mobile enzyme sequestration platforms may be one approach to maximizing enzyme-mediated sugar reduction for processes that feature low pH or high temperature conditions.

ACKNOWLEDGMENT

The authors would like to acknowledge and thank the following individuals: Dr. Ganti S. Murthy from Oregon State University (Corvallis, OR) for providing some of the pretreated feedstock; Drs. Jonathan Trent and Chad Paavola from NASA Ames Research Center (Moffett Field, CA) for providing the original "rosettazyme" prototypes fusion constructs; and Dr. Jim Driver from the University of Montana (Missoula, MT) EMtrix facility for assisting in the production of electron microscope images.

REFERENCES

- [1] Thomsen MH and Haugaard-Nielsen H (2008) "Sustainable bioethanol production combining biorefinery principles using combined raw materials from wheat undersown with clover-grass." *Journal of Industrial Microbiology and Biotechnology*. 35:303-311.
- [2] Ceballos RM, Cuesta-Ureña I, Rani A, Morales CT, Batchenkova NA, Ceballos RM Jr., Chan M, Murthy GS (2014) "Feedstocks, enzymes, and biofuel: A comprehensive review (submitted for publication)
- [3] Runge CF, and Senauer B (2007). "How Biofuels could starve the poor." *Foreign Affairs Issue* (Volume): 000-003. [Review]
- [4] Li C, Knierim B, Manisseri C, Arora R, Scheller HV, Auer M, Vogel KP, Simmons BA, Singh S (2010) "Comparison of dilute acid and ionic liquid retreatment of switchgrass: biomass recalcitrance, delignification and enzymatic saccharification." *Bioresource Technology* **101** (13): 4900-4906. [Review]
- [5] Alvira P, Tomás-Pejó E, Ballesteros M, Negro MJ (2010) "Pretreatment technologies for an efficient bioethanol production process based on enzymatic hydrolysis: A review." *Bioresource Technology* **101**: 4851-4861. [Review]
- [6] Zhang YH and Lynd LR (2006). "A functionally based model for hydrolysis of cellulose by fungal cellulase." *Biotechnology and Bioengineering* **94**(5): 888-898.
- [7] Lee SH, Doherty TV, Linhardt RJ and Dordick JS (2009). "Ionic liquid-mediated selective extraction of lignin from wood leading to enhanced enzymatic cellulose hydrolysis." *Biotechnology and Bioengineering* **102**(5): 1368-1376.
- [8] Sun, NM, Rahman, Qin Y, Maxim ML, Rodriguez H, Rogers RD (2009). "Complete dissolution and partial delignification of wood in the ionic liquid 1-ethyl-3-methylimidazolium acetate." *Green Chemistry* **11** (5): 646-655.
- [9] Li C, Cheng G, Balan V (2011) "Influence of Physico-chemical changes on enzymatic digestability of ionic liquid and AFEX pretreated corn stover" *Bioresource Technology* **13** (102): 6928-6936.
- [10] Qing Q, and Wyman CE (2011) "Supplementation with xylanase and β -xylosidase to reduce xylo-oligomer and xylan inhibition of enzymatic hydrolysis of cellulose and pretreated corn stover." *Biotechnology for Biofuels* **4** (18):
- [11] Esterbauer H, Steiner W, Labudova I, Hermann A, and Hayn M (1991) "Production of Trichoderma cellulase in laboratory and pilot scale" *Bioresource Technology* **36** (1): 51-65.
- [12] Gao D, Chundawat SPS, Uppugundla N, Balan V, and Dale BE (2011). "Binding characteristics of Trichoderma reesei cellulases on untreated, ammonia fiber expansion (AFEX), and dilute-acid pretreated lignocellulosic biomass." *Biotechnology and Bioengineering* **108**(8): 1788-1800.
- [13] Selig M, Knoshaug E, Adney W, Himmel M, and Decker S(2008). "Synergistic enhancement of cellobiohydrolase performance on pretreated corn stover by addition of xylanase and esterase activities." *Bioresource Technology* **99**: 4997 - 5005.
- [14] Banerjee G, Car S, Scott-Craig J, Borrusch M, and Walton J (2010). "Rapid optimization of enzyme mixtures for deconstruction of diverse pretreatment/biomass feedstock combinations." *Biotechnology for Biofuels* **3**(1): 22
- [15] Wiseman A (1993). "Designer enzyme and cell applications in industry and in environmental monitoring." *J Chem Technol Biotechnol* **56**(1): 3-13.
- [16] Banerjee G, Car S, Scott-Craig J, Borrusch M, Aslam N, and Walton J (2010). "Synthetic enzyme mixtures for biomass deconstruction: production and optimization of a core set." *Biotechnol Bioeng* **106**: 707 - 720.
- [17] Himmel ME, Ding SY, Johnson DK, Adney WS, Nimlos MR, Brady JW, and Fosut TD (2007) "Biomass recalcitrance: engineering plants and enzymes for biofuels production" *Science* **315** (5813): 804-807. [Review]
- [18] Brady D, and Jordaan J (2009) "Advances in enzyme immobilization." *Biotechnology Letters* **31** (11):1639-1650. [Review]
- [19] Mitsuzawa S, Kagawa H, Li Y, Chan SL, Paavola CD, Trent JD (2009) "The rosettazyme: a synthetic cellulosome." *Journal of Biotechnology* **143** (2): 139-144.
- [20] Moraïs S, Heyman A, Barak Y, aspi J, Wilson DB, Lamed R, Shoseyov O, Bayer EA (2010) "Enhanced cellulose degradation by nano-complexed enzymes: synergism between a scaffold-linked exoglucanase and a free endoglucanase." *Journal of Biotechnology* **147** (3-4): 205-211.
- [21] Doi RH, and Kosugi A (2004) "Cellulosomes: Plant-cell-wall-degrading enzyme complexes." *Nature Reviews Microbiology* **2** (7): 541-551. [Review]
- [22] Elkins JG, Raman B, Keller M (2010) "Engineered Microbial systems for enhanced conversion of lignocellulosic biomass" *Current Opinion in Biotechnology* **21** (5): 657-662. [Review]
- [23] Santoro N, Cantu SL, Tornqvist CE, Falbel TG, Bolivar JL, Patterson SE, Pauly M, Walton JD (2010) "A high-throughput platform for screening milligram quantities of plant biomass for lignocellulose digestibility." *Bioenergy Research* **3** (1):93-102
- [24] Cao L, van Langen L, Sheldon RA (2003) "Immobilised enzymes: carrier-bound or carrier-free?" *Current Opinions in Biotechnology* **14** (4): 387-394. [Review]
- [25] Hernandez K, Fernandez-Lafuente R (2011) "Control of protein immobilization: coupling immobilization and site-directed mutagenesis to improve biocatalyst or biosensor performance." *Enzyme and Microbial Technology* **48** (2): 107-122. [Review]
- [26] Brady D, Steenkamp L, Skein E, Chaplin JA, Reddy S (2003) "Optimization of the enantioselective biocatalytic hydrolysis of naproxen ethyl ester using ChiroCLEC-CR." *Enzyme and Microbial Technology* **34**: 283-291.
- [27] Paavola CD, Chan SL, Li Y, Mazzarella KM, McMillan RA, Trent JD (2006) "A versatile platform for nanotechnology based on circular permutation of a chaperonin protein" **17**(5):
- [28] Park TJ and Johnson MG (1949) "A submicroscopic determination of glucose" *Journal of Biological Chemistry* **181** (1): 149-151.
- [29] McMillan AR, Paavola CD, Howard J, Chan SL, Zaluzec NJ, and Trent JD (2002) "Ordered nanoparticle arrays formed on engineered chaperonin protein templates" *Nature Materials* (1): 247-252.
- [30] Kagawa HK, Osipiuk J, Maltsev N, Overbeek R, Quaiate-Randall E, Jochimiak A, and Trent JD (1995) "The 60kDa heat shock proteins in the hyperthermophilic archeon Sulfolobus shibatae" *J Mol Biol.* **253** (5): 712-725.
- [31] Hayashi H, Takehara M, Hattori T, Kimura T, Karita S, Sakka K, and Ohmia K (1999) "Nucleotide sequences of two contiguous and highly homologous xylanase genes xynA and xynB and characterization of XynA from Clostridium thermocellum" *Appl Microbiol Biotechnol* (51): 348-357.
- [32] Zverlov VV, Schantz N, Schmitt-Kopplin P, and Schwarz WH (2005) "Two new major subunits in the cellulosome of Clostridium thermocellum: xyloglucanase Xgh74A and endoxyylanase Xyn10D" *Microbiology* **151** (10): 3395-3401.
- [33] Maki ML, Armstrong L, Leung KT, and Quin W (2013) "Increased expression of beta-glucosidase A in Clostridium thermocellum 27405 significantly increases cellulase activity" *Landes Bioscience* (4): 15-20.

- [34] Jeffries TW (1991) "Biodegradation of lignin and hemicelluloses." Biodegradation **1** (2-3): 163-176.
- [35] Tuyet Lam TB, Iiyama K, and Stone BA (1992) "Cinnamic acid bridges between cell wall polymers in wheat and phalaris internodes. Phytochemistry" (31): 1179-1183.
- [36] Hatfield R, Ralph J, and Grabber J (2008) "A potential role for sinapyl p-coumarate as a radical transfer mechanism in grass lignin formation." Planta **228** (6): 919-928.
- [37] Watanabe T, Ohnishi J, Yamasaki Y, Kaizu S, and Koshuima T (1989) "Binding-site analysis of the ether linkages between lignin and hemicelluloses in lignin-carbohydrate complexes by DDQ-oxidation." Agric. Biol. Chem. **53** (8): 2233-2252.
- [38] Lamed R, Kenig R, Morgenstern E, Calzada JF, De Mico F, and Bayer EA (1990) "Efficient cellulose solubilisation by a combined cellulosome- α -glucosidase system." Appl Biochem Biotechnol **27**: 173-83; <http://dx.doi.org/10.1007/BF02921525>.
- [39] Gräbnitz F, Seiss M, Rücknagel KP, and Staudenbauer WL (1991) "Structure of the beta-glucosidase gene bglA of *Clostridium thermocellum*. Sequence analysis reveals a superfamily of cellulases and beta-glycosidases including human lactase/phlorizin hydrolase." Eur J Biochem **200**: 301-309.
- [40] Kruss K, Wang WK, Ching J, and Wu JH (1995) "Exoglucanase activities of the recombinant *Clostridium thermocellum* CelS, a major cellulosome component." Bacteriol **177** (6):1641-1644.

Estimation of Induced EMF Value in Ground Wire During Ice-Melting Procedure

Nikolay Korovkin, Valeriy Goncharov¹, Nikolay Silin²

¹Theoretical Electrical Engineering Department, St. Petersburg State Polytechnic University, St. Petersburg, Russian Federation

²Theoretical Electrical Engineering Department, Far Eastern Federal University, Vladivostok, Russian Federation

Abstract—Under a certain climatic conditions there is a possibility of icing of TL (transmission lines) wires and GW (ground wires) which may lead to their breakage. The currents of operating TL affect the de-icing process. In present paper the induced EMF values are calculated for different TL operation modes, different positional TL relationship and different ice-melting diagrams. In addition, a methodology of the induced EMF value calculation in the GW is described, a comparison of the EMF values for different TL operation modes and different ice-melting diagrams is made, and possible dangers during the ice-melting procedures are noted.

Keywords—de-icing, ground wire, ice covering, ice melting, induced EMF.

I. INTRODUCTION

The ice covering represents a huge danger to the power systems' operation. It can lead to the wires breakage and even to the towers destruction. In December 2001, the ice covering brought to the damage of TL (transmission lines) of total length 2500 km in Sochi. In early 2008, a severe ice storm occurred in Southern China, which caused at least 7541 TL above 10 kV and 859 substations above 35 kV to be out of service [1].

The necessity of GW (ground wires) de-icing is more urge because there are no currents flowing during normal operation mode through GW as opposed to TL.

The de-icing method using DC is most commonly used. DC is used more often than AC for the ice-melting procedures because the heating current adjustment is very limited in case of using AC [2]. The basic ice-melting diagram is given in Fig. 1. The typical diagrams are given in Table I.

II. PURPOSE OF WORK

It is desirable to conduct the GW ice-melting procedure without powering down the TL. The currents in the wires of the TL, located on the same tower as the GW, and the currents of the neighboring TL induce the EMF in the ice-melting loop (Fig. 1). This can lead to the rectifier's breakdown while engaging as well as while operating. The aim of this paper is an estimation of the EMF value induced in the ice-melting loop under different conditions (such as different TL operation modes, different TL types and different ice-melting

diagrams) and the development of an application to estimate the induced EMF value.

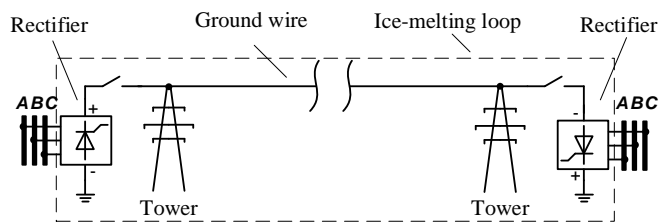


Fig. 1. Basic ice-melting diagram.

TABLE I. ICE-MELTING CIRCUIT DIAGRAMS

Name of the diagram	Diagrams
GW-ground	
GW1,2-ground	
GW1,2	

III. INDUCED EMF CALCULATION METHOD

The induced EMF value in the ice-melting loop is determined by a magnetic flux Φ (which is created by the TL currents) through the surface whose boundary is the ice-melting loop [3]. The most significant factors, which determine the values of magnetic flux and EMF, are currents' values, their phase lags, and distance between the ice-melting loop and the TL wires. The calculation method rests on the following assumptions:

- 1) the TL currents form the balanced three-phase system;
- 2) because the currents' phase lags of all TL are not defined, we consider that the currents of the same phase index of the different circuits and of different towers have the same phase lag;
- 3) all TL wires and GW are rectilinear (we neglect the wires' deflection).

Also, an influence of the ground should be taken into account. In this paper we consider that the ground is a perfect conductor ($\gamma = \infty$). Hence, we may implement the method of images [3]. The resulting picture in case of using ice-melting diagram "GW-ground" is shown on Fig. 2. With assumptions stated previously, the induced EMF value can be calculated analytically [3]:

$$\dot{\Phi}_B = (\dot{A}_1 - \dot{A}_2) \cdot l = \left(\frac{\mu_0}{2\pi} \sum_{k=1}^6 \dot{I}_k \ln r_k^{(1)} - \frac{\mu_0}{2\pi} \sum_{k=1}^6 \dot{I}_k \ln r_k^{(2)} \right) \cdot l, \quad (1)$$

where l is the length of the parallel TL and GW; A_1 , A_2 are the vector potential values on the GW and its image respectively; $r_k^{(1)}$, $r_k^{(2)}$ ($k = 1 \div 6$) are shown in Fig. 2.

The induced EMF value:

$$E = |\dot{E}| = |-j\omega \cdot \dot{\Phi}_B| = \omega \cdot \Phi_B \quad (2)$$

$$\omega = 2\pi \cdot f = 314 \text{ rad/s} \quad (3)$$

The RMS EMF value calculated in (2) is a result of the effect from one circuit of one TL. After that, we can calculate the influence from the other circuit of multiple TL and, taking into consideration the assumption 2, sum both reactions. Obviously, the result will be the majoring one.

IV. CALCULATION RESULTS

The calculations were made using the application developed specifically for the present paper that includes:

- 1) the TL map;
- 2) the TL data such as types of GW, wires and towers as well as a transposition data;
- 3) the nominal currents, voltages and electric power transported through TL.

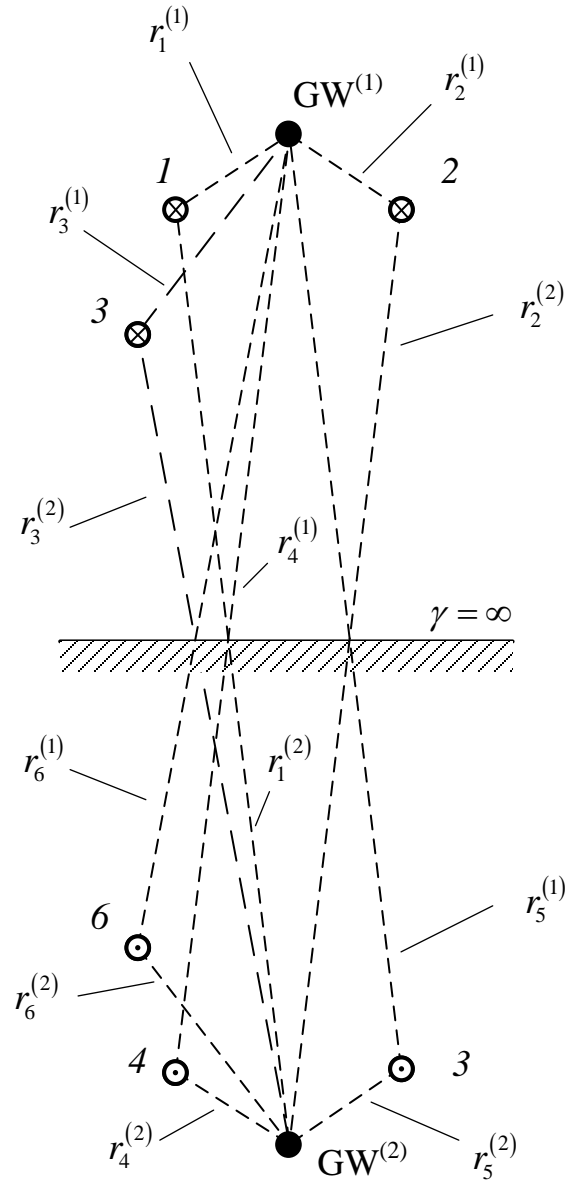


Fig. 2. Positional relationship of TL wires, GW and their images in case of using "GW-ground" ice-melting diagram. $GW^{(1)}$ – the ground wire, 1,2,3 – the TL wires, $GW^{(2)}$ – image of the ground wire, 4,5,6 – the images of TL wires.

Fig. 3(a) represents a map of a power system span in Moscow Oblast. TL 1, which is located on the same tower as GW in question, is located near TL 2, 3 and 4. All of them operate in nominal modes. Fig. 3(a) also contains the information of the nominal currents' values. Fig. 3(b) represents the tower dimensions.

The minimum distance allowed between the wires of neighboring 220 kV towers is 7 meters [4]. We consider that all towers are located in such a way that this condition is met for all TL.

The calculations for two ice-melting diagrams from Table I and two variants of phase disposition (see Fig. 4) are represented in Table II.

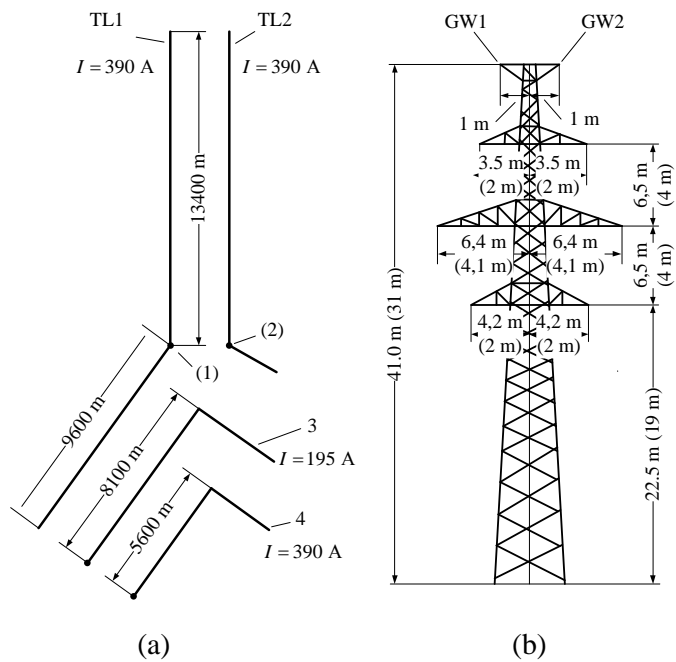


Fig. 3. Calculation data. (a) The map of a power system span. TL 1, TL 2, TL 4 – double-circuit TL 220 kV, TL 3 – double-circuit TL 110 kV. (b) The dimension of the towers used. The dimensions for 110 kV towers are given within brackets.

TABLE II. CALCULATION RESULTS FOR NORMAL MODE

№	Ice melting diagram	Phase disposition	Induced EMF value (RMS), kV
1	GW-ground	a	2.4
2	GW-ground	b	0.9
3	GW1,2-ground	a	2.4
4	GW1,2-ground	b	0.8
5	GW1,2	a	0.1
6	GW1,2	b	0.01

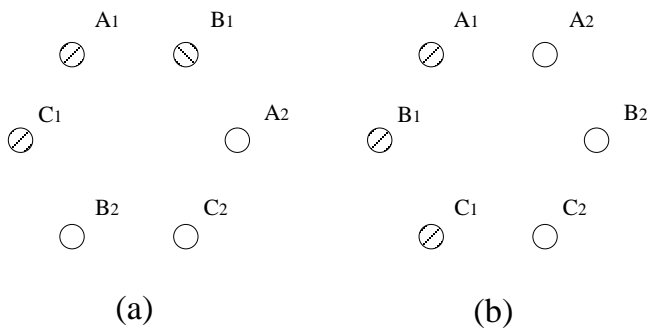


Fig. 4. Variants of phases' disposition. (a) The first variant. (b) The second variant.

EMF values vary from insignificant 0.01 kV to 2.4 kV. The lowest values correspond to diagram “GW1,2” due to the minimal ice melting loop surface area comparing to other ones. In worst case, the induced EMF increases RMS value of melting current up to 66% and therefore speeds up the de-icing process. When there is no monitoring equipment, the ice melting procedure is conducted for an estimated time.

Therefore, if the ice has been melted earlier than predicted, the wire will experience the unwanted heating. Excess heating decreases durability and lifetime of the wires.

In case of short circuit in TL1 (point (1) in Fig.3) and TL2 (point (2) in Fig. 3) of value 20 kA the induced EMF values are much higher (see Table III). For the cases of using ice-melting diagram “GW1,2” the induced EMF values are comparable to the highest values for the normal operational modes (see Table II). In other cases, the values are significant. Due to the power-system protection quick response, they cannot alter much the de-icing process. However, such high voltages represent a danger to the rectifier and may be the reason of rectifier’s breakdown. Such events were recorded to occur.

TABLE III. CALCULATION RESULTS FOR ABNORMAL MODE

№	Ice melting diagram	Point of short circuit	Induced EMF value (RMS), kV
1	GW-ground	1	82
2	GW-ground	2	51
3	GW1,2-ground	1	83
4	GW1,2-ground	2	51
5	GW1,2	1	3
6	GW1,2	2	2

V. DISCUSSION

When we calculated the induced EMF values we that the ground is a perfect conductor. In real situations, the ground has limited conductivity. Accounting for real current density distribution in the ground may be conducted using methods described in [5], [6]. This correction will lead to the decrease of induced EMF values calculated.

VI. CONCLUSIONS

When ice-melting procedure using rectifiers is going to be conducted, the induced EMF in GW from currents of neighboring TL should be taken into account.

The danger of inducing high EMF values in “GW 1,2” ice-melting diagram is significantly less than in the “GW-ground” and “GW1,2-ground” loops.

When the ice-melting procedure is conducted, a short circuit current in any TL, which is parallel to the GW, induces EMF enough to damage a rectifier.

REFERENCES

- [1] X. Shukai and Z. Jie, “Review of ice storm cases impacted seriously on power systems and de-icing technology”, Southern Power Syst. Technol., vol. 2, pp. 1–6, 2008.
- [2] Federal Grid Company Standart 56947007-29.060.50.122-2012. “Ice-melting modes calculation methodology fot optical ground wires”, 2012.
- [3] K. S Demirchyan, L. R. Neumann, N. V Korovkin., “Theoretical Foundations of Electrical Engineering”, Vol. 1, Vol. 2, Spb, 2009.
- [4] Rules of Electrical Installations Design, Novosibirsk. 2009.
- [5] G. A. Grinberg, B. I. Bonshtedt, “The basis of the exact theory of the wave field of a transmission line”, JTPh, vol. 24, no. 1, pp.67-95 1954.
- [6] H. Kikuchi, “Wave propagation along an infinite wire above ground at high frequencies,” Proc. Electrotech. J., Vol. 2, 73-78, 1956.

Influence of process parameters on the microstructural and mechanical properties of plasma sprayed nanostructured YSZ coatings

C. Lamuta, G. Di Girolamo, P. Caliandro and L. Pagnotta

Abstract— Plasma sprayed ceramic coatings can be used for thermal protection of hot-section metal components of turbine engines, in order to improve their durability and efficiency. The presence of nanostructures, deriving from partial melting of agglomerated nanostructured particles, represents an interesting technological solution in order to improve their functional characteristics. In this work nanostructured yttria stabilized zirconia (YSZ) coatings were deposited by plasma spraying. The influence of the main process parameters on their microstructural and mechanical properties was investigated by scanning electron microscopy (SEM) and indentation techniques at micro- and nano-scale. Their porous microstructure was composed of well melted overlapped splats and partially melted nanostructured areas. This bimodal microstructure led to a bimodal distribution of the mechanical properties. An increase of plasma power and spraying distance was able to produce denser coatings, with lower content of embedded nanostructures, which exhibited higher elastic modulus and hardness. With increasing the indentation load the mechanical properties decreased, due to the influence of microstructural defects.

Keywords— hardness, indentation, plasma spraying, thermal barrier coatings, Young's modulus, zirconia

I. INTRODUCTION

Ceramic coatings are suitable to be employed for thermal protection of Ni-based superalloy turbine components operating in power plants and aircraft engines. Their application allows to improve their high-temperature capability and durability, by reducing the heat flux and the temperature at the metal surface. Significant improvements in terms of engine efficiency and lower pollution are then expected [1]-[2]. A thermal barrier coating (TBC) is usually composed of a metal substrate, a metallic bond coat and a ceramic top coat [4]. The intermediate bond coat (MCrAlY) plays a meaningful role on the adhesion of the ceramic top coat and provides better resistance to the attack typically promoted by oxygen and molten salts in severe working environments [4]. Ceramic materials with low thermal conductivity and heat capacity are good TBC candidates.

C. Lamuta and L. Pagnotta are with the *Department of Mechanical Engineering, University of Calabria, Ponte P. Bucci, Cubo 44C, Rende, Italy* (e-mail: caterinalamuta@gmail.com, leonardo.pagnotta@unical.it).
G. Di Girolamo is with *ENEA, Materials Technology Unit, Casaccia Research Centre, Rome, Italy* (e-mail: giovanni.digirolamo@enea.it).
P. Caliandro is with *OPTEL InP, Brindisi, Italy*.

Partially-yttria stabilized zirconia (8YSZ) is the most common used TBC material, owing to its satisfactory thermal and mechanical properties (low thermal conductivity, relatively high thermal expansion coefficient, low Young's modulus, high hardness and toughness) [5]-[6].

It has been reported that significant enhancements can be achieved by using nanostructured materials in substitution of conventional ones. Indeed, the reduction of the grain size typically involves better mechanical strength and toughness [7]-[8].

Plasma spraying is suitable for fabrication of thick porous coatings on complex metal parts. In such process powder particles are injected in the plasma jet by an inert gas, melted and accelerated toward the substrate, where they impact at high speed and quench, thus producing the build-up of a coating with typical microstructural defects such as splat boundaries, pores and microcracks [9]. It is worth noting that single nanoparticles cannot be carried by plasma jet and deposited on the substrate, so that they are commonly pre-synthesized in micron-sized particle agglomerates. To this purpose, these agglomerates should be only partially melted to preserve part of their starting nanostructure. On the contrary, if the agglomerates are totally melted, grain growth occurs and the final microstructure resembles that of a conventional coating [10].

In the present work different process parameters were employed for coating manufacturing, in order to control the degree of melting of the powder particles and to obtain coatings with well-tailored characteristics. The morphology and the microstructure of nanostructured YSZ coatings were investigated by scanning electron microscopy (SEM), while Nano and Micro Indentation (NI, MI) were employed to study the evolution of the main mechanical properties, such as Young's modulus and hardness. A statistical approach was used to study the mechanical properties of YSZ coatings and their relationship with the microstructure.

II. MATERIALS AND METHODS

A. Plasma spraying

Six different sets of YSZ ceramic coatings were deposited on Ni superalloy disks (IN738, $\phi = 25$ mm, thickness = 4 mm). The substrates were sand blasted using an alumina abrasive powder to increase their surface roughness and to improve the mechanical interlocking between coating and substrate. The

substrate roughness, measured using three dimensional optical surface profilometry, was found to be $6.9 \pm 1.1 \mu\text{m}$. An atmospheric plasma spraying equipment, with a 4F-MB plasma torch with 6 mm internal diameter nozzle, was used for coating deposition. A metallic CoNiCrAlY coating (Amdry 995C, Sulzer Metco) with thickness of $150 \mu\text{m}$ was previously applied as bond coat on the substrate surface.

Nanostructured partially yttria stabilized zirconia TBCs were then deposited using the nanostructured $\text{ZrO}_2\text{-7wt\% Y}_2\text{O}_3$ powder feedstock (Nanox S4007, Inframat, US). The final thickness of the coatings was of about $300 \mu\text{m}$. Six different sets of parameters were employed: three different values of arc current (500 A, 565 A and 630 A) and two levels of substrate-torch distance (80 mm e 100 mm). The other parameters were kept constant and can be summarized as follows: primary gas flow rate (Ar) 40 slpm, secondary gas flow rate (H_2) 12 slpm, powder flow rate 28.5 g/min, substrate tangential speed 2086 mm/s. The cross sections of the coated samples were prepared using standard metallographic procedure for ceramic coatings, including low-speed sectioning, cold mounting in vacuum in two-part epoxy resin, grinding, polishing and finishing to $0.25 \mu\text{m}$.

B. Microstructure

The morphology and the microstructure of powder feedstock and as-sprayed YSZ coatings were analyzed by scanning electron microscopy (SEMLEO 438 VP, Carl Zeiss AG, Oberkochen, Germany). The SEM pictures were then processed by image analysis software (Image J, U.S. National Institutes of Health, Bethesda, MD, USA) to measure the percentage of molten and semi-molten areas embedded in coating microstructure, and the distribution of the nanostructured areas. The size of the regions used for porosity measurements was $350 \times 250 \mu\text{m}^2$.

C. Mechanical properties

The mechanical properties of YSZ coatings were determined by Micro and Nano Indentation tests. A measuring system of CSM Instruments SA, Peseux, Switzerland, equipped with three objective lenses (with magnitude of 5x, 20x e 100x) was used. The indentations were performed on a portion of the ceramic top coat containing areas with different melting degree and were equally spaced ($40 \mu\text{m}$ for NI and $60 \mu\text{m}$ for MI) in order to avoid the mutual influence of consecutive indentations [11]. Due to the presence of microstructural defects such as pores and poorly compacted areas, an Adjust Depth Offset operation was set every ten indentations in order to find the height position of the sample surface (acronym ADO in Fig. 1).

NI tests were performed according to a 4×10 matrix (with lines parallel to the substrate) by using a Berkovich tip, a loading and unloading speed of 3 mN/s, a hold time of 10 s and two different values for the maximum load: 8 and 100 mN. MI, distributed according to a 3×10 matrix, were also performed by using a Vickers microindenter with maximum loads of 50 gf and 100 gf and a hold time of 10 s.

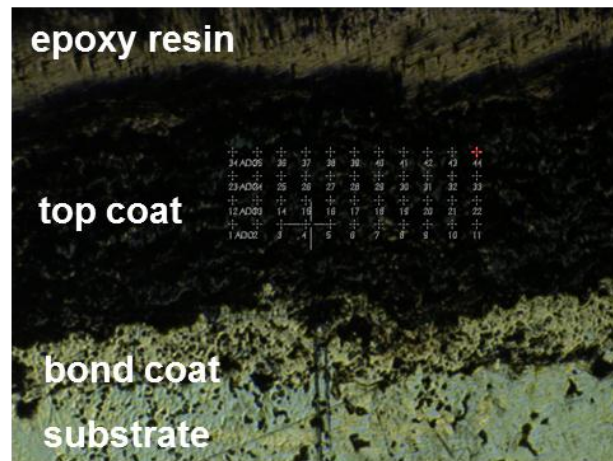


Fig. 1 disposition of NI on the top coat cross section. Starting from the top: epoxy resin, top coat, bond coat and metallic substrate (magnitude 5x)

The values of reduced Young's modulus E_r and hardness H were obtained by load-depth curves, according to Oliver and Pharr theory [12]-[13], and then the experimental data were analyzed by assuming a two-parameters Weibull statistical distribution [14].

III. RESULTS AND DISCUSSION

A. Microstructure

Fig. 2 shows the cross sectional SEM microstructure of nanostructured YSZ coatings produced at the spraying distance of 80 mm and using different values of plasma current (500, 565 and 630 A). The plasma current is proportional to the plasma power and to the temperature of the sprayed particles, so that it can be used to have a good control on the degree of melting of the particle agglomerates. All the coatings exhibited a bimodal microstructure composed of well melted splats (dark grey dense areas in the pictures) and partially melted nanostructured areas (light grey areas) possessing an intrinsic porosity derived from their pre-agglomeration, as shown in Fig. 3 (a). The nanostructured areas are composed of loosely bound nanostructured particles.

Fig. 3 (b) shows the morphology of the related powder particles, so that it can be deduced that the nanostructured zones retained in the final coatings were not affected by complete melting during processing. The inset shows some clusters of nanograined particles with size close to 100 nm. During processing the hot plasma gas penetrated inside the agglomerated particles of the powder feedstock, melting their surface, while their core remained unmelted. The low heat transfer associated to their intrinsic porosity, the short residence time of the same sprayed particles in the plasma jet and the high quenching rate of the solidified splats at the substrate surface are able to reduce the mechanism of grain growth and nucleation, thus preserving great part of the starting nanostructure in the final coating.

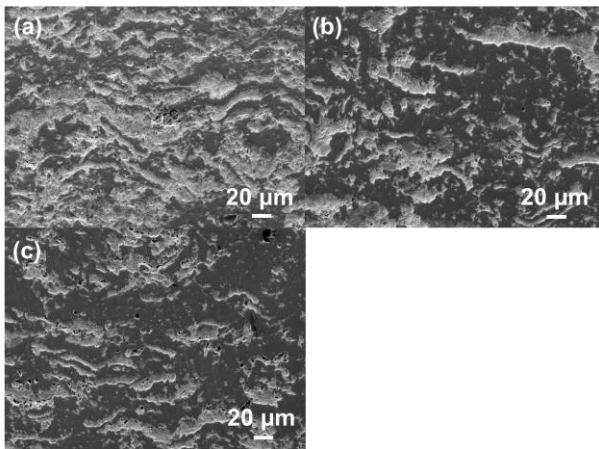


Fig. 2 cross sectional SEM microstructure of nanostructured YSZ coatings deposited at spraying distance of 80 mm and various plasma current levels (a) 500 A, (b) 565 A and (c) 630 A

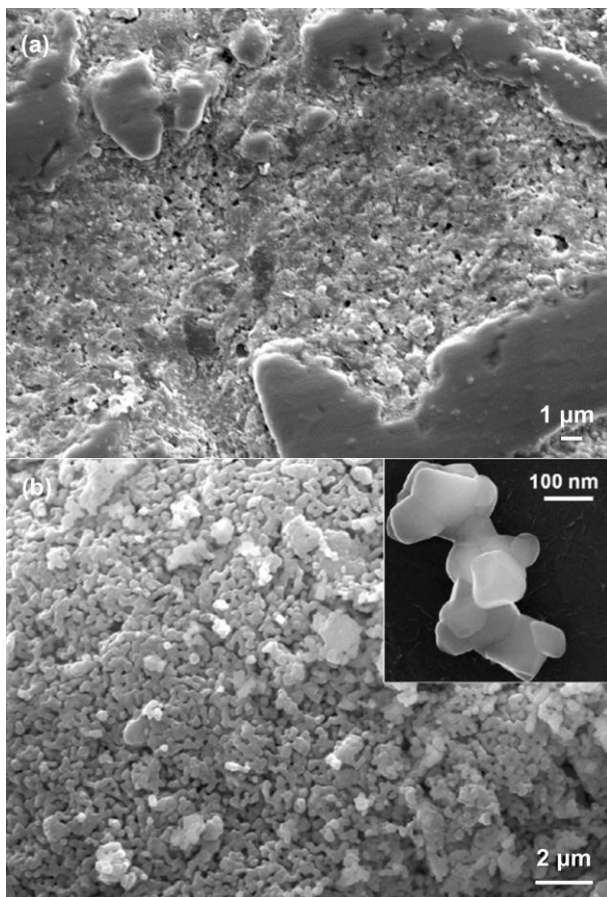


Fig. 3 (a) cross sectional SEM microstructure showing the morphology of retained nanostructured areas; (b) a view of agglomerated nanoparticles in the powder feedstock with detail of zirconia clusters

As well displayed in Fig. 2, the well melted areas cement the loose microstructure, providing good mechanical integrity. The distribution of the nanostructured areas is more uniform for lower values of plasma current. For increasing values of this parameter the melting degree of the powder particles enhances, thus leading to denser coating with lower content of nanostructured areas. The flight path and the temperature history of the agglomerated particles in the plasma jet affect their distribution in the final coatings. The melting process is

strongly related to the temperature distribution in the plasma jet and to the heat transfer to the porous agglomerates.

Table I reports the amount of retained nanostructured areas measured by image analysis along the cross section of nanostructured YSZ coatings produced using different process parameters. At constant spraying distance the percentage of nanozones decreases with increasing the plasma current, due to the better melting of the particle agglomerates, so that denser coatings are produced. This effect is more pronounced at 80 mm. The effect of spraying distance is more pronounced at the lowest value of plasma current. Higher spraying distance involves higher residence time of the sprayed particles in the plasma jet, better melting and thus higher deposition efficiency and higher coating thickness.

Table I. fractions (%) of retained nanostructured areas measured in YSZ coatings produced using different process parameters (plasma current and spraying distance)

Distance/current	500 A	565 A	630 A
80 mm	36 ± 4	23 ± 1	20 ± 4
100 mm	31 ± 2	25 ± 4	21 ± 1

It is worth noting that the percentage of nanostructured areas embedded in coating cross section can be properly optimized based on the application the coating is addressed to. High retention of nanozones (30-40 %) is particularly desired for manufacturing of abradable coatings with relatively low mechanical integrity. These coatings can be used in turbine engines to minimize the bypass flow of hot combustion or cold compressor gases through the spaces between the rotating blade tips and the walls of the shroud, in order to provide seal and improve the efficiency.

On the contrary, lower retention of nanostructures (20 %) is preferable for development of thermal barrier coatings with low thermal conductivity, high structural integrity and resistance to the infiltration of oxygen and molten salts in severe working environments (stator turbine blades and vanes). The presence of nanostructured areas with low sintering rate can counteract the high-temperature densification of YSZ coatings, which negatively affect the compliance and the thermal property, thus retarding extended microcracking and TBC delamination [10].

To this purpose, it has been reported that the presence of nanozones plays a significant role on the thermal shock resistance and durability of TBCs, because they act as crack arresters in the case of microcracking promoted by thermal stresses produced by thermal expansion mismatch between overlapped layers, thus increasing the fracture toughness [7]-[15]. Otherwise, microcracks tend to easily grow in more dense areas.

Fig. 4 shows the fractured cross section of the nanostructured YSZ coating: the morphology of well melted areas can be appreciated in.

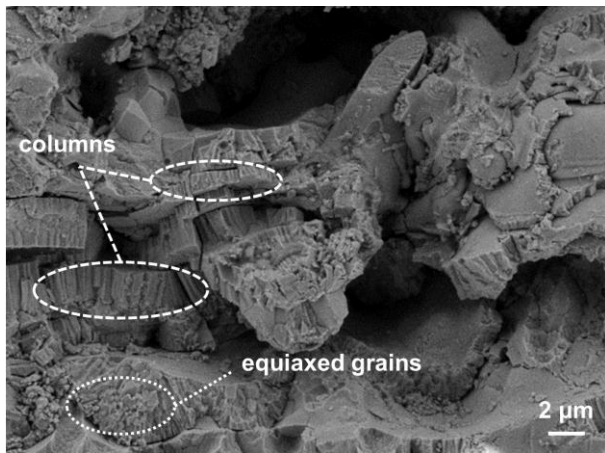


Fig. 4 fractured coating cross section showing the morphology of the melted splats, composed of columnar and equiaxed grains

Columnar grains with diameter in the range from 50 to 300 nm are detectable. They are oriented along the direction of grain growth and derived from heterogeneous nucleation at splat boundary produced by the heat flow released by the crystallization of the previous deposited splats. Some equiaxed grains can be also observed at splat boundary. They are produced by homogeneous nucleation, occurring when the heat loss promoted by cooling at substrate is higher than the heat released by crystallization [15].

B. Mechanical properties

Tables II and III summarize the values of Young's modulus, micro and nanohardness measured on the cross sections of nanostructured YSZ coatings, deposited at spraying distance of 80 and 100 mm, respectively, and using different values of plasma current parameter. The measured values magnitude is in good agreement with that of results in literature [16]-[17].

It should be noted that the mechanical properties tend to increase with increasing the plasma current and the spraying distance. Specifically, at constant spraying distance, for increasing values of current, an average increase of 9% and 30% for Er and 13% and 60% for H, was observed, from nanoscale to microscale, respectively. Instead, the influence of spraying distance is less prominent. At constant current value, for increasing values of torch-substrate distance, an average increase of 4% and 7% for Er and 3% and 34% for H was recorded, from nanoscale to microscale. It should also be noted that the values of mechanical properties exhibited large scattering.

Fig. 5 shows the load-depth (P-d) curves obtained by nanoindentations performed in the melted areas (grey line) and in partially melted ones (black line), respectively. The curves refer to coatings produced at 500 A and 100 mm, but similar behaviour was noticed for all the other samples. The parameters used for NI were: maximum load 100 mN, loading and unloading speed 3 mN/s, hold time 10 s.

It is possible to observe that in the melted phase lower maximum penetration was noticed (709 nm versus 2056 nm in the partially melted phase) as well as a higher unloading curve slope. This suggests that the melted phase is characterized by higher stiffness and hardness in comparison with the partially melted area [12]-[13].

Table II. mean values and standard deviations of the mechanical properties for YSZ coatings sprayed at 80 mm and using different values of plasma current, measured by Micro and Nano Indentation tests using various loads

Load	Current (A)	Er (GPa)	H (GPa)
8mN (NI)	500	151 ± 47	11.1 ± 5.4
	565	170 ± 33	11.8 ± 4.9
	630	174 ± 42	13.7 ± 4.8
100mN (NI)	500	100 ± 37	6.3 ± 3.9
	565	121 ± 37	8.3 ± 4.7
	630	125 ± 41	7.9 ± 4.3
50gf (MI)	500	76 ± 20	4.2 ± 2.4
	565	114 ± 28	6.1 ± 3.2
	630	123 ± 31	8.7 ± 5.0
100gf (MI)	500	80 ± 19	3.4 ± 1.4
	565	100 ± 26	4.4 ± 2.5
	630	125 ± 21	7.2 ± 2.7

Table III. mean values and standard deviations of the mechanical properties for YSZ coatings sprayed at 100 mm and using different values of plasma current, measured by Micro and Nano Indentation tests using various loads

Load	Current (A)	Er (GPa)	H (GPa)
8mN (NI)	500	159 ± 68	9.9 ± 5.8
	565	177 ± 54	11.7 ± 5.1
	630	170 ± 60	12.1 ± 6.2
100mN (NI)	500	108 ± 37	7.1 ± 4.3
	565	124 ± 53	9.1 ± 6.2
	630	135 ± 36	9.5 ± 4.0
50gf (MI)	500	78 ± 40	4.4 ± 3.3
	565	125 ± 40	10.3 ± 6.3
	630	158 ± 73	19.6 ± 12.9
100gf (MI)	500	76 ± 20	3.3 ± 1.9
	565	113 ± 29	5.9 ± 2.9
	630	109 ± 22	5.5 ± 2.6

Indeed, as shown in Fig. 6, the size of the imprint is bigger in partially melted area. The nanostructured areas are characterized by porosity at nanoscale which reduces the cohesion between the agglomerated nanostructured particles. In addition, curves in Fig. 5 show that melted phase doesn't reveal any creep phenomenon, whereas the unmelted one is affected by it: in fact, it presents a depth increase during the hold time at the maximum load. Based on the observations herein reported, one can conclude that the increase of the mechanical properties, observed in Tables II and III, is related to the increase of the melted fraction in YSZ coatings when higher values of current and distance are employed (Table I).

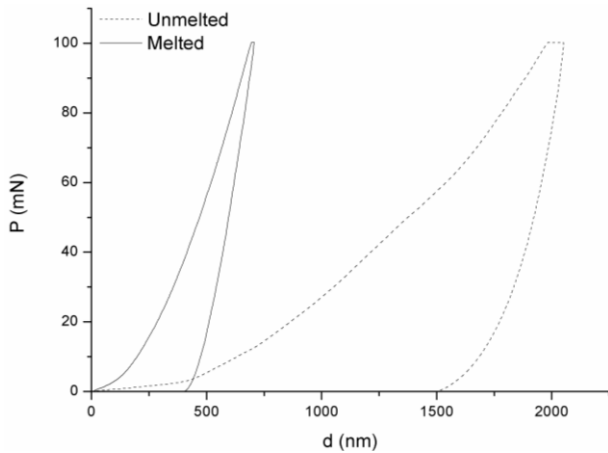


Fig. 5 load-depth (P-d) curves corresponding to melted and partially melted phases

The usage of increasing current values involves higher plasma power, higher temperature of the sprayed particles and therefore lower retention of nanostructured areas and higher coating density. As previously reported, higher distance involves higher residence time of the sprayed particles in the plasma jet and better degree of melting, even if the effect of distance on the experimental trend of the mechanical properties was not always consistent, probably because of a kind of mutual influence with current. This aspect could be analyzed in future works by performing an experimental plan that provide a third level of torch-substrate distance and more in-depth analysis. As clearly observed in Tables II and III, the values of the mechanical properties measured at microscale are lower than those obtained at nanoscale, because of the larger analyzed volume and the higher influence of typical defects embedded in coating microstructure, such as coarse pores, splat boundaries and microcracks.

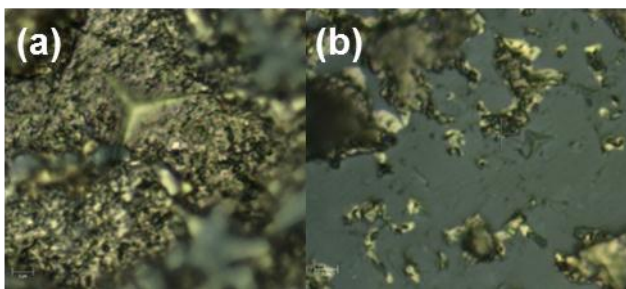


Fig. 6 indent of NI (Berkovich) in partially melted (a) and melted (b) phase (magnitude 100x)

Moreover, for each Indentation technique employed, as the indentation load rises the analyzed volume grows and the same microstructural defects becomes more significant, enough to bring down the mechanical properties, that result always more averaged and far from those of bulk stabilized zirconia [10]-[11].

Further analysis showed that the mechanical properties don't change across coating thickness and their variation is so small to be covered by the high scattering of the results (related to the different characteristics between melted and partially melted phases). In order to understand the reasons of this high scattering, two series of NIs were performed on the

areas with different morphology, by using a maximum load of 8 mN and a time for loading and unloading of 10 s. Fig. 7 shows some of the load-depth curves obtained.

It is interesting to notice that the curves related to the melted area (continuous lines) are very close and reproducible, whereas the curves acquired during indentation in the unmelted area (dashed lines) are somewhat different and dispersed. The well melted area is, in fact, characterized by lower scattering in the mechanical properties, whereas the second one exhibits widely scattered data (Table IV), typical of structures produced by nanostructured agglomerates assembly and characterized by intrinsic porosity.

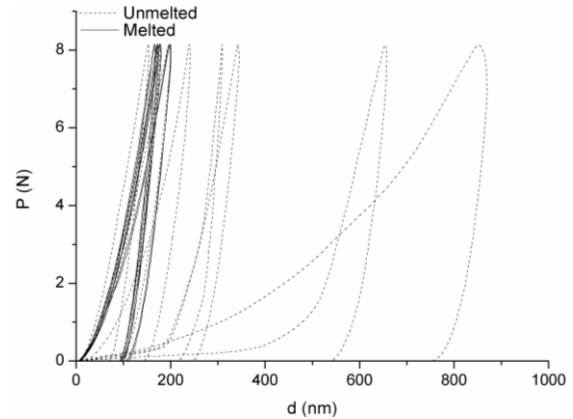


Fig. 7 load-depth (P-d) curves corresponding to melted and unmelted fractions and measured by NI at 8mN

Table IV summarizes the mean values and the standard deviations of the elastic modulus and hardness for both these areas.

Table IV. elastic modulus and hardness of melted and unmelted phases

Mechanical properties	Melted area	Unmelted area
E_r (GPa)	196 ± 29	131 ± 61
H (GPa)	$15,8 \pm 2,3$	$9,0 \pm 7,8$

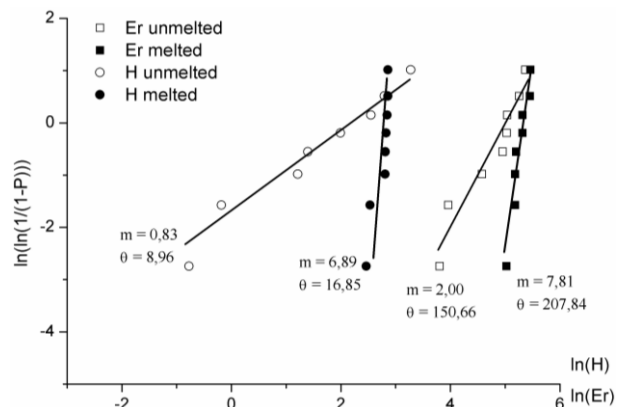


Fig. 8 Weibull plot of Er and H for melted and unmelted phases; the shape (m) and the scale (θ) parameters are also reported

These data can be used to predict the mechanical properties of nanostructured coatings, by using the typical mixture law: $X = X_m \cdot v_m + X_{nm} \cdot v_{nm}$, where X represents Er or H of the coating, X_m and X_{nm} Er and H of the melted and unmelted phases, respectively, v_m and v_{nm} the corresponding volumetric

fraction. Indeed, the nanostructured coatings can be considered as a composite consisting of two materials, melted and partially melted phases.

Fig. 8 shows the distribution of Er and H, in a bilogarithmic scale [14], for the well melted and unmelted areas, by assuming a two parameters Weibull distribution for the mechanical properties. The data can be approximated with a linear regression curve. On the same graph, the values of shape and scale parameters are reported. According to the previous assertions, the melted phase, characterized by less scattered data, presents greater values of m . The probability density functions of Er and H are plotted, respectively, in Figs. 10 (a) and (b), in grey for the melted area and in black for the partially melted one.

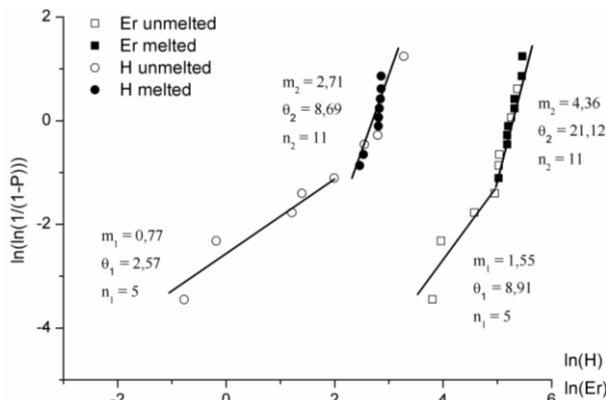


Fig. 9 Weibull plot of H and Er data for the sample obtained by merging the data arising from melted and unmelted areas

The sample obtained by merging the experimental data related to melted and unmelted areas can be considered like a coating with the 50% of the two phases. The analysis of the distributions concerning this kind of sample can be very useful for the prediction of the mechanical properties of any other nanostructured coating. For this purpose, in Fig. 9, Er and H Weibull plot of this simulated coating are shown, while Figs. 10 (a) and (b) show (dashed lines) the related probability density function (obtained as a weighted average of the probability density of the data referred to single zones). It can be noted that the points related to partially melted phase are so scattered that they contaminate the data of the second section, concerning the melted area, and go also beyond this region (in this example it is just a point). The slope of the mixed section (the second one) increases by decreasing the level of contamination. Despite the data merging, the bimodal behaviour of the coating can be clearly observed, due to the change in the slope of the Weibull plot. In order to find the transition point between the two regions the R^2 statistics analysis can be used [10]. It should be noted that the presence of points above the mixed zone may generate incorrect interpretations of the data distribution, by suggesting, erroneously, the existence of a third phase, and then a trimodal distribution. Fig. 11 shows the trends of the mechanical properties for all the coatings produced in this work and tested by Nano Indentation at 8 mN.

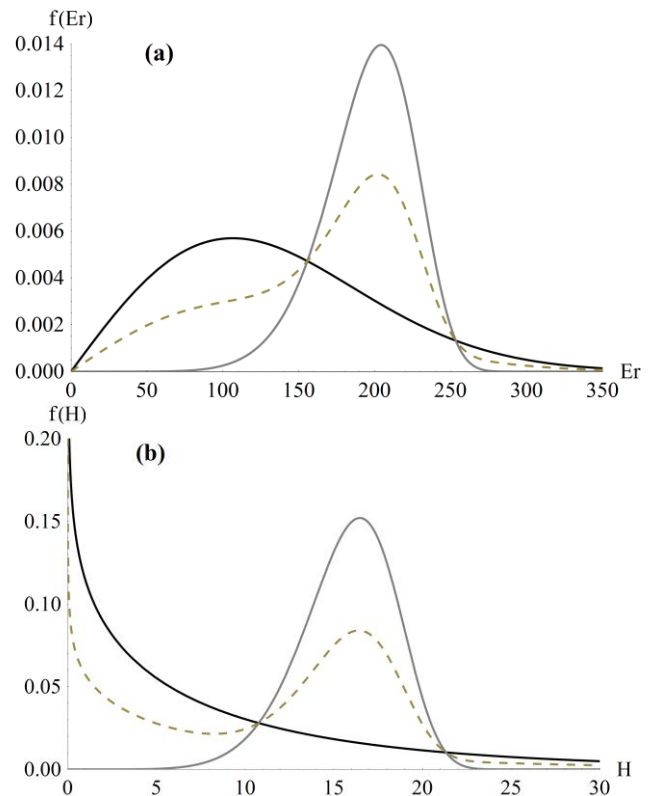


Fig. 10 probability density function of (a) Er and (b) H for melted (grey) and unmelted (black) phases and of the resultant bimodal distribution (dashed)

In all the cases a bimodal Weibull distribution can be noticed, as also observed in any previous works [10]-[16]. The zone in the graph characterized by lower values of H or Er reflects the mechanical behavior of the partially molten phase and it is characterized by lower slope, owing to greater scattering, whereas the second one is characteristic of the mixed area. It is interesting to notice that, at constant torch-substrate distance, as current value rises the slope of the second regression line increases: this is caused by the increase of the degree of melting of the sprayed particles which results in lower probability of contamination of the data pertaining to the molten zone. Note that, at constant current level, the increase of the torch-substrate distance produces different trend, but the results are in good agreement with the volume fractions of nanostructured areas listed in Table I.

The results obtained by NI tests performed at maximum load of 100 mN showed similar behaviour but less noticeable changes in slope between the interpolating sections were detected. This effect is the consequence of the greater size of the volume involved during NI at higher load, which mediates the local properties and makes the bimodality of the distributions more difficult to be observed.

In turn the results obtained by Micro Indentation for the coatings produced at 500 A and 100 mm are shown in Fig. 12. The second region of the distributions of MI data exhibit lower slopes with respect to the first one, unlike NI tests, and in agreement with the data reported in literature [10]-[16].

This behaviour can be addressed to the scale effect for which microcracks and globular pores embedded in the molten

areas are responsible of data scattering, since higher volume of material was under analysis [10].

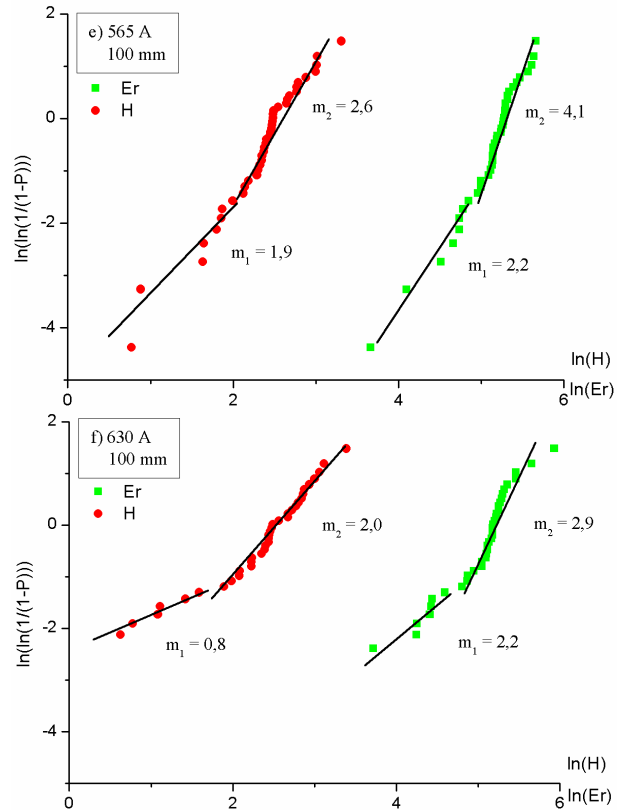
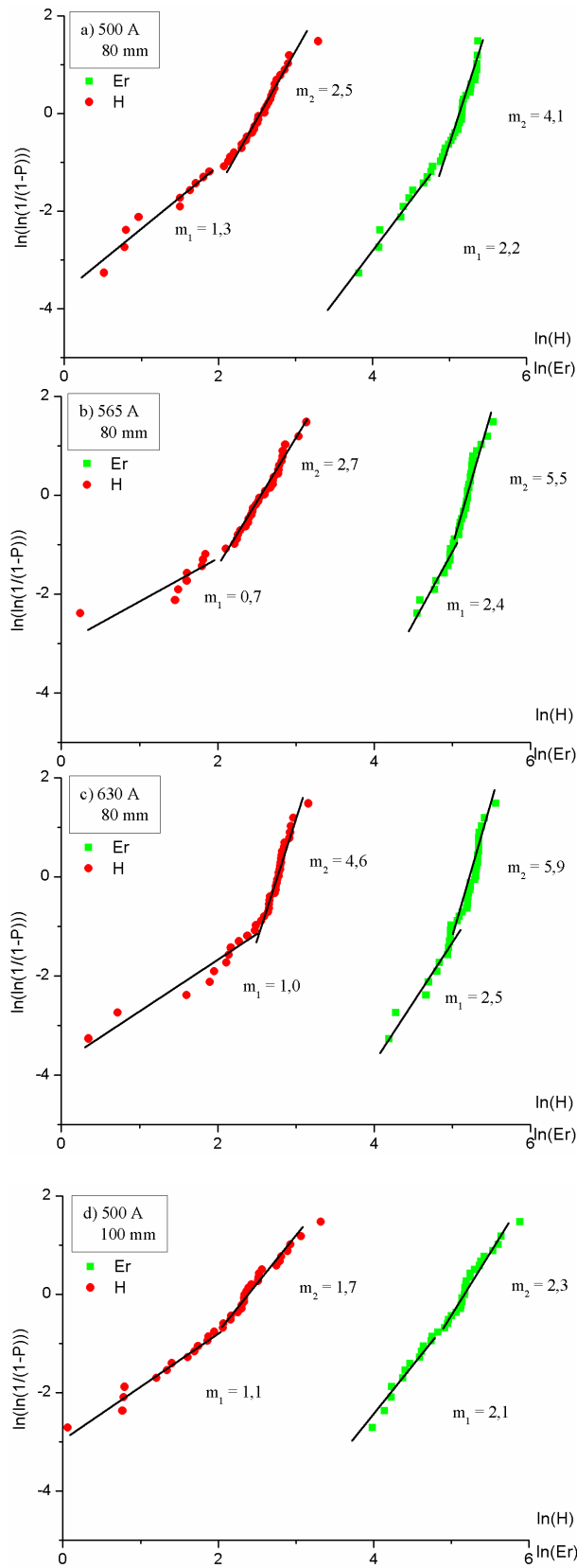


Fig. 11 Weibull plot of H and Er for nanostructured YSZ coatings fabricated using different process parameters (plasma current and spraying distance) and tested by NI at 8mN

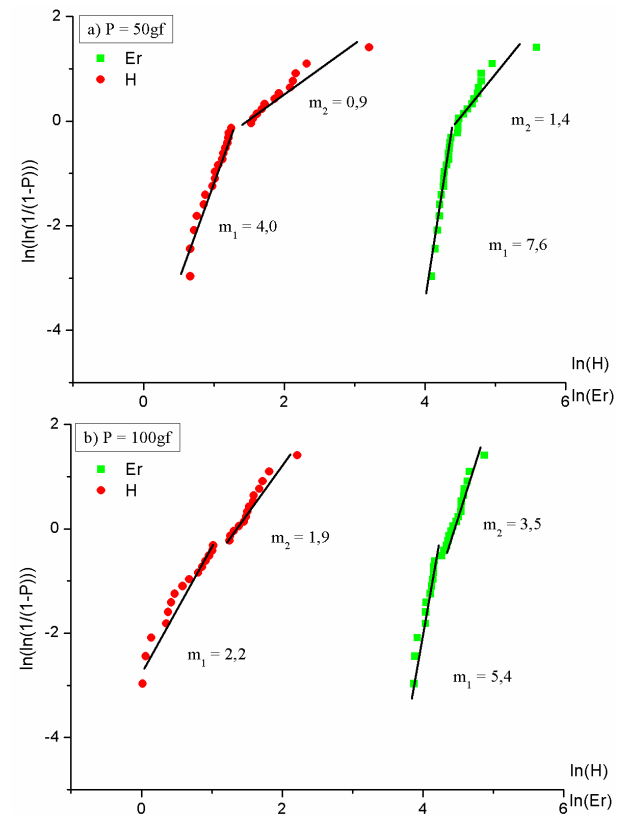


Fig. 12 Weibull plot of H and Er for nanostructured YSZ coating produced at 500 A and 100 mm and tested by MI at (a) 50 gf and (b) 100 gf

Therefore at higher indentation loads the data distribution is almost single-mode, as shown in Fig. 12 (b). Similar behaviors was observed for the other five specimens produced with different values of current and torch-substrate distance.

IV. CONCLUSION

In this work the influence of some process parameters (plasma current and stand-off distance) on the microstructural and mechanical properties of nanostructured YSZ coatings was investigated. The partial melting of the nanostructured particle agglomerates produced the formation of a bimodal microstructure composed of well melted splats and semimolten areas. Columnar and equiaxed grains were observed in melted splats, while the partially melted areas did not suffer grain growth and retained porosity at nanoscale. An increase of plasma current promoted the increase of the particle temperature, improving their melting degree and the density of the coatings.

The reduction of the retained nanostructured areas produced significant increases of Young's modulus and hardness values. The effect of the torch-substrate distance was more significant at lower current values. The Nano and Micro Indentation tests, performed at various loads, in conjunction with Weibull statistical approach, revealed that the bimodal microstructure involved a bimodal distribution of the mechanical properties, which tended to disappear with increasing the indentation load. The elastic modulus and the hardness decreased with increasing the indentation load, because of higher analyzed volume and stronger influence of the microstructural defects.

This is particularly promising in the purpose to predict the mechanical behaviour of nanostructured coatings.

The development of a reliable procedure allowing a proper control of the percentage of the nanostructured areas embedded in coating microstructure in the purpose to obtain well determined mechanical characteristics, is not easy to be achieved and will require further investigations.

ACKNOWLEDGMENT

The nano- and micro-hardness measurements were performed with equipment kindly provided by "Centro Materiali, Tecnologie e Ricerca Avanzata (MaTeRiA)" from University of Calabria, funded with "Pon Ricerca e Competitività 2007/2013, Asse I Sostegno ai Mutamenti Strutturali Obiettivo Operativo 4.1.1.4, Potenziamento delle Strutture e delle Dotazioni Scientifiche e Tecnologiche, Azione I - Rafforzamento Strutturale".

The authors wish to thank C. Blasi for her valuable contribution in plasma spraying and coating manufacturing.

REFERENCES

- [1] J. A. Nesbitt, "Thermal response of various thermal barrier coatings in a high heat flux rocket engine," *Surf. Coat. Technol.*, vol. 43/44, pp. 458-469, 1990.
- [2] N. Curry, N. Markocsan, X. A. Li, A. Tricoire, M. Dorfman, "Next generation thermal barrier coatings for the gas turbine industry," *J. Therm. Spray Technol.*, vol. 20, pp. 108-115, 2011.
- [3] N. P. Padture, M. Gell, E.H. Jordan, "Thermal barrier coatings for gas turbine engine applications," *Science*, vol. 296, pp. 280-284, 2002.
- [4] G. Di Girolamo, M. Alfano, L. Pagnotta, D. Sun, J. Zekonyte, R. J. K. Wood, "On the Early Stage Isothermal Oxidation of APS CoNiCrAlY Coatings," *J. Mater. Eng. Perf.*, vol. 21, pp. 1989-1997, 2012.
- [5] X. Q. Cao, R. Vassen, S. Stöver, "Ceramic materials for thermal barrier coatings," *J. Eur. Ceram. Soc.*, vol. 24, pp. 1-10, 2004.
- [6] G. Di Girolamo, L. Pagnotta, "Thermally sprayed coatings for high temperature applications", *Rec. Patent on Mater. Sci.*, vol. 4, pp. 173-190, 2011.
- [7] R. S. Lima, B. R. Marple, "Thermal spray coatings engineered from nanostructured ceramic agglomerated powders for structural, thermal barrier and biomedical applications: a review," *J. Therm. Spray Technol.*, vol. 16, pp. 40-63, 2007.
- [8] J. Wu, H. B. Guo, L. Zhou, L. Wang, S. K. Gong, "Microstructure and thermal properties of plasma sprayed thermal barrier coatings from nanostructured YSZ," *J. Therm. Spray Technol.*, vol. 19, pp. 1186-1194, 2010.
- [9] J. R. Davis, *Handbook of Thermal Spray Technology*, ASM International, Materials Park, 2004.
- [10] R.S. Lima, A. Kucuk, C.C. Berndt, "Bimodal distribution of mechanical properties on plasma sprayed nanostructured partially stabilized zirconia," *Mater. Sci. Eng. A*, vol. 327, pp. 224-232, 2002.
- [11] A. C. Fisher-Cripps, *Nanoindentation, 3rd edition*, New York: Springer, 2011.
- [12] W.C. Oliver, G. M. Pharr, "An improved technique for determining hardness and elastic modulus using load and displacement sensing indentation experiments," *J. Mater. Res.*, vol. 7, pp. 1564-1583, 1992.
- [13] W. C. Oliver, G. M. Pharr, "Measurement of hardness and elastic modulus by instrumented indentation: Advances in understanding and refinements to methodology," *J. Mater. Res.*, vol. 19, pp. 3-20, 2004.
- [14] W. Weibull, "A statistical distribution function of wide applicability," *J. Appl. Mech.*, vol. 18, pp. 293-7, 1951.
- [15] G. Di Girolamo, F. Marra, C. Blasi, E. Serra, T. Valente, "Microstructure, mechanical properties and thermal shock resistance of plasma sprayed nanostructured zirconia coatings," *Ceram. Int.*, vol. 37, pp. 2711-2717, 2011.
- [16] L. Wang, Y. Wang, X. G. Sun, J. Q. He, Z. Y. Pan, C. H. Wang, "Microstructure and indentation mechanical properties of plasma sprayed nano-bimodal and conventional ZrO₂-8wt%Y₂O₃ thermal barrier coatings," *Vacuum*, vol. 86, pp. 1174-1185, 2012.
- [17] M. Saremi, A. Keyvanimahmoud, H. Sohi, "Hot corrosion resistance and mechanical behavior of atmospheric plasma sprayed conventional and nanostructured zirconia coatings," *Int. J. Modern Phys.: Conf. Series*, vol. 5, pp. 720-727, 2012.

Mathematical model for calculation of power consumption and electromagnetic noise of resistance welding machines

L. Sakhno, O. Sakhno, S. Dubitsky*

St. Petersburg State Polytechnic University, Department of Theoretical Electroengineering,
Polytechnicheskaya 29, St. Petersburg, 190251, Russia, e-mail: lsahno2010@yandex.ru

*Tor Ltd, the vendor of QuickField FEA Software,
Moskovsky pr. 22, lit. T, St. Petersburg 190013, Russia. E-mail: simon.dubitsky@ieee.org

Abstract— Important features of resistance welding machines are substantial current pulsations in the welding circuit and a highly non-uniform power intake from the supply mains. In order to develop welders that would comply with electromagnetic noise level specifications and be compatible with the supply mains, a careful analysis of higher harmonics generated by resistance welders is therefore essential. With this end in view, a mathematical model was developed which makes it possible to calculate electromagnetic processes end to analyze harmonic composition of currents and voltages in any component of a resistance welder power source.

The model was used for the harmonic analysis of the mains current and the welding circuit in application to the inverter power unit for a steel pipe flash butt welder. The calculations yielded data which permitted selection of appropriate harmonic current suppression devices to be installed at the supply network buses and enabled quantization of the electromagnetic noise generated by welding current harmonics. The calculated electromagnetic processes in the welding source were corroborated experimentally.

Keywords— electromagnetic compatibility, power consumption, resistance flash welding, welding machine

I. INTRODUCTION

ELECTRIC welders represent a common source of electromagnetic noise in power networks. Such noise stems from a nonlinear and asymmetric load of power network. Works with the welders in operation, which results in distortion of their current and voltage curves. Moreover, an abruptly non-uniform power intake from the network or a limited power scarce (Diesel-generator set) is possible in welding, and inducing voltage drops. The quality of electric power may thus be deteriorated by the electromagnetic noise. Because of this industrial welders are generally powered by special networks equipped with noise suppression devices. Voltage drops at the power source buses adversely affect welder's operation, because high-quality welds can be obtained only with a stable voltage at the welder's input. The

voltage drops can also upset serviceability of the welder having an inverter power unit. The block diagram of an inverter source in fig1 consists of the three-phase bridge rectifier with the capacitor filter, the inverter, the welding transformer to which secondary windings via the single-phase two-half-period rectifier with an average point welded details are connected.

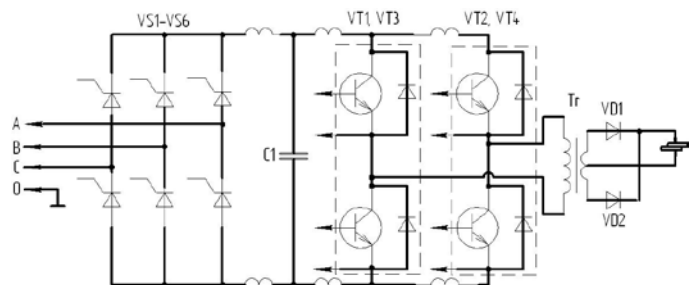


Fig. 1. Circuit diagram of the flashing butt resistance welder for steel pipes.

Hence development of new welders entails evaluation of their impact on supply mains or Diesel-generator sets and necessitates provision of their electromagnetic compatibility.

II. THE CALCULATION METHOD

The problem is generally solved by experimental investigation [1,2]. At the same time, efficient means for analysis of the noise level and electromagnetic compatibility of welders and power sources are provided by studies on the associated electromagnetic processes with the use of computer simulation making it possible to evaluate distortions of current and voltage in the power source, voltage drops and surges at the welder's power source input, to analyze operating conditions for a Diesel-generated set supplying power to the welder, to estimate flashing stability and impact of power source electric resistance on it, and to find the ways to ensure electromagnetic compatibility. Complexity of mathematical modeling stemming from a high order of the set of nonlinear differential equations that describe

electromagnetic processes and necessity to develop special mathematical models corresponding to various welder configurations and their load conditions made impossible a wide application of the method to solution of the above problems. However, availability of numerous multipurpose software packages makes unnecessary development of specialized mathematical models for each configuration of the power source and substantially reduces the time needed to obtain solution. The efficiency of application of a multipurpose software package is exemplified by analysis of electromagnetic compatibility for medium-power resistance welders and shop power network.

III. CALCULATION OF POWER CONSUMPTION

The power consumption of a welding machine:

$$S = U_1 I_1 \approx U_{OC2} I_2, \quad (1)$$

where U_1 and I_1 are primary voltage and current, I_2 is welding current, U_{OC2} is open circuit voltage of secondary winding of the welding transformer.

$$U_{OC2} = I_2 z, \quad (2)$$

where z is the full complex resistance of welding machine, I_2 is complex current.

The full complex resistance contains welder's load and a short-circuit three-winding transformer resistance.

IV. EQUIVALENT CIRCUIT OF WELDER'S LOAD

The present paper focuses on resistance flash welding which involves butting of parts preheated to a near-melting temperature. It should be noted that this technique can also be applied to other types of welding.

The welder's load is a welding circuit which represents a system of rigid and flexible current-conducting components connecting the secondary winding of the welding transformer to the welder's electrodes between which the parts to be welded are placed. The equivalent circuit thus comprises the inductances and resistances for secondary circuit, electrodes, sections of parts, through which welding current passes, and the nonlinear components substituting the flashing zone in welding. In development of an equivalent load circuit selection of such components presents a major difficulty because of complexity of physical processes in the flashing zone. Let us consider features of the flashing process with the view to replace the flashing zone with electric circuit components. On account of a high density of current at elementary contacts between parts, they heat up and convert to liquid straps on coming in contact with each other. Changes in the volume and shape of the liquid straps are due to metal melting, movement of the strap over the surface of parts, its compression by electrodynamic forces, and liberation of vapours and gases out of the overheated metal volume. Such phenomena are responsible for abrupt changes in resistance of the flashing zone. Disintegration of liquid metal straps occurs under the influence of electrodynamic forces and metal overheating. Such disintegration is accompanied by arcing with constant

voltage maintained at the flashing zone and the welding current dropping to zero. Experiments show that resistance at the flashing zone undergoes three-four-fold changes. Frequency of changes in resistance and arcing may range from 500 Hz to a few kHz, and arcing duration accounts for several tens of microseconds. With stable flashing, the welding current curve is not strictly cyclical, but, considering its recurrent nature in each cycle (both for the envelope curve and for single-pulsation currents), the welding current curve may be regarded cyclical for analysis of phenomena with an averaging interval of about 0.1 s, the cycle being equal to that of supply voltage. The flashing process generally takes tens of seconds and involves several stages. The first stage can be a condition close to the welder's short-circuit or a no-load condition caused by the slopping of the metal from the flashing zone under the action of electrodynamic forces. The second stage features contact and arc occurrences, their role depending on the properties of the flashed material and the flashing condition. At the last stage, when the film of molten metal forms on the surface of welded parts, these are pressed together, which corresponds to the welder's short-circuit. This stage lasts from 0.1 to 0.8 s. The basic parameters of the flashing condition, such as equivalent contact resistance, number of connections and disconnections for the flashed butts per unit time, and voltage at the flashing zone in arcing, were found experimentally for different materials and sections of the parts being welded.

Complying with the above features of the flashing process, the equivalent circuit for the flashing zone should fit the following load conditions:

- the short-circuit condition;
- the no-load condition,
- transition from the no-load condition to the short-circuit condition, characteristic of the initial flashing stage,
- step-type changes in resistance of the flashing zone,
- cycling arcing.

Depending on the condition under consideration, the flashing zone is replaced either by a resistance or by a source of constant electromotive force (emf) and a fully controllable value (fig.2).

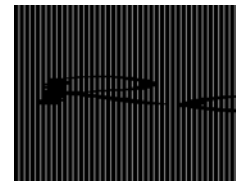


Fig. 2. Equivalent circuit of the flashing zone.

R_C - contact resistance,

U_g - arc voltage

The first of the above conditions reflects the contact occurrences at the flashing zone, and the second, the arc phenomena. When the valve is closed, the resistance or the emf source are disconnected from the welder's load; when it is opened, they are connected to the load.

V. THE EQUIVALENT CIRCUIT OF A THREE –WINDING TRANSFORMER

An example of a three –winding transformer with disk alternating windings and an armored magnetic conductor is shown in fig.3. This transformer is used in the inverter source in fig1 The primary winding consists of four series-connected coils made of wire with rectangular cross-section. The two secondary coils are made of copper tubes through which cooling water flows.

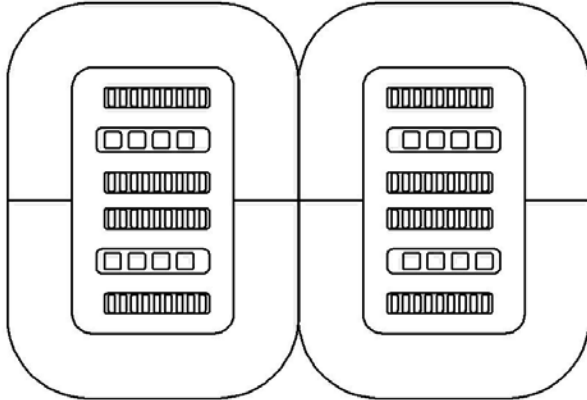


Fig.3. Design of the transformer with four primary coils

The main difference between the proposed equivalent circuit and the well-known one is that the windings not being electrically linked and always have positive inductances. Therefore, the circuit is suitable for the standard simulation program (P-Spice). It is very important that the circuit parameters have the clear physical sense and can be easily evaluated by FEA.

This circuit is based on replacing the three-winding transformer with two transformers: one with windings 1, 2 and the second with windings 1, 3 (further denoted as transformers 1-2 and 1-3) [3]. The mutual impact of transformers 1-2 and 1-3 is modelled as a change of EMF on the terminals of their secondary windings by magnetic leakage fields. The degree of magnetic coupling of these transformers is characterized by the magnetic coupling factor for the leakage fluxes

$$k = \frac{M}{\sqrt{L_{12}L_{13}}} \quad (L_{12} \text{ and } L_{13} - \text{the leakage inductances of the transformers 1-2 and 1-3 referred to their secondary sides, } M - \text{the mutual inductance of the leakage fluxes}).$$

(L_{12} and L_{13} - the leakage inductances of the transformers 1-2 and 1-3 referred to their secondary sides, M - the mutual inductance of the leakage fluxes).

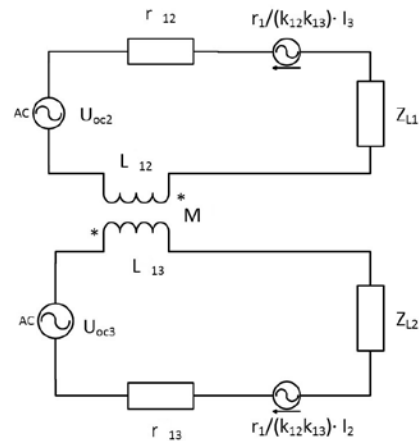


Fig.3. Equivalent circuit of three –winding transformer

The magnetic coupling factor k is convenient for the analysis of the transformer design influence on the power consumption. If $M > 0$ the direction of the leakage flux in winding 3 caused by transformer 1-2, is opposite to the direction of the main magnetic flux in this winding. If $M < 0$ the leakage flux and the main flux in winding 3 have the same direction. Similarly, if $M > 0$ the direction of the leakage flux in winding 2 caused by transformer 1-3 is opposite to the direction of the main magnetic flux in this winding. If $M < 0$ the leakage flux and the main flux have the same direction. In the equivalent circuit in fig. 2 r_{12} , r_{13} are resistances of transformers 1-2 and 1-3 referred to the secondary side, z_{L1} , z_{L2} are secondary load impedances. We also introduce dependent sources of EMF $\frac{r_1}{k_{12}k_{13}} I_2$ and $\frac{r_1}{k_{12}k_{13}} I_3$ (r_1 is an

active resistance of the primary winding). They take into account the change of the voltage at the terminals of the winding 3 and 2 due to a primary winding voltage drop of the transformer 1-3 and 1-2. The magnetic leakage fields in transformers 1-2, 1-3 (short-circuit tests for transformers 1-2, 1-3) was modelled by 2D FEA software QuickField [5]. From the FEA model we evaluate parameters L_{12} , r_{12} , L_{13} , r_{13} in the equivalent circuit. For evaluating the magnetic leakage mutual inductance M we made the FEA simulation of another short-circuit field in transformer 2-3 [2]. Calculation of electromagnetic processes in the scheme in fig.1 is made using the Microcap [4] software. The mathematical model was developed to analyze electromagnetic compatibility for welders, the load of which was given above. The model makes it possible to calculate electromagnetic processes and to analyze the harmonic composition of currents and voltages in any component of resistance welders having various circuit configurations and wide power and frequency ranges.

VI. AN EXAMPLE OF APPLICATION OF MATHEMATICAL MODEL FOR ANALYSIS OF ELECTROMAGNETIC NOISE GENERATED BY MEDIUM-POWER RESISTANCE WELDER

The above mathematical model is used to calculate electromagnetic processes in the thyristor inverter welding source for a flashing butt resistance welder which is intended for large-diameter steel gas and oil pipeline construction.

This source has no single-phase two-half-period rectifier. The welder's power is supplied from the mains transformer having the rated power 650 kVA, the secondary linear voltage 380 V, and the length of current-carrying wires from the welder to the transformer about 100 m.

The source is rated at 250 kVA, the inverter frequency ranges from 50 Hz to 100 Hz, and the rectified voltage is 400-430 V. The capacitance of the capacitor bank varies from 25,000 to 75,000 μF . The principal object of such calculations is to analyze the effect of medium-power flashing butt welders on most common shop networks.

Calculation of electromagnetic processes were carried out for different flashing stages modeled by the above equivalent circuit for the flashing zone.

Proceeding from the above calculations effective values for network current, voltage and power consumed in a variety of flashing stages were obtained.

In flashing, total power consumption from the mains varies by a factor of 3.2.

Calculations show that, in all flashing stages, deviations of effective values for phase currents in the mains account for 17% with 30,000 μF filter capacitance, or 10% with 75,000 μF filter capacitance. Momentary voltage surges caused by variations in the welder's load condition amount to 60 V. The coefficient of voltage distortions constitutes 16% for 50,000 μF filter bank capacitance and 15% for 75,000 μF filter bank capacitance.

The results of calculations were correlated with experimental data. Electrical characteristics of the welding process were recorded by mirror-galvanometer oscillographs, ammeters, voltmeters, and wattmeters. Shunts were used as sensors in oscillograph recording. A correlation between calculated and measured data demonstrated the capability of the mathematical model to find with a practical accuracy effective values for currents and voltages in different components of power sources and welder's circuits, and pulsations of power consumption in the welding processes.

The present analysis permits conclusion that power supply to the flashing butt welders through the converters of three-phase mains voltage to single-phase square-wave voltage can provide a uniform loading of mains phases. Such power supply smoothes pulsations in the mains currents and voltages, but does not actually reduce the nonuniformity of power consumption in various flashing stages.

VII. CONCLUSION

The present paper reports a mathematical model for analysis of electromagnetic noise generated by flash resistance welders and their power sources. The model permits estimation of load asymmetry for power source phases, nonuniformity of power consumption in welding, harmonic composition of currents and voltages in any circuit component, and voltage drops at welder's power source input.

For the flashing zone of welded parts an equivalent circuit is suggested obtained from analysis of experimental curves for currents and voltages reflecting their principal physical processes.

The calculated parameters of electromagnetic processes were corroborated by experimental data obtained for the inverter power source of steel pipe flash butt welders.

The mathematical model provides a broad spectrum of possibilities for studies on electromagnetic compatibility of various welders and power sources.

REFERENCES

- [1] S.I. Kuchuk-Yatsenko et al., Resistance Butt Welding of Pipelines, "N&ukova Dumka", Kiev, 1986, 205 p.
- [2] B.E. Paton, V.K. Lebedev. Electrical Equipment for Resistance Voiding, "Mashinostroyeniye", Moscow, 1960, 440 p.
- [3] L.I. Sakhno. On equivalent circuit of a three-winding transformer. *Elektrichestvo*, No 8, 2003, p.25-33.
- [4] Claycomb J. R. Applied Electromagnetics Using QuickField and MATLAB. – *Laxmi Publications, Ltd.*, 2010.
- [5] A. Vladimirescu The SPICE Book, *John Wiley & Sons, Inc.*, First Edition, 1994W.-K. Chen, *Linear Networks and Systems* (Book style). Belmont, CA: Wadsworth, 1993, pp. 123–135.

L.Sakhno graduated from the Electromechanical Faculty of the Leningrad Polytechnical Institute (LPI) in 1974. In 2006 she received the degree of Doct. Techn. Sci from the LPI. Her thesis dealt with the analysis and development of theoretical methods for calculation of welding transformers. She is a professor at St. Petersburg State Polytechnic University, Department of Theoretical Electroengineering.

O.Sakhno graduated from the Electromechanical Faculty of the Leningrad Polytechnical Institute (LPI) in 1974. In 1983 she received the degree of Cand. Techn. Sci from the LPI. Her thesis dealt with the analysis and development of theoretical methods for calculation of electric network electromagnetic processes. She is a lecturer at St. Petersburg State Polytechnic University, Department of Mathematics.

Application of multiobjective optimization methods for power system state control

Nikolay V. Korovkin N., Mikhail V. Odintsov, Dmitry A. Akimov, Oleg V. Frolov
Theoretical Electrical Engineering dept. St.Petersburg State Polytechnical University, Russia
JSC «Scientific and Technical Center of Unified Power System», Sankt-Peterburg, Russia

Abstract—In this article the possibility of application of multiobjective optimization methods for power system state control is considered. Search of Pareto set and analysis of results for electrical power system state control and dispatching are made for equivalent circuits of several real schemes of Russian UPS parts.

Keywords—genetic algorithm, multiobjective optimization; power flow optimization, quality vector criterion.

I. INTRODUCTION

Usually the problem of power system state optimization is considered as a problem of electrical energy generation and transfer cost minimization, i.e. as a problem with a scalar quality criterion. The decision is performed consequently – firstly the optimal power generation distribution between power plants is found, and then reactive power flows are optimized. Other important state characteristics are considered as constant and functional constraints [1-3]. This approach is mostly caused by the lack of multiobjective optimization effective methods and calculation means for power system state optimization problem.

However power system steady state could be effectively characterized by several quantity and quality criteria of its effectiveness. Possible sets of such criteria are shown in [4-7].

In such cases vector criterion is often converted to a scalar one with use of linear (1) or minimax (2) contraction with further use of scalar optimization methods. This approach allows to get only one decision [8], and in this case it will depend on taken weight coefficients set.

$$J(\mathbf{x}) = \sum_{i=1}^N f_i(\mathbf{x}) \rightarrow \min_{\mathbf{x} \in D} \quad (1)$$

$$J(\mathbf{x}) = \max_i \alpha_i (f_i(\mathbf{x})) \rightarrow \min_{\mathbf{x} \in D} \quad (2)$$

where $f_i(x)$ is a partial objective functional set, D – acceptable

N. V. Korovkin is with the Theoretical Electrical Engineering dept. St.Petersburg State Polytechnical University, Russia (corresponding author to provide phone: +7(921)303-40-64; e-mail: nikolay.korovkin@gmail.com).

M. V. Odintsov is with the Theoretical Electrical Engineering dept. St.Petersburg State Polytechnical University, Russia (corresponding author to provide phone: +7(921)977-17-58; e-mail: mixaodintsov@rambler.ru)

D. A. Akimov is with the JSC «Scientific and Technical Center of Unified Power System», Sankt-Peterburg, Russia (corresponding author to provide phone: +7(904)619-54-70; e-mail: akimovdmitry1@yandex.ru).

O. V. Frolov is with the JSC «Scientific and Technical Center of Unified Power System», Sankt-Peterburg, Russia.

solutions set, a – weight coefficient, N – number of objective functionals.

The use of Pareto set looks more promising [8],[9] for the search of decision of multiobjective optimization problem solution.

The aim of this article is consideration and analysis of the use of Pareto set and multiobjective optimization methods for power system state control.

II. PARETO SET

A. Pareto optimal solutions

Multiobjective (or vector) optimization is an optimization process of two or more conflicting objective functions in a determined definition domain. The multiobjective optimization problem consists of vector goal variables search, satisfying imposed restrictions and optimizing vector function, whose elements correspond to goal functions.

Multiobjective optimization problem is divided usually by two subtasks – the Pareto set search and decision making from Pareto set.

Pareto optimal solution is the solution from the multitude of admissible solutions where the improvement is impossible within the range of admissible solutions without deterioration of another criterion. Let us introduce the notion of “dominancy”. One solution is dominating the other, if it is better upon one of the criteria at least and is not worse than the second one. The multitude of Pareto optimal solutions forms Pareto multitude. The representation of Pareto multitude in criteria range is called Pareto front.

Mathematically Pareto set is defined as (3).

$$D_\pi = \{\mathbf{x} \in D \mid \forall \mathbf{x}' \in D \Rightarrow f_i(\mathbf{x}') \leq f_i(\mathbf{x}), i \in [1..k]\} \quad (3)$$

$$F(D_\pi) = P$$

where D_π – Pareto set, P – mapping of Pareto set in goal functionals space.

The notions of dominancy and Pareto front are explained on Fig. 1 for the case of two criteria.

The solution A is dominating solutions D_1, D_2, D_3 and is dominated by solutions P_1, P_2 . In their turn solutions P_1, P_2, P_3, P_4 constitute Pareto multitude with the respective Pareto front.

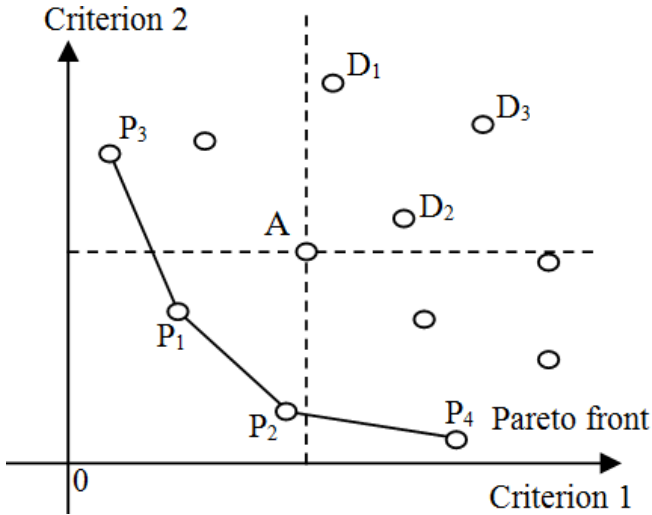


Fig. 1 Pareto front and “dominancy”

From the definition of Pareto set follows that optimal solution of multiobjective optimization problem should be chosen from that set. The decision making from Pareto set is made by a decision-maker (DM) and is grounded on his or her subjective estimate of quality criteria and their relationship.

B. Pareto set search methods and

These methods are usually used for Pareto set search:

Analytical methods are a search of counter-monoteness domains $f_i(x)$ [11]. Further surfaces contact condition is used for Pareto optimal decisions search, which causes a system of linear equations (4)

$$\text{grad}f_1(\mathbf{x}) = -\lambda \text{grad}f_2(\mathbf{x}) \quad (4)$$

The use of analytical methods for power system state optimization has many difficulties often because of big amount of functional and linear restrictions and impossibility of partial derivatives for criteria calculation.

Numerical methods demand a lot of partial objective functionals calculation and big machine time. As a numerical method these techniques could be used:

Random search does not demand continuity or differentiability of a function, it is grid simulation or functionals calculation with random input variables. It demands many calculations of goal functionals.

Guided search includes different methods of linear and stochastic optimization. Methods of linear or minimax contractions are often used for Pareto set search, making an optimization process for different weight coefficients sets.

Considerable attention is currently being focused on use of genetic algorithms for multiobjective optimization [12-15].

III. APPLICATION OF MULTIOBJECTIVE OPTIMIZATION FOR POWER SYSTEM UES STATE CONTROL

A. Example 1

As a test task 1 for multiobjective optimization the problem of optimal settings of phase-shifting transformer (PST), installed at substation 500 kV Ulke in Aktobe region of

Kazakhstan [16], choice. This PST is one of a few PSTs, installed on the territory of the Commonwealth of Independent States (CIS). The quantity of possible PST settings is 289 items, hence Pareto set could be found by a simple exhaustive search. Results are presented on the figure 1.

The following criteria were taken:

- increase of power flow on an overhead line 500 kV, to which PST is connected;
- decrease of active power losses;
- decrease of voltage deviation from defined value.

Pareto front for all criteria is shown on fig 2a. With use of criteria 1 and 2 the amount of Pareto optimal solutions is 100 items (fig.2b). Pareto set includes a big amount of decisions, because these criteria conflict with each other: increase of active power flow leads to increase of active power losses. With use of big numbers of booster transformer taps active power flow control can be done with less discreteness. One value of power flow (for example, 250 MW)

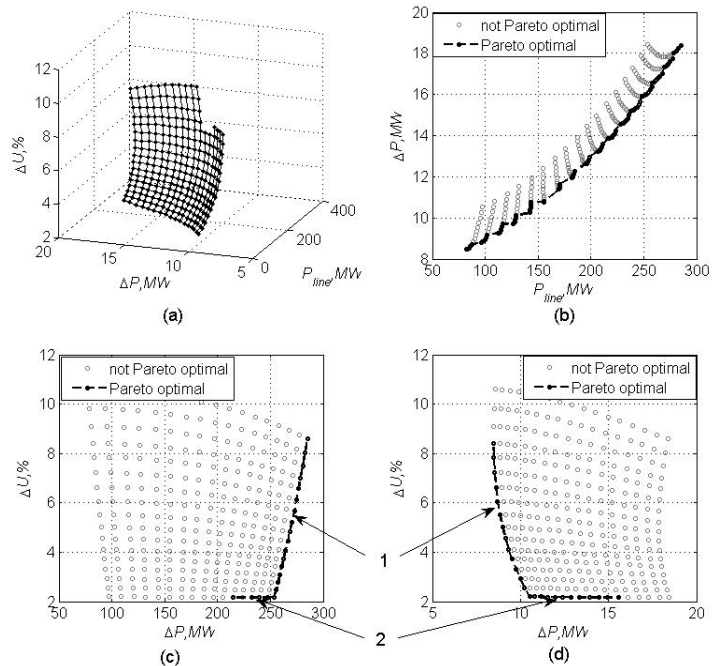


Fig. 2 Pareto front and its projections for example 1 can correspond to several different booster transformer and autotransformer tap changer combinations, however only one of these decisions is optimal. In the test task active losses decrease is about 0,7-1,7 MW, if we take Pareto optimal solution (with an active power flow 250 MW).

With use of criteria 1 and 3 the amount of Pareto optimal solutions is 21 items (fig.2c), for criteria 2 and 3 – 25 items (fig.2d). Relatively small Pareto set size is explained by relationship between these criteria, for criteria 1 and 2 – increase of power flow on overhead line 500 kV leads to decrease of voltage at the electric section 110 kV and at the load, for criteria 2 and 3 – decrease of voltage leads to increase of active power transfer losses.

Part 1 of Pareto front is an optimal for PST settings choice (considering chosen criteria), because it provides smooth

change of controlled parameters. Part 2 of Pareto front, even though is located in Pareto front, is not optimal – with these settings a small state change leads to sharp worsening of one of criteria (sharp losses increase) or exit of the state from the optimal zone.

With use of scalar optimization $\Delta U \rightarrow \min$ the decision on the part 2 will be got as an optimal, that shows inefficiency of that method in this situation.

B. Example 2

The aim of example 2 was a comparison of effectiveness of genetic algorithms for multiobjective optimization use to the random search methods. Algorithm NSGA-2 was taken as an example of genetic algorithm. Results are presented on the fig.2.

As a test scheme Kola electrical power system was taken, consisting of 452 nodes and 573 branches with a summary load 1900 MW. The power losses decrease and voltage deviation from nominal value in the load nodes were taken as the criteria. As variable parameters the value of reactive power generation of generators (13 nodes) and load tap changer setting of transformers (14 nodes) were taken.

The solution of this task by grid simulation method or simple exhaustive search is impossible due to big amount of variables. Therefore random input variables calculation is taken as a random search.

Results of the calculation (fig.3) show, that use of genetic algorithms give a big advantage in comparison to random search methods, because even 1000 calculations with use of NSGA-2 is much more effective than random search after 25000 calculations.

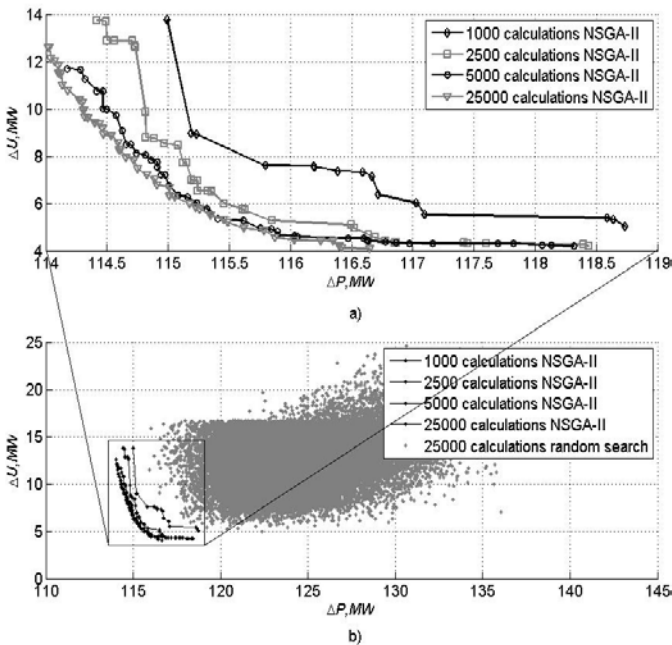


Fig. 3 Pareto front and it's projections for example 3

C. Example 3

The aim of example 3 was to estimate a possibility of getting Pareto front with use of three criteria for a big scheme.

As a test scheme equivalent circuit of North-West and Central parts of Russian UPS, electrical power systems of Baltia and Belarus. The scheme consists of 2044 nodes and 4009 branches with a summary load 52499 MW.

Active and reactive power generation of thermal and hydraulic power plants are taken as variables, and power active losses, power flow to "Center EPS" increase, power flow between "North-West EPS" and "Baltia EPS" decrease are taken as criteria in this example.

The received with use of NSGA-2 and after 25000 calculations Pareto front is presented at figure 4.

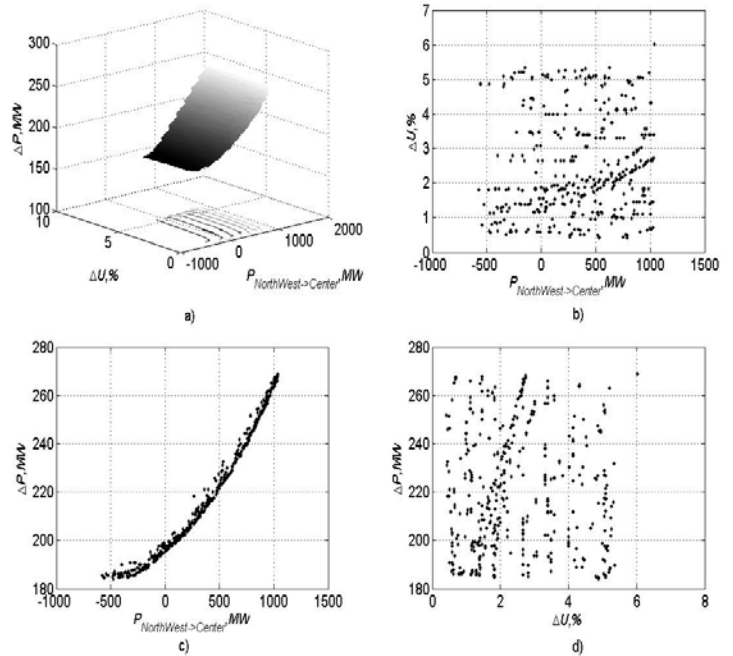


Fig. 4 Pareto front and it's projections for example 3

In this case Pareto front is a convex surface. The analysis of Pareto front projection to functional of voltage deviation and power flow "North-West EPS" → "Center EPS" surface shows, that it is possible to get minimal voltage deviation with any value of power flow "North-West EPS" → "Center EPS".

Projection to the voltage deviation and power losses axes is similar to the mentioned above one – it is possible to get power losses minimum with any deviation level.

Also an analysis of Pareto front projection to power losses and power flow "North-West EPS" → "Center EPS" axes shows a clear relationship between power losses and power flow "North-West EPS" → "Center EPS".

The received results show, that for this task it is advisable to define power losses and power flow levels, and then it is possible to uniquely say, what minimal voltage deviation can be received. It can be explained by the relationship between power losses, power flow and active power generation, and the relationship between voltage deviation and reactive power generation.

IV. CONCLUSION

Different examples of multiobjective optimization of power system states are considered for equivalent circuits of real

electrical networks. The expediency of using multicriteria optimization is shown.

For problems with a large number of input variables is shown the possibility of using multicriteria genetic algorithms for searching Pareto set.

REFERENCES

- [1] V.A. Venikov, "Electrical systems. Electrical networks" vol. 2, 1971, 440 p.
- [2] Idelchik V.I., "Electrical systems and networks", 1989, 592 p.
- [3] Acha E. Fuerte-Esquivel C. Ambriz-Perez H., "FACTS: Modelling and Simulation in Power Networks", England: John W&Ss LTD, 2004, 403 p.
- [4] Korovkin N.V., Frolov O.V., "A new approach to the study of modes of operation of EPS", Proceedings of the 83rd International Scientific Seminar "Methodical research questions of reliability of large electric power systems" named Rudenko Y.N., Ivanovo, 2011.
- [5] Belyaev N.A., Korovkin N.V., Frolov O.V., Chudnyy V.S., "Using bilinear theorem for solving optimization power flows in EPS", "Electrical systems and systems controlling", 2012, №1, pp 77–80.
- [6] Korovkin N.V., Chechurin V.L., Hayakawa M., "Inverse problems in electric circuits and electromagnetics", Springer, 2007, 332 p.
- [7] Van Hertem D., Rimez J., Belmans R., "Power Flow Controlling Devices as a Smart and Independent Grid Investment for Flexible Grid Operations: Belgian Case Study", IEEE Transactions on Smart Grid, Vol. 4, No. 3, September 2013, pp.1656-1664;
- [8] Luke S., "Essentials of Metaheuristics. A Set of Undergraduate Lecture Notes", [Online]. Available: <http://cs.gmu.edu/~sean/book/metaheuristics/Essentials.pdf>
- [9] Chernorutskiy I.G., "Decision making methods", Saint-Petersburg, 2005, 416
- [10] Podinovskii V.V., Noghin V.D. "Pareto-optimal solutions of multicriterion problems", Moscow, Science, 1982, 256 p.
- [11] Romanova I.K., "Application of analytical methods to Pareto optimal control systems research", 04.04.2014, [Online]. Available: <http://technomag.bmstu.ru/doc/704897.html>
- [12] C.M Fonseca, P.J. Fleming, "Genetic Algorithms for Multiobjective Optimization: Formulation, Discussion and Generalization", [Online]. Available: http://pdf.aminer.org/000/310/607/genetic_algorithms_for_multiobjective_optimization_formulationdiscussion_and_generalization.pdf
- [13] K. Deb, A. Pratap, S. Agarwal, T. Meyarivan, "A Fast and Elitist Multiobjective Genetic Algorithm: NSGA-II", [Online]. Available: http://www.iitk.ac.in/kangal/Deb_NSII.pdf
- [14] E. Zitzler, M. Laumanns, L. Thiele, "SPEA2: Improving the Strength Pareto Evolutionary Algorithm", [Online]. Available: <http://www.kddresearch.org/Courses/Spring-2007/CIS830/Handouts/P8.pdf>
- [15] D. W. Corne, J.D. Knowles, M. J. Oates, "The Pareto Envelope-based Selection Algorithm for Multiobjective Optimization", [Online]. Available: <https://www.macs.hw.ac.uk/~dwcorne/pesa.pdf>
- [16] Evdokunin G.A., Nikolaev R.N., Iskakov A.K., Ospanov B.K. Utegulov N.I. Phase-shifting transformer first in CIS is used in Kazakhstan [Text]. News of electrotechnik. - 2008, №6(48). – C. 38-41;

Parameters of the polymerization process of error in determining the thermochemical characteristics insulation

Yuliya V. Koroleva, Evgeniya V. Ivanova and Pavel A. Strizhak

Abstract—In this article the question of simulation of no stationary process in the polymerization of cable product is considered. The model allows predicting time of full polymerization rubber shell. There are shows the dependence of the polymerization time of thermochemical characteristics.

Keywords—cable product, mathematical modeling, polymerization, rubber.

I. INTRODUCTION

THERE are can allocate a large enough group of studies on the mechanical, thermal, thermochemical and other characteristics of the insulation materials and manufacturing processes of macroscopic regularities cable products with their use. For basic types of rubbers used in the cable industry, the value of the thermochemical characteristics is usually determined with an accuracy of up to $\pm 12\%$ [1].

The aim of this work is the development of predictive models for the theoretical analysis of the dependence of integral parameters of the polymerization process in the manufacture of a typical cable products from errors in the determination of the thermochemical characteristics of insulating materials.

II. PROBLEM STATEMENT

In numerical simulations using a system "heating chamber - air - insulation shell - cable core" diagram is shown in Fig. 1. Statement of the problem under consideration is the development of heat and mass transfer model [2]. In contrast to [2], the movement of the products within the heating chamber and leaks at the inlet and outlet.

This work is performed with financial support from the Russian Foundation for Basic Research (project No. 2.1321.2014).

Yuliya V. Koroleva is with the National Research Tomsk Polytechnic University, Tomsk, Russia (corresponding author to provide phone: 8-903-952-62-69; e-mail: zhenya1@tpu.ru).

Evgeniya V. Ivanova is with the National Research Tomsk Polytechnic University, Tomsk, Russia (e-mail: vasilisa1@sibmail.com).

Pavel A. Strizhak is with the National Research Tomsk Polytechnic University, Tomsk, Russia (e-mail: pavelspa@tpu.ru).

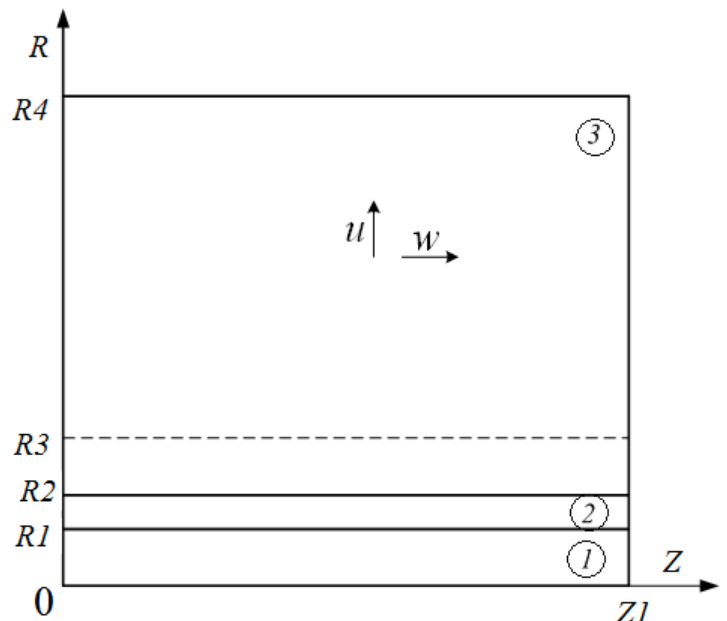


Fig. 1. Scheme for solving the problem in the region $0 \leq t \leq t_p$: 1 - core cable, 2 - cable-3 - the air in the heating chamber; u, w - component of the velocity of convective flow in the chamber

It was believed that the cable consists of strands 1 and shell 2. Product with an initial temperature T_0 and constant velocity w_c moves through the heating chamber. The shell is heated at a significantly high temperature 3. Low arch chamber (initial temperature of air in the chamber) T_v taken much more T_0 . Accounted leakage calandria inlet ($R_2 < R < R_3, Z = 0$) and exit ($R_2 < R < R_3, Z = Z_1$) - influx of relatively cool ambient air at a temperature T_h and $T_v \ll$ speed w_c .

The main characteristic of the studied complex physical and chemical processes in the system (fig. 1) is the fullness of the polymerization is completed in the insulating layer. The term "full cure" [1] involves the completion of a chemical process in the insulating layer to the condition $\varphi = 0.99 \div 1$ (φ - the degree of completeness the main chemical reaction at a given initial value φ_0).

III. MATHEMATICAL MODEL AND METHOD OF SOLUTION

The system of differential equations of unsteady heat transfer in a partial system "heating chamber - air - insulation shell - core cable" (Fig. 1), corresponding to the physical formulation of the problem formulated, has the following form.

Heat conduction equation for the cable core ($0 < R < R1$, $0 < Z < Z1$):

$$\rho_1 C_1 \frac{\partial T_1}{\partial t} = \lambda_1 \left(\frac{\partial^2 T_1}{\partial R^2} + \frac{1}{R} \frac{\partial T_1}{\partial R} + \frac{\partial^2 T_1}{\partial Z^2} \right). \quad (1)$$

The energy equation for cable insulation shell ($R1 < R < R2$, $0 < Z < Z1$):

$$\rho_2 C_2 \frac{\partial T_2}{\partial t} = \lambda_2 \left(\frac{\partial^2 T_2}{\partial R^2} + \frac{1}{R} \frac{\partial T_2}{\partial R} + \frac{\partial^2 T_2}{\partial Z^2} \right) + q_2 \rho_2 \frac{d\varphi_2}{dt}, \quad (2)$$

$$\text{when } \frac{d\varphi_2}{dt} = (1 - \varphi_2) k_2^0 \exp\left(-\frac{E_{a2}}{R_t T_2}\right). \quad (3)$$

Poisson equation for the air in the heating chamber ($R2 < R < R4$, $0 < Z < Z1$):

$$\frac{\partial^2 \psi}{\partial R^2} - \frac{1}{R} \frac{\partial \psi}{\partial R} + \frac{\partial^2 \psi}{\partial Z^2} = -r\omega. \quad (4)$$

The equation for the vortices of the air in the heating chamber ($R2 < R < R4$, $0 < Z < Z1$):

$$\begin{aligned} \frac{\partial \omega}{\partial t} + u \frac{\partial \omega}{\partial R} + w \frac{\partial \omega}{\partial Z} - \frac{\omega u}{R} = \\ = \nu_3 \left(\frac{\partial^2 \omega}{\partial R^2} + \frac{1}{R} \frac{\partial \omega}{\partial R} + \frac{\partial^2 \omega}{\partial Z^2} - \frac{\omega}{R^2} \right) + g\beta \frac{\partial T_3}{\partial R} a. \end{aligned} \quad (5)$$

The energy equation for air in the heating chamber ($R2 < R < R4$, $0 < Z < Z1$):

$$\begin{aligned} \rho_3 C_3 \left(\frac{\partial T_3}{\partial t} + u \frac{\partial T_3}{\partial R} + w \frac{\partial T_3}{\partial Z} \right) = \\ = \lambda_3 \left(\frac{\partial^2 T_3}{\partial R^2} + \frac{1}{R} \frac{\partial T_3}{\partial R} + \frac{\partial^2 T_3}{\partial Z^2} \right). \end{aligned} \quad (6)$$

Initial ($t = 0$) conditions: $T_1 = T_0$ by $0 \leq R < R1$, $0 \leq Z \leq Z1$; $T_2 = T_0$ and $\varphi = \varphi_0$ by $R1 \leq R \leq R2$, $0 \leq Z \leq Z1$; $T_3 = T_v$ by $R2 < R < R4$, $0 \leq Z \leq Z1$.

The boundary conditions for $0 < t \leq t_p$:

$$Z=0, Z=Z1, 0 \leq R < R1 \quad \frac{\partial T_1}{\partial Z} = 0;$$

$$Z=0, Z=Z1, R1 \leq R \leq R2 \quad \frac{\partial T_2}{\partial Z} = 0;$$

$$Z=0, Z=Z1, R2 < R < R3 \quad T_3 = T_h, \quad \frac{\partial \psi}{\partial Z} = 0, \quad \frac{\partial \psi}{\partial R} = -w_c R;$$

$$Z=0, Z=Z1, R3 \leq R \leq R4 \quad \frac{\partial T_3}{\partial Z} = 0;$$

$$R=0, 0 \leq Z \leq Z1 \quad \frac{\partial T_1}{\partial R} = 0;$$

$$R=R1, 0 \leq Z \leq Z1 \quad -\lambda_1 \frac{\partial T_1}{\partial R} = -\lambda_2 \frac{\partial T_2}{\partial R}, T_1 = T_2;$$

$$R=R2, 0 \leq Z \leq Z1 \quad -\lambda_2 \frac{\partial T_2}{\partial R} = -\lambda_3 \frac{\partial T_3}{\partial R}, T_2 = T_3, \psi = 0,$$

$$\frac{\partial \psi}{\partial Z} = w_c R;$$

$$R=R4, 0 \leq Z \leq Z1 \quad T = T_v, \psi = 0, \quad \frac{\partial \psi}{\partial Z} = 0.$$

Here ρ - density, kg/m^3 ; C - heat capacity, $\text{J} / (\text{kg} \cdot \text{K})$; T - temperature, K ; t - time, s ; λ - thermal conductivity, $\text{W} / (\text{m} \cdot \text{K})$; R, Z - coordinates of the cylindrical coordinate system, m ; q_2 - the thermal effect of the polymerization reaction, J / kg ; φ - the degree of polymerization; k_2^0 - pre-exponential factor of the chemical reaction, s^{-1} ; E_{a2} - activation energy of a chemical reaction, J / mol ; R_t - the universal gas constant, $\text{J} / (\text{mol} \cdot \text{K})$; ψ - stream function, m^3 / s ; ω - the vortices vector, s^{-1} ; u, w - component of the velocity of the heated air into the chamber, m / s ; ν - kinematic viscosity, m^2 / s ; g - acceleration of gravity, m/s^2 ; β - a thermal expansion coefficient, K^{-1} ; T_0 - initial temperature of the conductor and the cable sheath, K ; T_v - initial temperature in the chamber, K ; codes "1", "2", "3" correspond to the conductor, the cable sheath and the air in the chamber.

Similarly, setting [2] investigated the numerical analysis of physico-chemical processes using this model (Fig. 1) is made under the following assumptions do not impose significant restrictions on the generality problem statement:

1. Contact between a conductor and a layer of insulating material is ideal. In industries [1] this factor is given special attention. Acceptable dimensions of the gaps, as a rule, do not exceed 0.01 mm [1].

2. Cable has a right cylindrical shape. From the variety of possible configurations of cable products [3] extended along the axis of symmetry of the cylinder can be considered the most typical.

The system of nonlinear nonstationary differential equations (1) - (6) with appropriate boundary conditions is solved by finite difference method [4]. Difference analogues of differential equations (1) - (6) are solved locally one-dimensional method [4]. For solving nonlinear equations are used the method of iterations [4]. To assess the reliability of the results of numerical simulation algorithms are used [5], based on the verification of the conservativeness of difference schemes used.

IV. RESULTS AND DISCUSSION

Numerical simulations were performed for the following parameters: $\rho_1=8700 \text{ kg/m}^3$; $\lambda_1=400 \text{ W/(m}\cdot\text{K)}$; $C_1=385 \text{ J/(kg}\cdot\text{K)}$; $\rho_2=1200 \text{ kg/m}^3$; $\lambda_2=0,16 \text{ W/(m}\cdot\text{K)}$; $C_2=1380 \text{ J/(kg}\cdot\text{K)}$; $\rho_3=1,161 \text{ kg/m}^3$; $\lambda_3=0,026 \text{ W/(m}\cdot\text{K)}$; $C_3=1190 \text{ J/(kg}\cdot\text{K)}$; $v_3=1\cdot 10^{-5} \text{ m}^2/\text{s}$; $T_0=303 \text{ K}$; $T_v=450 \text{ K}$; $T_h=300 \text{ K}$; $k_2^0=4,9\div 5,1\cdot 10^5 \text{ s}^{-1}$; $E_{a2}=4,95\div 5,05\cdot 10^4 \text{ J/mol}$; $q_2=0,9\div 1,1\cdot 10^3 \text{ J}$; $\varphi_0=0,4$; $R1=0,002 \text{ m}$; $R2=0,004 \text{ m}$; $R3=0,006 \text{ m}$; $R4=0,01 \text{ m}$; $Z1=0,1 \text{ m}$; $w_c=0,1 \text{ m/s}$; $R_t=8,314 \text{ J/(mol}\cdot\text{K)}$; $g=9,8 \text{ m/s}^2$; $\beta=0,001 \text{ K}^{-1}$.

There is a significant drop in temperature of the product at the inlet and outlet of the heating chamber. Found that by minimizing w_c (as a consequence, increasing the residence time of the products in the heating chamber) and the sizes of input and output openings in the chamber impact of this effect can be practically excluded.

Table 1 shows the full polymerization time depends on the temperature of the heating chamber set for the three materials with different characteristics of the polymerization process (k_{20} , E_{a2} , q_2).

TABLE I. TIME DEPENDENCE OF THE CABLE SHEATH FULLY CURED PRODUCT DEPENDING ON THE TEMPERATURE OF THE ARCH CHAMBER, s

Temperature of the furnace roof, K	$E_{a2}=5,05\cdot 10^4 \text{ J/mol}$, $k_2^0=5,1\cdot 10^5 \text{ s}^{-1}$, $q_2=1,1\cdot 10^3 \text{ J/kg}$	$E_2=5\cdot 10^4 \text{ J/mol}$, $k_2^0=5\cdot 10^5 \text{ s}^{-1}$, $q_2=10^3 \text{ J/kg}$	$E_{a2}=4,95\cdot 10^4 \text{ J/mol}$, $k_2^0=4,9\cdot 10^5 \text{ s}^{-1}$, $q_2=0,9\cdot 10^3 \text{ J/kg}$
450	337,9	358,7	380,1
465	312,4	331	350,1
480	292,2	307,7	326,4

There are found that even a relatively small change k_{20} , E_2 and q_2 (within 15%) can result in significant (30%) integrated deviations polymerization characteristics (in particular, the time t_p) and, as a result, deterioration of the insulation product.

For example, it is known that "sub cooling" or "overheating" in the manufacture of insulating sheath of cables due to lower or, respectively, the large time of their stay in the heating chamber with respect to the required values of t_p , reduces the degree of polymerization of φ or material destruction and other negative consequences (at a temperature above 373 K for most intense starting rubber thermal decomposition process, combustible gases are allocated, and the components of the rubber composition reacts exothermically with oxygen).

Therefore, for the most efficient completion of the polymerization process with high-quality products must be as accurate as possible to determine the kinetic parameters of the polymerization. Thus, using the model (1) - (6) found that when deviations values k_{20} , E_{a2} and q_2 relative to the nominal corresponding rubber, within 5% change cured not exceed 8%. With such abnormalities t_p change the values φ does not reach 4% relative to $\varphi = 0.99$.

V. CONCLUSION

Performed numerical studies have shown that even a relatively small error in the determination of basic kinetic parameters of polymerization (within 15%) can lead to quite significant (30%) deviations of the integral characteristics of the process (table 1).

A predictive model of heat and mass transfer (1) - (6) can be used to analyze the quality of the insulation of cable products and energy efficiency of polymerization processes for their manufacture.

REFERENCES

- [1] Lukomskaya A.I., Badenkov P.Ph., Kepersha L.M. Thermal curing basis of rubber products. M.: Chemistry. 1972. 359 p. (In Russia)
- [2] Ivanova E.V., Kuznetsov G.V. Numerical modeling of temperature fields in cylindrical articles during vulcanization // Journal Of Chemical and Petroleum Engineering, Volume 47, Issue 7-8, November 2011, P. 447 – 450.
- [3] P.J. Roache. Computational Fluid Dynamics, Hermosa Publishers, Albuquerque, N. Mex., 1982. 616 p.
- [4] Alexander A. Samarskii. The Theory of Difference Schemes. USA, Marcel Dekker, Inc., 2001. 788 p.
- [5] Y. Jaluria, Natural Convection: Heat and mass transfer, Pergamon Press, 1980. 399 p.

Demand response in residential AC load using rescheduling strategy

Monika Arora, Saurabh Chanana

Abstract—During the recent years, interest in demand response (DR) has been growing. Improving the energy efficiency, ability to allow the connection of renewable resources in the existing power grid and reducing the peak load demand are some important factors that have led to its popularity. Traditionally, demand response programs involve large industrial consumers but with technological advancement, demand response is being implemented for small residential and commercial consumers also. In this paper, aim is to reduce overall energy consumption cost of the residential customers using variable set point technique. Also the paper determines the peak shifting capability of a community of houses provided with HVAC systems. Air conditioners are power intensive appliances and the prime reason of peak load in residential sector in summers. In this paper, an optimization problem has been formulated using variable thermostat set point implemented with the help of programmable communicating thermostat (PCT). A programmable communicating thermostat is a device that uses real time pricing (RTP) signals to control the thermostat setting. Results show that variable thermostat setting can result in reducing the electricity bills and provides the capability of shifting peak load to off peak periods.

Keywords— Demand response, Home energy management, Programmable communicating thermostat, Real-time pricing, Thermostatically controlled appliances.

I. INTRODUCTION

DEMAND response can be defined as the changes in electricity usage by end-use customers from their normal consumption patterns in response to changes in the price of electricity over time [1]. Need of such technique was realized when California energy crisis took place in 2001. It was estimated that a 5% lowering of demand would have resulted in a 50% price reduction during the peak hours of electricity crisis in 2000/2001 (Hirst& Kirby, Sustainable FERC Energy Policy project, Retail Load Participation in Competitive Wholesale Electricity Market report 2001). This situation could have been avoided if the demand response technique

had been in place.

Connection of large number of intermittent power resources such as wind power in distribution network and eliminating the need for building new power plants and expansion of transmission system to supply peak energy demand are some other factors that have led to the growing interest in demand response mechanism.

With competitive energy markets in place, many electricity pricing schemes have been introduced. These are mainly interruptible load, direct load control, real-time pricing and time of use programs (Federal Energy Regulatory Commission, Assessment of demand response and advanced metering Report 2011) etc. RTP is considered to be more effective for DR programs [1].

Demand response technique can provide huge benefits to customers as well as utility. By shifting the load from peak hours to off-peak hours, electricity bill of the consumer can be reduced. Reducing the peak energy demand eliminates the need for building new lines and expanding the system. Many DR programs are widely implemented by commercial and industrial customers. DR programs in these sectors are already mature. A very few DR programs are in operation today for residential customers. This work focuses on residential demand response.

In residential load context, individual loads can be categorized into different categories: Thermostatically controlled/Manual, Shiftable/Non-Shiftable, Scheduled interruptible/Uninterruptible etc. [2,3,4]. Thermostatically-controlled appliances (TCAs) such as air-conditioners, heaters and heat pumps contribute to the large portion of the residential loads. By controlling the ON/OFF cycle of these appliances, energy consumption of the customer can be managed. Thermal storage capability of these appliances helps in shifting energy consumption from peak period to off-peak period and also a considerable saving their electricity bills. Therefore thermostatically-controlled devices are taken into consideration in this study. Selection of suitable pricing scheme determines success of such programs.

The literature includes a wide range of work related to residential demand response. Zhu et al. performed benefit analysis of DR and explained the benefits of utility companies, society and customer [5]. Problems due to lack of DR and environmental impacts of DR have also been discussed. Results indicate that tons of coal is saved and emission of harmful gases is also reduced. In [5], a control scheme to reduce peak demand by load shifting has also been

Monika Arora is studying at National Institute of Technology Kurukshetra, Haryana, India. (e-mail: monika.gaba@gmail.com).

Saurabh Chanana is with the Electrical Engineering Department, National Institute of Technology Kurukshetra, Haryana, India. (e-mail: s_chanana@rediffmail.com).

explained. In [2], effects of the load parameters and the direct load control actions have been studied using stochastic difference equation of air conditioner model. In [6], a dynamic demand control mechanism based on frequency linked real-time prices has been proposed. Various set point control strategies were investigated by Nu and Katipamula for thermostatically controlled appliance (water heater taken as an example) [7]. Economic benefits of these control strategies and their effect on feeder load profiles were also obtained. In [8], an optimal and automatic residential energy consumption scheduling framework has been simulated which attempts to minimize the electricity payment and the waiting time for the operation of each appliance in household using Real Time Pricing (RTP) tariff along with inclining block rates. Similarly [9] presents a novel appliance commitment algorithm that schedules thermostatically controlled household loads based on price and consumption forecasts minimizing payment or maximizing comfort. Simulation results show a significant reduction in user payments and peak to average ratio. Saha and Kuzlu demonstrated the inclusion of smart thermostat into Home Energy Management (HEM) System for residential DR implementation [10]. Some advantages of temperature set point control over direct load control have also been discussed. Considering the increasing interest in demand response modelling and analysis, [11] presents the development of physical-based residential load models. [12] presents an intelligent Home Energy management algorithm for managing high power consumption of home appliances. A simulation tool is developed to analyse the demand response capability of this algorithm. In [3], a scheduling mechanism has been proposed for home area load management to minimize peak hourly load in order to achieve optimal daily load schedule. Results show that scheduling mechanism is able to reduce maximum load while satisfying user preference. In [13], a control method is employed to solve the scheduling of smart appliances to achieve maximum cost benefits. Washing Machine, Dish washers, Tumble dryers are considered in the study. [14] addresses the problem of peak load shaving in smart homes in view of improving energy efficiency. A layered architecture of Home Power Management has been introduced. Operation of appliance is modelled as a finite state machine which enables the implementation of online scheduling. Scheduling Algorithm is developed for peak-load shaving. Load shaving is achieved keeping in view the comfort of the customers.

In this paper, an optimization strategy has been proposed for reducing the energy bill of consumers by rescheduling the air conditioning load based on real time price information. At the same time, user preferences and comfort requirements are satisfied. Smart controllers in each house vary thermostat set point as a linear function of Real time price of electricity. In first part of study, reduction in energy consumption and billing for a single household due to proposed strategy has been reported. In next part, a community of residential houses is considered to check the impact of rescheduling strategy on peak demand reduction and peak load shift. Mixed integer

programming is used for solving the optimization problem.

II. RESIDENTIAL DEMAND RESPONSE FRAMEWORK

Implementation of demand response requires implementation of dynamic pricing in open electricity markets. In this work, we are using real time pricing signals to control the energy consumption of air conditioning load. DR requires technologies of smart grid to be in place. First step is to install Smart meters at customer premises. Role of Smart meters is to share the information between customer and the utility. Utility provides real time pricing signal to customer. Smart meter receives this information at customer end and passes on to the home energy management (HEM) system. HEM system contains a controller which can communicate with all the home appliances. Controller houses optimization solvers. It collects information like user settings and preferences from user and performs optimal scheduling of home appliances. This schedule is then communicated to the appliances by controller.

In addition to smart meter, we assume advanced metering infrastructure, two way communication and control system are also in place. A typical architecture of interaction of smart meter with Home energy management system and home appliances is shown in Figure 1. Successes of DR programs ultimately depend upon the acceptance from customer side. Customer and utility both need to be aware of the benefits of participating in DR programs. Customer and utility should be able to invest their money in implementing the smart technology/equipment.

Air conditioner, a thermostatically controlled device, along with programmable communicating thermostat is being used to achieve the objective of reducing overall electricity cost of a house. PCT varies the set point of thermostat such that when demand is high and the price of electricity increases, thermostat set point is raised reducing the peak energy demand. As a result energy consumption cost is reduced. Raising the set point of thermostat for short interval of time may not impact the comfort level of user significantly.

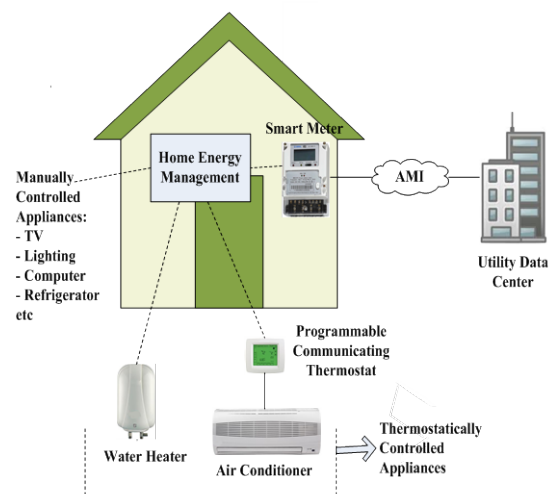


Figure 1: Residential demand response framework

Moreover as a result of application of rescheduling strategy, shift in peak demand of a community of several houses is also observed. This will benefit customer and utility both. Let us go through the modelling of air conditioner and programmable communicating thermostat that has been explained in section 3.

III. MODELLING OF AC AND THERMOSTAT SETTING

A. Model of residential air conditioning load

A lot of work has been done in past to model air conditioner load so as to represent AC behavior accurately. A discrete-time continuous state stochastic model has been developed in [15]. A Markov chain model which reproduces the steady-state features of stochastic nonlinear difference equation has also been reported in [15]. In this study, discrete time model of air conditioner is used as explained in [16]. Model explains the variation of inside temperature of the house with time. Inside temperature at time slot t depends on the inside temperature at previous time slot i.e. $t-1$ and other factors like ON/OFF state of ac thermostat and difference of inside and outside temperature during time slot. ON state of AC thermostat has the effect of decreasing the inside temperature. Difference in outside and inside temperature has the effect of increasing the temperature. The model is as follows:

$$T_{in}(t) = T_{in}(t-1) + \tau \times (E \times (T_{out}(t) - T_{in}(t)) - \phi \times s(t)); \tag{1}$$

Where

$T_{in}(t)$ – Inside Temperature of a house at time slot t

$T_{out}(t)$ – Forecasted Outdoor temperature at time slot t

$s(t)$ – Status of AC at time slot t , binary ON/OFF

E – Warming effect of difference in outside and Inside temperature on inside temperature

ϕ – Cooling effect of ON state of AC on Inside temperature

τ – Time Interval duration

B. Thermostat setting

(i) Normal thermostat control

Conventionally, air conditioner works on a fixed thermostat setting. Let the fixed thermostat setting point be T_{st} . If house temperature exceeds above $T_{st} + \Delta T$ and thermostat is in OFF state, it would be switched ON. Whenever house temperature is less than $T_{st} - \Delta T$ and thermostat is in ON State, it would be switched OFF as shown in Figure 2.

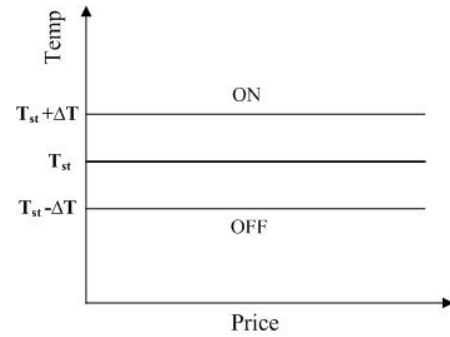


Figure 2 : Thermostat set point in normal thermostat control.

(ii) Rescheduling strategy

Rescheduling strategy introduced here suggests the thermostat set point is varied in such a way that it results in saving in electricity bill without sacrificing user comfort. As per this approach, the thermostat setting varies linearly with change in real time price as described by (2). Thermostat set point variation is graphically shown in Figure 3. Real time price and thus thermostat set point is different during different time slots of the day. Thermostat set point is increased during peak hours when price of electricity is high. Thus in this case, energy consumed in maintaining house temperature during peak hours is reduced due to higher set point. It results in reduction in electricity cost. During any time slot t , house temperature minimum and maximum limits are $T_{st}(t) - \ell$ and $T_{st}(t) + \ell$ respectively. Temperature during any time slot is constrained to be within the minimum and maximum temperature limits.

$$T_{st}(t) = a \times \lambda(t) + b; \tag{2}$$

Where

$T_{st}(t)$ – Thermostat set point of programmable communicating thermostat at time slot t .

$\lambda(t)$ – Real Time price of electricity during time slot t .

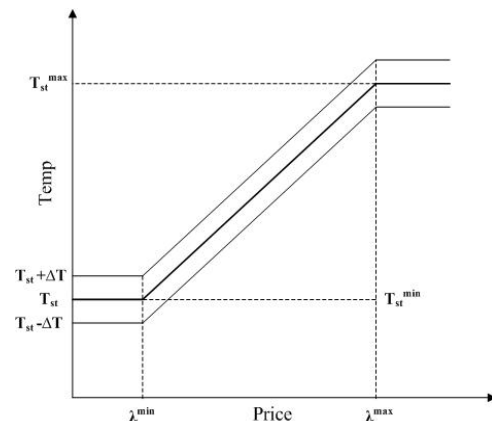


Figure 3: Thermostat variation with RTP in case of rescheduling strategy

IV. PROBLEM FORMULATION

In this section, a mixed integer linear programming formulation of scheduling problem is presented. The objective of problem is to minimize cost of air conditioner load. Objective function of cost includes price signal which is real time price in this case. RTP price may vary throughout the day. Price is higher during the peak hours and less during off-peak hours. Optimization program tries to maximize the electricity usage during off peak hours while reducing the use of electricity during peak hours keeping temperature within a comfortable range. Inside temperature variation of a house with time has been explained in (1). However temperature needs to be constrained within a maximum and minimum range according to user's comfort requirements. Optimization is performed on both the thermostat models mentioned above. One is with normal thermostat control. Maximum and minimum allowable temperature is fixed. Second is rescheduling technique, where thermostat set point varies with price of electricity. Mixed integer problem contains one integer variable $s(t)$. $s(t)$ represents the status of AC thermostat. When thermostat is ON, AC is assumed to draw rated power. In case AC is OFF, AC consumes zero power. Objective function used as follows:

$$\text{Min } C = \sum_t \lambda(t) \times P_{\text{Rated}} \times s(t) \quad (3)$$

For all $t = [1, 2, \dots, N]$;

Where

t - Time slot

N - Total no of time slots.

C - Cost of electricity over the entire time period

$\lambda(t)$ - Real time price of electricity during time slot t

P_{Rated} - Rating of air conditioner inside a house

$s(t)$ - Status of air conditioner thermostat during time slot

t ('0'/'1')

subject to

Equality Constraint:

1 Temperature dynamics of centralized air conditioner of a house.

Temperature of air conditioner varies as described in (1). This equation is mentioned below as well. In (1) ambient temperature, parameters E and ϕ needs to be known. Status

of AC $s(t)$ and inside temperature $T_{In}(t)$ are obtained from this equation. Inside temperature at the start of the period under study needs to be specified.

$$T_{In}(t) = T_{In}(t-1) + \tau \times \left(E \times (T_{Out}(t) - T_{In}(t)) - \phi \times s(t) \right) \quad (4)$$

Symbols have same meaning as explained earlier in section 3.

2 Thermostat setting point

In case of Normal Thermostat control, set point of AC thermostat $T_{st}(t)$ is fixed. Equation representing thermostat setting is shown below:

$$T_{st}(t) = \text{Const.} \quad (5)$$

In rescheduling technique, set point $T_{st}(t)$ varies linearly with price as presented in (6).

$$T_{st}(t) = a \times \lambda(t) + b; \quad (6)$$

3 Minimum and Maximum Thermostat setting Limits

$$T_{min}(t) = T_{st}(t) - \Delta T; \quad (7)$$

$$T_{max}(t) = T_{st}(t) + \Delta T; \quad (8)$$

Where

$T_{min}(t)$ - Minimum temperature limit during time slot t , below which if house temperature falls, thermostat is turned OFF.

$T_{max}(t)$ - Maximum temperature limit during time slot t , above which if house temperature rises, thermostat is turned ON.

Inequality Constraint:

4 ON/OFF status of thermostat

$s(t)$ represents the status of thermostat. Its value can be ON or OFF. $s(t) = '1'$ represents thermostat is ON, '0' represents thermostat is OFF. Thus $s(t)$ is considered as binary variable in the problem.

$$0 \leq s(t) \leq 1; \quad (9)$$

5 Temperature constraints

Temperature inside the house needs to be constrained within minimum and maximum temperature limit (specified in (7) and (8)). Temperature constraint equations have been presented below.

$$T_{min}(t) \leq T_{In}(t) \quad (10)$$

$$T_{In}(t) \leq T_{max}(t) \quad (11)$$

V. RESULTS

In order to demonstrate the utility of proposed rescheduling strategy, in first part of study, reduction in energy consumption for a single household has been observed. In next part, peak load shift property of a community of residential houses (provided with ACs) is considered to check the impact of rescheduling strategy.

MATLAB and GAMS software are used for implementing the program. MATLAB program provides the input variables to GAMS program. Input variables are ambient temperature, real time price of electricity, parameters λ , ϕ and starting temperature etc. The optimization problem is solved using MIP solver –DICOPT in GAMS. Optimization program included electricity cost as objective function, along with temperature dynamics of air conditioner and thermostat setting model equations. For keeping in mind user comfort, temperature is constrained to vary between temperature minimum and maximum limits.

Each time slot in optimization problem is taken as 15 min. The model is run for 24 hours (96 slots). Ambient temperature variation and RTP variation for the day under study is shown in Figure 4 and Figure 5, respectively. This data is based on the day-ahead market price variation at IEX during a typical summer day (Indian Energy Exchange 2013).

A. For single household

In this case, optimization problem is run considering a smart home with centralized air conditioner of 11.5 KW rating. The air conditioning load model parameters λ and ϕ for 15 min interval are taken as .0408 and 2.64 respectively. Electricity cost and user comfort are observed in both Normal Thermostat and Rescheduling techniques.

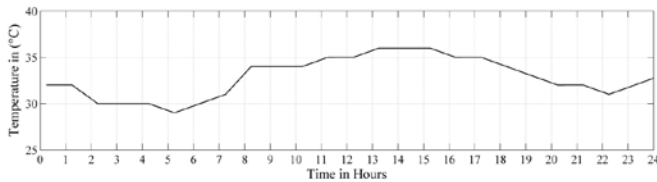


Figure 4 : Variation of ambient temperature with time

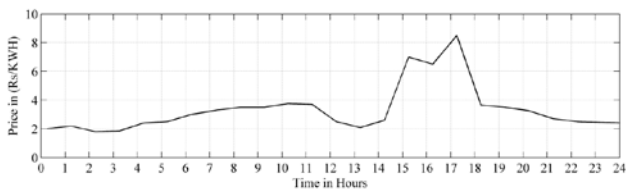


Figure 5 : Variation of RTP with time

B. Normal thermostat control

For Normal thermostat operation, the set point $T = 22 \text{ }^\circ\text{C}$. $\Delta T = 2 \text{ }^\circ\text{C}$. Room Temperature variation and the ON/OFF Status of Air conditioner are shown in Figure 6 and Figure 7 respectively. Status ‘1’ represents ON state, ‘0’ represents

OFF State.

Room temperature remains within $20 \text{ }^\circ\text{C}$ and $24 \text{ }^\circ\text{C}$ temperature limit. Optimal cost of air conditioner comes out to be 557.073 Rs /day.

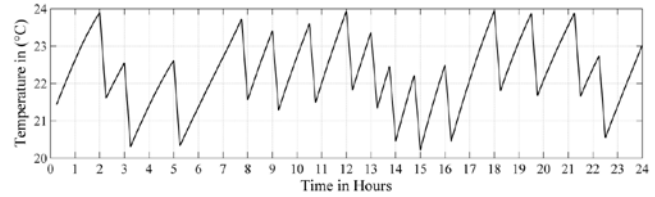


Figure 6 : Variation of room temperature with time in case of normal thermostat control

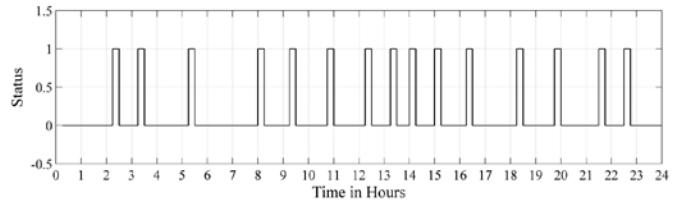


Figure 7 : ON/OFF status of air conditioner in case of normal thermostat control

C. Rescheduling strategy

In this technique, minimum limit of temperature is set constant. Set point varies linearly as shown in (13). $\Delta T = 2 \text{ }^\circ\text{C}$ and maximum limit of temperature varies as displayed in (14).

$$T_{min}(t) = Const = 20 \tag{12}$$

$$T_{st}(t) = 0.89 \times \lambda(t) + 20; \tag{13}$$

$$T_{max}(t) = T_{st}(t) + \Delta T; \tag{14}$$

Room temperature variation and status of air conditioner are as shown in Figure 8 and Figure 9 respectively.

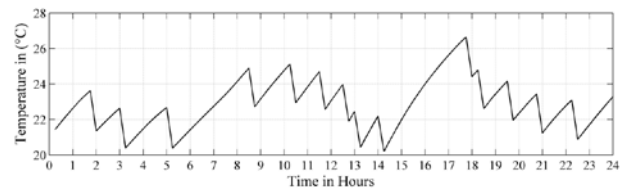


Figure 8 : Variation of room temperature with time in case of rescheduling technique

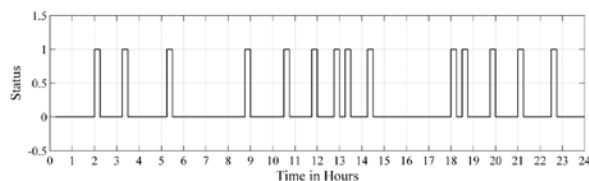


Figure 9 : ON/OFF status of air conditioner in case of rescheduling technique

In this case, optimal cost comes out to be 468.529 Rs/day. A comparison of the results of both these techniques has been performed in Table below.

Table1: Comparison of electricity cost of a single house for normal thermostat control and rescheduling strategy

Function	Temperature Range	Cost (Rs/Day)	% Reduction
$T_{st} = 22\text{ }^{\circ}\text{C}$	20-24 $^{\circ}\text{C}$	557.07	-
$T_{st} = a \times \lambda + b$	20-27 $^{\circ}\text{C}$	468.52	15.89

Results show that rescheduling strategy can be useful in reducing the electricity bill by increasing the thermostat set point during peak hours. From Figure 8 it can be seen that during off-peak period, inside temperature remains within comfortable range i.e. 20 $^{\circ}\text{C}$ to 24.5 $^{\circ}\text{C}$. Only during peak period, temperature reaches near 27 $^{\circ}\text{C}$ but it remains there for a small interval of time. Thus Rescheduling strategy brings down the electricity cost by 16% for a single house while keeping the temperature with in a comfortable range.

D. Community of houses

Section 5.1 contains results for a single house. For a community of houses, a number of houses with different values of parameters and ϕ are considered. Initial house temperature for each house has also been taken different. A Community of 100 houses is considered in this case. Mean value of ϕ and stating temperature are taken as .0408, 2.64 and 21 respectively. For each house, different values corresponding to each of these parameters are obtained by creating 100 random values with 20% standard deviation around mean value. Total electricity cost and peak electricity demand of all the houses are compared for normal thermostat control and rescheduling strategy.

(i) Normal thermostat control

In this case, the set point $T_{st} = 22\text{ }^{\circ}\text{C}$. $L = 2\text{ }^{\circ}\text{C}$. Assuming occupants of all houses specify the comfortable temperature range as 20 $^{\circ}\text{C}$ to 24 $^{\circ}\text{C}$. On solving optimization problem, total electricity cost comes out to be 56187.78 Rs/day. Total peak power of all the houses due to air conditioner load during 24 hours of study, has been shown in Figure 10. From the results, peak power of 816.5 KW can be

observed during peak period at 16:15 hours. Electricity rates are higher during 15:00 hours to 18:00 hours (Refer Figure 5). Another peak of electric power of 816.5 KW is also observed during time slot starting at 13:15 hours where electricity price is lowest.

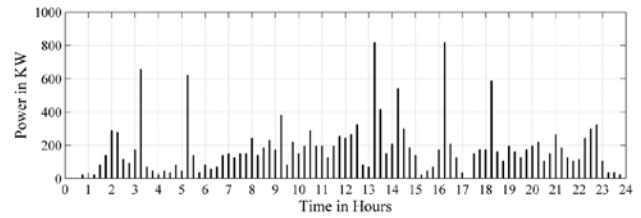


Figure 10 : Electric power demand due to air conditioner load for a community of 100 houses during a typical summer day, in case of normal thermostat control.

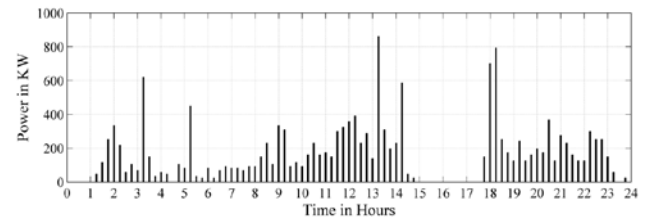


Figure 11 : Electric power demand due to air conditioner load for a community of 100 houses during a typical summer day, in case of rescheduling strategy.

(ii) Rescheduling strategy

In this case, minimum and maximum limit of temperature varies according to (12) and (14), mentioned previously. As a result of executing the optimization program, total cost comes out to be 45872.02 Rs/day. Total peak power of all the houses during 24 hours has been displayed in Figure 11. Comparison of cost of electricity obtained from both techniques shows that Rescheduling technique results in 18.35% reduction in electricity cost. From the results, it has also been observed that peak power of 816.5 KW shown in Figure 10 at 16:15 hours has been completely removed. Almost all electricity demand during peak hours i.e. 15:00 hours to 18:00 hours has been shifted from peak price period to off-peak period. Instead two peaks of electric power demand have been observed pre and post peak price period. A peak of 862.5 KW has been observed at 13:15 hours where the electricity price is lowest. Another peak of 793.5 KW has been observed at 18:15 hours. Literature studies have observed an increase in electricity use at the ends of demand response event. As the demand response event is over (end of peak price period in this case), all the air conditioners are turned ON to maintain the house temperatures with the comfortable range. Hence electricity demand increases and a peak - post DR event is observed.

Thus as a result of application of rescheduling approach, peak power of 816.5 KW at 16:15 hours has been shifted to

time slot starting at 18:00 hours and 18:15 hours. Increase in power in these time slots is 529 KW and 207 KW respectively. Pre - event increase of electric power demand of 46 KW is observed at 13:15 hours. Hence electricity cost has been reduced by reducing the use of electricity during peak period and increasing the use of lowest cost electricity. Also peak demand has been shifted from peak pricing period to off-peak pricing period.

VI. CONCLUSION

This study proposes a real-time price based DR program for reducing the energy cost of the customer and power shifting from peak pricing period to off-peak pricing period. The DR program uses Real Time price as a control signal for controlling the thermostat setting of air conditioner. Centralized air conditioners with PCT have been considered for participation in DR Program. Results of Normal Thermostat control and the proposed Rescheduling technique have been compared for a single house and a community of 100 houses. In Rescheduling strategy, thermostat set point varies as a linear function of price. The results of optimization show that relaxing temperature limit only during peak price period results in approx. 16% reduction of electricity cost of a single house without significantly sacrificing user comfort. Application of this technique on a community of houses displays approx. 19% reduction in electricity cost and also shifting of peak power of 816.5 KW to off-peak period. Thus the study demonstrates the advantages of proposed rescheduling strategy to customers as well as utilities. Other TCA appliances water heater; heat pumps etc. can also contribute in leveling power curve by participating in this program. This type of proposed technique can be applicable to the Indian market and also to the other markets.

REFERENCES

- [1] Albadi MH, El-Saadany EF. A summary of demand response in electricity market. *ElectrPowSyst Res* 2008; 78: 1989-96.
- [2] Ucak C, Caglar R. The effects of load parameter dispersion and direct load control action on aggregated load. In: 1998 Proceedings of International Conference on Power System Technology; 18-21 Aug 1998; Beijing, China: POWERCON. pp. 280-284.
- [3] Zhu Z, Tang J, Lambbotharan S, Chin WH, Fan Z. An integer linear programming based optimization for home demand-side management in smart grid. In: IEEE PES 2012 Innovative Smart Grid Technologies Conference; 16-20 Jan 2012; Washington, DC, USA: IEEE. pp. 1-5.
- [4] Tsui KM, Chan SC. Demand Response Optimization for Smart Home Scheduling Under real-Time Pricing. *IEEE Trans. on Smart Grid* 2012; 3: 1812-1821.
- [5] Zhu N, Bai X, Meng, J. Benefits Analysis of All Parties Participating in Demand Response. In: 2011 Power and Energy Engineering Conference; 25-28 March 2011; Wuhan, Hubei, China: APPEEC. pp. 1-4.
- [6] Chanana S, Kumar A. Demand response by dynamic demand control using frequency linked real time prices. *International Journal of Energy Sector Management* 2010; 4: 44-58.
- [7] Lu N, Katipamula S. Control strategies of thermostatically controlled appliances in a competitive electricity market. In: IEEE 2005 Power Engineering Society General Meeting; 12-16 June 2005; IEEE. pp. 202-207.

- [8] Mohsenian-Rad AH, Leon-Garcia A. Optimal Residential Load Control with Price Prediction in Real-Time Electricity Pricing Environments. *IEEE Trans. on Smart Grid* 2010; 1: 120-133.
- [9] Du P, Lu N. Appliance commitment for household load scheduling. *IEEE Trans. on Smart Grid* 2011; 2: 411- 419.
- [10] Saha A, Kuzlu M, Pipattanasomporn M. Demonstration of a Home Energy Management System with Smart Thermostat Control. In: IEEE PES 2013 Innovative Smart Grid Technologies Conference; 24-27 Feb 2013; Washington, DC, USA: IEEE. pp. 1-8.
- [11] Shao S, Pipattanasomporn M, Rahman S. Development of physical-based demand response-enabled residential load models. *IEEE T Power Syst* 2013; 28: 607-614.
- [12] Pipattanasomporn M, Kuzlu M, Rahman M. An Algorithm for Intelligent Home Energy Management and Demand Response Analysis. *IEEE Trans. on Smart Grid* 2012; 3: 2166-73.
- [13] Nistor S, Wu J, Sooriyabandara M, Ekanayake J. Cost Optimization of Smart Appliances. In: IEEE PES 2011 International Conf. and Exhibition on Innovative Smart Grid Technologies (ISGT Europe); 5-7 Dec 2011; Manchester, United Kingdom: IEEE. pp. 1- 5.
- [14] Costanzo GT, Kheir J, Zhu G. Peak Load shaving in Smart Homes Via Online Scheduling. In: IEEE International Symposium on Industrial Electronics (ISIE); 27-30 June 2011; Gdansk, Poland: IEEE. pp. 1347-1352.
- [15] Mortensen RE, Haggerty KP. A stochastic computer model for heating and cooling loads. *IEEE T Power Syst* 1998; 3: 1213-1219.
- [16] Bozchalui MC, Hashmi SA, Hassen H, Cañizares CA, Bhattacharya K. Optimal Operation of Residential Energy Hubs in Smart Grids. *IEEE Trans. on Smart Grid* 2012; 3: 120-133r

Multiphysics Finite Element Analysis of Underground Power Cable Ampacity

Simon Dubitsky¹, George Greshnyakov², and Nikolay Korovkin³

¹Tor Ltd., St. Petersburg, Russia

²Research Institute "Sevkabel", St. Petersburg, Russia,

³St. Petersburg State Polytechnical University, Russia

Abstract— A method for calculating the ampacity of underground electric power cable line is discussed. The proposed method differs from the previous works by using coupled electromagnetic and thermal FEA analysis. Electromagnetic analysis is used to calculate the resistive AC losses in conductor, shield, and metallic sheath, taking into account skin and proximity effects. The equations of 2D AC magnetic field are coupled together with circuit equations in order to account different grounding modes. The resistive losses calculated by electromagnetic part of the model are summed up with the dielectric losses and transferred to the thermal part of the model as a heat sources.

The proposed method can be used in cases where the standard IEC 2087 calculation gives unreliable results due to unusual cable line formation, inhomogeneous soil, presence of metallic or concrete supports and other difficulties.

Keywords—Cable ampacity, buried cable, finite element analysis, multiphysics, shield grounding

I. INTRODUCTION

The rated current of the underground electric power cable line is limited by the maximal allowable temperature of cable conductor, given by the standard or the cable manufacturer. The temperature raise in turn depends on resistive and dielectric losses in cable as well as on thermal conductivity of cables materials and the ability of surrounding media to conduct and dissipate the heat flux.

To calculate the ampacity of the cable line one must first assess the AC resistive losses in conductive cable elements: conductor, screen and armor.

The classical method of ampacity calculation is given by the IEC 60287 standard. Its theoretical background is a Neher-McGrath model [2], which was generalized later by many authors, in particular G.J. Anders [3]. The

S. D. Dubitsky is with Tor Ltd., St. Petersburg, Russia (phone: +7 812 710 1659; e-mail: simon@tor.ru).

G. V. Greshnyakov, is with Sevkabel plant, R&D Department, St. Petersburg, Russia. He also works with the Department of Cable Engineering, St. Petersburg State Technical University, Russia (e-mail: g.greshnyakov@sevkab.ru).

N. V. Korovkin is a head of Electromagnetic Theory Department, St. Petersburg State Technical University, Russia (e-mail: nikolay.korovkin@gmail.com).

Neher-McGrath model relies on the thermal equivalent circuit technique. The parameters of the equivalent circuit are calculated by using a simplified 1D-model of the thermal field. Electromagnetic part of a calculation intended to assess the resistive and dielectric losses in the cable, is also based on a simplified model of the skin effect and proximity effects.

When the cables are located close to each other, it is necessary to take into account their thermal and electromagnetic interference. Electromagnetic interference is the proximity effect and the skin effect, and the fact that, depending on the chosen grounding mode, the screens and sheaths appear electrically connected into a closed loop. The thermal interference is that neighboring cables warm up to each other and the surrounding soil. Accounting of the mutual heating is especially complicated when cables are laid out in the open air or in restricted airspace - in a pipe or a rectangular conduit. In such case, the multiphysics model should be supplemented with fluid dynamics analysis.

Today FEA software [12] allows combining into a single model the AC electromagnetic analysis, grounding electric circuit, and the thermal analysis. Because the material properties, such as electric resistivity, depends on the temperature, one have to repeat electromagnetic and thermal analyses iteratively until the solution converges. Complexity of the model, however, is quite acceptable for engineering practice.

The advantages of FEA model is particularly evident when power cable line has rather complex structure of the , i.e. includes soil layers with different properties, strong electromagnetic interference between cables, metallic supporting structure, crossing pipelines e.t.c.

In this paper, we consider only steady-state cable ampacity calculation. Nevertheless, the FEA based approach, allows the ampacity calculation in transient conditions: the long-term transient, where the a priori known load curve allows a short-term uprating due to the inertia of thermal processes, and short-term transient, such as the raise of cable temperature due to short circuits of different kinds.

The history of FEA analysis for cable ampacity calculation begins presumably with [4], where the transient heat transfer FEA analysis was used three-phase buried cable line. Later

many authors have contributed to application of the FEA technique for accurate predicting the ampacity of a cable line. Those include: clarification of the model geometry – the shape and the size of modelling area, optimal mesh density [5], short-term and long-term transient simulations [6], [7], taking into account the effect of the temperature on the cable losses, combining the heat transfer analysis with fluid dynamics [8], [9], estimation of resistive AC losses using the electromagnetic FEA model [10]. The accumulated engineering experience of the FEA simulation of the temperature field of cable lines was summarized in the IEC technical report [11].

The contribution of this paper is the combining of AC magnetic FEA simulation, Kirchhoff's equations of the grounding circuit, and steady state heat transfer FEA analysis into a single model of the power cable line.

II. ELECTROMAGNETIC MODEL

A. Equations of AC Magnetic Field

The governing equations of quasi-stationary magnetic field in frequency domain are written with respect to the phasor of the vector magnetic potential \mathbf{A} , which has in the 2D-domain only one nonzero component $A = A_z$ [11]:

$$\frac{\partial}{\partial x} \left(\frac{1}{\mu} \frac{\partial A}{\partial x} \right) + \frac{\partial}{\partial y} \left(\frac{1}{\mu} \frac{\partial A}{\partial y} \right) = -j_{\text{extern}} + j\omega\sigma \cdot A, \quad (1)$$

where μ – is the absolute permeability (H/m), σ – electric resistivity (S/m), ω – cyclic frequency (rad/s), j_{extern} – the external current density (A/m²).

The need of taking into account of the grounding circuit (with one end, with two ends or with transposition) requires combining the field equation (1) with the Kirchhoff's equation of the connected circuit. The equation of a circuit branch containing a solid conductor in magnetic field looks like this:

$$I = \frac{U}{R} = -\sigma \int_{\Omega} i\omega A \cdot ds, \quad (2)$$

where U – is the conductor voltage drop (V), R – the DC resistance (Ohm), The integration is made over the conductor's cross-sectional area Ω .

Solving the equations (1) and (2) one obtains the distribution of the current density in all conductive parts of the model: conductor, shield, metallic sheath, and some metallic supporting structure.

B. Model Geometry

With two dimensional electromagnetic FEA simulation the model geometry contains the cross-sections of all cables, buried into the soil on the given depth. The left and right side borders of the modelling area located far enough to assign on it the no-field border condition.

Our experiments show that for a model containing one cable line increasing the model width over 15 m does not effect on the solution accuracy. The model allows taking into account the electric conductivity of soil as well as supporting metallic parts or pipes nearby.

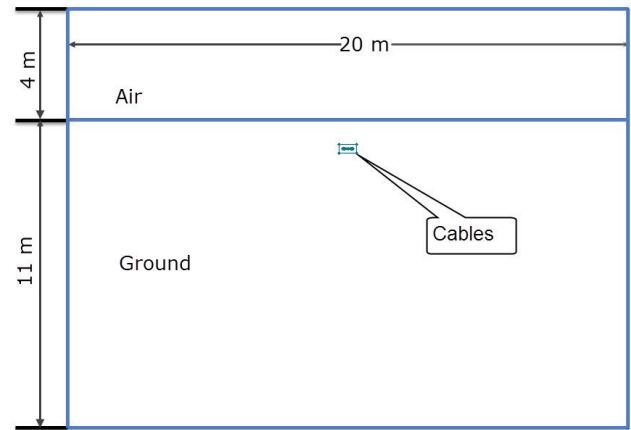


Fig. 1 The model geometry

The discretized cross section of the cable is shown on the figure 2.

In the real world, the conductive parts of the cable are made from separate wires or strips. Constructing the FEA model one can include the detailed geometry of wires or replace them by a solid metal cylinder. In many cases, the conductor wire structure plays an important role and cannot be neglected, for example with modelling of a pulse mode, high frequency losses and others. In our case – the steady state simulation by the fundamental frequency – the exact representation of the conductor's structure does not increase the accuracy, but requires much more resources. Moreover, the exact modelling of the wires is not an easy task because of some uncertainty of the shape of deformed wires and the contact resistivity between them.

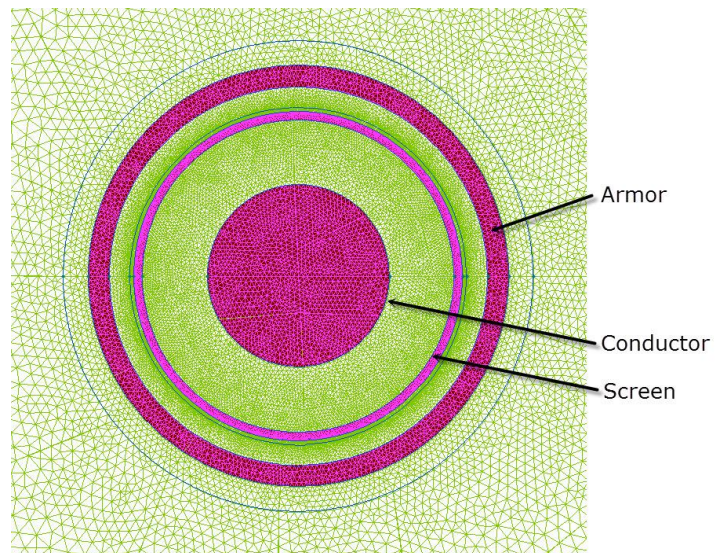


Fig. 2 The cable cross section with the FEM mesh

A separate question is how to choose properly the cross section and the conductivity of the solid cylinder representing the stranded conductor. In our experience, the best results can be obtained by choosing the inner and outer diameters of the conductor the same as in reality. Acting in this way we set the total cross sectional area a bit more than the sum of cross

section area of all wires. To compensate that we propose proportionally decrease the electric conductivity and the thermal conductivity of the simplified conductors.

C. Single Point and Both Ends Grounding

The shield of a cable section can be grounded with one side or with two sides. With two-side grounding the closed loop is formed for circulating current. This current is induced by the alternating magnetic field created by the cable conductor current. The one-side grounding does not provide the loop for induced currents. On the other hand on the unbounded end of the cable shield the induced voltage is observed, that should be limited for sake of safety. We have to note that even with one-side grounding of the cable having both a screen and metallic sheath, these two are always electrically connected with both sides of the cable. This forms a closed loop for circulated current even with one-side grounding.

Presence or absence of a closed loop significantly affects on the amount of losses in the shield and sheath. To consider those one have to couple field equations (1) with the circuit equations (2).

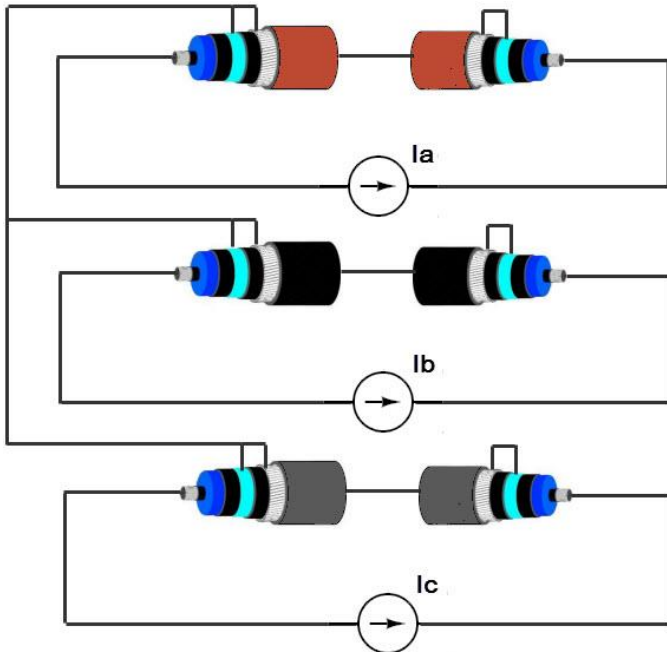


Fig. 3 Grounding the cable with one side

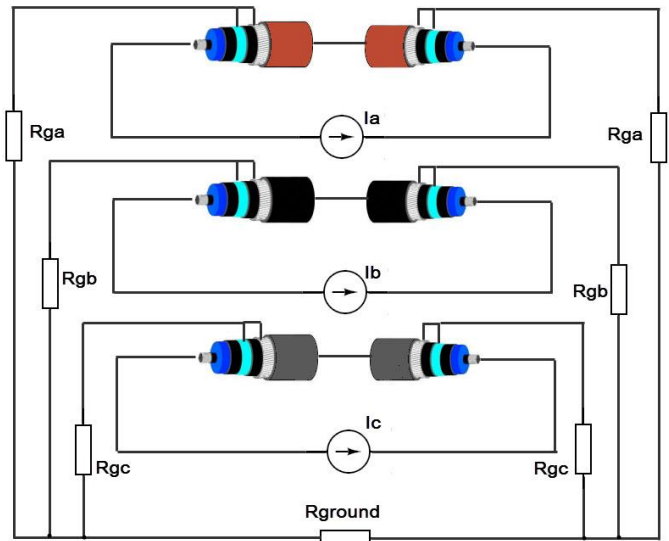


Fig. 4 Grounding the cable with two sides

The values of resistance in the grounding scheme are known with some degree of uncertainty. Therefore, we evaluated the sensitivity of the FEA solution to the values of the resistances R_{gX} and R_{ground} . The study shows that the variation of resistance R_g in the range from 1 to 10 Ohms has virtually no effect on the integral value of losses. The earth resistance R_{ground} has almost no effect for our model until the three phase cable loading is symmetric and zero sequence current is almost zero.

D. Dielectric Losses

According to IEC 60287-1-1 the dielectric losses per unit length of the cable can be calculated by the known value of the dielectric loss factor $tg\delta$:

$$W_d = \omega C U^2 \cdot tg\delta, \tag{3}$$

where $\omega = 2\pi f$, C is the capacitance per unit length (F/m), U_o – is the voltage to earth (V).

The capacitance of a cylindrical capacitor is calculated by:

$$C = \frac{2\pi\epsilon\epsilon_0}{\ln\left(\frac{D_i}{d_c}\right)} \tag{4}$$

As long as we remain in the class of cables and conductors with cylindrical conductors and screen screens the refinement of formulas (3) and (4) by means of FEA is not required. The FEA model of dielectric losses may be needed for more complex geometry configurations such as cable joint and termination.

III. HEAT TRANFER MODEL

The thermal state of the loaded power cable line is defined by the partial differential equation of thermal conductivity. With steady state analysis it is reduced to:

$$\frac{\partial}{\partial x} \left(\lambda_x \frac{\partial T}{\partial x} \right) + \frac{\partial}{\partial x} \left(\lambda_x \frac{\partial T}{\partial x} \right) = -q, \tag{5}$$

where T is the temperature (K), t – time (c), λ – the thermal conductivity ($W/(m \cdot K)$), q – the heat source density (W/m^3).

The thermal conductivity equation (5) is solved numerically on the same computational domain as the magnetic field equation (1) (see fig. 1) with the difference that the air above the ground surface is excluded from the domain. On the side boundaries of the domain we define the boundary condition of thermal insulation, on the bottom border – an isothermal boundary condition with the value of 4 deg. C, which is almost constant throughout the year. On the earth surface the convective boundary condition is set with the ambient temperature $T_0=25 \text{ deg C}$ and the convection coefficient α . The suitable value of the convection coefficient we choose by the dimensionless empirical equation:

$$Nu = 0.54 \cdot (Pr \cdot Gr)^{0.25}, \tag{6}$$

where Nu is the Nusselt number, Pr is the Prandtl number, and Gr is the Grashof number.

From (6) obtain the convection heat transfer coefficient α :

$$\alpha = Nu \cdot \frac{\lambda}{L_{ref}}, \tag{7}$$

where L_{ref} is a characteristic length of the model.

Using the equation (6) takes into account the average wind speed if such data are available.

IV. SIMULATION RESULTS

The modern approach to field simulation in electrical equipment often is multidisciplinary [13] in order to catch the mutual interference of processes from different domains of physics.

The steady-state simulation loop begins with magnetic field simulation (1.) for obtaining the spatial distribution of the restive losses. The calculated resistive losses are summed up with the dielectric losses (2.) and transferred to the heat transfer analysis (3.). The thermal simulation gives us the temperature field, which is used for adjusting the conductivity of copper and aluminum (4.). Then the loop (1.–4.) is repeated until the solution converges (normally 3-4 loops is sufficient).

The simulated cases include the cable formation in line (fig. 5 and 6) and the touching triangle formation (fig. 7, 8).

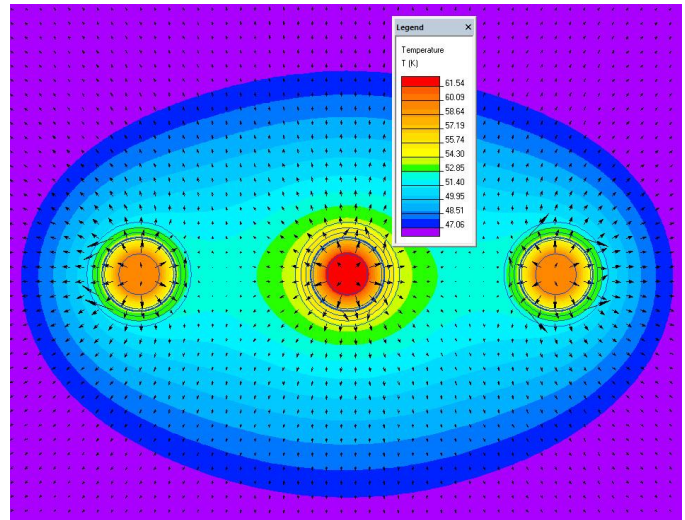


Fig. 6 Temperature field and heat flux vectors with line formation

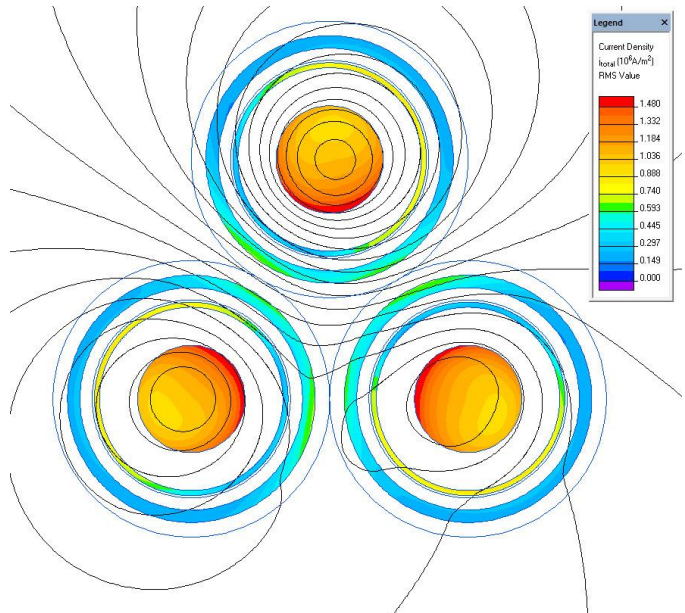


Fig. 7 Magnetic field and current density with triangle formation

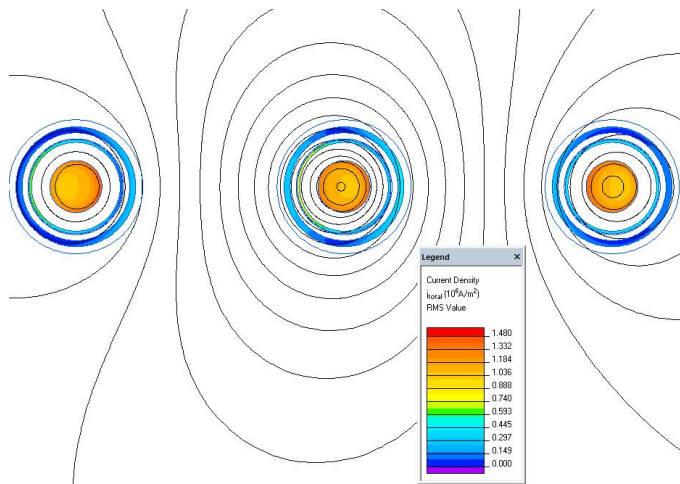


Fig. 5 Magnetic field and current density with line cable formation

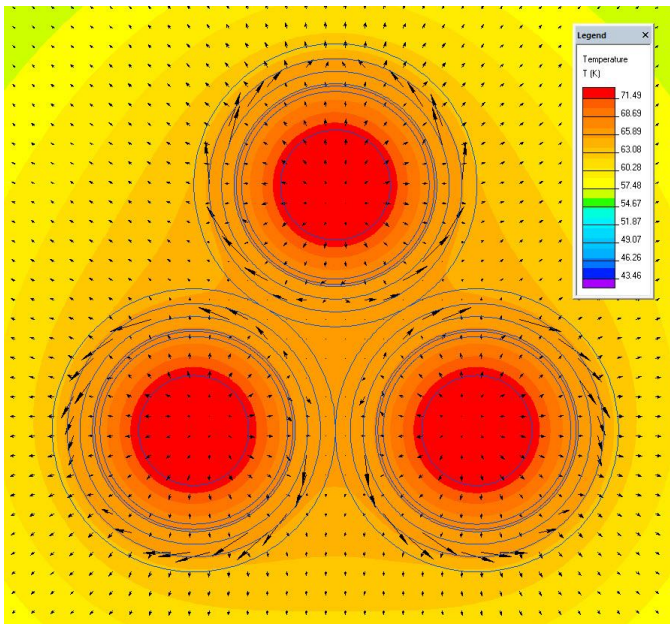


Fig. 8 Temperature field and heat flux with triangle formation

The resistive losses in cable conductors, screens and sheaths with two different formations are summarized in the table 1:

Table 1: Resistive losses in cable elements

		CURRENTS AND LOSSES: GROUNDING WITH BOTH SIDES					
		LAYOUT IN LINE			LAYOUT IN TRIANGLE		
		PHASE B	PHASE A	PHASE C	PHASE A	PHASE B	PHASE C
		● ○ ○	○ ● ○	○ ○ ●	● ○ ○	○ ● ○	○ ○ ●
CONDUCTOR	Current, A	700	700	700	700	700	700
	Losses, kW/km	15.27	15.27	15.27	15.57	15.57	15.57
SCREEN	Current, A	47.6	50.4	47.5	75.9	76.3	76.1
	Losses, kW/m ³	1.07	0.93	1.09	1.52	1.53	1.53
ARMOUR	Current, A	27.3	32.9	27.3	62.1	58.0	58.2
	Losses, kW/m ³	0.72	0.73	0.74	3.03	3.03	3.04

V. CONCLUSION

Proposed further development of prediction the ampacity of underground cable line using multiphysics FEA simulation. The main contribution is the detailed consideration of cable grounding, taking into account more than one electromagnetic screen (namely the copper shield and the aluminum sheath). The proposed approach combines in a single model the AC magnetic FEA simulation, the grounding circuit, and the heat transfer FEA. The first two parts coupled by the strong link, i.e. they produced a single matrix after discretization. The magnetic and thermal parts of the model a coupled together by a two-directional loose (consecutive) link.

The FEA based calculation gives almost the same result as the standard IEC 60287 calculation when the construction of the cable line is ordinary. The dedicate software gives the answer almost as quickly as the IEC based software.

Benefits of the multiphysics FEA appears in situations more complex than those described in the standard, such as heterogeneous soil with thermal backfill, using of steel or

concrete supporting construction. An important case is a line with two or more circuits.

Benefits of the FEA simulation also expected with very rapid transient conditions, such a direct lightning stroke [14].

Moreover, the FEA simulation of magnetic field gives exhaustive information about inductive interference of two or more circuits, both cable and overhead ones. In addition, the magnetic and electric field profiles on the earth surface can be used to fulfill the rules of electromagnetic ecology and designing magnetic shielding when needed.

REFERENCES

- [1] IEC Standard-Electric Cables – Calculation of the Current Rating – Part 2: Thermal Resistance – Section 1: Calculation of the Thermal Resistance, IEC Standard 60287-2-1, 1994–12
- [2] J. H. Neher, M. H. McGrath, "Calculation of the temperature rise and load capability of cable systems," AIEE Trans., Vol. 76, Part 3, 1957, pp. 755-772.
- [3] G. J. Anders Rating of electric power cables: ampacity computations for transmission, Distribution, and Industrial Applications. - McGraw Hill Professional, 1997, 428 c
- [4] N. Flatabo Transient heat conduction problems in power cables solved by the finite element method. -IEEE Trans. on PAS. Jan, 1973 pp. 56-63
- [5] [5] Aras F., Oysu C., Yilmaz G. An assessment of the methods for calculating ampacity of underground power cables //Electric Power Components and Systems. – 2005. – T. 33. – №. 12. – C. 1385-1402
- [6] Liang Y. Transient temperature analysis and short-term ampacity calculation of power cables in tunnel using SUPG finite element method //Industry Applications Society Annual Meeting, - IEEE, 2013. - C. 1-4.
- [7] Haripersad P. Uprating of cable current capacity for Utilities where load cycle profiles are known - Cigre 2005 Regional Conference paper, Capetown
- [8] Sedaghat A., de Leon F. Thermal Analysis of Power Cables in Free Air: Evaluation and Improvement of the IEC Standard Ampacity Calculations. - IEEE Transactions on Power Delivery
- [9] Mahmoudi A., Kahourzade S., Lee D. S. S. Cable ampacity calculation in heterogeneous soil using Finite Element Analysis //Power Engineering and Optimization Conference (PEOCO), 2011 5th International. – IEEE, 2011. – C. 416-421
- [10] Labridis, D.; Hatzathanassiou, V. "Finite element computation of field, forces and inductances in underground SF6 insulated cables using a coupled magneto-thermal formulation", Magnetics, IEEE Transactions on, On page(s): 1407 - 1415 Volume: 30, Issue: 4, Jul 1994
- [11] IEC Technical Report TR 62095, Electric Cables—Calculations for Current Ratings—Finite Element Method, 2003
- [12] Claycomb J. R. Applied Electromagnetics Using QuickField and MATLAB. – Laxmi Publications, Ltd., 2010.
- [13] Dubitsky S. D., Korovkin N.V., Hayakawa, M.; Silin N.V., Thermal resistance of optical ground wire to direct lightning strike //Electromagnetic Theory (EMTS), Proceedings of 2013 URSI International Symposium on. – IEEE, 2013. – C. 108-111.
- [14] Korovkin N.V., Greshnyakov G.V., Dubitsky S.D. Multiphysics Approach to the Boundary Problems of Power Engineering and Their Application to the Analysis of Load-Carrying Capacity of Power Cable Line - Electric Power Quality and Supply Reliability Conference (PQ2014), 11-13 June 2014, Rakvere, Estonia

Simon D. Dubitsky is currently with Tor Ltd, St. Petersburg. He receives MSc degrees in electrical engineering in 1983 and in computer science in 2003 both from SPbSPU. His main area of activity is development of QuickField FEA software in cooperation with Tera Analysis company locates in Svendborg, Denmark. Main research interest is implementing FEA as a handy tool for everyday engineering practice, advanced postprocessing of electromagnetic field solution, multiphysics FEA analysis coupled with circuit equations and surrogate models.

George V. Greshniakov is currently a head of laboratory in the Sevcabel research institute. He receives the MSc and PhD degrees in electrical engineering from St. Petersburg technical university (SPbSPU) in 1983 and

1992 respectively. He is also a docent in SPbSPU teaching cable and insulation engineering. Author of more than 30 reviewed papers. His research interest is electromagnetics and thermal analysis of power cable installation and development of advanced cable accessories.

Nikolay V. Korovkin, professor, is currently head of Electromagnetic Theory Department of St. Petersburg State Polytechnic University (SPbSPU). He received the M.S., Ph.D. and Doctor degrees in electrical engineering, all from SPbSPU in 1977, 1984, and 1995 respectively, academician of the Academy of Electrotechnical of Russian Federation, (1996) Invited Professor, Swiss Federal Institute of Technology (EPFL), Lausanne (1997), Professor, University of Electro-Communications, Department of Electronic Engineering, Tokyo, Japan (1999-2000), Professor EPFL (2000-2001), Otto-von-Guericke University, Germany (2001-2004). Head of the Program Committee of the Int. Symp. on EMC and Electromagnetic Ecology in St. Petersburg, 2001-2011.

His main research interests are in the inverse problems in electro-magnetics, optimization of power networks, transients in transmission line systems, impulse processes in linear and non-linear systems, "soft" methods of optimization, systems described by stiff equations, the problems of the electromagnetic prediction of earthquakes and identification of the behavior of the biological objects under the influence of the electromagnetic fields

High Performance Concrete Using Blast Furnace Slag as Coarse Aggregate

Dr. V.P. Singh

Abstract— High performance concrete is a construction material which is being used in increasing volumes in recent year due to its long term durability, performance and better rheological and mechanical properties than conventional concrete. Till date concrete was made using cement, coarse aggregate, fine aggregate and water. The coarse aggregate were obtained by crushed stone as well as fine aggregate were obtained either by river bed. With the increase environmental awareness and its potential hazards effect caused by blasting as well as crushing of stone, it become an important issue for construction industry to think about an alternative material for coarse as well as fine aggregate. Utilization of industrial byproduct has become an attractive alternative to disposal. One such byproduct of silica fume, which is a byproduct of smelting process in the silicon and ferrosilicon industry. Silica fume is very effective in the design and development of high performance concrete. Its particles are approximately 100 times smaller than the average cement particles. Because of its extreme fineness and high silica content, it is a highly effective pozzolanic material.

The one major problem in the construction industry nowadays is the non-availability of coarse aggregate and it has compelled the researchers to think about some alternate option. The one such type material is aggregate made from Blast Furnace slag and can be used to replace coarse aggregates. Slag, which is a waste product produced during the manufacturing process of ferro-alloys, requiring a vast land to dump and thus polluting the environment. In the present study it was observed that, it could be better substitute for natural coarse aggregates. In the present study the coarse aggregate made by crushing of slag has been used. The well-graded aggregate made from slag has 0.01% water absorption, 19 % crushing value and 22% impact value. The weight loss in soundness test when treated with sodium sulphate as well as magnesium sulphate was also observed negligible. The compressive strength concrete made up from slag aggregate has been 10 to 15 % more than the crushed natural stone aggregate concrete. From the study it was conclude that aggregate made from slag can be used as an good alternate for stone aggregate and to develop eco-friendly construction materials based on recycling of waste resources on the basis of the concept of sustainable development for solving an environmental problem that is a major issue of the twenty-first century all over the world.

Keywords— silica fume, blast, impact, slag, pozzolanic.

I. INTRODUCTION

The use of various types of waste products from various industries plays an important role in making a eco-friendly concrete. Sometimes these waste products are used directly in the concrete in their actual form as these are produced, but

sometimes these are processed and than used. In present time the major requirement of concrete is that, it should be more workable, durable and should have high compressive strength then normal concrete by using waste products like silica fume, fly ash blast furnace slag etc. The concrete meeting special combinations of performance and uniformity requirement cannot be achieved by using conventional constituent and normal mixing. To achieve these properties, concrete requires the use of various admixtures as well as ingredients which could impart strength and performance to concrete simultaneously. Many researchers worked on the use of silica fume in different percentage to study the various properties of concrete. Bentur et al. [1] reported that the strength of silica fume concrete is greater than that of silica fume paste which they attributed to the change in the role of the aggregate in concrete. In cement concrete, the aggregate functions as inert filler but due to the presence of weak interfacial zone, composite concrete is weaker then cement paste. But, in silica fume concrete, the presence of silica fume eliminates this weak link by strengthening the cement paste aggregate bond and forming a less porous and more homogenous microstructure in the interfacial region.

Mazloom et al.[5] made high performance concrete containing silica fume. The silica fume content was kept as 0, 6, 10, and 15% and water cement ratio being 0.35. It was observed that mixes incorporating higher silica fume content tended to required higher dosages of super-plasticizer. The higher demand of super-plasticizer with the concrete containing silica fume was attributed to the very fine particle size of silica fume that causes some of the super-plasticizer being adsorbed on its surface.

Wong et al. [4] examined the effect of silica fume (5, 10 and 15%) on the slump and vee-bee time of concrete. It was observed that mixture achieved slump values ranging from 30 to 260mm with varying percentage of silica fume i.e. 15, 10 and 5 percent, while Vee-Bee time was observed in the range of 1 to 15 seconds. The large variation of workability across mixtures was due to the constant super-plasticizer dosage used for mixture with the same w/c ratio. The compressive strength of concrete containing silica fume was also studied. A Concrete mixtures with w/c ratios of 0.27, 0.30 and 0.33 were prepared. It was observed that silica fume did not produce an immediate strength enhancement; instead, the blended mixtures only achieved higher strength from 7 days onwards. Strength loss in the early ages, which was proportional to the cement replacement level, was probably due to the dilution

Dr V.P. Singh, Professor, Civil Engineering Department, National Institute of Technology, Kurukshetra, India. (Phone: +91 9416038460; fax: +91 1744 233354; e-mail: vpsingh72@gmail.com)

effect of the pozzolana and as well as the slow nature of pozzolanic reaction. Further, it was observed that after 90 days of curing, the average strength enhancement with 10% silica fume achieved 17% increment. It was also found that reducing the w/c ratio from 0.30 to 0.27 did not trigger a significant strength enhancement as anticipated.

Kayali and Zhu [7] performed tests on high-strength reinforced silica fume–cement concrete slabs with a compressive strength of 70MPa for chloride diffusion and corrosion activity after partial immersion in a 2% chloride solution. It was found that high-strength concrete containing 10% silica fume possessed exceedingly high corrosion resistance. It was also observed by various researchers that the addition of silica fume accelerates the hydration of cement at all stages of hydration. The pozzolanic action of silica fume seems to be very active at early hours of hydration. The addition of silica fume also gives results in significant reduction in the chloride-ion diffusion. This could be attributed to have been caused by addition of silica fume cause considerable pore refinement i.e. transformation of bigger pores into smaller one due to their pozzolanic reaction concurrent with cement hydration. Silica fume improves the long-term corrosion resistance, alkali silica expansion, but increases the carbonation depth.

Anastasiou E. et al. [8] experimentally studied the utilization of fine recycled aggregate in concrete with fly ash and steel slag. Various mortar and concrete mixtures were prepared using different aggregate and binder combinations to determine the feasibility of producing concrete with maximum use of alternative materials. Concrete prepared using construction and demolition waste as fine aggregate and steel slag as coarse aggregate obtained compressive strength of 30 MPa at 28 days and adequate durability of low grade application. The porosity of the control mixtures as well as mixtures with High Calcium Fly ash HCFA and Electric arc Furnace EAF slag was 13.5-17.9 % and the porosity of mixtures with Construction & Demolition Waste CDW aggregate was observed as 18.8-20.7%. So, it was observed from the results that the use of fine construction and demolition waste aggregate increases the porosity in concrete and reduces strength and durability but when it combine with steel slag aggregate, it partly recovers strength and durability loss. Concrete prepared with mixed construction and demolition waste as fine aggregate and steel slag as coarse aggregate gives 30 MPa compressive strength at 28 days. The cement replacement with 50% with high calcium fly ash and use only of steel slag and recycled aggregates resulted in concrete of adequate strength.

Arivalagan S. [9] reported the use of copper slag, a waste product from sterlite industries. Experimental investigations were carried out to study the possibility of using copper slag as a replacement of sand in concrete mixtures. The copper slag is used in various percentage ranging from 0%, 20%, 40%, 60%, 80% and 100%. The compressive strength of cubes, split tensile strength of cylinder and flexure strength of beams were evaluated. The maximum compressive strength obtained

was 35.11 MPa for 40% replacement and strength of control mix was 30MPa and maximum split tensile strength of cylinder were obtained as 2.86 N/mm² in comparison to control mix of 1.55. Similarly the maximum flexural strength of beams was 28.80 N/mm² and strength of control mix was 18.95 N/mm². It was observed from the results that the addition of copper slag has improved the compressive strength, split tensile strength and flexure strength of concrete and it was also observed that sand replaced copper slag beams showed an increase in energy absorption capacity.

Monshi A. et al. [10] used slag from iron and steel industry as raw material for Portland cement production before firing. The slag from blast furnace and converter are mixed with limestone of six different proportions. The ground material is fired in rotary kiln having temperature of 13500 C for 1 hour to have clinker which were crushed and mixed with gypsum of 3%. It was observed that Cement prepared with 49% iron slag, 43% calcined lime and 8% steel slag gives the compressive strength of Type-1 ordinary Portland cement (OPC).

Khanzadi M. et al. [12] reported the effect of using copper slag as coarse aggregates in high-strength concrete. The compressive strength, split tensile strength, and rebound hammer values of high-strength concretes are evaluated in this study. Concrete mixtures prepared with different proportion of silica fume with water to cementitious materials ratios of 0.40, 0.35, and 0.30. The various percentages of the cement replacements by silica fume were 0%, 6%, and 10%. It was seen from the results that replacement of limestone coarse aggregate by copper slag aggregate increases the compressive strength from 84-96 MPa and 102-120 MPa at 28 and 91 days respectively. It can be concluded that the incorporating copper slag coarse aggregate increases the compressive strength by about 12% on average. The split tensile strength of CSAS and LSAS concrete increases from 6.1 to 7.1 MPa and 5.5 to 6.2 MPa after 28 and 91 days of curing respectively. The concrete with copper slag aggregate, CSAF, CSAS, CSAT YIELD 2.6%, 7.5% and 9.3% higher rebound value than the concrete mixes with limestone aggregate.

From the literature survey it was observed that different types of industrial waste has been use to produce a good quality concrete, but the use of slag aggregate produced after transformation of blast furnace slag for making fresh concrete was not studied. Hence, in the present study, the use of another material i.e. the use of blast furnace slag as coarse aggregate in concrete has been made. Crushing of blast furnace slag, a waste product of steel industries produces the aggregate. The air-cooled blast furnace slag is the nonmetallic product, consisting essentially of silicates and aluminosilicates of calcium and other bases that is developed in a molten condition simultaneously with iron in a blast furnace. ACBFS is the material resulting from the solidification of molten blast furnace slag in a slag pit under atmospheric conditions with some spraying of water to accelerate cooling so the materials can be moved to the processing plant. Due to a relatively slow rate of cooling, which may contain some glassy and dense

particles and which can be crushed to produce an angular and roughly cubical coarse aggregate for use in highway construction including use in stabilized and unstabilized base courses, fill and embankment, hot mix asphalt and hydraulic cement concrete.

II. EXPERIMENTAL STUDY

2.1 Physical Properties of Coarse and Fine Aggregates

The various physical properties of coarse aggregate as shown in Fig. 1 and 2, has been find out as per the requirement of BIS:383-1970 (Reaffirmed 1997) [2] for making a high performance concrete. The various properties are given in Table-1 and 2.

2.2 Proportioning of Concrete mix

The concrete mix design was carried out as per the guidelines of BIS:10262:2009[3] and ACI 211.4R-08[11]. The proportions were fixed on the basis of trials. The main ingredients of concrete were Cement: Sand (natural sand i.e.river sand): Coarse aggregate (natural stone and crushed



Fig. 1. Blast furnace slag



Fig. 2 Crushed blast furnace slag aggregate

Table 1

Physical Properties of Coarse aggregate

Name of Test	Observed Values
1. Sieve Analysis	
I.S. Sieve Size	% age Passing
20 mm	100
16 mm	75
12.5 mm	60

10 mm	38.55
4.75 mm	1.0
2. Water Absorption	0.01 %
3. Crushing Value	24.04 %
4. Impact Value	22 %

Table 2

Physical Properties of Fine aggregate

Name of Test	Observed Values
1. Sieve Analysis	
I.S. Sieve Size	% age Passing
4.75 mm	100
2.36 mm	77.9
1.18 mm	46.1
600 micron	36.0
300 micron	19.0
150 micron	10.4
2. Fineness Modulus	3.1
3. Silt Content	1.8 %

crushed slag aggregate) with Silica fume and without Silica fume. To keep the Water:Cement ratio as low, the admixture SIKA Viscocrete 20 HE has been used. The admixture dose was kept as 0.8 –1.0 percent. Table 3 shows the various proportions of ingredients used to attain high performance concrete. The water Cement ratio has been kept uniform for all the mixes i.e.0.37. The compressive and indirect tensile strengths of the concrete has been studied by testing cube of size 150x150x150 mm and 150x300 mm size cylinders specimens, respectively

2.3 Casting and Testing of Concrete cubes

The concrete cubes of size 150x150x150 mm were cast under strictly controlled water –cement ratio. The admixture was added in the water prior to add in the dry mix. After thoroughly mixing of aggregates, the green concrete was filled in cubes and vibrated on table to avoid any air voids in the body of concrete. The cubes were removed from moulds after 24 hours and kept in curing tank at an temp of 25 to 27 degree centigrade. The cubes were tested after 7 and 28 days under compression. It was observed during casting that no segregation and bleeding occurs because of the presence of silica fume which makes the mixture cohesive. Similarly the cylinders of size 150mm x 300mm sizes were cast, cured and tested after 28 days.

2.2.1 Compressive and Split Tensile Strength

The concrete is mainly considered for its compressive strength in the design. Hence to compare the conventional concrete and concrete made up of blast furnace slag, the compressive strength has been observed through concrete cube and cylindrical specimens. Table 3 shows the compressive strength of concrete having different mix proportion and tested after 28 days.

III. DISCUSSION OF RESULTS

From Table 3, it has been observed that presence of silica fume reduce the requirement of cement without significant change in the final strength of concrete. It was also observed that change in percentage of adding blast furnace slag aggregate i.e. 10, 20 and 30 percent, hardly make a change in the compressive strength of final product i.e. concrete. Finally the casting was made only by using slag aggregate and the strength of the order of 72.16 Mpa has been achieved while all the ingredients were kept same.

IV. CONCLUSIONS

In the present study the effects of replacement of cement by silica fume and aggregate by blast furnace slag in varying percentages on strength of conventional concrete and blast furnace slag concrete were observed. The following conclusion has been made.

1. It was observed that the cement replaced by 10% silica fume only achieves the maximum compressive strength, which increases the strength up to 13.83% as compared with conventional concrete.
2. The Compressive strength of 100% blast furnace slag concrete has been increased up to 2.8% in comparison to conventional concrete.

3. The maximum compressive strength was obtained at 10% silica fume and 30% blast furnace slag aggregate combination concrete.
4. It has been observed that the cement replace by 7% silica fume achieves the maximum split tensile strength, which increases the strength up to 56.93% as compared with conventional concrete.
5. The maximum split tensile strength has been observed with 10% blast furnace slag aggregate and silica in concrete.

The present study shows that the use of blast furnace slag aggregate not only an substitute of stone aggregate but also increases the strength of concrete. The present study is important to develop eco-friendly construction materials based on recycling of waste resources on the basis of the concept of sustainable development for solving an environmental problem that is a major issue of the twenty-first century all over the world, and help in preserving the environment and recycling resources for saving the natural resources.

TABLE -3
Compressive and Split Tensile Strength

S.No:	Mix Proportion				Compressive strength (MPa)	Split Tensile strength (MPa)	
	Cement (Kg)	Percentage of Silica Fume (Kg)	Sand (Kg)	Aggregate (Kg)			
				Stone Aggregate			Slag Aggregate
1	481	-	370	921	-	63.34	2.02
2	456.95	5% (24.05)	370	921	-	68.45	2.50
3	447.33	7% (33.67)	370	921	-	69.16	3.17
4	432.9	10% (48.1)	370	921	-	72.10	2.34
5	456.95	5% (24.05)	370	828.9	10% (92.1)	64.50	3.05
6	456.95	5% (24.05)	370	736.8	20% (184.2)	68.05	2.11
7	456.95	5% (24.05)	370	644.7	30% (276.3)	67.43	1.88
8	447.33	7% (33.67)	370	828.9	10% (92.1)	69.54	3.50
9	447.33	7% (33.67)	370	736.8	20% (184.2)	70.03	2.17
10	447.33	7% (33.67)	370	644.7	30% (276.3)	71.52	3.30
11	432.9	10% (48.1)	370	828.9	10% (92.1)	70.48	2.39
12	432.9	10% (48.1)	370	736.8	20% (184.2)	70.97	2.06
13	432.9	10% (48.1)	370	644.7	30% (276.3)	72.73	2.03
14	432.9	10% (48.1)	370	-	921	72.16	3.20

REFERENCES

- [1] A. Bentur, A. Goldman and M.D. Cohen, (1998), The Contribution of the Transition Zone to the Strength of High Quality Silica Fume Concrete, Proc Mater Res Soc., 114 pp. 97-102.
- [2] BIS 383, (1970), Specification for Coarse and Fine Aggregates from Natural Sources for Concrete, Bureau of Indian Standards, India.
- [3] BIS 10262, (2009), Concrete Mix Proportioning-Guidelines, Bureau of Indian Standards, India.
- [4] H.S. Wong, H. Abdul Razak, (2005), Efficiency of Calcined Kaolin and Silica Fume as Cement Replacement Material for Strength Performance, *Cement and Concrete Research*, **35**, pp. 696-702.
- [5] M. Mazloom, A.A. Ramezani-pour, J.J. Brooks, (2004), Effect of Silica Fume on Mechanical Properties of High-

- Strength Concrete. *Cement and Concrete Composites*, **26**, pp.347-357.
- [6] S. Bhanja, B. Sengupt (2005), Influence of silica fume on the tensile strength of concrete, *Cement and Concrete Research*, 35, 744, pp 743–747.
- [7] Kayali O., Zhu B,(2005), Corrosion performance of medium-strength and silica fume high-strength reinforced concrete in a chloride solution, *Cement & Concrete Composites*, **27**, pp. 117–124.
- [8] Anastasiou E., Geosgiadis K. and Stefanidou M. (2014) “utilization of fine recycled aggregate in concrete with fly ash and steel slag” *construction and building materials* vol. 50, pp-154-161.
- [9] Arivavalagan S. (2013) “experimental study on the flexural behavior of reinforced concrete beams as replacement of copper slag as fine aggregate” *civil engineering and urbanism* vol. 3 pp. 176-182
- [10] Monshi A. and Asgarani M.K. (1999) “producing Portland cement from iron and steel slag and limestone” *cement and concrete research* vol. 29 pp-1373-1377 .
- [11] ACI 211.4R-08, "Guide for selecting proportions for high strength concrete using Portland cement and other cementitious materials".
- [12] Khanzadi M. and Behnood Ali (2009) “mechanical properties of high strength concrete incorporating copper slag as coarse aggregate” *construction and building materials* vol.23 pp-2183-2188.

Capacitance and Impedance Methods of Electric Field Grading in Cable Joint and Termination

George V. Greshnyakov¹, Simon D. Dubitskiy², and Nikolay V. Korovkin³

¹ Research Institute "Sevkabel", St. Petersburg, Russia,

²Tor Ltd., St. Petersburg, Russia

³St. Petersburg State Polytechnical University, Russia

Abstract— Designing and manufacturing of competitive cable joints and terminals is one of the most complicated high-tech challenges in the modern cable industry. The known methods for electric field grading are based either on proper selection of the geometric configuration and physical properties of the stress cone, or on controlling the field within the tube coupling. We propose the new capacitive method that combines advantages of geometric and refractive methods, as well as stress control method by resistive tube regulator. The optimal configuration of the active elements and properties of materials is proposed, which is based on the FEA simulation of the electric field.

Keywords—Cable joint, cable termination, stress cone, field grading, capacitive field grading, impedance field grading, finite element analysis

I. INTRODUCTION.

The known equivalent circuit of the cable ending [1], [2], [3] is a RC network with longitudinal and transverse parallel RC elements. The RC network contains two lateral elements per cell. One of the RC filters represents the impedance between the conductor and the shield, whereas another RC filter represents the impedance of the reinforcing insulation of the cable joint between the conductor and the ground. The difference between these capacitive currents is the reason of non-uniform electric field distribution.

One way of grading the electric field along the cable end is modifying the longitudinal conductivity. That is known as an *impedance method* of the field grading. It is implemented by applying one or more semi-conductive coating layer over the cable insulation.

Another option is increasing of the capacity C_0 [3] of the reinforcing insulation to the ground. The grading effect of this capacity appears in conjunction with the conductive and semi-conductive shields, including the reflector of a stress cone. The curvature of the reflector should provide compensation of capacitive current by the displacement current through the

reinforced insulation. This is the essence of the *geometric method*.

The *refraction method* involves increasing of the C_0 capacity by means of greatly increased permittivity of the main body of stress cone. To achieve this goal the stress cone is made from silicone rubber with a special filler, which increases the permittivity up to 10 times more than the XPLE insulation. However, the field grading effect of refraction method heavily depend on the harmonic spectrum of the cable voltage.

II. CAPACITIVE METHOD OF ELECTRIC FIELD GRADING.

A. Definition

The capacitive field grading method is a combination of geometric and refractive methods [4], [5]. It provides reducing of the tangential electric field in the cable end, where the factory sheath, shield, and the polymer semi-conductive coatings are removed. This approach do not involve complex technological procedures of formation of the special properties of materials.

For example, the main module – the stress cone - can be made as a double-layered conical body (Fig. 1). The outer part – the main insulation body - is made from the rubber with good insulating properties, whereas the inner part - a reflector – is made from a molded rubber with simple conductive fillers (i.e. fine soot, metal dust). The reflector provides grading of the electric field in reinforced insulation. The space between the stress cone and the outer insulating sleeve is filled with liquid dielectric.

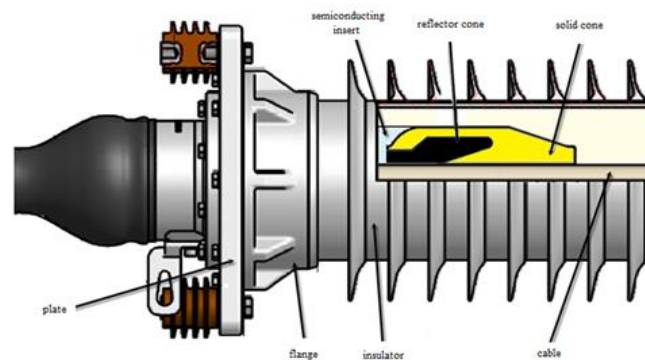


Fig. 1. Cable termination with a stress cone

We perform a number of finite element (FEA) simulations

G. V. Greshnyakov, is with Sevkabel plant, R&D Department, St. Petersburg, Russia. He also works with the Department of Cable Engineering, St. Petersburg State Technical University, Russia (e-mail: g.greshnyakov@sevkab.ru).

S. D. Dubitskiy is with Tor Ltd., St. Petersburg, Russia (phone: +7 812 710 1659; e-mail: simon@tor.ru).

N. V. Korovkin is a head of Electromagnetic Theory Department, St. Petersburg State Technical University, Russia (e-mail: nikolay.korovkin@gmail.com).

to obtain optimal geometry and material properties (permittivity and conductivity) of the stress cone reflector [6], [10], [11], [12].

The simulation geometry domain is shown on the fig. 2. We use triangular finite elements of the first order. The mesh density is non-uniform. It highly increases around the area where the semi-conductive coater over the XPLE insulation is broken. In the figure 2, the stress cone reflector shown in pink.

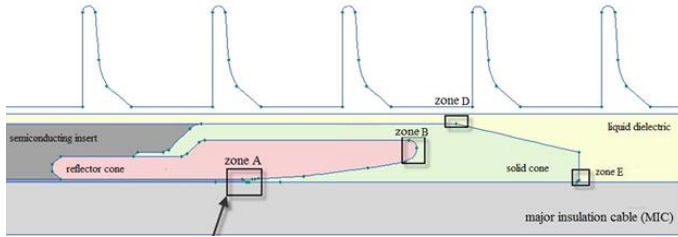


Fig.2. Geometric design model stress cone

The operating experience of the high voltage cable joints [5], [7], [8] indicates that we can identify the following problem zones in terms of strong electric field:

- 1) Zone of broken semi-conductive coating over the XPLE cable insulation (marked as Zone A on the figure 2)
- 2) The rounding area of the reflector (zone B),
- 3) Liquid-filled space between the stress cone and the outer insulator (zone D), and
- 4) The end of the cone body adjacent to the XPLE insulation (zone E).

We focus on the zone A where most defects are reported. Therefore, we choose the minimum of electric field magnitude E_A as an optimization criterion.

We adopted the one-factor-at-a-time strategy for finding the global near to optimum set of parameters [5], [10], [11], [12]. The border conditions are following: the conductor potential is equal to the peak value of the phase voltage, the screen potential is zero. The reflector part of the stress cone for its intended use must be electrically connected to the grounded screen, acting as recover of the removed original screen.

The FEA analysis of AC electric field is formulated using the phasor notation with respect to electric potential U , the current density vector \mathbf{j} , and electric field vector \mathbf{E} . The overall geometry of the cable joint is considered as axisymmetric, therefore we able to employ time effective 2D FEA calculation.

The problem formulation is based on the Gauss's law for electrostatic field [1]:

$$\text{div}(\epsilon \mathbf{E}) = \rho, \quad (1)$$

the current conservation law:

$$\text{div} \mathbf{j} = -i\omega \rho, \quad (2)$$

the Ohm's law,

$$\mathbf{j} = \sigma \mathbf{E}, \quad (3)$$

here \mathbf{E} is electric field vector, ρ is the charge density, i is imaginary unit, $i\omega$ is the phasor notation of time derivation, and σ is the electric conductivity.

The resulting equation for the electric potential U is:

$$\nabla \left(\left(\epsilon - \frac{i\sigma}{\omega} \right) \nabla U \right) = 0 \quad (4)$$

The solution of (4) gives the electric potential U and electric field $\mathbf{E} = -\text{grad}U$ at any point of the model.

B. Electric Field in the Cable Termination

We investigated the following design options:

Table 1

Option	Stress Cone Body		Stress Cone Reflector	
	Permittivity ϵ	Conductivity σ , (S/m)	Permittivity ϵ	Conductivity σ , (S/m)
1	1	0	1	0
2	2.5	0	2.5	0
3	22	0	2.5	0
4	22	0	2.5	0.0002

We want to know the electric field pattern in the area of breakage of the semi-conductive polymer core coating over the XPLE insulation. The electric field plot below is built over a horizontal line corresponding to the ending point of the polymer coating, where the field strength reaches its maximum.

Fig. 3. shows the electric field distribution along the horizontal line with the four design options from the table 1.

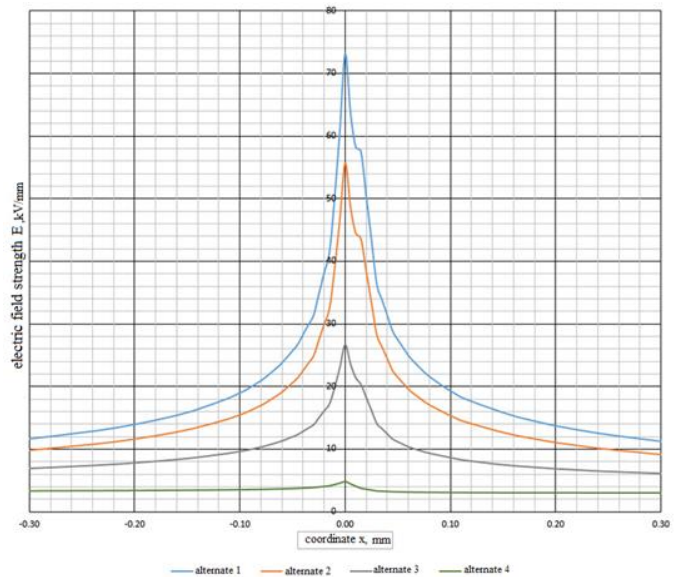


Fig.3 The field distribution in three different versions and properties of the cone reflector

Then we choose the design option that provides the greatest electric field reduction in the area A (Fig. 2), namely option 4, to see the field patterns in the other two problem areas: B (at the end of the cone reflector) and D (in a liquid dielectric). The plot of the maximum field in the zones B and D vs. the permittivity of liquid dielectric is shown in Fig. 4

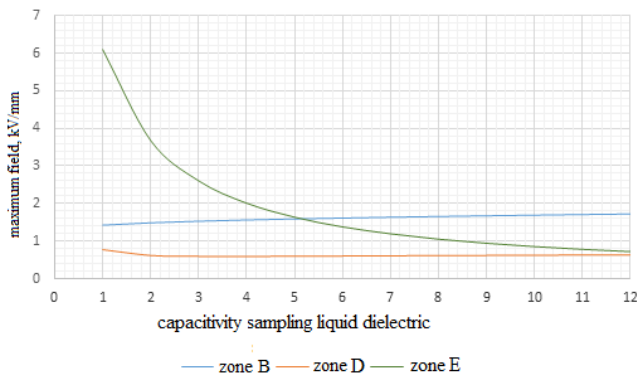
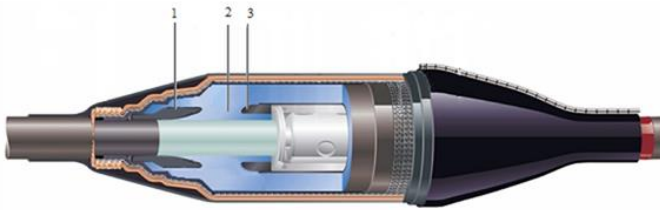


Fig. 4. Maximum field strength in areas B, D and E.

C. Electric Field simulations in the Cable Joint.

The field grading system of the cable termination is a bit more complicated than one of the cable joint we consider earlier. It contains two double-layer conical bodies (see fig. 5) connected by a cylindrical part, which also is double layered. The main body is manufactured from rubber with high insulating properties. The internal layers (shown in black on the fig. 5) include two cones (deflectors) and a cylindrical high voltage electrode are made from the molded rubber with relatively high conductance. Their role is grading of the electric field in the reinforcing insulation. The design of each deflector is similar to the stress cone reflector of the cable termination, which was described early. Therefore, the above consideration of problem areas A and B are still valid for the cable joint. In addition, we should focus on is another problem area - the zone C, located on the ends of the high voltage electrode.

The purpose of modeling - finding the optimal length of the baffle and the high voltage electrode. [7] Criteria - minimum electric field strength in the areas A, B and C.



1 - left side deflector; 2 - main insulating body; 3 - high-voltage electrode

Fig. 5 Stress cone coupling

We want to find the optimal length of each deflector and the length of the high-voltage electrode that minimize the magnitude of electric field E in the problem areas A, B and C. The FEA formulation (4) is used in an axisymmetric geometry domain. We have varied the length of the reflector in range from 250 mm to 170 mm with the step 20 mm. The electric field magnitude was recorded at two points:

1. Ending point of the semi-conductive coating over XPLE insulation, labeled as **P**;
2. Ending point of the reflector, which is the closest to the high voltage electrode, labeled as **Q**;

Table 2

The length of the Reflector, mm	E, κ V/mm at the point P	E, κ V/mm at the point Q
250	4,89	1,17
230	4,86	1,23
210	4,82	1,25
190	4,75	1,26
170	5,00	1,33

If the length of the high voltage electrode is smaller than the length of the sheath, another critical area is detected. It is located at the edge of the liner, where the electric field is much greater than the field at the end of the high voltage electrode.

The simulation results are summarized in Table 3

Table 3

The length of the high voltage electrode, mm	E, κ V/mm. (near electrode)	E, κ V/mm. (at the edge of the conductive sleeve)
280	5.11	0.0001
260	4.8	0.0008
200	4.79	0.0024
180	4.71	0.017
160	4.75	0.2
140	4.61	7.84

III. IMPEDANCE METHOD OF ELECTRIC FIELD GRADING.

A promising alternative to the capacitive stress grading with specially profiled stress cones is the impedance method. It is essentially the increasing of the longitudinal conductivity in cable joint or termination, and can be implemented by coating the XPLE cable insulation with one or more semi-conductive layers.

We consider a single layer coating over the insulation, called as *field grading tube*.

To simulate the effect of the parameters of the field grading tube we consider the following simplified model of the cable termination (fig. 6):

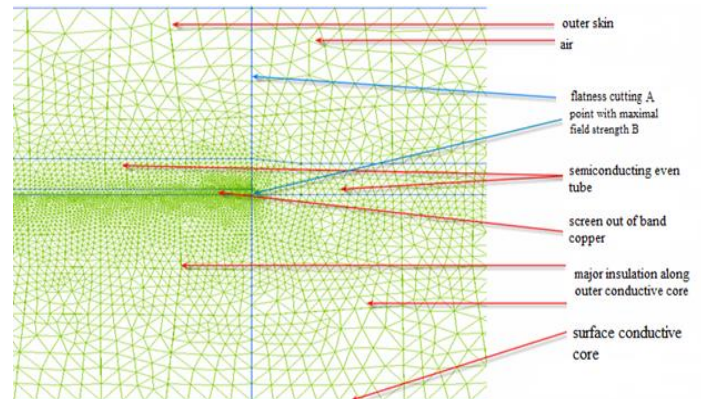


Figure 6 Calculation model cutting

There is a longitudinal sectional view of the cable [9] to the cutting of the outer shell.

The vertical line (indicated in blue) is a trace of the cutting plane A. To grading the electric field the XPLE insulation is coated by the semi-conductive tube with nonlinear electrical properties. The FEA simulation shows that the maximum magnitude of E field arises in the intersection of the plane A with the outer surface of XPLE insulation (point B).

The goal of analysis is finding the dependency of maximal electric field E on the conductivity of the grading tube. In this study we consider the conductivity as a constant in sake of simplicity.

The simulation results are presented in fig. 7

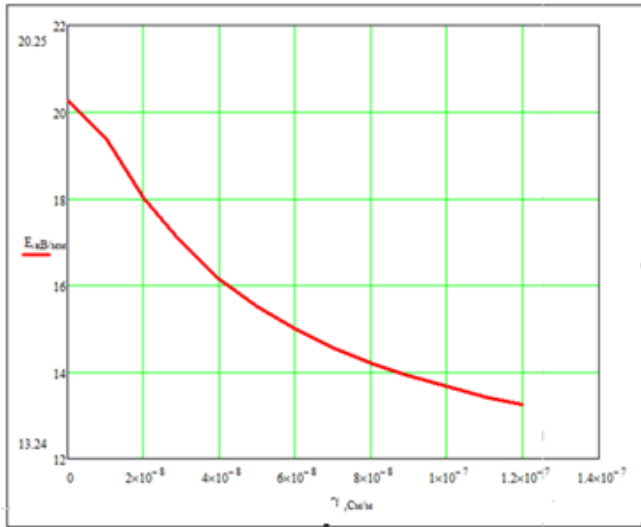


Figure 7. Maximum electric field vs. conductivity of grading tube

IV. CONCLUSION

The paper describes a method for electric field grading at the end of cable conductor, shield and semi-conductive coating. The method is based on a combination of material properties and the shape of the stress cone. The most dangerous area in the cable termination and joint are identified. FEA simulation of the electric field over dangerous areas is done with varying of geometric parameters and permittivity and conductivity of materials:

The most important results are following:

- The optimal shape of a semi-conductive reflector is a hollow cone with a specially selected length at a fixed angle between the generatrix and the longitudinal axis of the cable.
- The optimal value of the cone aperture is in range $\varphi = 8 \dots 14$.
- The optimal permittivity of the main insulation body of the stress cone is in range $\varepsilon = 22 \dots 24$.
- Comparing to cable termination, cable joint involves additional parameters to optimize. Recommendations are given concerning the length of the central high-voltage electrode.

Normally the mixture of an elastic polymer material with a conductive particulate filler can be used for the reflector.

When the line voltage is far from be pure sinusoidal, the refractive stress grading may be less effective. In such case the combination of geometrical and impedance stress grading method is applicable.

The FEA model of the impedance field grading method is proposed. The dependency of field grading effectiveness vs. the conductivity of grading tube is given. The using of stress grading tube with field dependent conductance is a subject of

further investigation.

REFERENCES

- [1] T. Christen, L. Donzel, and F. Greuter, "Nonlinear resistive electric field grading part 1: Theory and simulation," *IEEE Electr. Insul. Mag.*, Vol. 27, no. 2, pp. 18-28, March. / April. 2011.
- [2] T. Christen, L. Donzel, and F. Greuter, "Nonlinear resistive electric field grading part 2: Materials and Applications," *IEEE Electr. Insul. Mag.*, Vol. 26, no. 6, pp. 48-60, Nov. / Dec. 2010.
- [3] Schwartzman L.G "Regulation of the electric field in the terminations of high voltage cables" *M., Energy, Proceedings VNIIEP, Issue 13, 1969.* (in Russian)
- [4] Demirchyan K.S, Neumann L.R, N.V Korovkin - Theory of Electrical Engineering. In 2 volumes, St. Petersburg, 2009, Peter. (in Russian)
- [5] G.V Greshnyakov, N.V Korovkin, S.D Dubitskiy, G.G Kovalev, "Numerical simulation of the electric field in increasing isolation pothead" *Cables and wires, № 4, 2013, p.9-14.* (in Russian)
- [6] Claycomb J. R. *Applied Electromagnetics Using QuickField and MATLAB.* - Laxmi Publications, Ltd., 2010.
- [7] Patent number 97013 "Coupling power cable." Authors: Greshnyakov GV, Zhuravlev I.V., Matveev A.V.. Registered in the State Register of Utility Models 20 August 2010. Patent validity expires on 29 December 2019. (in Russian)
- [8] Greshnyakov G.V, S.D Dubitskiy "Combined method for reducing non-uniformity of the electric field in the terminations of power cables," *Power Electronics, № 2, 2010.* (in Russian)
- [9] Greshnyakov G.V, Dubitskiy S.D "Mathematical modeling of the electric field in the terminations of power cables," *Power Electronics, № 3, 2010.* (in Russian)
- [10] Adalev,A.S., Korovkin,N.V., Hayakawa,M., Nitsch,J.B. Deembedding and unterminating microwave fixtures with the genetic algorithm (2006) *IEEE Transactions on Microwave Theory and Techniques, 54(7), pp. 3131-3139.*
- [11] Adalev,A.S., Korovkin,N.V., Hayakawa,M. Identification of electric circuits described by ill-conditioned mathematical models. (2006) *IEEE Transactions on Circuits and Systems I: Regular Papers, 53 (1), pp. 78-91.*
- [12] Adalev,A.S., Korovkin,N.V., Hayakawa, M. Using linear relations between experimental characteristics in stiff identification problems of linear circuit theory. (2008) *IEEE Transactions on Circuits and Systems I: Regular Papers, 55 (5), pp. 1237-1247.*

George V. Greshniakov is currently a head of laboratory in the Sevcabel research institute. He receives the MSc and PhD degrees in electrical engineering from St. Petersburg technical university (SPbSPU) in 1983 and 1992 respectively. He is also a docent in SPbSPU teaching cable and insulation engineering. Author of more than 30 reviewed papers. His research interest is electromagnetics and thermal analysis of power cable installation and development of advanced cable accessories.

Simon D. Dubitskiy is currently with Tor Ltd, St. Petersburg. He receives MSc degrees in electrical engineering in 1983 and in computer science in 2003 both from SPbSPU. His main area of activity is development of QuickField FEA software in cooperation with Tera Analysis company located in Svendborg, Denmark. Main research interest is implementing FEA as a handy tool for everyday engineering practice, advanced postprocessing of electromagnetic field solution, multiphysics FEA analysis coupled with circuit equations and surrogate models.

Nikolay V. Korovkin, professor, is currently head of Electromagnetic Theory Department of St. Petersburg State Polytechnic University (SPbSPU). He received the M.S., Ph.D. and Doctor degrees in electrical engineering, all from SPbSPU in 1977, 1984, and 1995 respectively, academician of the Academy of Electrotechnical of Russian Federation, (1996) Invited Professor, Swiss Federal Institute of Technology (EPFL), Lausanne (1997), Professor, University of Electro-Communications, Department of Electronic Engineering, Tokyo, Japan (1999-2000), Professor EPFL (2000-2001), Otto-fon-Guericke University, Germany (2001-2004). Head of the Program Committee of the Int. Symp. on EMC and Electromagnetic Ecology in St. Petersburg, 2001-2011.

His main research interests are in the inverse problems in electro-magnetics, optimization of power networks, transients in transmission line systems, impulse processes in linear and non-linear systems, "soft" methods of

optimization, systems described by stiff equations, the problems of the electromagnetic prediction of earthquakes and identification of the behavior of the biological objects under the influence of the electromagnetic fields

Redundant generating supply in electric power systems

Nikolay A. Belyaev, Nikolay V. Korovkin, Oleg V. Frolov and Vladimir S. Chudny
Saint-Petersburg State Polytechnic University, RUSSIA

Abstract—Issues pertaining to calculations of parameters of capacity adequacy and redundant generating supplies in power systems have been studied in this paper. Basic procedures and algorithms for determination of loss-of-load probability and reserve power capacity have also been studied. Relevant calculations have been performed for power system of Saint-Petersburg and Leningrad region. Taking into account the main influence factors calculations of distribution series of loss-of-load probabilities in power systems have been executed. The necessary power reserve corresponding to different values of survival probability has been determined.

Keywords - electric power system, power deficiency, capacity adequacy, reserve power.

I. INTRODUCTION

TO assure a required level of power supply reliability in electric power systems (EPS) the reserve is provided to compensate power deficiency. The deficiency occurs due to some factors:

- accidental failure of EPS equipment;
- line interconnection imperfection,
- seasonal losses of available capacity and consumption deviations.

The above factors are generally of arbitrary nature, so occurrence of power deficiency in EPS is an accidental event that increases the complexity of power reserve calculations [1, 2].

Studies concerning the determination of required power reserve are vital both in Russia and abroad. Due to a high level of time consuming and computational complexity of this type of tasks no common approach has been elaborated to assess power reserves in EPS of arbitrary configuration. This condition makes impossible to perform a clear validation of option strategy for generating facilities development and EPS as a whole and to define meaningful levels of generation redundancy and modes of its usage in EPS [1].

The goal of this paper is to develop and study the procedure for determination of capacity adequacy (CA) levels and to

calculate the reserve capacity corresponding to CA target value. The studies are performed with the use of prospective plan of Saint-Petersburg and Leningrad region EPS [1].

The proposed approach is based on the application of high-performance algorithms to calculate the loss-of-load probability in EPS making possible to determine CA parameters of reserve capacity with due account made for influence factors for EPS of maximum comprehensive model.

II. PARAMETERS OF CAPACITY ADEQUACY AND APPROACHES TO CALCULATE THEM

The level of CA is defined on the basis of parameters featuring the loss of load probability in EPS. The most important are the following: frequency and duration of outages due to power deficiency, volume of unserved energy, volume of redundant generating supplies. The main parameters used abroad for CA rating are the following [3, 4]:

- loss of load probability (LOLP), loss of load expectation (LOLE) over particular periods of time;
- expected unserved energy (EUE);

In Russian practice is used the notion of integral probability J of power shortage absence (system survival probability) whose value is specified as a relative duration of EPS survival:

$$J = 1 - \frac{t}{T},$$

where t – number of operating hours of EPS with power shortage specified over a base period, T – total duration of base period. The parameter J has been successfully used in practice for the assessment and comparison of CA levels of EPS. Hereinafter the parameter J will be used. The values of parameters given above (LOLE, LOLP, EUE) at designed value of J may be specified by using equations [3].

The complexity of CA level assessment is due to an ambiguity of some source data. For example, an accidental failure of a generator is considered as causal event, so an emergency decrease of power generation is an uncertainty factor. This factor is available in forecasts of disposable capacity for power plants. An uncertainty factor is the forecast error of volumes and power-ups.

Because of these uncertainty factors there are two major approaches for calculating power deficiency in EPS: statistical simulation methods and analytical methods. Methods of statistical chronological or non-chronological simulation calculate CA parameters when analyzing a multitude of EPS arbi-

Nikolay A. Belyaev is with the Saint-Petersburg State Polytechnic University, Russia (e-mail: Belayev.NA@yandex.ru).

Nikolay V. Korovkin is with the Saint-Petersburg State Polytechnic University, Russia (e-mail: nikolay.korovkin@gmail.com).

Oleg V. Frolov is with the JSC «Scientific and Technical Center of Unified Power System», Russia (e-mail: ntc@ntcees.ru).

Vladimir S. Chudny is with the Saint-Petersburg State Polytechnic University, Russia (e-mail: chudnyvs@yandex.ru).

trary states. Methods of chronological simulation provide for successive simulation of base time at each time segment. The non-chronological simulation means the consideration of extreme and the most dangerous from the point of view of power shortage situations with respect to system configuration and operating modes, at that an auxiliary device detecting such situations is required. A large amount of calculations and the use of extended statistical data allowing to obtain rather objective results characterize these methods.

Analytical methods use a functional representation of distribution of probability values defining the deficiency occurrence and further addition of distribution series of given probabilities in order to build the distribution of loss of load probabilities in EPS. Analytical methods make possible to calculate the occurrence probability and loss of load value. Moreover, these methods allow to perform the analysis of studied EPS as a whole, in particular to define the factors of full influence on shortage occurrence and its value. An essential fault of these methods was a high complexity of obtaining analytical distribution of loss of load probabilities which resulted in unfounded simplifications of original model. The use of modern software systems allows to reject simplifications and obtain a certainty with accuracy corresponding to that one of initial data.

As it was mentioned above, CA levels of EPS are assured by power reserve. The value of power reserve determines the probability value J of EPS survival. In this context the value of power reserve may be also a value featuring CA of EPS and the task to ensure a target level of EPS CA at long-term planning is equivalent to the determination of the value of required power reserve and its location. The task of capacity reserve calculation with due account made for all influence factors as well as that one for calculation of CA parameters are time consuming computational processes.

In the present paper is described the development of an approach to calculate redundant generating supply and define EPS CA parameters. Designed algorithms allow to calculate in an efficient way the target values and assess the influence of major factors. Algorithms are developed for a comprehensive model of EPS, where interconnections between EPS nodes and generating supplies do not limit their mutual redundancy. The structure of prospective plan of Saint-Petersburg and Leningrad region EPS corresponds to a typical structure of large city EPS featuring a relatively high network density and a short length of power transmission lines. In this context the application of a complete model for calculations of studied EPS may be considered as correct. Factors defining CA levels and respectively the value of power reserve may be divided into two groups when considering a complete EPS model – those associated with state changes of generating equipment and those ones pertaining to power consumption modes.

Among first group factors the major are the following: fault rates of power plant units and seasonal variation of available power plant capacity. The fault rate is due to a final level of power plant equipment reliability when each unit or power set features a specific probability of its breakdown. An accidental failure of a set or unit will result in decrease of power generation in EPS. A seasonal variation of available power plant

capacity is due to variation of heat demand over a year and variation, throughout the year, of water flow in rivers fed by snow. A particular factor of this group is a scheduled outage of power plant equipment, for example, for planned repairs. A scheduled outage of sets and power units is not an accidental event and it may be provided when designing the structure of generating capacities of EPS and calculating the value of available capacity. Among the factors associated with power consumption modes we shall note the following: irregular power consumption and forecast error of energy and capacity demand. Irregular power consumption is due to regular consumption variations both daily and annual. In this context during different time periods the loss of load probabilities are also different being increased during peak loads and decreased during energy saving. While considering particularly winter and summer conditions one should take into account daily irregular power consumption. Moreover, when performing long-term planning one should consider potential deviations of consumption as compared to forecast values which are due, for example, to weather or economic factors that affect CA levels of EPS.

III. CALCULATION OF CAPACITY ADEQUACY LEVELS AND POWER RESERVES

The calculation of CA levels and justification of generation reserves are based on the calculation of loss of load probability and its value in EPS which in its turn is necessary to perform calculations of CA parameters. When calculating the loss of load one must consider influence factors and build the distribution of loss of load probabilities for a studied EPS.

Let us consider the distribution of loss of load probabilities with due account made for three major influence factors studied here above:

- fault rate of generating equipment;
- irregular power consumption;
- forecast error of energy and capacity demand.

To know the target distribution one should add obtained distributions of emergency generating power decrease, regular consumption decreases and deviations of consumption as compared to forecasted ones. Let us summarize in brief the peculiarities of given distributions. The distribution of emergency generation decrease is discrete and suggests only the decrease of generation capacity, that is to say the deficiency increase. The regular consumption decreases vice versa may result only in deficiency decrease and are also discrete if we consider the consumption chart presented as 24-value power consumption. The distribution of consumption deviations as compared to forecasts as it was noted above, is symmetrical and continuous while suggesting both increase and decrease of power deficiency.

To build the distribution of loss of load probabilities means an addition of distribution series of established values. The addition is performed according to known rules and, due to the use of modern computers, there are no computational difficulties for a studied task. An integral curve of loss of load probabilities obtained for a studied EPS of Saint-Petersburg and Leningrad region is shown on Fig. 1. On this chart on x-

axis is plotted the deficiency $P_{def.}$, while on y-axis – its probability $Q_{def.}$. The peculiarity of obtained distribution is to be mentioned: an integral curve presented on figure 1 crosses y-axis not in point 1 but at y-coordinate equal to $\sim 0,72$. It means that the probability of any deficiency occurrence in EPS is equal to 72 % while if the probability makes 28% the EPS operates without deficiency even in the absence of power reserve. This is due to the fact that in obtained distribution all potential decreases of power consumptions caused by irregular consumption and forecast errors have been accounted for.

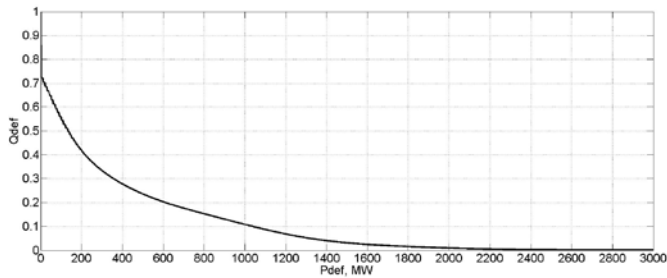


Fig. 1 – Integral distribution of loss of load probabilities for SPb and Leningrad region EPS

An integral distribution of loss of load probabilities may be used to determine CA parameters or redundancy value. These two tasks are reciprocal in terms of problem formulation, that is to say that CA parameters shall be established for a given composition of generating equipment including reserve capacity and the value of required reserve capacity shall be defined upon a set value of CA parameter to be assured by reserve capacity. The graph shows an integral curve, in this case y-coordinates mean the loss of load probability in value greater or equal to respective values of x-coordinates. That is the probability of loss of load exceeding 600 MW is equal to 0,2 and to 0,1 in case of exceeding 1000 MW (Fig. 1) and so on. In this context the capacity reserve in EPS up to 1000 MW will ensure the probability of loss of load occurrence of not greater than 0,1 (10%) as any loss of load up to 1000 MW may be compensated by redundant supply and the state of EPS deficiency may occur only when it exceeds the reserve. When the loss of load probability is 0,1 the probability of system survival J will be equal to 0,9.

On Fig. 2 is presented a zoomed segment of integral curve of loss of load probability distribution (full line graph) given on figure 1. The process of establishing target values is shown here. In Russian practice of EPS designing the rated CA value is $J=0,996$ which is justified by relevant technical and economic assessment [3]. $J=0,996$ corresponds to the probability of loss of load not exceeding 0,004. To ensure a given probability it is necessary to have the capacity reserve in EPS of 2256 MW (Fig. 2). When solving a reciprocal task if the reserve of 2256 MW is available in EPS, the probability of system survival will make 0,996. To ensure a higher level of CA $J=0,998$ (value adopted in Slovenia) and $J=0,999$ (value adopted in Finland) it is necessary to provide the probability of loss of load not greater than 0,002 and 0,001 and capacity

reserve of 2455 MW and 2671 MW respectively. That is to say that to increase the level of CA from $J=0,996$ to $J=0,999$ the reserve of capacity must be increased by 415 MW.

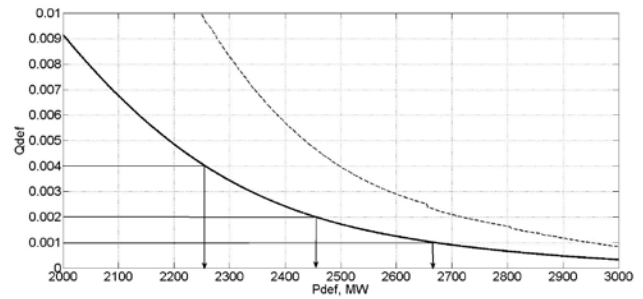


Fig. 2 – Establishing CA parameters and capacity reserve values

On figure 2 is also shown a dotting presentation of integral curve of distribution of emergency generation decrease probabilities. The comparison of two curves on figure 2 shows that the probability of loss of load of the same value is below the probability of generation decrease. That is to say that an addition of irregular power consumption and consumption deviations as compared to forecasted values made it possible to decrease a required reserve in EPS by ~ 250 MW (for $J=0,996$).

Hence, the developed approach allows to perform the calculation of loss of load probabilities in EPS and to define CA parameters and required redundant capacities with due account made for influence factors. If necessary, the account for influence factors may be extended, for example, consideration of weekly irregular consumptions, characteristic spread of load curve, deviations of power plant available capacity at weather conditions changing etc. To calculate the loss of load probabilities the developed algorithms allow to process a larger amount of initial data without increasing span times for their calculations.

This chapter gives the calculation results for a complete model of EPS the utilization of which in large city, as it was mentioned above, is correct. However, the consideration of final transmission capacities between EPS nodes imposes constraints on the transfer of reserve power [5, 6]. That may require an increase of power reserve to keep an established level of capacity adequacy. The value of required power reserve in this case will also depend on its location. To optimize the power reserve location there may be used different approaches including those based on application of fractional-polynomial functions [7-9].

IV. CONCLUSION

The development and study of the method for calculation of CA parameters and redundant generating supplies have been performed in this paper, relevant calculations have been done for Saint-Petersburg and Leningrad region power system. The structure of generating equipment has been analyzed for a studied EPS as well as energy consumption regimes and forecasting accuracy of energy and capacity demands. Taking into account the major influence factors there has been performed

a series of calculations of loss of load probabilities of EPS and the values of required redundant capacity corresponding to different values of system survival probabilities have been set.

To solve the formulated tasks special algorithms have been developed, they allow to build in an efficient way the series of probability distribution and their processing and to define an emergency decrease of generating power in EPS, the loss of load probability, the required redundant capacity. These algorithms are aimed at creating a specialized programming and computing suite to solve the tasks of prospective planning of EPS.

REFERENCES

- [1] Belyaev N.A., Yegorov A.Ye., Korovkin N.V., Chudny V.S. Analysis of capacity adequacy as a critical task for Russian UES electric power system development // Scientific-technical gazette of SPbPU – 2013 – №2 – pp. 44-51.
- [2] Calculation of operative reserve in electric power systems // N.A.Belyaev, A.Ye. Yegorov, N.V.Korovkin, V.S.Chudny // Proceedings of Scientific Research Center of United Energy System. – 2013. – № 2(69). – pp. 50-68.
- [3] Chukreev Yu.Ya. Comparison of national and foreign probability parameters of CA of electric power systems. // Proceeding of the Russian Academy of Sciences. Energetika – 2012. – №6. – pp. 27 – 38.
- [4] Billington Roy, Ronald N. Allan. Reliability Evaluation of Power Systems. Second Edition, – New York and London: Plenum Press, 1996 – 509 p.
- [5] Korovkin, N.V., Berlin, E.M., Efimov, K.A. The operation modes of the controlled electric transmission with the link based on the multiphase thirsters switch phase convertor (1991) Izvestiya Akademii Nauk Energetika, (1), pp. 28-37.
- [6] Adalev, A.S., Korovkin, N.V., Hayakawa, M. Using linear relations between experimental characteristics in stiff identification problems of linear circuit theory. (2008) IEEE Transactions on Circuits and Systems I: Regular Papers, 55 (5), pp. 1237-1247.
- [7] Belyaev N.A., Korovkin N.V., Frolov O.V., Chudny V.S. Using bilinear expression to solve the problems for optimization of power flows in electric power systems // Electric power facilities and control system – 2012 – №1 – pp. 77 – 80.
- [8] Research of approaches for optimization of power system performance / N.A.Belyaev, N.V. Korovkin, O.V. Frolov, V.S. Chudny // Elektrotehnika – 2013. – №2. – pp.21-29.
- [9] Mathematical description of active-adaptive devices affecting EPS performance / N.A. Belyaev, N.V. Korovkin, V.S. Chudny //Elektrichestvo. – 2014. – №2 – pp. 18-24.

Nikolay A. Belyaev was born in Leningrad, Russia, on February 20, 1989. He received the M.S. degree in electrical engineering from St. Petersburg State Polytechnical University, Russia, in 2012. In 2012 he graduated the St. Petersburg State Polytechnical University. From 2009 he worked as an engineer of JSC «Scientific and Technical Center of Unified Power System», Russia. The main directions of his investigations are capacity and recourse and capacity adequacy, power systems optimization and optimal choice and allocation of FACTS devices.

Nikolay V. Korovkin was born in Leningrad, Russia, on January 09, 1954. He received the M.S., Ph.D. and Doctor degrees in electrical engineering, all from St. Petersburg State Polytechnical University in 1977, 1984, and 1995 respectively. He worked as a Professor for the University of Electro-Communications (Tokyo, Japan), for the Swiss Federal Institute of Technology (EPFL) Switzerland, and for Otto-von-Guericke University (Magdeburg, Germany). His main scientific interests are EMC problems, stiff systems, impulse processes in linear and non-linear systems, "soft" methods of optimization. Now he is the head of the department of Theoretical Engineering in St. Petersburg State Polytechnical University. Prof. N. Korovkin is a Member of the Academy of Electrotechnical Science of the Russian Federation, (since 1996).

Oleg V. Frolov was born in Leningrad, Russia, on July 29, 1972. Graduated from Saint-Petersburg State Polytechnical University, "Electrical power systems and networks" department in 1995. Worked in Saint-Petersburg and North-West region electrical systems management companies. Received the Ph.D. degree in 2007. Now he is a CEO of the High Voltage Direct Current Transmission System Research Institute, Russia. His main scientific interests are smart grids, stability of power grid parallel operation and application of controllable shunt reactors and FACTS devices.

Vladimir S. Chudny was born in Leningrad region, Russia, on August 22, 1975. He received the B.S., M.S. and Ph.D. degrees in electrical engineering, all from St. Petersburg State Polytechnical University, Russia, in 1996, 1998, and 2002, respectively. In 2002 he worked as a Teaching Assistant for St. Petersburg State Polytechnical University, Department of Electrical Power Systems and Networks, and became an Assistant Professor at the same organization in 2003. He gained a practical experience at the High Voltage Direct Current Transmission System Research Institute, Russia, filling a post of Researcher Engineer from 1998. The main directions of his investigation are stability of power grid parallel operation and application of controllable shunt reactors and FACTS devices.

New approach to the power network protection against ultrawide band pulses

Alexander T. Gazizov, Alexander M. Zabolotsky

Abstract— Use of modal filtration is proposed as a new approach of power network protecting against threat of ultra wide band pulses. A new structure of modal filter, based on widely used FR-4 material, is considered. Dependencies of its characteristics on width and separation of conductors and thickness of a dielectric are simulated. Possibility for modal filter 0.75 m in length to decrease by factor 7 the magnitude of input pulse with total duration of 3 ns is shown. Possibility of fast estimations for asymmetrical structures of modal filter is revealed.

Keywords—FR-4, modal filter, PCB technology, power system, protection, ultrawide band pulse

I. INTRODUCTION

Nowadays there is an increasing threat of the impact of ultrawide band (UWB) pulses in power systems. Such an impact can result in a malfunction or failure of electronic equipment. Therefore, protection of computer devices and systems, controlling the critical equipment (especially energy equipment), is extremely important. As a rule, existing surge protectors do not protect against UWB pulses [1]. It is known only about some industrial devices that protect against UWB pulses but have large dimensions and high cost. Thus, currently there is no both effective and cheap protection against UWB pulses. However, the increasing role of electronics in our life makes this protection essential.

The idea of modal filtration has been suggested recently and several devices based on modal filtration principle have been developed. Among them there are symmetrical structures of modal filters (MF) for the Fast Ethernet network [2], for lightning [3] and electrostatic discharge [4] protection. However, the usage of the MF in power systems is investigated insufficiently. Particularly, MF based on PCB technology (PCB MF) built into the power supply filter has not been considered yet. Meanwhile, such an application of the MF can provide effective and cheap protective device.

In this paper we propose creation of the MF embedded to a power supply filter for UWB pulses suppression. For example, the MF can be formed as a thin strip of foiled fiberglass and this strip can be inserted into the socket unit: a

separate one or as a part of the power supply filter. To realize this idea it is necessary to do: preliminary analysis of the possibility of MF usage in the power network; tentative simulation of electrical characteristics of a device; optimization of its parameters on the specified criteria; design and development of a prototype device. The paper focuses on the first two stages of this idea realization.

II. COMPARISON

Creation and implementation of the MF prototype embedded in the process of power supply filters production opens several prospective advantages over existing solutions. Initial comparison of the characteristics of proposed MF and existing devices (a typical surge protector and special industrial design of a new UWB pulse suppression filter [5]) is presented in Table I. It can be seen that the MF built in power supply filter combines all the advantages of common devices, and at the same time it costs just slightly more expensive.

Table I. Comparison of the characteristics of protective devices

Parameters	Modal filter	Surge protector	Industrial Filter
Duration of impulse noise (ns)	<1	>1	<1
Cost (rub.)	50+cost of surge protector	500–2500	183000
Dimensions	Inside the surge protector	Surge protector dimensions	400*300*5 mm
Resistance to radiation	High	Low	High
Durability	High	Low	Low

Thus, the proposed solution can provide an affordable, popular and effective protection of electronic devices from UWB pulses propagating through the mains.

III. SIMULATION

Simulation is based on quasi-static analysis which has been implemented in the TALGAT system [6]. Matrixes **L**, **C** are calculated by a method of moments with following parameters of the proposed MF having asymmetrical cross section (Fig. 1a): separation of conductors $s=5, 10, 15$ mm; width of conductor $w=5, 10, 15$ mm; dielectric thickness $h=0.5, 1, 1.5$ mm (typical substrate values); conductor thickness

This work was supported under of Russian Science Foundation grant (project №14-19-01232) in Tomsk State University of Control Systems and Radioelectronics.

A. T. Gazizov is with National Research Tomsk Polytechnic University, Tomsk, 634050, Russia (phone: +7 3822 413439; e-mail: alexandr.bbm@gmail.com).

A. M. Zabolotsky is with Tomsk State University of Control Systems and Radioelectronics, Tomsk, 634050, Russia (zabolotsky_am@mail.ru).

$t=105 \mu\text{m}$ (high thickness of foil to withstand high currents); distance between the edge of the structure and the conductor $d=w$; relative permittivity $\epsilon_r=4$ (cheap and widely used FR-4).

Calculation of time response is carried out in a lossless approximation. Pulse signal was excited between active (A) and reference (R) conductors (Fig. 1a). MF circuit diagram is shown in Fig. 1b, where e.m.f. source parameters: rise, top and fall times $t_r=t_f=t_d=1 \text{ ns}$ while the magnitude is 2 V ; length $l=0.75 \text{ m}$; U_1-U_5 – nodes; R – resistances equal to the geometric mean of the even and odd modes impedances.

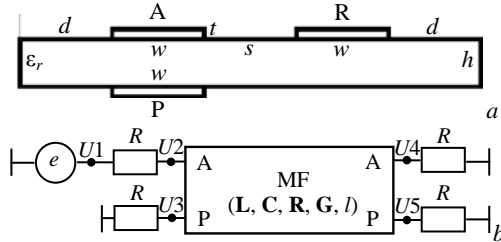


Fig. 1. Cross section (a) and circuit diagram (b) of the MF

Waveforms at the near and far ends of an active conductor of the MF and also a number of important parameters are calculated. Among them there are per unit length delays of even and odd modes and their differences, geometric means of even and odd modes impedances, MF attenuation coefficient calculated by analytic formula (obtained for MF cross sections being symmetrical about the reference conductor) [7]:

$$U_A=2k/(k+1)^2, \quad (1)$$

where $k=(Z_e/Z_o)^{1/2}$ with $Z_e>Z_o$.

Waveforms, calculated for $h=0.5; 1; 1.5 \text{ mm}$, are shown in Fig. 2–4 respectively, and other parameters are presented in Tables II–IV. It should be noted that the waveforms are presented only for $s=5 \text{ mm}$, because effects of the s value on calculated waveforms for each w value are negligible. Meantime, the small effects exist, and to show it the calculated parameters for each s value are presented in Tables II–IV.

As one can see from the plots of Fig. 2–4 there is no complete pulse decomposition with selected parameters of the structure and the pulse. However, the complete pulse decomposition is not required, because it only increases an undershoot between two decomposed pulses not decreasing their magnitudes (see Fig. 2). On the other hand, the increase of two pulses overlapping increases an overshoot degrading the protection (see Fig. 4). In any case, a desired result can be achieved by proper choice of the MF parameters with defined pulse duration. For example, it is enough to achieve the MF output waveform (U_4) as in Fig. 2a or Fig. 3c. Anyway, one can see from Fig. 2–4 that MF attenuates input pulse, because U_4 value is less than U_2 value about: 5.3 times for $h=0.5 \text{ mm}$; 4 times for $h=1 \text{ mm}$; 3.5 times for $h=1.5 \text{ mm}$. As for w value, its increasing improves attenuation for defined h values.

From the Tables II–IV it can be seen that the maximum value of the per unit length modal delays difference is about 3 ns/m for $h=0.5 \text{ mm}$ and the value decreases to 2.67 ns/m with increase of the h value (Table IV, $w=s=15 \text{ mm}$). It increases slightly with increase of the s value for defined w

value, while it increases more considerably with increase of the w value for defined s value. Exact estimations can be seen from the Tables II–IV.

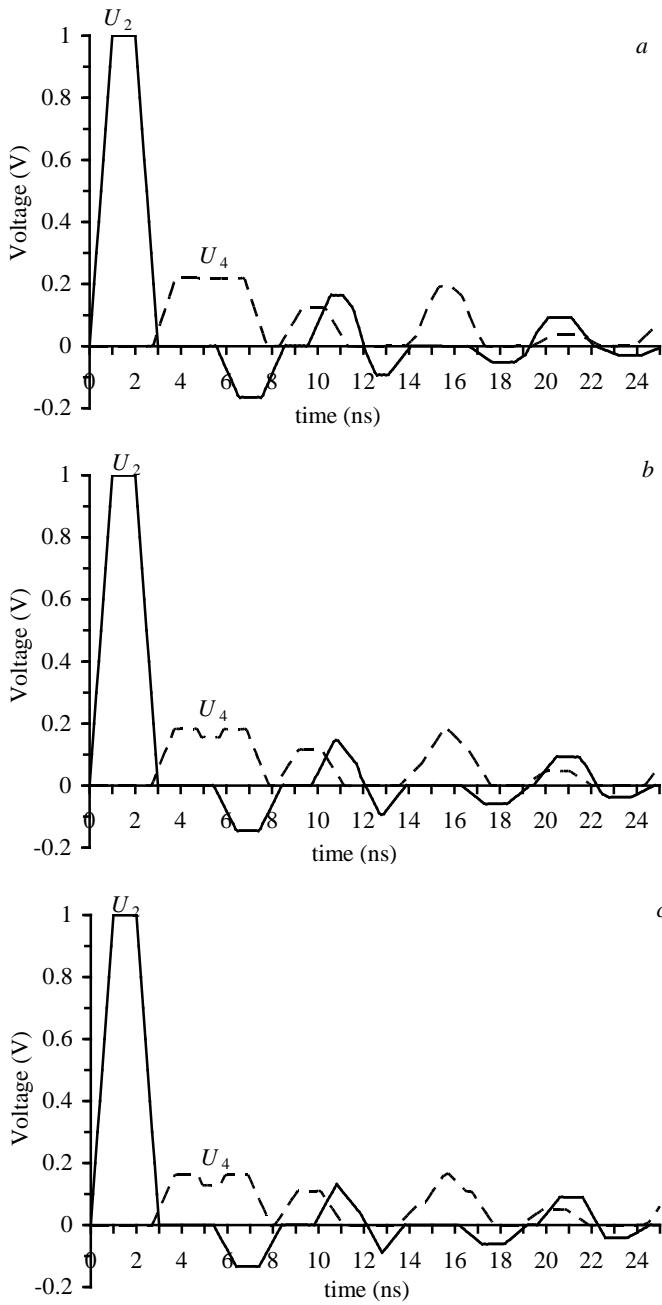


Fig. 2. Waveforms at the near and far ends of an active conductor of the MF with $h=0.5$ mm, $s=5$ mm for $w=5$ (a), 10 (b), 15 (c) mm

Table II. Per unit length delays of even and odd modes and their differences, geometric means of even and odd modes impedances, magnitudes of decomposed pulses (analytics and simulation) from Fig. 2

w , mm	s , mm	τ_e , ns/m	τ_o , ns/m	$\Delta\tau$, ns/m	$(Z_e Z_o)^{1/2}$, Ω	U_A , V	U_S , V
5	5	3.69872	6.37276	2.67403	57.9027	0.219	0.22
	10	3.61557	6.37277	2.75721	65.2746	0.2	0.2
	15	3.57982	6.37278	2.79295	69.748	0.19	0.19
10	5	3.62877	6.49007	2.8613	38.8676	0.182	0.184
	10	3.55632	6.49009	2.93377	43.5997	0.166	0.174
	15	3.52627	6.49009	2.96382	46.5709	0.157	0.167
15	5	3.59534	6.53826	2.94292	30.629	0.161	0.162
	10	3.52749	6.53828	3.01079	34.1987	0.147	0.156
	15	3.49987	6.53828	3.0384	36.4754	0.139	0.15

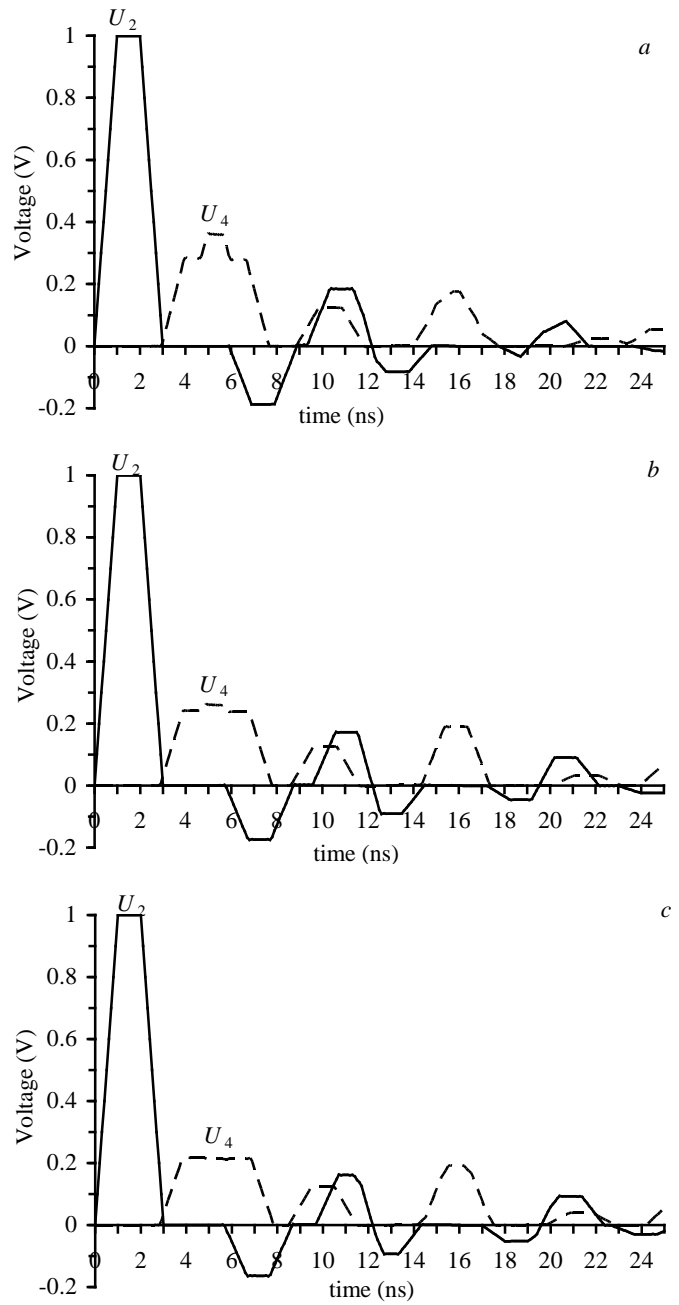


Fig. 3. Waveforms at the near and far ends of an active conductor of the MF with $h=1$ mm, $s=5$ mm for $w=5$ (a), 10 (b), 15 (c) mm

Table III. Per unit length delays of even and odd modes and their differences, geometric means of even and odd modes impedances, magnitudes of decomposed pulses (analytics and simulation) from Fig. 3

w , mm	s , mm	τ_e , ns/m	τ_o , ns/m	$\Delta\tau$, ns/m	$(Z_e Z_o)^{1/2}$, Ω	U_A , V	U_S , V
5	5	3.93615	6.2275	2.29135	75.0687	0.28	0.28
	10	3.79757	6.22754	2.42997	85.3977	0.257	0.27
	15	3.73422	6.22755	2.49332	91.6787	0.244	0.26
10	5	3.83132	6.38645	2.55513	51.5882	0.239	0.24
	10	3.70961	6.3865	2.67689	58.3563	0.218	0.23
	15	3.65593	6.38651	2.73058	62.5919	0.2	0.22
15	5	3.77899	6.45671	2.67772	41.0766	0.215	0.21
	10	3.66448	6.45676	2.79228	46.2361	0.196	0.2
	15	3.61502	6.45677	2.84175	49.5065	0.186	0.2

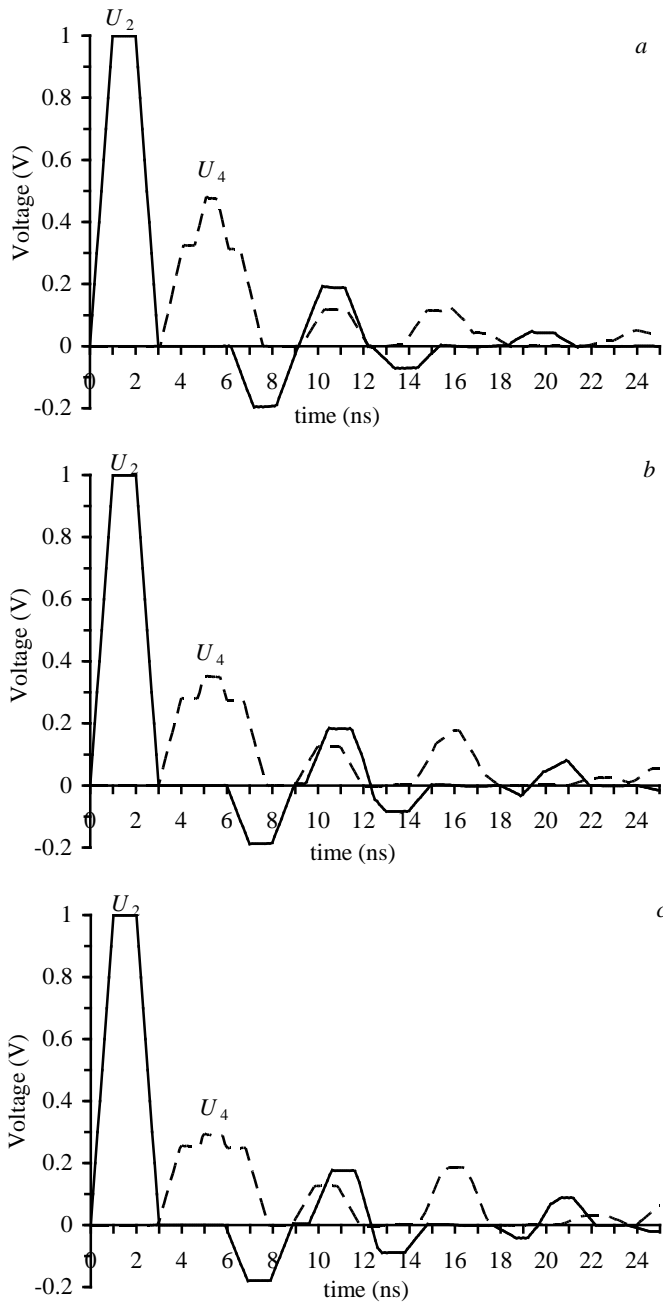


Fig. 4. Waveforms at the near and far ends of an active conductor of MF with $h=1.5$ mm, $s=5$ mm for $w=5$ (a), 10 (b), 15 (c) mm

Table IV. Per unit length delays of even and odd modes and their differences, geometric means of even and odd modes impedances, magnitudes of decomposed pulses (analytics and simulation) from Fig. 4

w , mm	s , mm	τ_e , ns/m	τ_o , ns/m	$\Delta\tau$, ns/m	$(Z_e Z_o)^{1/2}$, Ω	U_A , V	U_S , V
5	5	4.12025	6.1263	2.00605	85.794	0.318	0.32
	10	3.94481	6.12636	2.18155	98.1383	0.293	0.311
	15	3.85987	6.12637	2.2665	105.719	0.279	0.3
10	5	3.99303	6.30743	2.3144	60.0036	0.277	0.28
	10	3.83783	6.30754	2.46971	68.2368	0.253	0.269
	15	3.76535	6.30755	2.5422	73.4182	0.24	0.26
15	5	3.92751	6.39198	2.46448	48.1629	0.251	0.25
	10	3.78086	6.39209	2.61123	54.4967	0.23	0.243
	15	3.7139	6.3921	2.6782	58.525	0.218	0.235

It is important to note that similar dependences on h , s and w are also observed for magnitudes of decomposed pulses as it may be concluded after close examination of two last columns of the Tables II–IV. However, there is another important conclusion also. Comparison of decomposed pulses magnitudes obtained from analytic calculations using (1) (U_A) and from waveforms (U_S) show its very close coincidence. Consequently, the analytic formula (1) obtained for symmetrical MF structures can be used for fast estimations of asymmetrical MF structures, at least, in the considered (matched) case when all the resistances are equal to geometric mean of the even and odd modes impedances.

IV. CONCLUSION

In this paper the asymmetrical structure examination has been carried out for the purpose of implementation of the MF, based on widely used FR-4 material for typical thicknesses of 0.5–1 mm with 105 μm foil thickness. Besides, calculations in parameter ranges which allow the evaluation of structure parameters influence on the difference between per unit length delays of modes and the evaluation of MF attenuation coefficient are accomplished. As a result, the maximum value of difference between per unit length delays of modes, 3 ns/m, and the maximum MF attenuation coefficient, 0.15, are obtained when $h=0.5$ mm, $s=w=15$ mm. It permits for MF 0.75 m in length to decrease by factor 7 the magnitude of input pulse with total duration of 3 ns. At last, a possibility of fast estimations for asymmetrical MF structures is revealed.

REFERENCES

- [1] Zabolotsky A.M., Gazizov T.R., Bova A.G., Radasky W.A. Dangerous pulse excitation of coupled lines. 17-th Int. Zurich Symp. on Electromagnetic Compatibility. EMC-Zurich 2006, pp. 164–167.
- [2] Gazizov T.R., Samotin I.E., Zabolotsky A.M., Melkozerov A.O. Design of printed modal filters for computer network protection. Proc. of 30-th Int. conf. on lightning protection. Sept. 13–17, 2010. Cagliari, Italy, pp. 1246-1–1246-3.
- [3] Gazizov T.R., Zabolotsky A.M., Melkozerov A.O., Dolganov E.S., Orlov P.E. Improved design of modal filter for electronics protection. Proc. of 31-st Int. conf. on lightning protection. Sept. 2–7, 2012. Vienna, Austria, pp. 1–4.
- [4] Gazizov T.R., Zabolotsky A.M., Dolganov E.S. Modal filter as a device for electrostatic discharge protection of onboard computers and control units of space vehicles. Russian Physics Journal. August 2012. Vol. 55, No. 3, pp. 282–286.
- [5] <http://www.emcotec.ru/catalog/fpsi/>
- [6] Gazizov T.R. Analytic expressions for Mom calculation of capacitance matrix of two dimensional system of conductors and dielectrics having arbitrary oriented boundaries. Proc. of the 2001 IEEE EMC Symp. Montreal, Canada. August 13–17, 2001. Vol. 1, pp. 151–155.
- [7] Zabolotsky A.M., Gazizov T.R. Modal filters for protection of onboard electronic equipment of a spacecraft. Tomsk State University of Control Systems and Radioelectronics Press. Tomsk. 2013. P. 151.

Modeling of grounding systems of power lines under pulse influence

Kirill I. Netreba
Ph.D. Student at Electrical
Engineering Department
SPbSPU, Russia
kirill.netreba@gmail.com

Nikolay V. Korovkin
Head of Electrical
Engineering Department
SPbSPU, Russia
nikolay.korovkin@gmail.com

Nikolay V. Silin
Head of Electrical
Engineering and
Electrotechnical Department
FEFU, Russia
silin22@mail.ru

Abstract: - The technique of determination of equivalent electromagnetic parameters of grounding systems of power lines is offered and examined. The technique is based on use of the experimental data gained by means of specially developed mobile experimental set. The result of identification is the linear circuit correctly reproducing electromagnetic characteristics of the grounding systems of power lines under arbitrary influences.

Key-Words: - grounding system, pulse influence, *RLC* model, lightning overvoltage

1 Introduction

In present time in Russia [1] and in other countries [2] so called resistive model of grounding system (GS) is used. According to this model grounding system is characterized by stationary resistance R on main (low) frequency and by “pulse” resistance $R_{imp} = \max(u)/\max(i)$ or $r(t) = u(t)/i(t)$ on pulse influences. It should be noted that in theoretical electrical engineering by pulse resistance it is traditionally understood reaction of the circuit on delta function [3], therefore term “pulse” resistance used in grounding theory is in quotes.

Resistive model of GS is simple but theoretically substantiated only for stationary regimes. In [4] absence of correlation between “pulse” resistance obtained under aperiodic and damped vibrational influences is shown. In [5] dependence of “pulse” resistance on frequency (or duration of pulse front) is demonstrated. Therefore when the frequency is changed correction coefficient has to be applied to R_{imp} .

Despite imperfections of usage R_{imp} as main characteristic of GS experimental and theoretical researches are conducted based on “pulse” resistance. To be able to compare “pulse” resistance of different GS without usage of correction coefficient special pulse generator with reference pulse characteristics 0.25/100 and 10/350 mcs is created [6]. In [7, 8] an attempt to synthesize equivalent *RLC* circuit of GS based on specially defined “local pulse resistance” at time interval till 1mcs was made. Obviously, synthesis of equivalent *RLC* circuits is the next step in GS model development. However, synthesis of such circuits on “pulse” resistance basis, which doesn’t take into

account electromagnetic energy in reactive elements, without usage of standard electrical circuit synthesis methods is not substantiated and unpromising.

Exception is [9] where oscillogram of transient resistance was obtained as a result of pulse experiment’s data processing. Based on this oscillogram the simplest *RL* model was fitted. Time constant was also found graphically. In [10] parametric synthesis of the second order passive impedor was done based on pulse experiment data. However, in case of GS not only parameters of equivalent circuit are unknown, but its topology as well.

So, resistive model of grounding systems based on “pulse” resistance does not fully reproduce real processes result in GS under pulse influences.

2 Synthesis of *RLC* models of ground grids

In this paper methodic of synthesis of GS *RLC* models is presented. It allows to analyse pulse regimes of GS work in lightning protection systems on strict theoretical basis as opposed to methods based on “pulse” resistance. Transient resistance $z(t)$ is used as primary parameter of grounding system. Numerically it is equal to voltage on the GS under current unit step and it is defined from voltage oscillograms for any current test pulse. Realization of $z(t)$ by methods of electrical circuit synthesis allows to define equal circuit and electromagnetic parameters of GS.

2.1 Initial data processing

Experimental data (see Fig.1) $i(t)$ and $u(t)$ obtained under standard lightning pulse influence include information about different physical processes going with process of current flow through GS. Sparking in the soil, wave processes in grounding ware, electromagnetic radiation by tower pole for aerial lines are among these processes. They are quite high-frequency, fast damped and not associated with equivalent circuit of GS though its influence is clearly seen in experimental data. For reduction of this influence experimental data is smoothed and then used for equivalent circuit synthesis.

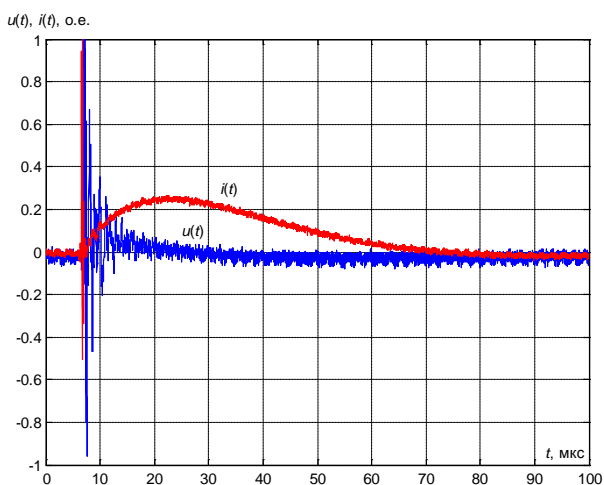


Fig.1. Experimental data.

Experimental data smoothing process is not formal because smoothing degree influence on topology and parameters of equivalent circuit of GS. Smoothing algorithm used in this work for typical set of experimental data is shown below. Initial data is obtained for rod-shaped GS of overhead line tower.

Experimental data (about 10^4 points) obtained by double-channel oscilloscope in $0-10^{-4}$ s time range is interpolated on 2^{15} points and then by Fast Fourier Transform (FFT) converted into frequency domain (2^{14} of complex amplitudes). After this frequency spectrum is cut off up to 2^{11} harmonics. Therefore, frequency of the highest harmonic is 20 MHz which correspond to bandpass of used oscillograph. So, on this stage only high frequency noises appearing due to decimation of analog signal, high frequency noses of measuring complex and electromagnetic environment are removed.

For further smoothing equal frequencies of the processes going with process of current flow through GS have to be evaluated. For this purpose let's use next appropriate estimations. Supposing 25 meter tower pole as quarter-wave oscillator this kind

of antenna will have frequency about 1 MHz. Wave processes due to wave reflection in grounding ware from power line towers have frequencies ($v_C/4l$, $v_C/8l$) 0.5–1 MHz. Sparking and wave processes in the grounding system itself have higher equal frequencies because of small geometrical size of areas where they occur. So, initial data can be smoothed up to 500 kHz equivalent frequency.

With decrease of smoothing frequency complexity of parametric synthesis task reduces and accuracy of initial data approximation increases. Therefore GS models for relatively short frequency range (switching overvoltage) can be obtained quite easily and significantly increase modeling accuracy.

2.1.1 Usage of optimization algorithms for synthesis of RLC models

In general parametric synthesis problem can be definitely solved by exhaustive search among all possible values of varying parameters. However, huge amount of possible solutions makes such approach unreasonable concerning time resources. In case of continuous varying parameters which is the case for this work such approach is found to be impossible.

Application of different optimization algorithms allows significantly reduce number of estimated solutions. Gradient methods are widely used to solve optimization problems with continuous parameters and with possibility to calculate gradient of functional. However in present work since optimization problem is not unimodal soft compute techniques which allow to find global extremum of the problem are preferable [11, 12].

To do parametric synthesis of equivalent circuit of GS next optimization algorithms were studied and software realized: simulated annealing, genetic algorithm and artificial bee colony algorithm (bee algorithm). These algorithms are able to work with large number of optimized parameters which allows to synthesize circuits of any order to approximate transient processes with high equivalent frequency.

Let's consider application of artificial bee colony algorithms to parametric synthesis problem.

Let's equivalent circuit of the GS has topology as it is shown in Fig.2, a. Voltage source $e(t)$ is experimentally obtained and smoothed voltage oscillogram $u(t)$. The task is to fit values of circuit's parameters so the error between circuit current $i_{circ}(t)$ and experimental smoothed current $i_{exp}(t)$ was minimized (Fig.2, b):

$$I(p) = \int_0^t |i_{exp}(t) - i_{circ}(t)| dt, I(p) \xrightarrow{p \in \Pi} \min, (1)$$

where I – minimizing function, Π – tolerance range of parameter's vector p , $p=[R_1 R_2 R_3 L C]$ – vector of equivalent circuit parameters.

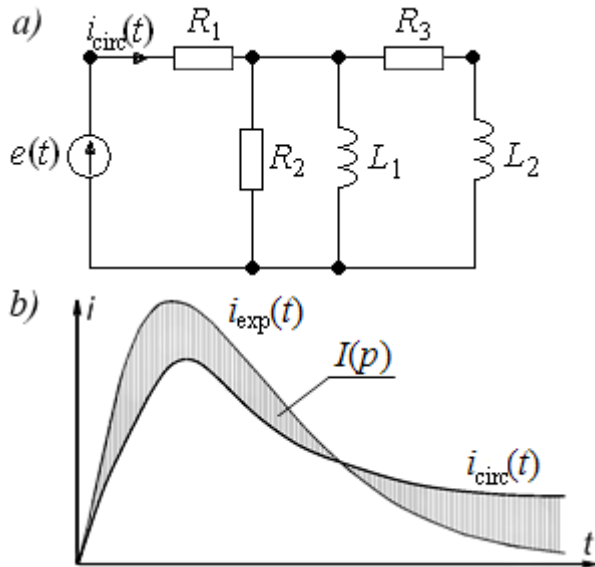


Fig.2. *a* – example equivalent circuit, *b* – formulation of optimized function.

Next parameters were applied for bee algorithm: number of scouts $s = 20$, number of best patches $n = 4$, number of perspective patches $m = 20$, number of bees following best patches $N = 15$, number of bees following perspective patches $M = 6$.

The result is shown in Fig.3. One may see that current $i(t)$ and voltage $u(t)$ smoothed up to 500 kHz are rapidly oscillating functions, however approximation accuracy of obtained equivalent circuit enough high. Thus, average error is $\varepsilon_{ave500}=2.7\%$ and maximum error is $\varepsilon_{max500}=25.8\%$.

In Fig.4 equivalent circuit for voltage and current oscillograms smoothed up to 75 kHz is shown. Comparison between Fig.3 and Fig.4 allows to estimate influence of smoothing degree of initial data on topology and parameters of equivalent circuit of GS.

As one may see with increase of equivalent frequency of experimental data circuit topology is changed, however not in essence. New physical processes are modeled by appearance of new elements in the circuit. As one may see moving from 75 kHz to 500 kHz one RC chain was added to approximate high frequency processes. At the same time common parameters of the equivalent circuit

found for lower frequency oscillograms stay the same for higher frequency oscillograms.

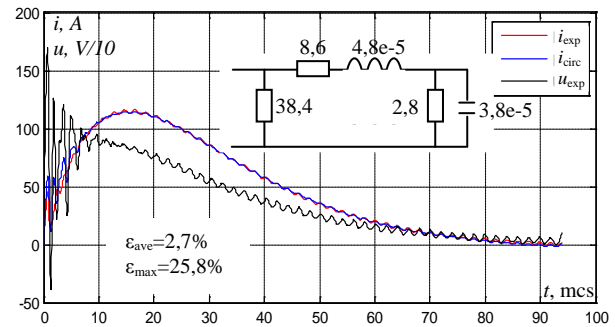


Fig.3. Voltage and current oscillogram smoothed under 500 kHz equal frequency and equivalent circuit.

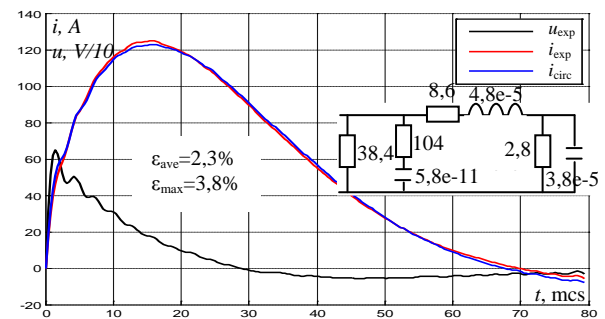


Fig.4. Voltage and current oscillogram smoothed under 75 kHz equal frequency and equivalent circuit.

3 Calculation of lightning surge

Let's estimate influence of GS model on overvoltage at substation and its protecting surge arrester after lightning stroke at overhead line 150 kV. Fig.5 shows system model to calculate overvoltage for different GS models.

Standard lightning impulse 1,2/50 mcs with 350 kV amplitude is appear at voltage maximum in stationary regime. Overvoltage wave goes to protected object PO (substation) and its surge arrester SA through Line1. The length of Line1 enough large so wave processes between PO and SA is damped before arrival of reflected from voltage source wave on Line1.

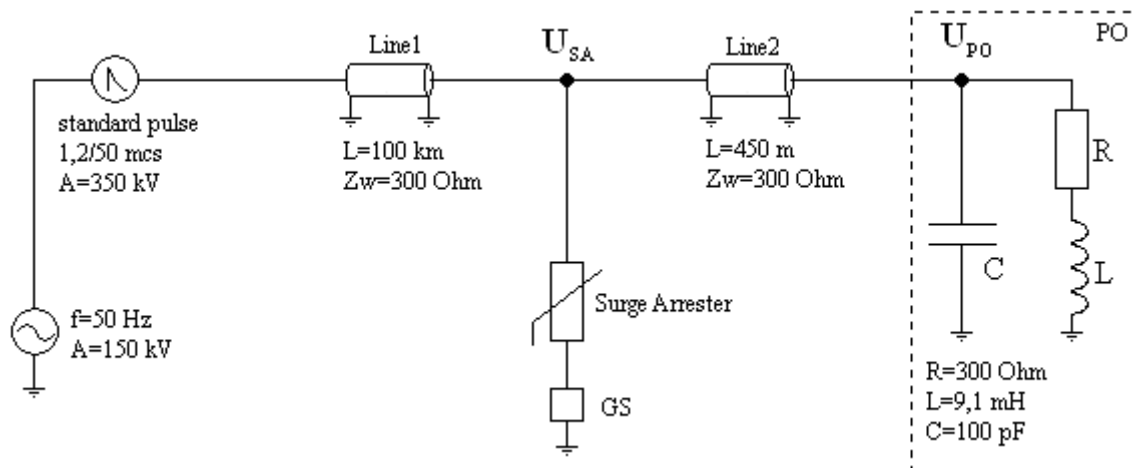


Fig.5. Test model to calculate overvoltage dependence on GS model.

Protected object is the transformer working at active-inductive load. Active resistance of the load is equal to wave impedance ($R = 300 \text{ Ohm}$). Surge arrester is placed 450 m from PO and connected to grounding system GS.

Let's consider several GS models. The first one (Fig.6, a) neglects active-inductive resistance of the ground system. In this resistive model the value of the R and calculated as stationary resistance of the equivalent circuit.

The second one (Fig.6, b) GS is modeled simply as part of full equivalent circuit. The third one (Fig.6, c) is full equivalent circuit obtained by method described above. Calculation results of the overvoltage at surge arrester and protected object are shown in Fig.6.

Let's describe wave processes between SA and PO in general on resistive model sample (curve 1, 5 in Fig.6). As it is seen in the figure protected object voltage may significantly exceed SA voltage. Overvoltage wave is reflected from transformer without sign change which leads to voltage double at protected object comparing to incoming wave (by duration of lightning impulse about a few microseconds transformer is equal to capacitor)

Going back to surge arrester reflected from transformer wave goes though protected span almost without distortion at the beginning while total stress of incoming from Line1 wave and reflected from

transformer wave is less than discharge voltage of surge arrester (U_{dis}). When total voltage of SA is close to U_{dis} reflected from transformer wave starts to reflect from surge arrester with sign change. Therefore after several reflections overvoltage at transformer gradually becomes equal to discharge voltage of surge arrester.

According to results shown in Fig.6 GS model has significant influence on maximum overvoltage which occurs at protected object and surge arrester. Usage of RLC circuits as GS models leads to appearance of maximums at each transitional process. For resistive model with surge arrester response its current increase instantly limiting its voltage level. For RLC model current through surge arrester cannot increase immediately because of inductance (see Fig.7) which lead to transitional process and thus higher voltage level. As one can see maximum overvoltage at SA for resistive model is 10,3 % less than for full model which is considerable.

For protected object errors for the first maximums are even larger because of voltage doubling (see table in Fig.6). When used resistor as a GS model maximum voltage level at protected object is 13,8 % less comparing to maximum voltage with full circuit as a GS model.

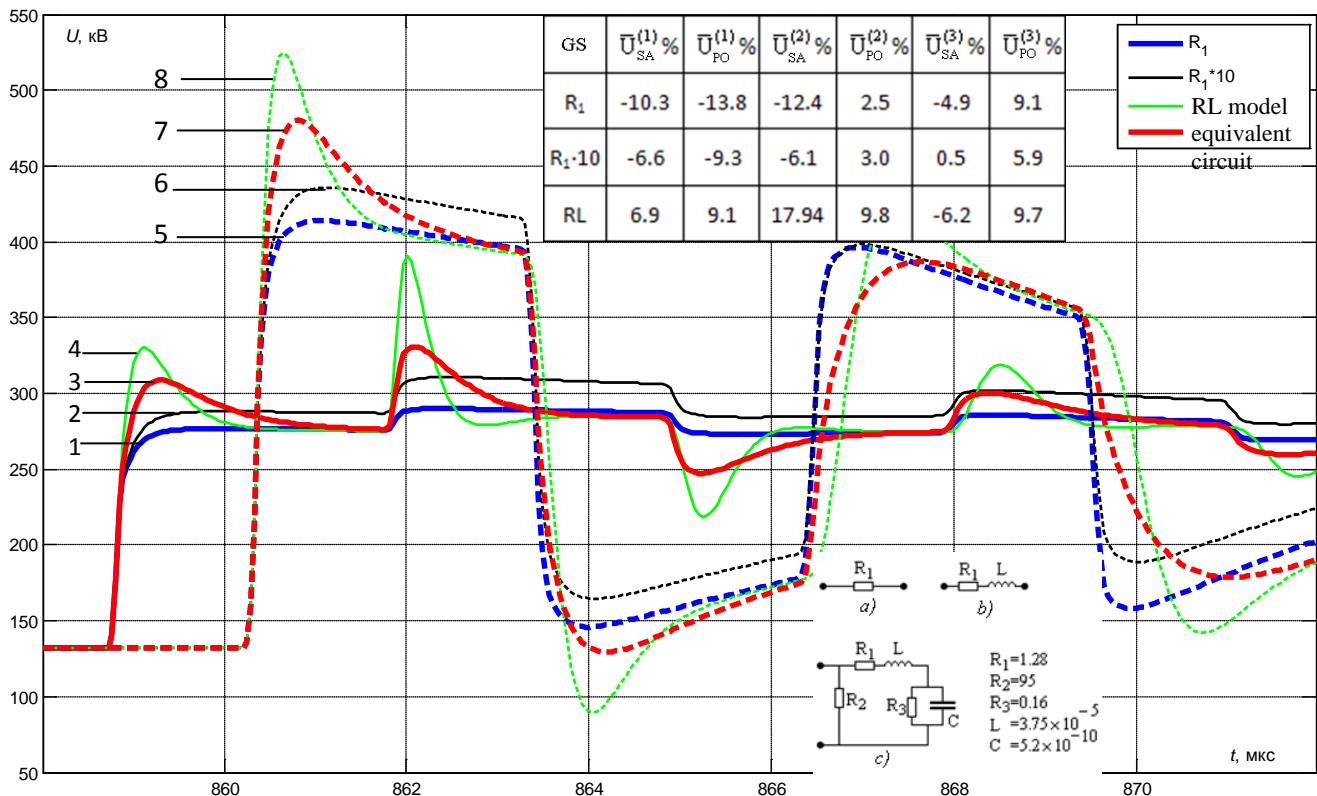


Fig.6. Overvoltage at SA (1,2,3,4) and PO (5,6,7,8), table of maximum errors (relative to equivalent circuit), variants of GS models.

To compensate active-inductive character of GS it is suggested sometimes to increase simply the value of active resistance. Such an approach as results shows does not give qualitative and quantitative correlation. Increase of active resistance value ten times (from 1,28 Ohm to 12,8 Ohm) remains error between maximum voltage values considerable high (see curves 2, 3 and 6, 7 in Fig. 6). At the same time approximate accounting of GS inductive characteristics leads to wrong results. For concerned case the results are overrated (see curves 4, 8 in Fig. 6).

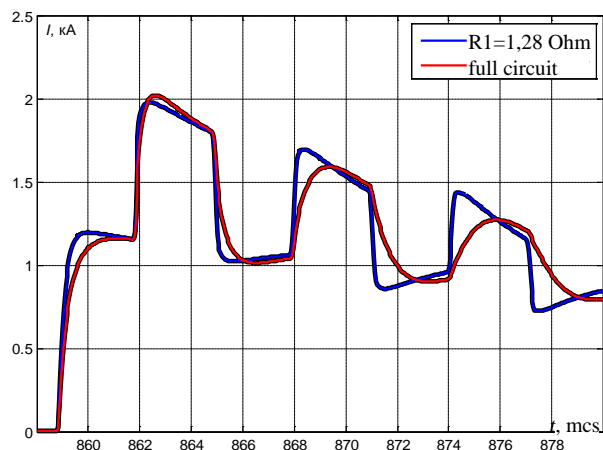


Fig.7. Current through surge arrester.

From obtained results one may see that the reason of overvoltage at protected objects depends not only on surge arrester characteristics. Significant error in real overvoltage definition is the error in calculation of grounding system's transient resistance.

4 Conclusion

The technique of determination of equivalent electromagnetic parameters of grounding systems of power lines is offered and examined. The technique is based on use of the experimental data gained by means of specially developed mobile experimental set. Calculations of the overvoltage occurring due to lightning stroke show significant dependence of maximum voltage levels at protected object on GS models.

References:

- [1] РД 153-34.0-20.525-00. Методические указания по контролю состояния заземляющих устройств электроустановок. М.: СПО ОГРЭС, 2000.
- [2] Methods for measuring the earth resistance of transmission towers equipped with earth wires /

- Technical Brochure № 275, WG C4.2.O2 // Electra. 2005. № 220.
- [3] К.С. Демирчян, Л.Р. Нейман, Н.В. Коровкин, В.Л. Чечурин, *Теоретические основы электротехники: В 3-х т. // СПб.: Питер, 2003.*
- [4] Ю.В.Целебровский, С.В.Нестеров, В.А.Цилько, *Импульсные сопротивления заземления молниеводов ОРУ подстанций // Первая Российская конф. по молниезащите: Сб.докл. – Новосибирск: Сибирск. энерг. академия, 2007. – С. 243–248.*
- [5] Е.Я. Рябкова, *Заземления в установках высокого напряжения. – М.: Энергия, 1978. – 224 с.*
- [6] М.В.Матвеев, М.Б. Кузнецов, М.Ю. Лунин, *Исследование высокочастотных характеристик ЗУ с помощью испытательных генераторов на базе управляемых нелинейных элементов // Третья Российская конф. по заземляющим устройствам: Сб.докл. – Новосибирск: Сибирск.энерг.академия, 2008. – С.55–60.*
- [7] Н.И. Гумерова, А.Н. Данилин, Б.В. Ефимов, В.В. Колобов, Ю.М. Невретдинов, В.Н. Селиванов, Ф.Х. Халилов, *Влияние локальных импульсных сопротивлений заземления основного и защитного оборудования на надежность грозозащиты подстанций // Первая Российская конф. по молниезащите: Сб.докл. – Новосибирск: Сибирск.энерг.академия, 2007. – С.383–392.*
- [8] А.Н.Данилин, Д.В.Куклин, *Импульсные измерения заземлителей аппаратов высоковольтных подстанций и опор ВЛ на подходах // 8-й межд. симп. по электромагнитной совместимости: Сб.докл. – Санкт-Петербург, 2009. – С.54–57.*
- [9] З.Стойкович, М.Савич, *Инженерный метод определения грозоупорности линий высокого напряжения с учетом импульсных характеристик заземлителей // Электричество. – 1999. – № 3. – С.16–22.*
- [10] Ю.Н.Исаев, В.А.Колчанова, Т.Е.Хохлова, *Определение параметров двухполюсника при воздействии импульсного напряжения // Электричество. – 2003. – №11. – С.64–67.*
- [11] Н.В. Коровкин, В.Л. Чечурин, А.А. Поттиенко, *Обратные задачи в теоретической электротехнике, Изд. СПбГПУ, 2003.*
- [12] N.V. Korovkin, V.L. Chechurin, M. Hayakawa, *Inverse problems in electric circuits and electromagnetics, USA, Springer, 2006.*

Authors Index

Adamyan, Y. E.	32	Korovkin, N. V.	100, 108
Akimov, D. A.	70	Korzinin, N. M.	26
Arora, M.	77	Krivosheev, S. I.	32
Batchenkova, N. A.	47	Lamuta, C.	58
Belyaev, N. A.	100	Madanipour, V.	35
Caliandro, P.	58	Mahmoodi-Kaleybar, M.	35
Ceballos Jr., R. M.	47	Minevich, T. G.	43
Ceballos, R. M.	47	Montazeri-Gahjavarestani, M.	35
Chanana, S.	77	Morales, C. T.	47
Chudny, V. S.	100	Netreba, K. I.	108
Di Girolamo, G.	58	Odintsov, M. V.	70
Dubitskiy, S. D.	66, 84, 95	Pagnotta, L.	58
Egorov, A.	21	Rani, A.	47
Frolov, O. V.	70, 100	Sakhno, L.	66
Gazizov, A. T.	104	Sakhno, O.	66
German-Galkin, S.	21	Silin, N. V.	26, 55, 108
Goncharov, V.	55	Singh, V. P.	90
Greshnyakov, G. V.	84, 95	Strizhak, P. A.	74
Ivanova, E. V.	74	Titkov, V. V.	32
Koroleva, Y. V.	74	Tomasov, V.	21
Korovkin, N. V.	26, 43, 55	Virva, E. A.	32
Korovkin, N. V.	70, 84, 95	Zabolotsky, A. M.	104